UNIVERSITAT DE BARCELONA

Regulation of synthesis, transport and accumulation of lipids in Lipid droplets by Acetyl-CoA carboxylase and Caveolins. How cells accumulate lipids but reduce lipotoxicity

Frederic Morales Paytuví

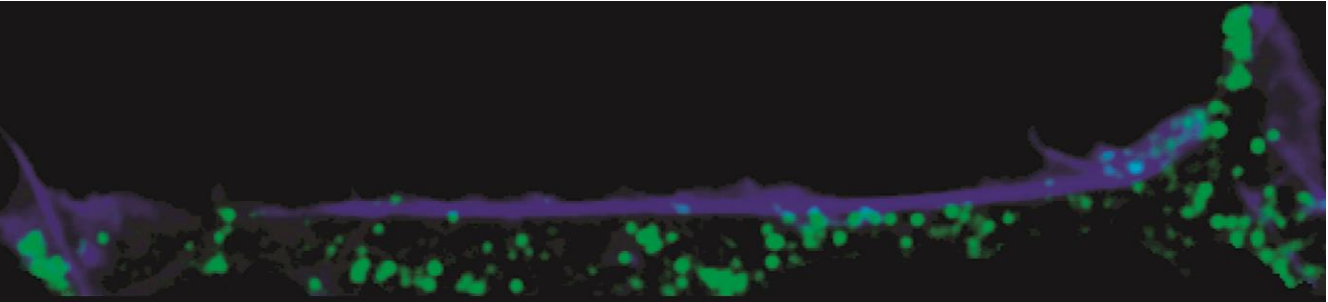
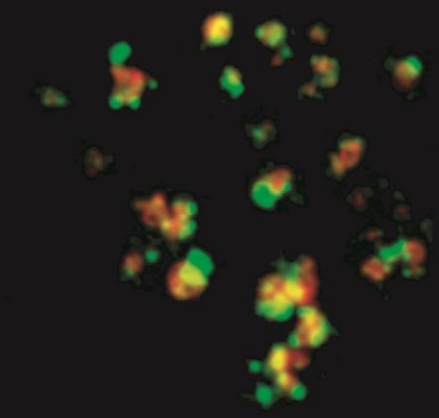
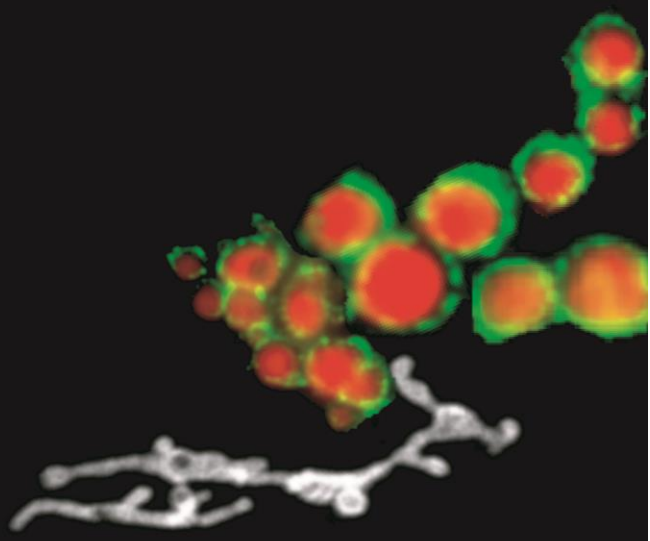
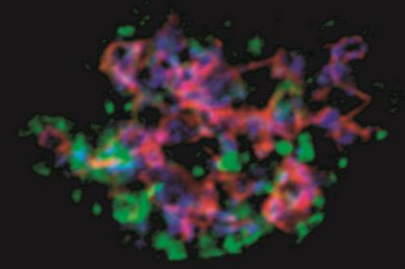

REGULATION OF SYNTHESIS, TRANSPORT AND ACCUMULATION OFLIPIDS IN LIPID DROPLETS BY ACETYL-CoA CARBOXYLASE AND CAVEOLINS

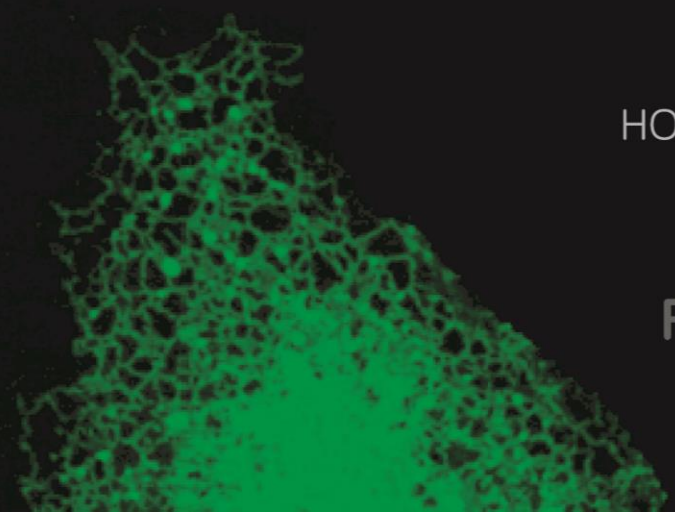

HOW CELLS ACCUMULATE LIPIDS
BUT REDUCE LIPOTOXICITY

Frederic Morales Paytuví

DOCTORAL PROGRAMME IN BIOMEDICINE
UNIVERSITAT DE BARCELONA

REGULATION OF SYNTHESIS, TRANSPORT AND ACCUMULATION OF LIPIDS IN LIPID DROPLETS BY ACETYL-COA CARBOXYLASE AND CAVEOLINS. HOW CELLS ACCUMULATE LIPIDS BUT REDUCE LIPOTOXICITY

DOCTORAL MEMORY SUBMITTED BY THE PhD STUDENT

FREDERIC MORALES PAYTUVÍ

LIPID TRAFFICKING AND DISEASE GROUP
INSTITUT D'INVESTIGACIONS AUGUST PI I SUNYER (IDIBAPS)
AND UNIVERSITAT DE BARCELONA (UB)

TO OBTAIN THE DOCTORAL DEGREE
BY THE UNIVERSITY OF BARCELONA

UNIVERSITAT DE BARCELONA

UNDER THE DIRECTION OF ALBERT POL SOROLLA AND MARTA BOSCH RODRÍGUEZ FROM THE BIOMEDICINE DEPARAMENT OF THE FACULTY OF MEDICINE AT THE UNIVERSITY OF BARCELONA

PhD student	Tutor and director	Director
FREDERIC MORALES PAYTUVÍ	**ALBERT POL SOROLLA**	**MARTA BOSCH RODRÍGUEZ**

A tota la meva família,

A tots els meus amics,

I a tothom que ho ha fet possible.

“The good thing of Science is that it’s true,
whether or not you believe in it”

Neil deGrasse Tyson

CONTENT

Figures and Tables

Common Abbreviations

ACC	Acetyl-CoA Carboxylase
BAT	Brown adipose tissue
Ca^{2+}	Calcium ions
CAC	Carboxylic acid cycle
CAV	Caveolin protein
CHOP	C/EBP-homologous protein
CPT1	Carnitine palmitoyltransferase 1
DAG	Diacylglycerol
DNL	De novo lipogenesis
ER	Endoplasmic reticulum
ERAD	Endoplasmic reticulum associated degradation
ER-phagy	Autophagy in ER
FA	Fatty acid
FAO	Fatty acid oxidation
GC	Golgi Complex
GSH	Glutathione antioxidant
HFD	High fat diet
LD	Lipid droplet
NAFLD	Non-alcoholic fatty liver disease
OA	Oleic acid
PA	Palmitic acid
PLIN	Perilipin proteins
PM	Plasma membrane
ROS	Reactive oxygen species
T2DM	Type 2 diabetes mellitus
TAG	Triacylglycerol
UPR	Unfolded protein response
WAT	White adipose tissue
WT	Wild type
XBP1S	X box-binding protein 1 spliced

INTRODUCTION

1. Caveolae and Caveolins

Caveolae are described as 60-80 nm bulb shaped or cup-like invaginations of the plasma membrane (PM) early discovered in 1953 (**Fig. 1A**) (*1, 2*). Caveolae are a striking feature of many cell types such as endothelia, smooth muscle and adipocytes (*3*). They comprise as much as 50% of the PM area in primary fat cells, which denotes the importance of this structure for some functions of the tissue (*4*). Those are related to endocytosis, mechanoprotection, and signalling processes (*5*).

Caveolin-1 protein (CAV1) was discovered in 1992 as the main component of caveolae (*6, 7*), and the solely transient expression of this protein drives *de novo* caveolae formation at the PM (*8*). Moreover, CAV1 presents cholesterol binding properties when it oligomerizes, which is required for the transport of the protein to the PM and the formation of caveolae (*9-11*). CAV1 expression is also regulated by cholesterol, since *CAV1* gene is under the control of sterol regulatory element-like sequences, which are directly activated by this molecule and inhibited by SREBPs (sterol regulatory-element binding proteins) (*12*). CAV1 presents two different isoforms, α and β, which are generated by alternative splicing of the CAV1 gene (*13*), but the differences of both isoforms in function remain unknown (*14*). **CAV2** was discovered by sequencing proteins purified from caveolar membranes (*15*) and **CAV3** was identified by the screening of cDNA libraries looking for CAV1 homologs (*16*). CAV2 was clearly linked to CAV1 since both *CAV1* and *CAV2* genes are close located in the chromosome 7 (*17*). In this manner, CAV1 and CAV2 are ubiquitously expressed and they oligomerize to form caveolae, otherwise CAV2 alone cannot reach the PM nor promote caveolae formation (*18*). In contrast, *CAV3* gene is located in chromosome 3 (*19*), CAV3 expression is restricted to skeletal muscle (*16*), and the expression of it drives caveolae formation independently from the other proteins of the family (*20, 21*).

The physiological reason for the existence of 3 caveolin members, two alternative CAV1 isoforms, or a differential tissue-dependent expression of them are puzzling questions (*3*).

1.1. Caveolae formation

Apart from caveolins, caveolae formation requires the action of cavins and accessory proteins for the precise assembly of the structure and for achieving a proper lipid microenvironment (**Fig. 1B**).

1.1.1. Cavins

Cavin proteins display two positively charged helical regions (HR1 and HR2) flanked by negatively charged disordered regions (DR1, DR2 and DR3) (*3*). By these domains, cavins can hetero- or homo-oligomerize forming trimers with high promiscuity (*22*), but with the exception of cavin2 and cavin3 which are unable to associate with each other, and they segregate in different caveolar domains (*23*). Cavin1 is ubiquitously expressed, and, with caveolin proteins, they are the two minimum required components for caveolae formation (*24*). Cavin2 is suggested to participate in shaping caveolae at lung and cardiac endothelia, since the loss of this protein depletes caveolae formation in those tissues (*25*). Cavin3 plays a helper role with cavin1 for caveolae formation (*26*). Cavin4, which is specific for muscle, is thought to form muscle-specific caveolae by interacting with CAV3 (*27*). Cavin trimers are only targeted to caveolae by cavin1 binding to PtdIns(4,5)P_2 (phosphatidylinositol 4,5-bisphosphate) and PtdSer (phosphatidylserine) (*22*). Caveolin and cavin interaction is stabilized by the cytoplasmatic domain of RORα (retinoic acid receptor (RAR)-related orphan receptor alpha), although it is only occurring during some processes such as cancer progression (*28*).

1.1.2. Caveolar accessory proteins and lipid composition

Other proteins of the EHD (Eps15 homology domain) protein family have been shown to oligomerize around the neck of caveolae and stabilize preformed caveolae (*29*). EHD2 also binds to Pacsin2/Syndapin2, which contains a F-bar domain with membrane curvature-inducing properties necessary for caveolae formation (*30, 31*). Caveolin and cavin lipid-binding activities promote the caveolae enrichment of cholesterol, glycosphingolipids, PtdINs(4,5)P_2, PtdSer, and GM3 ganglioside, which favour the separation of caveolar nanodomains from the bulk of the PM (*32, 33*). On the other hand, cholesterol or PtdINs(4,5)P_2 depletion promote the disassembly or flattening of caveolae, remarking the importance of lipid microenvironment for caveolae formation (*24, 34*).

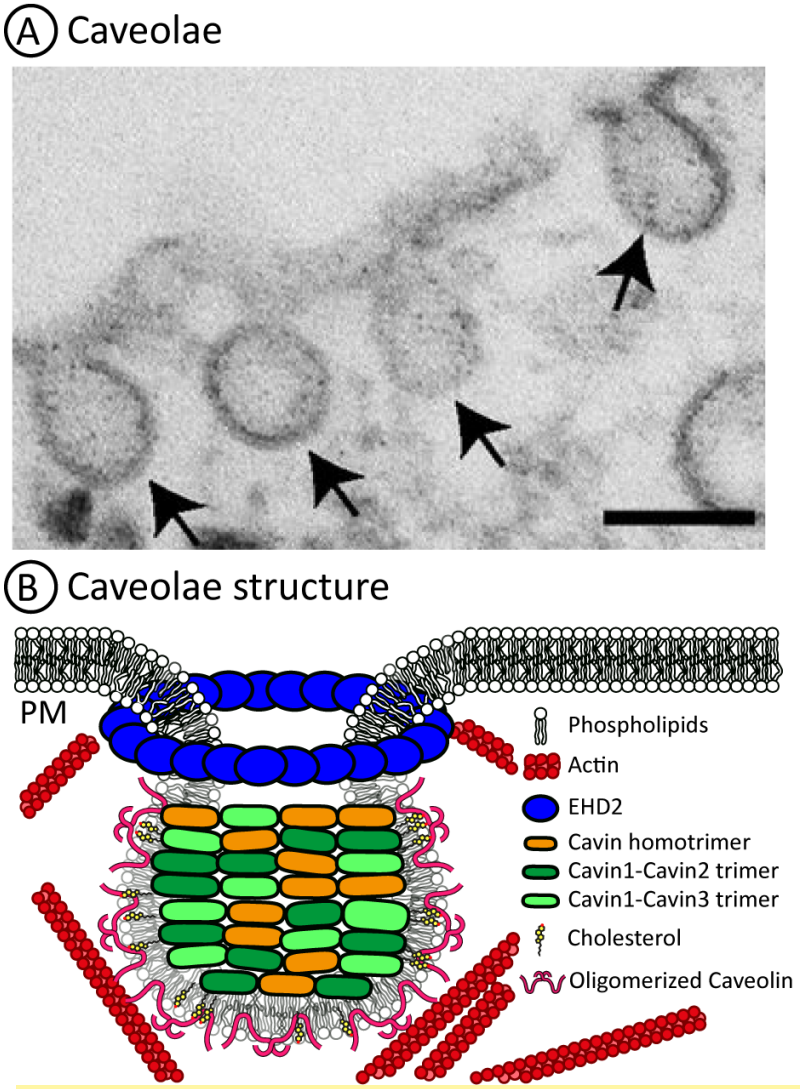

Figure 1. Caveolae.
(**A**) Electron micrograph (scale bar=100nm) and (**B**) Structure.
Abbreviation: Eps15 homology domain 2, EHD2.
Modified: (A) from (*35*), and (B) from (*36, 37*).

1.2. Caveolae functions

Canonical functions of caveolae have been related to **endocytosis**, **signal transduction**, and **sensing of extracellular stress** (*5*) (**Fig.2**). Additionally, CAV3 in muscle is associated with the dystrophin-glycoprotein complex for the organization of the T-tubule system (*38*).

1.2.1. Endocytosis

Initial studies described caveolar endocytosis for many cargoes such as albumin, iron-transferrin, insulin, cholesterol, low density lipoproteins (LDL), simian virus 40 and chemokines (*39*). Despite that, subsequent studies demonstrated that these substrates are rarely dependent of caveolae for their endocytosis; for example, Simian virus 40 was better internalized in cells lacking caveolae (*40*). Nowadays, caveolae budding from the PM is related to the control of caveolar density, rather than the endocytosis of specific cargoes (*41*). CAV1 knock-out (KO) mice fed with high-fat diet (HFD) showed an impaired ability to uptake LDL proteins from the blood, which protected them from atherogenesis and atherosclerosis (*42*). Thus, transendothelial endocytosis of LDL, from the apical blood vessel lumen to the basal membrane, seems to be the only contrasted specific cargo for caveolar endocytosis (*43*).

1.2.2. Signal transduction

Endothelial nitric oxide synthase (eNOS) (**Fig. 2A**). In steady state, eNOS is bound to caveolae preventing the spontaneous activation of the pathway (*44*). Increase in vascular tension is signalled by the entry of calcium ions (Ca^{2+}) inside the cell, which activates calmodulin (*45*). Then, calmodulin binds to eNOS by displacing CAV1 and promotes nitric oxide (NO) production, which in turn increase vascular permeability and reduce blood pressure (*46*).

Lipid metabolism (**Fig. 2B**). Adipose tissue is one of the tissues with highest CAV1 expression and caveolar density (*47*). Loss of CAV1 promotes a severe atrophy of the tissue (lipoatrophy) but prevents from body weight gain the mice fed with HFD (*48*). Lipoatrophy decreases the tissue capacity to properly store triacylglycerols or triglycerides (TAGs), which are then accumulated in blood (*48*). Similar phenotypes were appreciated in cavin1 KO mice (*49*), denoting that the functions of these proteins in adipose tissue are performed through caveolae. Mechanistically, it was described that CAV1 transports the fatty acid translocase (FAT/CD36) to PM controlling by this mechanism the overall fatty acid (FA) uptake of the cell (*50*).

Glucose metabolism (**Fig.2C**). Mice with CAV1 or cavin1 mutations showed defects in insulin signalling and glucose uptake, meaning that caveolae participates also in those processes (*48, 49, 51, 52*). First, it controls the distribution of insulin receptor since loss of CAV1 decreases in a 90% the localization of this receptor at the PM (*53*). The availability of this receptor is also controlled after insulin signalling: CAV1 is phosphorylated on Y14 residue and promotes the internalization of both bound caveolae and insulin receptor to stop this pathway (*54-56*). Second, CAV1 controls glucose receptor transporter type 4 (GLUT4) translocation and therefore glucose uptake, despite their mechanisms are unknown (*52*). Third, it also controls glucose-mediated insulin secretion in pancreatic β-cells, where it forms a complex with inactive cdc42 protein bound to GDP in insulin granules (*57*). When blood glucose levels raise, CAV1 is phosphorylated and dissociated from cdc42-GDP (*57, 58*), which allows GTP binding to cdc42 for the activation of the protein (*59*) and insulin granule secretion through the interaction with VAMP (vesicle-associated membrane protein) (*60*).

1.2.3. Stress sensors

Caveolae were first described as sensors for stress (mechanosensors, **Fig. 2D**) in models of membrane tension (hypotonic media and physical stretch), where after inducing a mechanic stress caveolae were flattened to avoid PM damage (*61*). In parallel, disassembled caveolar components were released to the cytoplasm, where they act as signalling molecules (*36*). Thus, cavins, which were first described as transcription factors (*62*), promote a pro-apoptotic signal linking PM damage with gene expression (*63*). EHD2 is also a transcription factor which downregulates the expression of caveolar components in response to increased membrane tension, and vice versa (*64*). Low membrane tension is also sensed by increasing caveolae density (*65*). During migration, low tension in the rear of the cell is also sensed by increasing caveolae density, allowing Rho activation and PM reorganization. UV (Ultraviolet radiation) and oxidative stress are also signalled through CAV1 phosphorylation, caveolae disassembly and release of caveolar components (*54, 61, 66*). As an example, cavin3 amplifies the DNA damage caused by UV light to trigger apoptosis in this case (*67*).

1.2.4. Caveolae in muscle

Caveolae have additional functions in muscle formation and healing. When muscle tissues are wounded, acid sphingomyelinase release by lysosome exocytosis is a signal of injury, which is sensed by caveolae for the removal of the injured tissue through caveolae endocytosis and allowing the resealing of the PM in muscle fibres (*68*). Responding to mechanical stress, caveolae trigger IL6/STAT3 (interleukin 6/signal transducer and activator of transcription 3) to buffer the increase in membrane tension (*69*). Moreover, during myoblast differentiation to myotubes, caveolae are specifically enriched in the invaginations of cardiac and skeletal muscle sarcolemma (t-tubules) (*16*). This way, they help in maintaining a proper action potential transmission between the exterior and the interior of the cell (*21*), likely through the interaction with β-dystroglycan complex (*38, 70*).

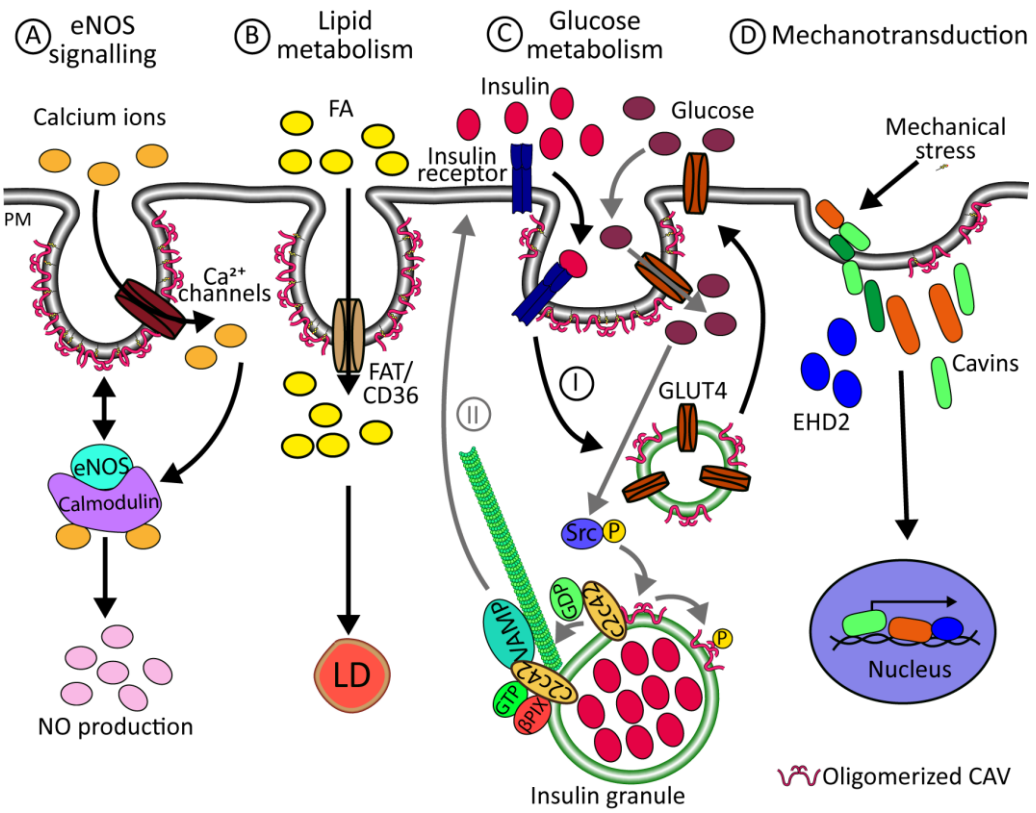

Figure 2. Caveolae functions.
Caveolae perform functions related to: (**A**) endothelial nitric oxide synthase (eNOS) signalisation, (**B**) fatty acid (FA) internalization, (**C**) insulin signalling (**I**) and secretion (**II**), and (**D**) sensing and transduction of mechanical stress.
Abbreviations: calcium ions, Ca^{2+}; nitric oxide, NO; FA translocase, FAT or CD36; glucose transporter type 4, GLUT4; vesicle-associated membrane protein, VAMP; Proto-oncogene tyrosine-protein kinase Src, Src; and p21-activated protein kinase exchange factor, βPIX.
Modified: (A) from (*46*), (C) from (*51*), and (D) from (*37*)**.**

1.3. Caveolin proteins

Caveolins present certain degree of homology: CAV1 and CAV3 share a 65% identical sequence and 85% similarity, whereas CAV2 only reaches 30% of identity and 50% similarity with the other two members (pairwise alignment, Needle, EMBOSS). CAV1α and CAV2 are similar in length, and have a molecular weight of ~21 kDa (*6*), while CAV1β lacks the residues 1-32 of α isoform (*13*) and presents a similar molecular weight than CAV3 (~18kDa) (*16*). Most of the differences in the aminoacidic sequence between caveolin proteins are in the first 15 residues of the N-terminal region and in the last 20 residues of the C-terminal region (see Results section).

1.3.1. Caveolin domains

Despite these slight differences, caveolins have equivalent domains and they can be extrapolated from CAV1, where most of the research has been carried out. They present a characteristic hairpin topology (**Fig.3**): central hydrophobic and scaffolding domains anchor the protein to membranes(*71, 72*), and are flanked by the N- and C-terminus facing the cytoplasm (*73*).

CAV N-terminal domain (light blue). It is in charge of the proper trafficking and oligomerization of caveolins (*74*). In this region, caveolin presents a diacidic (DXE) COPII (coat complex protein II) binding motif required for its transport to the Golgi complex (GC) (*75, 76*). Moreover, phosphorylation of the S80 residue control CAV1 exit from the endoplasmic reticulum (ER)(*77*). The N-terminal region is also necessary for caveolin oligomerization, where the conserved "FEDVIAEP" stretch (or signature domain) presents a pivotal role (*15, 74*). In this region, CAV1 shows a high regulation through the conserved tyrosine 14 (Y14), whose phosphorylation is involved in caveolae intracellular signalling as mentioned (*3, 54, 58, 66*).

Scaffolding domain (SCD, in green). It was proposed to participate in signalling since it potentially interacts with many proteins containing a putative caveolin binding domain (CBD) (*78*), and when solely injected in mice it triggers cell signalling (*79*). Despite these evidence, SCD domain is at least partially buried in the PM (*80*), and CBD-containing receptors are often presented in organisms lacking caveolae (*36*), which suggest that the SCD functions are not achieved by direct interaction. Alternatively, it was hypothesized that SCD peptide could affect the lipid composition of the PM and thereby affect signalling (*36, 80*). Lipid environment is controlled by SCD through hydrophobic anchoring into the cell membranes (*72*), and CLR recognition/interaction amino acid consensus (CRAC, L/V-$(X)_{1-5}$-Y-$(X)_{1-5}$-K/R) motif binding of cholesterol (*71, 81*).

Hydrophobic domain (in red). It is responsible for caveolin anchoring in the ER bilayer due to its high hydrophobicity (*82, 83*). Central prolines (P132L for CAV1, P117 for CAV2, and P104L for CAV3) induce a proline knot which is required for the protein topology (*84*). For example, CAV1 P132L mutations completely alter CAV1 folding by inducing dimerization, which is a good model to study the effects of misfolded caveolins (*85*). These mutations also exert a dominant-negative effect and promote a decrease in the stability (*85, 86*). CAV1 has been demonstrated to be palmitoylated in residues from the hydrophobic domain and the C-terminal region (*87, 88*). Although palmytoilation is not required for caveolae formation (*87*), it could influence caveolin oligomerization (*88*).

C-terminal (in orange). It is involved in the retrieval transport of caveolin from GC to ER, since both the addition of a dilysine motif (KKSL) at the C-terminal, or the natural frame-shift mutation CAV1 P158 introducing many acidic residues at the same region promoted caveolin accumulation in ER (*89, 90*).

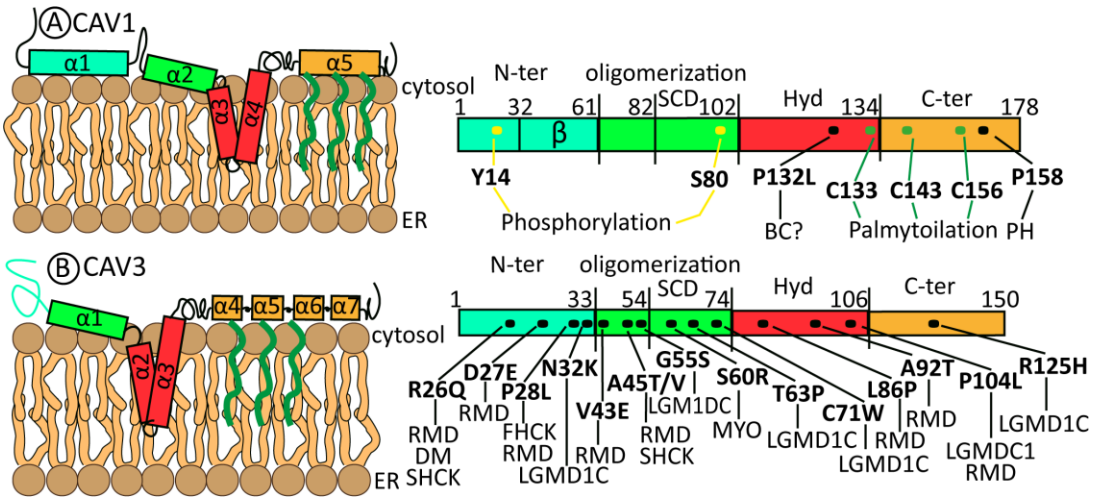

Figure 3. Caveolin topology and domains.
Topology and domains of (**A**) CAV1 and (**B**) CAV3. Important residues for phosphorylation, palmytoilation or mutation of caveolin are pointed in yellow, green, or black respectively. **Abbreviations:** N-ter, N-terminal domain; SCD, scaffolding domain; hyd, hydrophobic domain; C-ter, C-terminal domain; BC, breast cancer; RMD, Rippling muscle disease; SHCK, spontaneous hyperCKemia; FHCK, familial hyperCKemia; DM, distal myopathy; LGMD1C, limb girdle muscular dystrophy 1C, Myo, myopathy and PH, pulmonary hypertension. **Modified** from (*91, 92*).

1.4. Non-caveolar functions of caveolins

Although expressing caveolins, neither organisms such as *Caenorhabditis elegans* nor some mammalian cells such as hepatocytes, neurons, or lymphocytes, promote the formation of distinguishable caveolae (*93, 94*). This fact clearly suggests that additional functions of the protein are taking place outside caveolae, but they are largely unknown. A representative example of this organization in cells without caveolae was shown in PC3 prostate cancer cells (caveolin1 is expressed but cavin1 no), where caveolin forms the intermediate state of polyhedral scaffolds (*24, 95*). Therefore, non-caveolar actions of caveolin organized in scaffolds can take place before caveolae assembly (**Fig. 4B**).

1.4.1. Regulation of cholesterol

Caveolins outside caveolae are not restricted to the PM and they can be distributed in most of the cellular organelles (*93*). Moreover, their expression is regulated by cholesterol levels (*12*) and can also bind cholesterol (*81*). By these particularities, non-caveolar caveolin could act as a lipid sensor capable of redistributing cholesterol to cellular organelles when required (*93*), and additionally prevent cholesterol imbalances in cells (*93, 96*).

Cholesterol transport by caveolins is particularly important in liver, where only few caveolae are appreciated (*97*). Lack of CAV1 promotes a toxic mitochondrial accumulation of cholesterol, which favours the progression of non-alcoholic steatohepatitis (NASH) (*96*). In addition, it completely impairs liver lipid metabolism making the organ dependent on glucose oxidation as a source of energy (metabolic inflexibility) (*98-100*). Since lipid metabolism is affected, liver is unable to regenerate after partial hepatectomy, unless mice are additionally supplied with glucose (*98-100*). CAV1 also balances cholesterol levels of the mitochondria-associated membranes (MAMs), which are crucial for their functioning (*101*).

1.4.2. Structural roles

In brain, where CAV1 expression and caveolae formation are similar to liver (*25*), absence of caveolin promotes a 10% brain reduction and several behavioural and motor abnormalities in mice (*102*). At a cellular level, the lack of this protein impairs neuron pruning because the cholesterol membrane nanodomains required for Rho GTPases action are not formed, and therefore actin cytoskeleton is not regulated (*103*). In this case the structural role as organizer of membrane nanodomains is denoted.

A similar action was appreciated in lymphocytes, where CAV1 levels are even lower than hepatocytes and brain, representing only a 0.001% of lung endothelial expression (*104*). Despite these low levels, caveolin is active, functional, and regulated since it responds for example to LPS-simulated infection (*105*). For this, cholesterol nanodomains induced by CAV1 are important for immunological synapses: I) between T cells and antigen presenting cells (APC) and II) between B cell and T cell receptors (*106-108*). If these interactions fail because lack of CAV1, mice are sensitized to bacterial, viral, and parasitic infections (*106-108*). Autoimmunity symptoms such as high autoantibody titters or Immunoglobulin G (IgG) deposits in kidney were also appreciated (*104*).

1.5. Caveolins and disease

CAV1 P132L mutation was detected at 16% of breast cancers, which was the first evidence of CAV1 implication in cancer progression (*109*). On the contrary, this mutation was not detected on tumour samples of further studies (*110*), which made the implication of this mutation in the progression of the disease controversial, but first established a link between caveolin and cancer. Furtherly, expression levels of CAV1 were related to the prognosis of many cancers such as prostate (*111*) or breast (*112*). Low stromal expression of CAV1 could decrease caveolae regulation of protein kinase B (PKB or Akt) and TGFβ1 (tumour growth factor β1) signalling, which increases the aggressiveness of the cancer (*111*). High expression of CAV1 was detected in prostate and breast cancer patient samples (*113*), where CAV1 sustains Akt signalling and inhibits the tumour suppression activity of the serine/threonine PP1 and PP2A (*114*).

CAV3 mutations promoted a myriad of muscular diseases confirming the role of CAV3 and caveolae on muscle (**Fig. 3B**). Most of them were associated to muscle damage such as CAV3 R26Q, which caused increased creatine kinase levels on blood, rippling muscle disease, and distal myopathy (*115*). CAV1 presents fewer mutations triggering disease than CAV3, but the reason is unknown.

1.6. Caveolin trafficking

CAV trafficking can be divided in two steps: caveolin oligomerization for **transport to the PM**, and **caveolae budding-off** for lysosomal degradation.

1.6.1. Caveolin transport to the plasma membrane (PM)

CAV is synthesized and transported to the PM, where it forms caveolae (**Fig.4**). It is inserted into the ER by a signal recognition particle (*9*), and it rapidly oligomerizes in ~15nm complexes formed by ~15 caveolin proteins with a sedimentation coefficient of 8 Svedbergs (8S), which serve as building blocks for caveolae formation (*75, 116*). Complexes of 8S are then transported to GC via COPII transport, where they are furtherly oligomerized in 60S filament-like complexes (*75*). Oligomers of 60S are proposed to be formed by oligomerized small scaffolds (S1A, equivalent to 8S complexes) and big scaffolds (S2B), which finally form caveolae (*95*). Caveolin in the GC is then transported to the PM by vesicular delivery in a process favoured by cholesterol addition or slowed by cholesterol depletion (*11*). There, they remain stable and form caveolae (*117*).

During this process, approximately 140 CAV1 proteins and 20,000 molecules of cholesterol need to be oligomerized and bound to achieve the formation of 1 caveola (*73, 93*). Thereby, transport of caveolin to the PM is expected to require a specific regulation to achieve caveolae formation. Mutations of CAV1 and CAV3 have in common that alter the normal transport and reduce the stability of the protein, retaining the protein in the ER or GC (*73*).

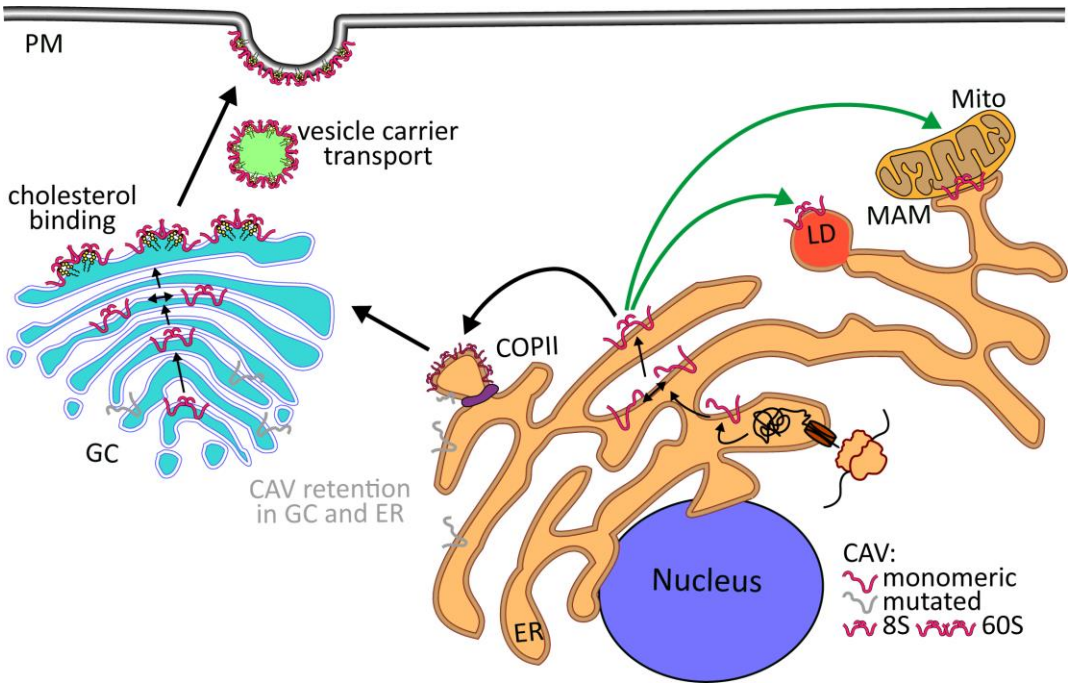

Figure 4. Caveolin transport to the plasma membrane (PM).
Caveolin is synthesized, inserted, and oligomerized in 8S complexes in the endoplasmic reticulum (ER). During this process, non-caveolar functions of caveolin can take place inside the ER nanodomains: lipid droplets (LDs), and mitochondria-associated membranes (MAMs). Alternatively, caveolin is transported to Golgi complex (GC) through COPII (coat complex protein II) vesicles, and to the plasma membrane (PM). Caveolin mutants which fail to reach PM (in grey) are retained in the ER or GC.
The different forms of caveolins are indicated in the legend.
Abbreviations: mitochondria, mito.
Modified from (*73*)**.**

1.6.2. Caveolae bud off and lysosomal degradation of caveolins

Caveolae buds off from PM to endosomes (**Fig.5**) to maintain the required amount of caveolae during mitosis (*118*). This process is repressed by EHD2 and activated by cavin3 (*119*). On the other hand, ATP-dependent oligomerization of EHD2 around the caveolae neck is important to induce membrane tubulation (*67, 119*). This tubulation favours dynamin 2 binding, which promotes the bending, constriction, and fission of the membrane in a GTP-dependent manner (*120*). After detachment of caveolae from PM, it is fused to early endosomes by rab5 transport through the microtubules (*121*).

Caveolin from the PM is targeted to lysosomal degradation by the ESCRT (endosomal sorting complex required for transport) (*122*). Then it is first reoriented to face the lumen of endosomes (retrotranslocation) (*122-124*). Retrotranslocation starts with the monoubiquitylation of caveolin N-terminal region (*123*), which is then recognized by UBXD1 (ubiquitin-like domain 1 adaptor protein) (*124*). VCP/p97 (Valosin-containing protein/p97, or Cdc48) recognizes UBXD1 bound to caveolin and then retrotranslocates both proteins in an ATP-dependent manner (*124*). Alternatively, caveolin can be also polyubiquitylated (lysine-48 ubiquitin complexes), which is a known signal to target proteins to lysosomal degradation (*125*). Then, the ankyrin repeat domain 13 family of proteins (Ankrd13) binds to the polyubiquitylated CAV1 through its ubiquitin-interacting motif and promotes the action of VCP/p97 (*126*). Finally, with a proper luminal orientation of caveolin, lysosome fusion is promoted during multivesicular body formation (MVB) and caveolin is finally degraded (*122*).

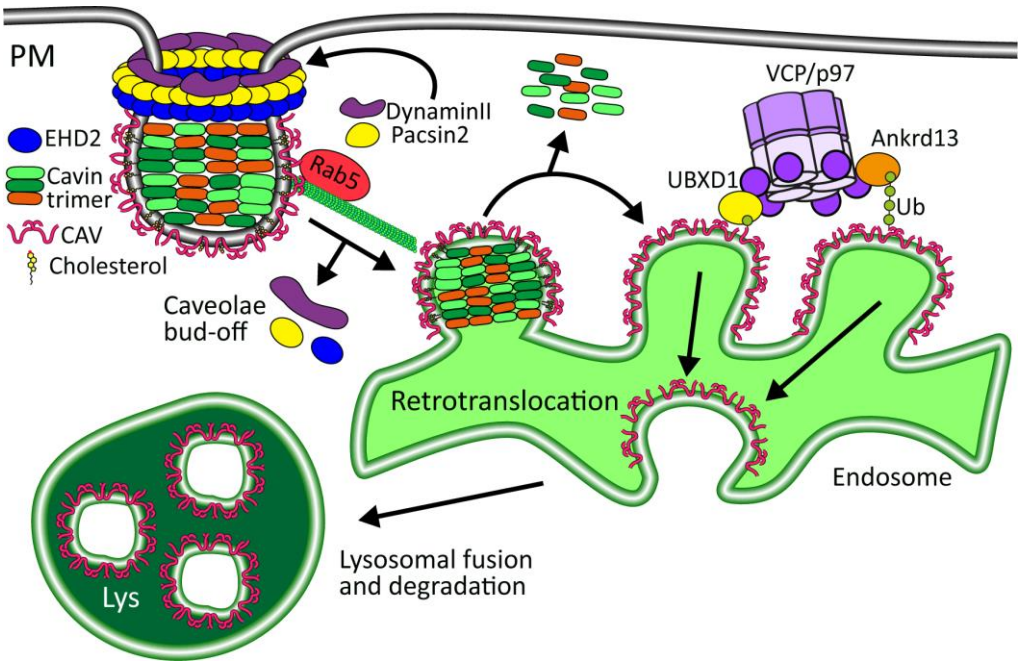

Figure 5. Fates of internalized caveolin.
Caveolae are internalized by budding off from the PM while releasing caveolin to the endosomes. Then, it is retrotranslocated and targeted to lysosomes (Lys) for degradation.
Abbreviations: Ankyrin repeat domain 13 protein, Ankrd13; ubiquitin, Ub; ubiquitin-like domain 1, UBXD1; Valosin-containing protein/p97, VCP/p97.
Modified from (*36, 122*).

2. Proteostasis in the Endoplasmic Reticulum (ER)

2.1. Proteostasis

Proteostasis, or protein homeostasis, refers to the cellular processes controlling the expression, folding, transport, and degradation of proteins (*127*). Aging-related diseases such as Alzheimer or Parkinson are caused by protein aggregation, which is the consequence of proteostasis disruption (*127*). On the other hand, improving proteostasis could also prevent the onset of other diseases such as type 2 diabetes mellitus (T2DM) (*127*).

ER is the site of protein synthesis and the starting point of the exocytic pathway; therefore, most of protein control steps are performed in this compartment (*128*). Proteostasis is linked to many other ER functions such as lipid metabolism, calcium regulation, or redox state (*128, 129*). Mechanisms involved in the ER proteostasis are summarized in **Fig.6** and will be introduced in the following sections.

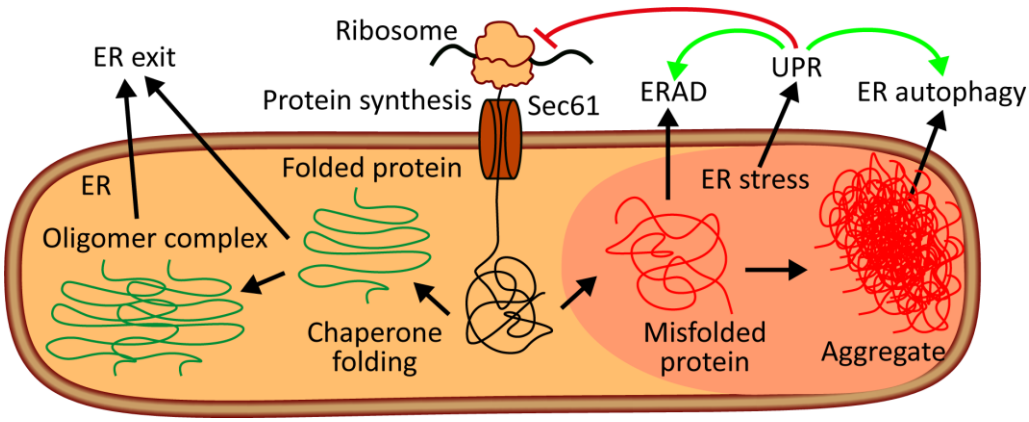

Figure 6. Proteostasis in the Endoplasmic reticulum (ER).
Nascent proteins are recruited in the ER, translocated to the ER lumen, cotranslationally folded, and oligomerized if required before exiting the ER. Errors of folding lead to protein misfolding and even aggregate formation promoting ER stress (in red). Misfolded proteins trigger the unfolded protein response (UPR), which increases their degradation through ER-associated degradation (ERAD) or through autophagy engulfment if aggregated. UPR also stops protein synthesis.
Modified from (*127*)

2.2. Protein folding and ER stress

Nascent proteins, while being synthesized, are cotranslationally transported to the lumen of the ER by the Sec61 protein in the translocon complex (*130*). OST (Oligosaccharyl-transferase) glycosylates the side chains of asparagine residues in the nascent polypeptides, which targets the protein to the calnexin/calreticulin system to check for proper folding (*131, 132*). PDI (Thiol-disulphide oxidoreductase and isomerase) assists in the disulphide bond formation (*133*), and if the protein is properly folded, it exits the ER (*134*). If not, protein is reglycosylated to restart the cycle (*132*). Continuous unsuccessful cycles targets the protein to ER-associated degradation (ERAD) by the removal of a mannose on the glycan chain (*135*).

If errors are produced during folding, because ER machinery is not able to cope with high levels of protein synthesis, proteins are accumulated in a misfolded or aggregated state that leads to ER stress (*127*). Three factors determine the folding of proteins in the ER: correct protein N-glycosylation, redox state, and calcium concentration (*133, 136, 137*). The implication of these processes in lipid and ER homeostasis is introduced in section 3.4.

2.3. Unfolded protein response (UPR)

UPR is activated to translate ER protein folding deficiencies into coordinated cell changes to maintain proteostasis (**Fig. 7**). Unfolded proteins are sensed by BIP (binding-immunoglobulin protein) chaperon, which is usually bound to the UPR signal transducers IRE1α (inositol-requiring protein 1α), PERK (protein kinase RNA-like ER kinase) and ATF6 (activating transcription factor 6) (*138*). Under ER stress, BIP displacement from IRE1α and PERK promotes the autophosphorylation, activation, and dimerization of these receptors (*138*). The RNAse domain of IRE1α is activated and induces the alternative splicing of the XBP1 (X box-binding protein 1) transcription factor to its activated form (**XBP1S**) (*139*). Activated PERK phosphorylates EIF2α (eukaryotic translation initiation factor 2α), which in turn activates ATF4 (activating transcription factor 4) (*140*). ATF6, when released from BIP is transported to the GC, where it is cleaved by site-1 and site-2 proteases (S1P and S2P) for activating its transcription factor activities (ATF6f) (*141*).

This response primarily promotes an immediate adaptive response to prevent the synthesis of more proteins which would exacerbate ER stress (*142*). Protein translation is reduced generally by EIF2α (*143*), and particularly for some ER-located proteins by IRE1-dependent decay (RIDD) (*144*). Secondly, IRE1α, XBP1S, ATF4 and ATF6f promotes the activation of genes related to ER folding, ERAD, protein quality control, ER biogenesis and autophagy to counteract unfolded protein accumulation (*142*). Unsuccessful amelioration of ER stress triggers apoptosis of the damaged cell (*142*), which is prevented in normal conditions by the mitochondrial caspase pathway through Bcl-2 (B cell lymphoma 2) protein family (*145*). Bcl-2-associated X protein and Bcl-2 homologous antagonist killer apoptosis (Bid/Bax apoptosis) are activated through the downregulation of Bcl-2 (*145*). **CHOP** (C/EBP-homologous protein), whose expression and transcription activity are activated by the continuous signalling through the PERK-ATF4 axis, also downregulate Bcl-2 and promote apoptosis (*146*).

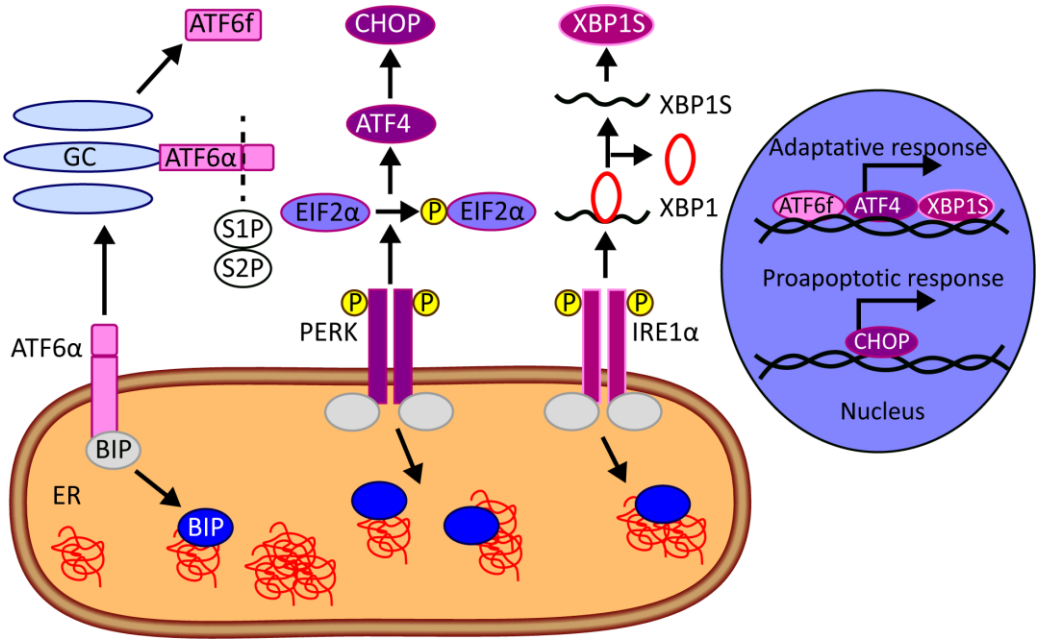

Figure 7. Unfolded protein response (UPR) triggered by ER stress.
Three axes of the unfolded protein response (UPR): I) ATF6 (activating transcription factor 6), II) PERK (protein kinase RNA-like ER kinase) and III) IRE1α (inositol-requiring protein 1α). The transcription factors involved and the responses they promote are represented.
Abbreviations: binding-immunoglobulin protein, BIP; site-1 and site-2 proteases, S1P and S2P; eukaryotic translation initiation factor 2α, EIF2α; activating transcription factor 4, ATF4; C/EBP-homologous protein, CHOP; X box-binding protein 1, XBP1; and XBP1 spliced, XBP1S.
Modified from (*147*).

2.4. ER-associated degradation (ERAD)

Unfolded or misfolded proteins, which have not passed the ER quality control, are targeted to degradation by ERAD (**Fig. 8B**). The process starts with the recognition of misfolded proteins by cytosolic or ER luminal chaperones (*148*), such as heat-shock protein 70 or 40 (hsp70 or 40) or BIP, which recognize the unfolded hydrophobic domains of proteins (*149, 150*). Mannose trimming in the N-glycosylation pattern of the protein is also a signal that targets proteins to ERAD by favouring the interaction with EDEM, OS9 (Osteosarcoma amplified 9) and XTP3B adaptor proteins (*134, 151*). Moreover, non-native disulphide bridge formation is also detected through PDI which targets the protein to ERAD through BIP binding (*152*).

Targeted ERAD substrates are retrotranslocated (or dislocated) to face the cytoplasm where they are degraded. The best characterized system is formed by Sel1L (suppressor/enhancer of lin-12-like) and Hrd1 (3-hidroxy-3-metylglutaryl-coenzime A reductase degradation protein 1) (*153*), but other proteins such as sec61 can be involved (*154*). Adaptor proteins of the system (such as EDEM, PDI, OS9, XTP3B or chaperons) bound to ERAD substrates are then transferred to Sel1L for the Hrd1 retrotranslocation (*145*). In this complex, Derlin1 also can cooperate with Hrd1 as a helper (*155*). While protein face the cytoplasm, it is polyubiquitylated directly by Hrd1 (*156*) or other E3 ubiquitin ligases (*153*). Polyubiquitinated proteins are completely extracted to the cytoplasm by VCP/p97 in an ATP-dependent manner (*157*), and finally degraded by the proteasome catalytic subunits (*158*). Inhibition of proteasomal degradation by MG132 treatment leads to ER stress and the overloading of UPR and ERAD (*159*). ERAD also targets proteins that are prone to aggregation such as CFTR (cystic fibrosis transmembrane receptor), whose 75% is degraded right after its synthesis (*160*). On the other hand, ERAD also modulates the function of some proteins such as HMG-CoA reductase during cholesterol synthesis by promoting the degradation of the protein (*161*).

Figure 8. Protein degrading systems in ER: Autophagy (ER-phagy) and ER-associated degradation (ERAD).
(**A**) Representation of the three endoplasmic reticulum autophagy (ER-phagy) mechanisms: autophagosome-mediated macro-ER-phagy, micro-ER-phagy of ER domains and vesicular delivery.
(**B**) ER-associated degradation (ERAD) of misfolded proteins by protein delivery to Sel1L (suppressor/enhancer of lin-12-like) and Hrd1 (HMG-CoA reductase degradation protein 1) retrotranslocation system, E3 protein ubiquitination, VCP/p97 (valosin-containing protein/p97) cytosolic extraction, and proteasomal degradation.
Abbreviations: autophagy-related protein 8, atg8; and microtubule associated protein 1A/1B-light chain 3, LC3

2.5. Autophagy in ER (ER-phagy)

Substrates that fail to enter ERAD or are prone to be aggregated need complementary systems to be degraded. Proteasome and autophagy are the two major cell mechanisms involved in eukaryotic protein degradation, whose action is interdependent (inhibition of one system promotes the activation of the other) (*162*) (**Fig. 8A**). Autophagy in ER (ER-phagy) is also triggered by UPR (*142*) and degrades ER structures or protein aggregates which are too big or tightly folded to enter ERAD (*163*). Three types of autophagy exist depending on the lysosome targeting: delivery of budded vesicles from ER containing misfolded proteins, micro-ER-phagy, consisting in the direct engulfment of small ER portions by lysosomal invaginations, or macro-ER-phagy of autophagosome-enclosed ER fragments (*163*). Macro-ER phagy is useful for removing protein aggregates detected by adaptor proteins, which interact with both the unfolded protein in the ER lumen, and atg8 (the autophagic protein 8) (*163*) or LC3 (microtubule-associated protein 1A/1B-light chain 3) cytosolic members (*163*). Then, the ER is encircled by an autophagosome and degraded by lysosomal fusion (*164*).

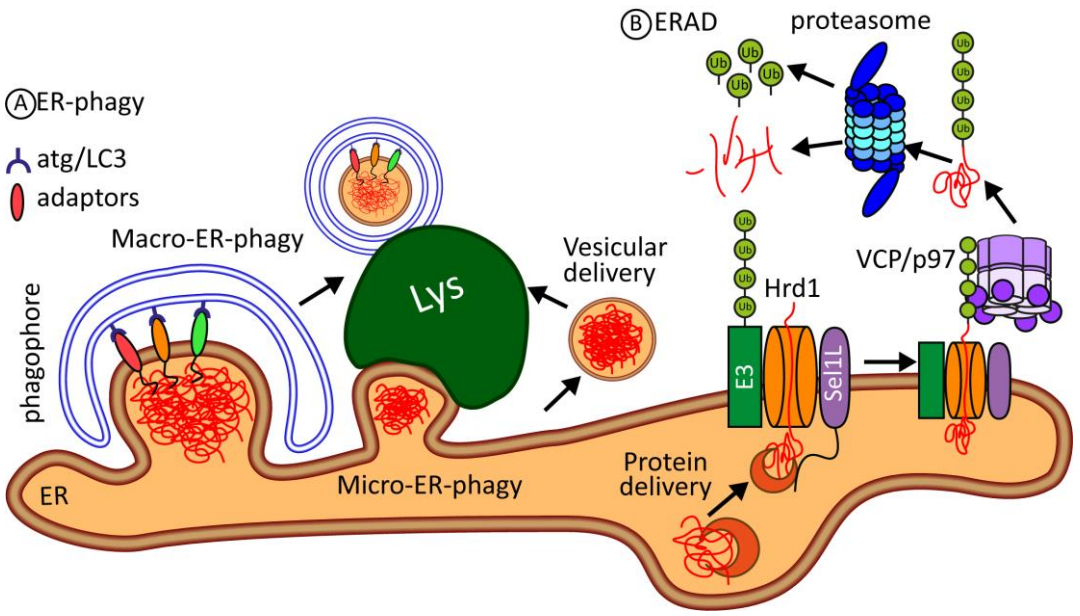

3. Lipid droplet (LD)

Lipids are essential for many cellular processes such as membrane formation (phospholipids and cholesterol), energetic metabolism (FAs), signalling (diacylglycerols, DAGs), and production of physiological compounds (lipoproteins, bile salts or hormones) (*165, 166*). This explains why most of eukaryotic cells (from unicellular yeasts to complex plants or mammals) possess the ability to assemble, storage, and supply lipids through a specialized organelle: lipid droplet (LD) (*167, 168*). LDs have a unique structure consisting of a neutral lipid core (TAGs and cholesterol esters) encircled by a phospholipid monolayer, which is coated by LD proteins (*169*). Despite being considered as passive cytosolic fat depots for decades, LDs are a highly dynamic and controlled organelle not only involved in lipid metabolism and energy supply (*167, 168*), but also in cell proteostasis (*170, 171*), storing of bioactive lipids such as vitamins (*172*), and even in primary immunity against pathogenic infections (*173*). However, if lipid metabolism of LDs is deregulated, FAs outside LDs can be toxic and ultimately trigger cell death (*174*). Therefore, LDs also prevent lipotoxicity by buffering toxic lipids (*169*).

3.1. LD proteins

LD proteins can be divided in two subtypes: class I hairpin and class II amphipathic proteins (**Fig. 9A**) (*169*). Proteins from other cellular compartments can also be targeted to LDs through lipid modifications or by interacting with resident proteins (*175*).

Type I: hairpin. They are anchored in the ER membrane while synthesized in a signal recognition particle manner (*175, 176*). Alternatively, they can be anchored to the ER membrane post-translationally through specific binding partners, such as in the case of UBXD8 (*177*). Type I proteins adopt a hairpin topology, where a central hydrophobic membrane-embedded domain links both N- and C-terminal ends facing the cytoplasm (*9, 178*). Many proteins are included in this group such as UBXD8, AUP1 (ancient ubiquitous protein 1), ACSL3 (long-chain-FA-ligase-Coenzyme A (CoA) proteins 3), DGAT2 (diacylglycerol O-acyltransferase 2), glycerol-3-phosphate acyltransferases 4 (GPAT4), caveolins, and ALDI (associated with LD protein 1) (*179*). When inserted into the ER, type I proteins can traffic to LDs through their amphipathic helix, which senses and accommodates the protein at the LD monolayer (*180, 181*).

Type II: amphipathic. They are directly targeted from the cytoplasm to the LD coat by their amphipathic helices, but why they are selective for the LD monolayer is the subject of active investigation (*175*). Current models propose that the particular composition of the LD monolayer, with low levels of phosphatidylserine and lack of cholesterol (*182*), may help in the folding of otherwise disordered amphipathic helices of type II proteins (*183*). For example, CCT (CTP:phosphocoline cytidyltransferase) senses the LD monolayer through the lipid packing defects characterized by high levels of DAGs and phosphatidylethanolamine (PE), and low levels of phosphatidylcholine (PC) (*184*). Examples of this group include CTP, perilipins, and viperin (*175*).

The perilipin (PLIN) or PAT (perilin-ADRP-TIP47) family. PLINs 1-5 are the major group of LD-binding proteins (*185*). By three differential properties, PLINs in the LD surface control LD stability and supply of lipids (see section 3.2). First, they present a tissue-dependent expression: PLIN2 and 3 are ubiquitous, PLIN1 and PLIN4 are expressed in adipose tissue, and PLIN5 is mainly expressed in oxidative tissues including heart, liver, and skeletal muscle (*186*). Second, PLINs presents a differential lipid affinity: PLIN1, PLIN2 and PLIN5 binds preferentially to TAG-enriched LDs (*187*), while PLIN4 binds to cholesterol ester enriched LDs, and PLIN3 to LDs or ER membranes with a high DAG content (*188*). Third, they also differ on the sub-cellular localization: PLIN1 and PLIN2 mostly localize to LD (they are commonly used as LD markers (*189*)), whereas PLIN3 and PLIN5 are also present into the cytosol (*190*).

3.1.1. Protein sorting and degradation in LDs

On the one hand, LD proteins need to be properly sorted into LDs so that they achieve their correct formation and stabilization (*175*). A part of their LD-targeting motif, proteins must be retained into LDs by some active mechanism, otherwise they would diffuse from LDs to the ER or the cytoplasm. One of these mechanisms is through the degradation of the proteins as soon as they leave the LDs. This is especially important for hairpin proteins, because when present in the ER they can induce a change in the morphology of this organelle by inducing membrane curvature (*191*). Therefore, hairpin proteins are degraded by ERAD through the ubiquitination by E3 ligase Doa10, which results in the net accumulation of the proteins in LDs (*192*). These could also occur to type II LD proteins such as perilipins, which are ubiquitylated when they are in the cytosol (*175, 193*).

On the other hand, LDs can act as degrading hubs for LD-resident (*175*) and external proteins from other compartments such as histones (nucleus), chaperones (cytosol), caveolins (PM), or apolipoproteins (ER) (*194*), which are targeted to LDs under ER stress (*195*) (**Fig. 9B**). It suggests that LD targeting is an escape hatch which prevents the accumulation of misfolded proteins in the ER (*195*). Consistently, LDs act as protein depots (*170*), and they contain ubiquitin-ligases or VCP/p97 proteins involved in ER protein degradation (*175, 193*). Proteins can also be degraded in LDs by autophagy (lipophagy), which presents two different mechanisms that also helps in the lipid supply of LDs. Macrolipophagy targets the engulfment of portions or small LDs by LC3-II signalling in the surface of LDs, autophagosome encirclement, and lysosome fusion (*196, 197*). Another relevant mechanism is chaperon-mediated autophagy (CMA) that was described for PLIN2 and PLIN3 (*198*), where both PLINs contains a CMA-targeting motif pointing them to lysosomal degradation by binding to LAMP-2A (lysosome-associated membrane protein 2A) (*198, 199*).

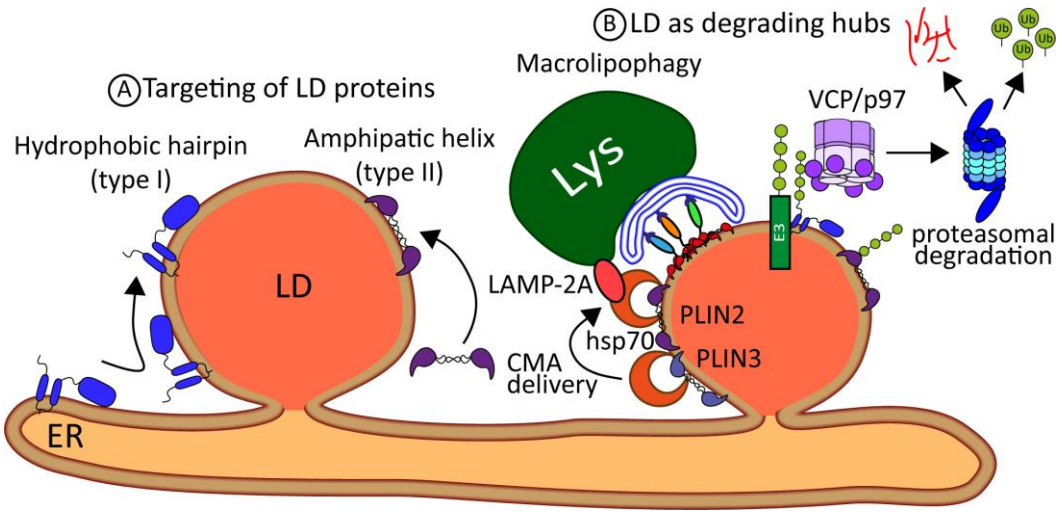

Figure 9. Protein targeting and sorting to lipid droplets (LDs).
(**A**) Trafficking of LD type I and type II proteins.
(**B**) LD as protein degradation hubs: LD autophagy (Macrolipophagy), chaperon-mediated autophagy (CMA), and proteasomal degradation of LD and LD-targeted proteins.
Abbreviations: heat-shock protein 70, hsp70; lysosome-associated membrane protein 2A, LAMP-2A; and ubiquitin-ligase E3, E3.

3.2. LD biogenesis

LD biogenesis starts with the accumulation of TAGs between the two leaflets of the ER bilayer (*200*) (**Fig.10**). These TAGs are synthesized from glycerol and FAs in the ER (**Fig.15**) (*165, 201, 202*): FAs are activated by ACSL proteins, which adds a CoA, and then undergo the sequential reactions of GPAT, PAP (acyl-glycerol-3-phosphatase), and DGAT enzymes from the TAG synthesis pathway. Cholesterol esters are also formed in the ER by ACAT1 and 2 (cholesterol O-acyltransferase 1 and 2) (*203*).

Both hydrophobic TAGs and cholesterol esters are accumulated between the ER bilayer and form globules (*166*), which are stabilized by the ER transmembrane protein FIT2 (fat storage-inducing transmembrane protein 2) (*204*). FIT2 has the capacity to bind DAGs and TAGs and starts the partitioning of the ER bilayer (*204*). Globule formation promotes an ER membrane bending which is sensed by ACSL3 (*180*). When localized at nucleation sites, ACSL3 couples FA activation to TAG synthesis, which favours the accumulation of TAGs inside LDs (*205*). Phospholipase A2 (PLA2) action is also required since it increases the production of lysophosphatidic acid (LPA) from phosphatidic acid (*206*), which with only one FA chain facilitates the negative curvature of the neck of LDs (*207*).

While emerges from the ER, the LD is stabilized by the action of PLIN3, that senses DAG formation and coats the monolayer of LDs (*188*). Complementary proteins such as the transmembrane protein seipin, participate in the growing of the nascent LDs by sensing early TAG accumulation on LDs, and controls LD growing by regulating the machinery involved in TAG synthesis (*208*). VPS13 A and C (Vacuole sorting-associated protein 13 A and C proteins) are in ER-LD contact sites, where they deliver the necessary phosphatidylcholine for LD monolayer expansion (*209*).

Growing and stability of LDs is increased depending on the amount of lipids to be stored, and by the action of PLINs in the LD surface which is essential (*210*) (**Fig.10**). Their presence on LDs is regulated through a crowd control mechanism (*199*), where PLIN3 is displaced by PLIN2 (*211*), which in turn is displaced by PLIN1 (*212*). This is possible because thanks to the different lipid-binding affinities of PLINs: PLIN3 senses DAGs only exposed during the early formation of LDs, while PLIN2 and PLIN1 have a greater affinity for TAGs of grown LDs (*187*). That way, LD is stabilized while growing, since PLIN2 prevents the release of lipids with a higher effectivity than PLIN3, but less than PLIN1 (*213*). LD stability also fits with the tissue requirements: in enterocytes, where TAG and DAG storing from dietary absorption is transitory, PLIN3 is upregulated (*214*), while in liver and adipose tissue, which have the highest lipid storing capacity, PLIN2 and PLIN1 respectively are highly expressed (*211, 213*).

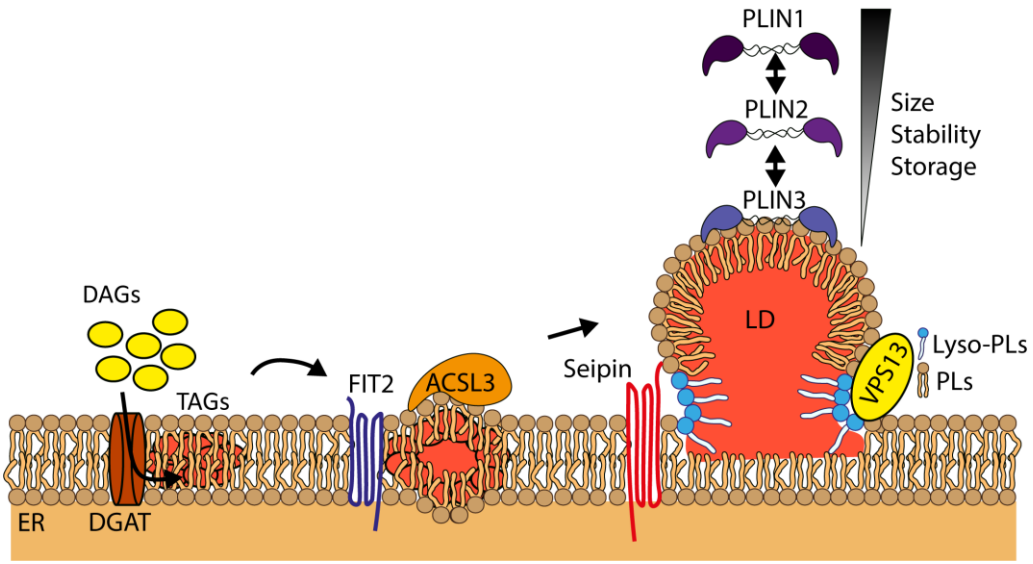

Figure 10. LD biogenesis.
Triacylglycerol (TAG) accumulation between ER leaflets promoted by diacylglycerol (DAG) O-acyltransferase I (DGAT), lipid globule stabilization by FIT2 (fat storage-inducing transmembrane protein 2), and ACSL3 (long-chain-FA-ligase-CoA protein 3). Then, LD growing is promoted by seipin, lysophospholipids (Lyso-PLs) supply by VPS13 (vacuole sorting-associated protein 13 protein); and stabilised by perilipin proteins (PLINs).
Modified from (*215*).

3.3. LD's supply of lipids

When nutrients are scarce, TAGs stored inside LDs are converted into 3 FAs and 1 glycerol (**lipolysis**) for supplying the cell with FAs that will be oxidized by the mitochondria to ultimately provide metabolic energy (*165*). Lipolysis is a regulated process carried out by the coordinated action of three neutral lipases: ATGL, HSL (hormone sensitive lipase), and MAGL (monoacylglycerol lipase) (**Fig. 11 and 15**). In basal conditions, the action of these proteins and the ATGL cofactor CGI-58 (comparative gene identification-58) are blocked by PLINs (*216, 217*).

During fasting, PKA (protein kinase A) is activated and promotes the phosphorylation of PLIN1, PLIN2, CGI-58, ATGL, and HSL (*165*). AMPK (AMP-activated protein kinase) is also activated by a decreased ATP/AMP ratio and promotes the phosphorylation of ATGL (*218*). Phosphorylation of PLIN1 and 5, facilitates HSL recruitment to LDs for stimulation of lipolysis (*219*). It is also increased by HSL and ATGL phosphorylation, which enhances their activity (*220*). As above stated, prolonged fasting increases the CMA-targeting of PLIN2 and 3, which further activates lipolysis by facilitating the recruitment of ATGL (*198*). Additionally, phosphorylated PLIN5 physically links LDs with mitochondria, which cluster around this organelle to promote FA release and increased mitochondrial FA oxidation (FAO) (*221*). Similarly, PLIN1 on LDs and mitofusin 2 (Mfn2) in mitochondria interact to favour lipid transference in BAT thermogenic processes (*222*). Activated PLIN5 also acts as a transcription factor to activate the expression of mitochondrial biogenesis and oxidative genes through SIRT1/PPARα/PGC1α axis (sirtuin1/ Peroxisome proliferator activator receptor α/ PPARα coactivator 1) (*223*).

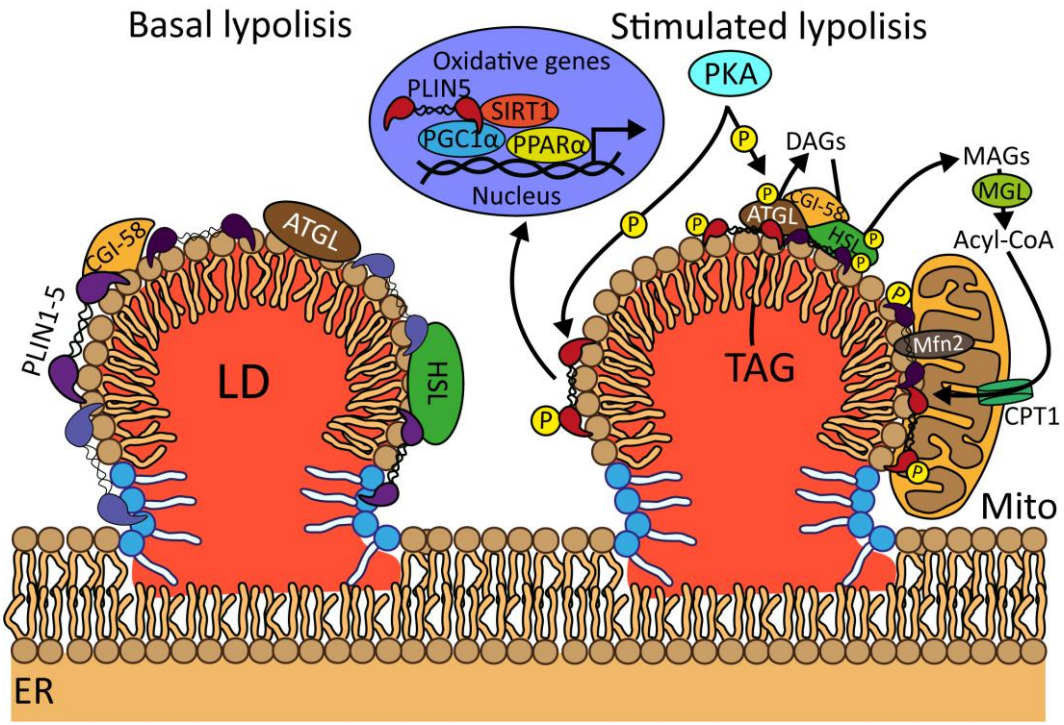

Figure 11. LD consumption by lipolysis.
In basal conditions, Plin coating of LDs prevents the action of HSL (hormone sensitive lipase), ATGL (adipose triglyceride lipase) and CGI-58 (comparative gene identification-58) cofactor. During starvation, upon PKA (protein kinase A) phosphorylation, PLIN1 and 5 favour the relocation of ATGL, HSL, and CGI-58, which are also further activated by phosphorylation. Both PLINs can tether LD and mitochondria coupling lipolysis and lipid oxidation. Phosphorylated PLIN5 promotes the transcription of oxidative genes through SIRT1/PGC1α/PPARα axis.
Abbreviations: monoacylglycerols, MAGs; monoacylglycerol lipase, MAGL; carnitine palmitoyltransferase I, CPT1; sirtuin 1, SIRT1; Peroxisome proliferator activator receptor α, PPARα; PPARα coactivator 1, PGC1; and mitofusin2, Mfn2.

3.4. LD buffering of lipids to prevent lipotoxicity

LDs do not only accumulate lipids to be supplied when there is a cell energy requirement, but also have a protective role against the deleterious effects of free FA accumulation that may lead to an increase of complex species (DAGs or ceramides) that interfere with cell organelle functions (**lipotoxicity**) (*169, 174, 224, 225*). These effects are exaggerated by saturated FAs such as palmitic acid (**PA**), which presents low affinity for DGAT (*226*), and ameliorated by monounsaturated FAs such as oleic acid (**OA**), which are easily incorporated into TAGs, and even help in the esterification of saturated FAs (*227*). Lipotoxicity consists in the **ER stress**, **calcium dysregulation**, **ROS production**, and **interference with the insulin signalling** promoted by the excess of FAs (*174*) (**Fig.12**).

3.4.1. Mitochondrial oxidation and dysfunction

When the capacity of LDs to store lipids is surpassed, lipids are alternatively transported to the mitochondria in an adaptative attempt to consume them and prevent lipotoxicity (*174, 228*) (**Fig.12**). They are oxidized through β-oxidation for breaking FA-CoA into acetyl-CoA, which then enters the carboxylic acid cycle (CAC) to produce both $FADH_2$ (reduced flavin adenine dinucleotide) and NADH (reduced nicotinamide adenine dinucleotide) used by the electron transport respiratory chain (ETC) for ATP production by oxidative phosphorylation (OXPHOS) (*165*) (**Fig.15**). This last step requires the polarization of the mitochondrial inner membrane (increase in membrane potential) coupled to ATP synthase action (*229*). As a by-product, ROS species such as O_2^- superoxide are produced by complex I and III of the mitochondrial respiratory chain (*230*).

Initially, excess of FAs enter this pathway to avoid lipotoxicity, but it leads to a higher ROS production (*230*). At some point, the oxidant activity of ROS cannot be neutralized by the antioxidant response of $Mn2^+$-superoxide dismutase, and ROS is accumulated (*230*). FAs in the vicinity of mitochondria are susceptible to be peroxidised by ROS, which can produce mitochondrial DNA, RNA, and protein damage (*231*). The excess of FAs can also cause a depletion of free CoA leading to a higher accumulation of free FAs and increasing lipotoxicity (*174, 228*). Furthermore, free FAs promote the depolarization of the mitochondrial inner membrane potential, which impedes ATP production (*231*) through the intrinsic uncoupling activity of FAs or the indirect FA stabilization of uncoupling proteins 1-3 (UCP1-3) (*232*). Mitochondrial dysfunction impairs the oxidation of FA-CoA, which furtherly increase their concentration and exacerbates mitochondrial dysfunction in a negative feedback (*231*).

As a consequence, they induce the opening of a permeability transition pore in the outer membrane, which allows the release of proapoptotic factors (such as apoptosis inducing factor, smac-DIABLO or cytochrome C) confined in the

intermembrane space (*233*). Opening of this pore also culminates with the collapse of membrane potential and the rupture of the outer mitochondrial membrane to further trigger apoptosis (*233*). Permeabilization can also be induced by the pro-apoptotic Bcl-2 family members (Bax, Bak and truncated Bid) or ceramides, which oligomerize in the membrane to form a permeable pore (*233, 234*).

3.4.2. ER stress, reactive oxygen species (ROS), and calcium dysregulation

Another consequence of an excess of intracellular lipids is the accumulation of FAs in the ER membrane promoting the apparition of oversaturated intermediates which interrupt TAG synthesis (*235*) (**Fig.12**). The resulting membrane presents a dramatic dilatation which compromises the integrity of the whole organelle (*236*). Increased PA concentration in the ER can also lead to protein aberrant palmitoylation and the subsequent ER stress caused by protein unfolding (*237*). Differential membrane composition increases the permeability of this organelle and the release of Ca^{2+} (*238*). Ca^{2+} depletion inhibits the action of calcium-dependent chaperones and leads to protein unfolding, ER stress, and UPR signalling (*239*). Ceramide production from FA surplus also depletes Ca^{2+} in the ER by interfering with the action of SERCA (sarco/ER Ca^{2+} ATPase) (*240*). Released Ca^{2+} into the cytosol signals PLC (phospholipase C) activation and cleavage of PIP_2 (phosphatidylinositol 4,5 bisphosphate) into IP_3 (1,4,5-inositol triphosphate) and DAG (*241*). Accumulated DAGs, formed from both PLC signalling and the excess of FAs, activate PKC (phosphokinase C), which increase ROS production through NOX2 (NADPH oxidase 2) (*242*).

Despite the fact that mitochondria has been considered for decades the major source for ROS, ER has evolved as the platform for redox signalling (*243*). ER integrates the ROS from PKC-NOX2 and mitochondrial FAO, whose induction alters the ER redox state (*129*). Altering the ER highly oxidizing environment (*133*), promotes a defective protein disulphide bond formation by PDI and ERO1α (oxidoreductin 1α), which depletes glutathione (GSH) antioxidant and also cause ROS accumulation (*244*). Further increase in ROS, decreases disulphide bond formation in a negative feedback loop, which finally leads to aberrant disulphide bond formation, unfolded proteins, and ER stress (*244*). Intriguingly, ROS accumulation activates IP3 receptor (IP3R), which stimulates Ca^{2+} release from the ER and aggravates lipotoxicity (*245*). Ca^{2+} release is coupled to its mitochondria internalization by GRP75/VDAC1/ MCU calcium regulation axis (glucose-regulated protein 75/voltage-dependent anion channel/mitochondrial calcium uniporter) (*246*). It increases mitochondria outer membrane permeability and promotes apoptosis (*246*). Chronic ER stress also targets the cell to apoptosis through CHOP expression, which induces a higher ROS production through ERO1α upregulation (*247*).

3.4.3. Insulin signalling and insulin resistance

Insulin signalling can also be altered by FAs. Insulin is secreted by pancreatic β-cells into the blood in response to high glucose levels after a meal, and targets glucose storage mainly in liver, skeletal muscle, and adipose tissue (*248*). Insulin binding to insulin receptor triggers the autophosphorylation (tyrosine residues) and activation of the receptor (*249*) (**Fig.12**). Once activated, insulin receptor recruits and phosphorylates IRS 1/2/3 (insulin receptor substrate 1, 2 and 3) in muscle, liver or adipose tissue (*250*), which binds PI_3K (phosphatidylinositol kinase), and promotes the formation of PIP_3 (phosphatidylinositol 3,4,5 triphosphate) (*250*). PIP_3 activates the Akt phosphorylation and the downstream translocation of GLUT4 receptor to the PM for glucose uptake (*250*).

Insulin resistance is a condition where insulin-stimulated glucose uptake is diminished in peripheral tissues (*251*), which results in a raise of blood glucose (**hyperglycaemia**) (*252*). Despite being initially hypothesized that hyperglycaemia is caused by a preferred lipid consumption to glucose during obesity (*253*), it was then confirmed that a deficient insulin signalling is the step causing hyperglycaemia (*254*). At a molecular level, the high accumulation of PA, cytosolic DAGs, or ceramides promoted during obesity induce the serine phosphorylation of IRS1 (*234, 255, 256*). It affects the interaction with the insulin receptor and promotes the degradation of IRS1 by the proteasome (*257*), which leads to a defective downstream signalling and GLUT4 translocation (*258*).

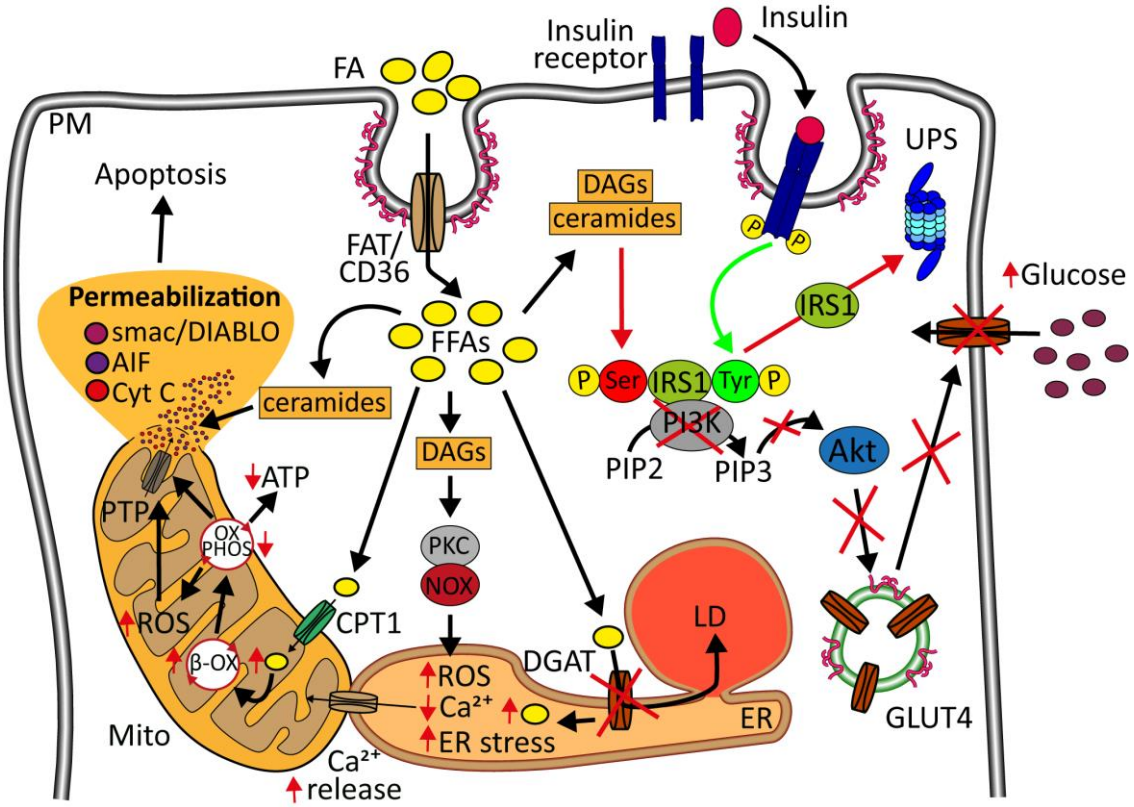

Figure 12. Cell lipotoxicity promoted by free fatty acids (FA).
Excess ectopic free FAs (FFAs) collapse LD store capacity, mitochondria oxidation capacity, and alters ER homeostasis. Thus, malfunction of the three organelles leads to higher FFA accumulation, reactive oxygen species (ROS) production, calcium ions dysregulation and ER stress. It culminates with the triggering of cell apoptosis through mitochondrial membrane permeabilization and release of proapoptotic factors. FFAs also induce de production of complex lipids such as DAGs and ceramides. DAG exacerbate ROS production, which are then accumulated in ER. Ceramides promote mitochondrial membrane permeabilization. Moreover, DAGs and ceramides interrupt insulin signalling and its downstream actions (insulin resistance) by increasing IRS1 serine phosphorylation, which inactivates it and promotes the proteasomal degradation of the protein.
Abbreviations: phosphokinase C, PKC; NADPH oxidase, NOX; β-oxidation, β-ox; oxidative phosphorylation, OXPHOS; permeability transition pore, PTP; cytochrome, Cyt C; apoptosis inducing factor, AIF; Second mitochondria-derived activator of caspase/direct inhibitor of apoptosis-binding protein with low pI, smac/DIABLO; insulin receptor substrate 1, IRS1; phosphatidylinositol kinase, PI3K; phosphatidyl inositol phosphate, PIP; and protein kinase B, Akt.
Modified from (*51, 129, 232*).

4. Lipotoxicity and metabolic syndrome:

Industrialized modern society has rapidly changed human dietary and physical patterns (*259*). Excessive calorie intake combined with low energy expenditure results in an overaccumulation of lipids, initially stored in the adipose tissue (*260*). When the caloric surplus exceeds the storage capacity of the LDs of the adipocytes, ectopic lipid deposition begins, affecting liver, skeletal muscle, and heart (*261*). The LD overload of these tissues results in the accumulation of FA derivatives promoting lipotoxicity and the metabolic syndrome (*262*).

4.1. Physiological progression of metabolic syndrome

Metabolic syndrome is defined as a cluster of conditions (hyperglycaemia, insulin resistance, obesity, and non-alcoholic fatty liver disease) causing heart disease, stroke and T2DM (*263*).

4.1.1. Obesity and adipose tissue dysfunction

Obesity is the root-cause of metabolic syndrome, and it is defined as a complex disease promoted by an excessive amount of body fat (body mass index, or BMI, above 30 kg per m^2) (*264*).

Obesity disease results from inherited, physiological, environmental, diet, and physical activity disorders among other factors (*265*). Thus, an imbalance between energy uptake and energy consumption promoted by unhealthy dietary habits and poor physical activity results in a chronic energy surplus (*265, 266*) stored as fat (lipids) in the adipose tissue (*267*). That way, adipose tissue controls whole-body metabolism and prevents elevated circulating concentrations of TAGs and FAs (**dyslipidaemia**) (*268*) (**Fig.13**). Adipose tissue can be divided in two subtypes with different properties: white and brown adipose tissue (WAT and BAT). WAT has a high capacity of TAG synthesis and storage due to the large unilocular LDs present in white adipocytes (*269*). BAT promotes heat production through lipid consumption and the uncoupling of the respiratory chain, which is facilitated by the high presence of small LDs and mitochondria in brown adipocytes (*269*). WAT can be partially converted to BAT under chronic cold stress by the transformation of white adipocytes to beige (intermediate LD and mitochondria number) in a process called browning (*270*).

During obesity, adipocytes first enlarge to accommodate the increased TAG deposition from the excess of FAs, which is also favoured by the expression of enzymes involved in TAG synthesis (*260, 271*). Hypertrophied adipocytes start secreting the MCP1 (monocyte-chemoattractant protein 1), which promotes macrophage infiltration and basal low-grade inflammation (*260*). Inflammatory state is further developed by the secretion of IL1β (interleukin 1β) and TNFα (tumour necrosis factor α) (*260, 272*). These factors prevent TAG storing and increase the lipolysis of LDs, where FAs and TAGs are released into the blood (*260, 272*).

4.1.2. Lipid ectopic accumulation and non-alcoholic fatty liver disease (NAFLD)

Excess of FAs, which are unable to be stored in dysfunctional adipocytes during obesity, are subsequently collected by peripheral tissues such as skeletal muscle and liver (**lipid ectopic accumulation**) (*260*) (**Fig. 13**). These tissues extend the capacity to accumulate FAs as TAGs inside LDs. For example, in muscle, where the storing capacity in normal conditions remains low (~0.5% of the total lipids), it raises to a five-fold concentration of TAGs during high FA supply (*273*). However, when surpassed the maximal FA storing capacity, FAs cannot be anymore buffered by LDs and trigger lipotoxicity on those tissues.

In liver, the accumulation of FAs (**liver steatosis**) originates the NAFLD, which is defined as a 5% lipid ectopic accumulation not related to alcohol consumption, medication use, or hereditary disorders (*274*) (**Fig. 13**).

Liver steatosis is not only promoted by a high uptake and accumulation of lipids, but also for other disturbances in the normal metabolism of both glucose and lipids. After a meal, insulin signalling, which activates glucose uptake, also decreases hepatic glucose production (HGP or gluconeogenesis, **Fig.15**) through the activation of glycogen synthesis (*275*), and the downregulation of gluconeogenic enzymes (*276*). ***De novo lipogenesis*** (**DNL**, **Fig.15**) using glucose as a substrate is also activated through SREP1C, mTORC1, and PPARγ transcription factors (*277*). During NAFLD, HGP is paradoxically sustained since insulin resistance of liver prevents the activation of insulin-mediated glycogen synthesis (*276, 277*). On the other hand, DNL is maintained using the produced glucose as a substrate and increasing lipid accumulation (*278*). Moreover, DNL activity in this organ is further increased since it also uptakes glucose from other tissues such as muscle, which first becomes insulin resistant (*279*). Patients with NAFLD also presents an upregulated expression of DNL enzymes, which further contributes to the activation of this pathway and liver steatosis (*277*). Consequently, sustained DNL is one of the major contributors to the progression of NAFLD and a specific target for emerging therapies (see section 4.4) (*280*).

4.1.3. Type 2 diabetes mellitus (T2DM) and β-cell dysfunction

When peripheral tissues become resistant to insulin action due to lipid ectopic deposition, the increase in blood glucose (**hyperglycaemia**) forces pancreatic β-cell production and secretion of insulin (**hyperinsulinemia**), and leads to the dysfunction of these cells which is the critical determinant of T2DM (*281*).

T2DM is a chronic metabolic disorder characterized by elevated levels of fasting plasma glucose (above 200 mg/dL) (*282*).

Physiologically, T2DM onset occurs in a hyperbolic loop: increase in glycaemia caused by decreased glucose uptake in peripheral tissues leads to a higher insulin secretion in pancreatic β-cells, which forces glucose uptake in peripheral tissues making them more insulin-resistant (*283*). Thus, there is a 50-90% increase in β-cell mass (*284*), and 2-3 fold increase in insulin secretion as a pancreatic adaptative response (*285*). When the elevated secretion of insulin by β-cells collapses, T2DM develops with a decrease of both β-cell mass (24-65%) and insulin levels (50-97%) (*284*).

At a cellular level, secretion of insulin granules is physiologically regulated through Ca2+ influx into the cell, which is ultimately controlled by mitochondrial ATP production from glucose consumption (*281*). Thereby, glucose blood levels are sensed by β-cells through glucose oxidation, which triggers insulin secretion. When there is hyperglycaemia, higher glucose oxidation on mitochondria triggers an amount of ROS production unable to be counteracted by the weak antioxidant response of β-cells, which leads to mitochondrial dysfunction and apoptosis of the cells (*286*). High glucose or FFA concentration also stimulates the pancreatic inflammatory response through the production of macrophage interleukin 1β (IL-1β) (*287*). Hence, IL-1β signalling leads to the production of a wide range of cytokines and chemokines through NF-κβ (nuclear factor of kappa light polypeptide gene enhancer) activation, which culminates in higher β-cell apoptosis (*287*).

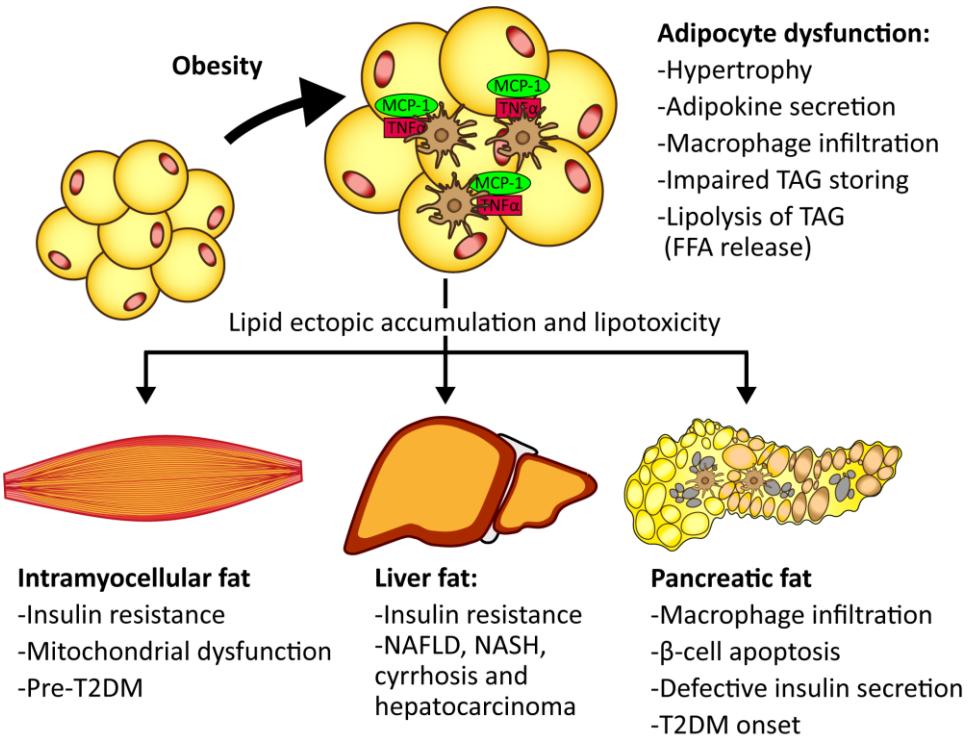

Figure 13. Adipocyte dysfunction and lipid ectopic deposition during metabolic syndrome.
Obesity causes adipocyte dysfunction, which disrupts the capacity of the tissue to store lipids. Lipids in the blood are then uptake by peripheral tissues (muscle, liver, and pancreas among others), whose accumulation (lipid ectopic accumulation) promote lipotoxic effects and metabolic syndrome progression.
Abbreviations: monocyte chemoattractant protein 1, MCP-1; tumour necrosis factor α, TNFα; type 2 diabetes mellitus, T2DM; non-alcoholic fatty liver disease, NAFLD; non-alcoholic steatohepatitis, NASH; and hepatocellular carcinoma, HCC.
Modified from (*261*).

4.2. Epidemiology and comorbidities

Metabolic syndrome is considered an epidemic since the prevalence of this diseases is in expansion all over the world: the obesity prevalence doubled since 1980 (*288*), T2DM increased from 6.28% of the total population on 2017 to 7.02% by 2020 (*289*), and NAFLD is expecting to grow from 25.24% in 2016 to 32% by 2030 (*290*). It is a huge medical concern since 4 million deaths were attributed to being overweight or obese in 2015 (*288*), 1 million to be diabetic (T2DM) (*289*), and 3.5% of the total liver diseases to present NAFLD (*291*).

These metabolic disorders can also cause a large list of disabling and life-threatening conditions, for example, obesity progression curses with other chronic diseases including cardiovascular disease, T2DM, kidney disease, musculoskeletal disorders, and many cancers (*288*). T2DM derived from obesity and physical inactivity cause chronic hyperglycaemia, microvascular complications (retinopathy, nephropathy and neuropathy), and a 2 to 4-fold increased risk of cardiovascular disease (*282*). Moreover, 55% of patients with NAFLD are obese and 22.51% presents T2DM (*292*). NAFLD can progress to NASH through a process of inflammation, hepatocyte degeneration, and liver injury (*280*), which are scarred by the activation and migration of hepatic stellate cells (liver fibrosis) (*293*). Advanced fibrosis onsets liver dysfunction (cirrhosis) and hepatocellular carcinoma, whose only treatment is liver transplantation (*294*).

4.3. Clinically established treatments

Following the guidelines, the first suggested intervention for the treatment of metabolic syndrome is to promote weight loss (*295*).

4.3.1. Weight loss: lifestyle and surgical interventions

Body weight is a critical parameter during the progression of metabolic syndrome since a moderate ~10% decrease in patients is enough to reduce hepatic steatosis, insulin resistance, and T2DM progression (*296*). Multiple diets have been proposed to restrict the calorie apport and promote weight loss (*297*), where dietary patterns such as Mediterranean diet (35-45% of fat, 15% from protein, and 40-45% from carbohydrates) presents a 19% resolution of metabolic syndrome (*298*). Increasing the monounsaturated fat apport in those diets, such as OA from olive oil, is associated with increased protective LD accumulation (*166, 227*), and improvements in insulin resistance, lipid profile and blood pressure (*299*). Adding an exercise routine to dietary approaches synergistically improves weight loss by a higher 20% (*300*).

Patients that present severe obesity (or obesity with comorbidities) are eligible for stomach and/or intestine surgical reduction by bariatric surgery (*301*). It efficiently promotes permanent weight loss in a triple way: I) malabsorption of nutrients such as fat, II) decreased calorie intake and III) gastrointestinal hormone change increasing satiety (*302*). Bariatric surgery showed to decrease a mean 20% of body weight after a 10-year follow up, which drastically reduced the all-cause mortality (59%), increased the mean life expectancy of obese patients (5.1 years), and promoted an outstanding remission of T2DM (70%) and NAFLD (55.5%) (*303-305*).

4.3.2. Pharmacological treatments

Since the efficacy of lifestyle changes rely on the individual compliance of the guidelines (*306*), and only <1% of eligible patients undergo bariatric surgery for concerns about surgical procedures (*307*), pharmacological treatments are required for most of the patients (*295*).

Several drugs approved by the FDA and EMA promote weight loss for the overall treatment of metabolic syndrome and specifically for obesity (*308*). These drugs achieve mid-term weight loss through different mechanisms such as reduction of fat intestinal digestion and absorption (orlistat, 3.1 kg) (*309*), or suppressing appetite and increasing satiety (phentermine/ topiramate, naltrexone/bupropion or liraglutide; 9.8, 4.4 and 5.6 kg respectively) (*308*). None of the actual treatments are directed to increase the consumption of lipids (*308*).

Treatments of T2DM are focused on reducing hyperglycaemia, where metformin is the first-line oral therapy with well-stablished glucose-lowering effects and without major side effects (*310*). In physiologically relevant concentrations, it is widely accepted that metformin improves body control of glycaemia by reducing ∼20% liver HGP (*311*), but the exact mechanism of action is still under a high debate (*310*). Initial results showed that metformin inhibition of the mitochondrial complex I in the respiratory chain decreased ATP production activating in turn AMPK, which prevents the transcription of enzymes in the HGP pathway (*312*). However, glucose-related effects of metformin are maintained in liver-specific AMPK knock out mice, indicating additional mechanisms of action (*313*). Recently, metformin showed to alter the cell redox state through the inhibition of glycerol 3-phosphate dehydrogenase, which leads to the accumulation of oxidized NAD^+ (*314*). This way, HGP of redox-dependent substrates glycerol and lactate could be inhibited by the metformin depletion of NADH cofactor (*315*).

Complementary treatments to metformin, decrease hyperglycaemia by altering other steps on the glucose metabolism: potentiating insulin secretion (sulfonylureas and meglitinides), increasing incretin half-life circulation (DPP-4 inhibitors), activating PPARγ to increase insulin sensitivity (thiazolidinedione), inhibiting SGLT2 to prevent glucose reabsorption in kidney (SGLT2 inhibitors), and diminishing carbohydrate absorption in the intestine (α-glucosidase inhibitors) (*316*). At present, there are no specific drugs approved for the treatment of NAFLD, although some T2DM treatments helps in the control of the NAFLD and can be used in patients with both diseases (*280*). In these cases, many of the effects are not liver-related, but to an indirect increase of insulin sensitivity or weight loss.

4.4. Emerging therapies: Acetyl-CoA carboxylase (ACC) inhibitors

There is an endless list of new molecules being evaluated for the treatment of obesity, T2DM and/or NAFLD (*280, 308, 317*). For the aim of this project, **acetyl-CoA carboxylase protein (ACC)** as a target, and the inhibitors of this enzyme will be introduced below. ACC is positioned as a central enzyme in lipid metabolism (**Fig.15**), and the inhibition of this enzyme is persistently tested for the treatment of NAFLD (*280, 318*).

4.4.1. ACC protein

Acetyl-CoA carboxylase catalyses the first committed step on DNL: the transformation of acetyl-CoA into malonyl-CoA (**Fig.14**). ACC carboxylation is a two-step reaction: first, a biotin domain of ACC is carboxylated in an ATP-dependent manner (**BC reaction**), and then this carboxy group is transferred onto acetyl-CoA (**CT reaction**) (*319, 320*). **Malonyl-CoA** is the primary substrate for FA biosynthesis, but also allosterically inhibits **carnitine palmitoyltransferase I (CPT1)** (*321*). In the outer mitochondrial membrane, CPT1 mediates the transfer of the acyl group from acyl-CoA to a carnitine molecule, and that way controls the FA flux into mitochondria for β-oxidation (*322*). Thereby, ACC regulates both the rate of FA synthesis through DNL, and the rate of FA internalization and consumption into the mitochondria by controlling malonyl-CoA formation (**Fig.15**).

ACC presents two isoforms generated by alternative splicing: ACC1 and ACC2 (265 and 280 kDa respectively), whose differences in tissue expression and cell localization help to control ACC activity (*323*). ACC1 is localized in the cytosol of the cells with high lipogenic capacity (such as those from adipose tissue and mammary gland), where it controls the rate of DNL pathway (*324*). On the

contrary, ACC2 is located on the mitochondria of oxidative tissue cells (such as skeletal or cardiac muscle cells), where malonyl-CoA formation is coupled to CPT1 inhibition to control the rate-limiting step of FA flux into the mitochondria (*325*). Liver, which presents both high capacity of FAO and DNL, presents a balance of ACC1 and 2 isoforms (*326*).

Due to the central role of ACC in lipid metabolism, it is not surprising that multiple signals regulate this step (**Fig.14**). ACC expression is upregulated by SREBP-1C, ChREBP (carbohydrate response element binding protein) and LXR (liver X receptor); or in response to insulin or glucose availability to activate DNL (*327*). ACC activity can also be activated by citrate (*328*) or through the interaction with MIG12 protein (*329*), which both induce ACC polymerization in filaments of up to 1 µm length. ACC is inactivated by the phosphorylation of AMPK (at Ser80, Ser1201 and Ser1216) and PKA (at Ser78 and Ser1201), in response to AMP/ATP low levels or glucagon and catecholamines respectively (*330-332*). Both kinases induce FAO during fasting conditions. ACC expression is also allosterically repressed by malonyl-CoA and palmitoyl-CoA to regulate the DNL pathway depending on the product formation (*327*). ACC regulation is physiologically relevant in breast and ovarian cancer, since BRCA1 (breast cancer susceptibility gene 1), which binds and inhibits ACC by preventing Ser79 dephosphorylation, is mutated elevating lipogenesis, and supplying cancer cells with lipids for growing (*333*).

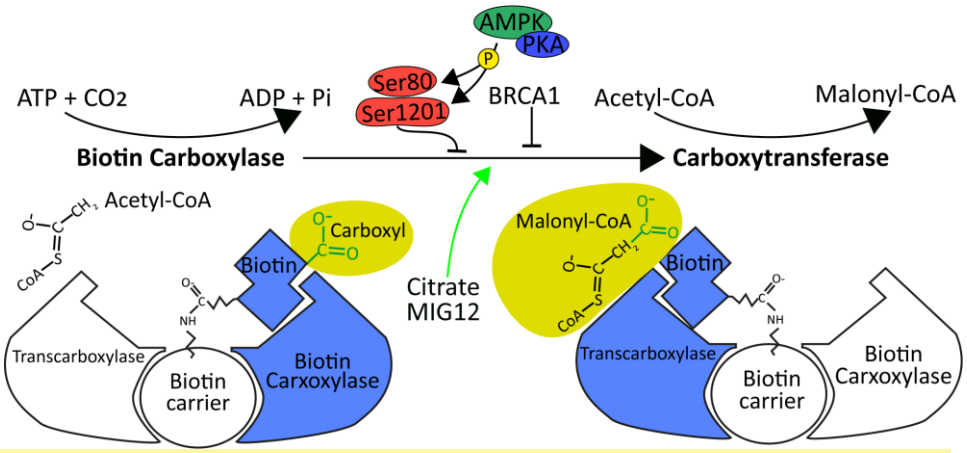

Figure 14. Acetyl-CoA carboxylation.
Two-step reaction of acetyl-CoA carboxylase (ACC) and the domains of the protein involved. The regulation steps of this reaction are also indicated: the inhibitors with capped lines and the activators in green.
Abbreviations: Breast cancer susceptibility gene 1, BRCA1; and AMP-activated protein kinase, AMPK.

4.4.2. ACC as a promising drug target

Initial approaches to study the potential of ACC inhibition for the treatment of obesity were provided using ACC KO mice (*277*). While whole-body ACC1 depletion displayed embryonic lethality (*324*), conditional KO showed a 50% lower adipose tissue weight and a 40-70% reduction of TAGs in liver (*334, 335*). ACC2 KO mice were described to be protected from weight gain and hypertriglyceridemia (*336*), although the results are controversial since they could not be replicated in other mouse strains (*337*). In another study, rats targeted with synthetic antisense oligonucleotides (ASOs) for both isoforms reversed HFD-induced hepatic accumulation and reduced insulin resistance (*338*).

Several inhibitors were then developed to inhibit ACC by different mechanisms: I) block acetyl-CoA binding site, II) inhibit the transference of carboxyl group to Acetyl-CoA, and III) impede the biotin carboxylation (*280, 339*).

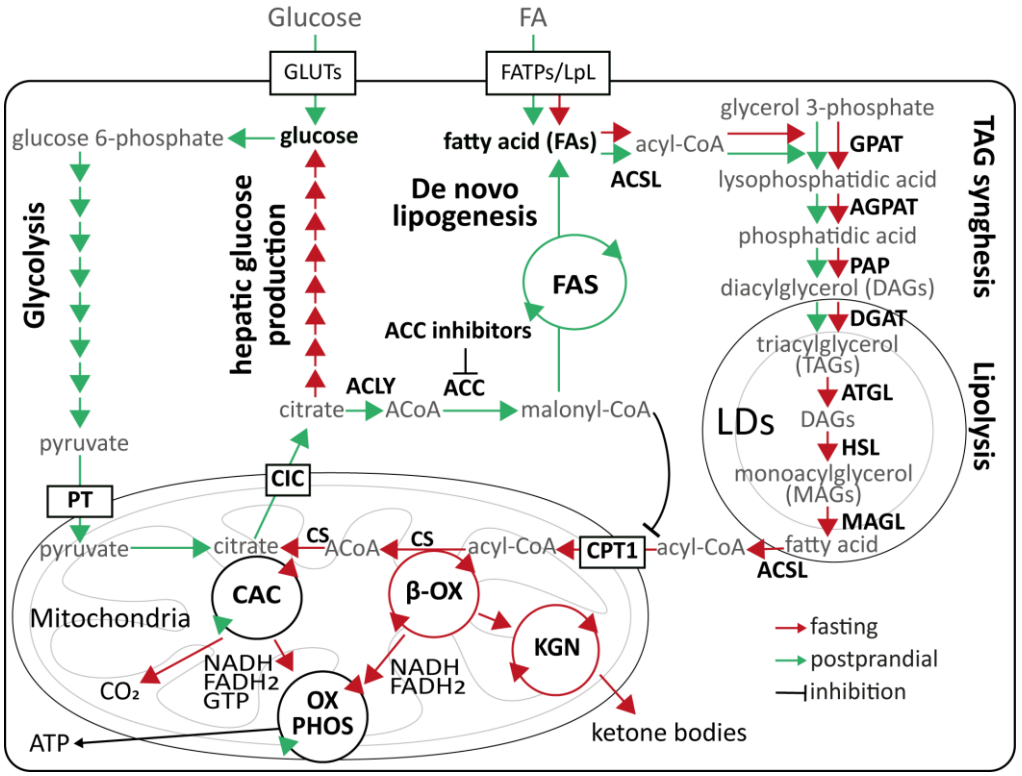

Figure 15. Glucose and lipid metabolism connected by *de novo lipogenesis* (DNL). Main pathways of glucose (glycolysis and hepatic glucose production, HGP) and lipid (triacylglycerol (TAGs) synthesis and lipolysis), which are connected by DNL and inhibited by acetyl-CoA (ACC) inhibitors. Some pathways are simplified since they are out of the scope of the thesis. Metabolites are in grey, enzymes are in black, and transporters are framed. Lines indicate the reactions occurring during fasting in red and postpandrial in green. Capped lines indicate allosteric inhibitions.
Abbreviations: glucose transporters, GLUTs; glycerol-3-phosphate acyltransferase, GPAT; phosphatidic acid phosphatase, PAP; diacylglycerol O-acyltransferase I, DGAT; ketogenesis, KGN; PT; citrate transporter, CIC; ATP citrate lyase, ACLY; fatty acid synthase, FAS; and Acetyl-CoA, ACoA.
Modified from (*165*).

4.4.2.1. Class I. Fatty acid mimetics inhibitors of the active site: TOFA.

The first class of ACC inhibitors are lipophilic FA mimetics, which when bound to CoA block the catalytic site of the enzyme avoiding acetyl-CoA binding (*318*). This group includes many molecules such as aryloxyphenoxypropionate, acycloheanedione herbicides, MEDICA 16, ESP-55016, S2E or 5-**tetradecyloxy-2-furancarboxylic acid (TOFA)** (*318*).

TOFA, which was first discovered as an hypolipidemic drug in 1977, presents a PA mimetic structure (16:0) with a non-hydrolysable furane ring (*340*) (**Fig.16**). The effect of the drug on reducing DNL, TAG, apolipoprotein secretion, plasma levels of cholesterol and TAGs, body weight, LD, and increased ketone body production was shown in different studies using cultured hepatocytes and animal models (*340-345*).

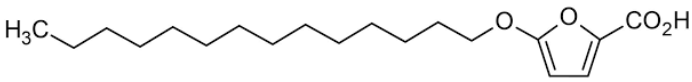

Figure 16. FA mimetics structure of TOFA.

4.4.2.2. Class II. Carboxy transferase inhibitors: CP-640186.

The second class are bipiperidylcarboxamides, which inhibit the carboxyltransferase reaction and include isozyme-nonselective inhibitors such as CP-640186, and derivatives of (4-piperidinyl)-piperazine, 1,4-disubstituted cyclohexane, spirochromanone, spirodiamine, spiro-pentacylamide, and pseudopeptide pyrrolidinedione (*318, 346*).

The first identified inhibitor and representative of the group was CP-640186, whose allosteric binding in the dimerization site of ACC blocks CT reaction in a reversible non-selective manner (IC_{50} ~50nM) (*347*). In liver HepG2 cells, it demonstrated to inhibit DNL, TAG synthesis, and apolipoprotein B secretion without affecting cholesterol metabolism (*347*). In muscle C2C12 cells and rat muscle strips, it also activated FAO (*347*). In rats, CP-640186 lowered malonyl-CoA production in liver, muscle, and cardiac tissues by inhibition of DNL, which in turn stimulated the whole-body FAO (*347*).

Two derivatives of CP-640186, ND-646 and ND-654 (with IC_{50} of 3.5-4.1nM and 3-8nM respectively), found to be effective against non-small cell lung cancer and hepatocarcinoma preclinical models (*348, 349*). ND-646 interacts with several residues of the BC domain promoting a conformational change like phosphorylation, which stopped tumour growth on KRAS-mutated mice models (*348*). With increased liver affinity, ND-654 favoured the survival of tumour-bearing rats alone or in combination with the multi-kinase inhibitor sorafenib (*349*). Cancer cell lines require chronic lipid apport to serve as building blocks for supporting continuous proliferation (*350*). Therefore, they present an altered metabolism with increased DNL (*351*), where ACC inhibition demonstrated to be an effective target (*348, 349*).

4.4.2.3. Class III. Biotin carboxylase inhibitors: from Soraphen A to firsocostat.

The third class of inhibitors includes all the compounds that inhibit the carboxylation of ACC biotin carrier such as polyketide natural fungicides, thiophene pyrimidone derivatives, amino-oxazole derivatives, an azobenzimidazole derivatives (*318, 346*).

Soraphen A, which was first isolated from bacterium *Sorangium celullosum (352)*, showed to inhibit ACC activity in a isozyme non-selective manner and through the binding of biotin carboxylase domain (IC_{50} 1-5nM) (*353*). Thereby, Soraphen A stabilized the non-catalytic conformation of ACC and also prevents dimerization and/or oligomerization (*353*).

Despite the outstanding affinity for ACC, Soraphen A synthesis resulted complicated and led to the discovery of novel analogues whose properties were also improved (*354*). Using the human ACC2 crystal structure complexed with Soraphen A, firsocostat (ND630 or GS0976) was discovered, which also prevented ACC oligomerization and enzymatic activity (IC_{50} 2-6nM) (*355*). *In vitro*, firsocostat prevented acetyl-CoA incorporation to FAs and increased FAO in HepG2 cells (*355*). I*n vivo*, it activated FA consumption, which promoted a decrease on body weight gain (∼8%), hepatic steatosis, dyslipidaemia, and insulin resistance on diet-induced obese and diabetic Sprague-Dawley rats (*355*). Further clinical trials in obese adults demonstrated the well-tolerance and dose-dependent inhibition of hepatic DNL (phase I) (*356*), and reduction of liver steatosis below 30% from baseline in half of the treated (20mg/kg) NAFLD and NASH patients (phase II) (*357*).

4.4.3. Side effect: hypertriglyceridemia

Despite the efficacy of ACC inhibitors some of them demonstrated one clear side-effect, which could worsen the prognosis of metabolic syndrome. Firsocostat showed a ∼12 mg/dL median increase on plasma TAGs in human clinical trials (*357*), which was also shown with the inhibitor MK4074 (∼170 mg/dL) (*358*), and the liver specific PF05221304 inhibitor (∼40 mg/dL) (*359*). Further investigations found that deletion of ACCs decreased polyunsaturated FAs in liver, which induced SREBP-1C and GPAT1 expression promoting VLDL secretion and hypertriglyceride-mia (*358*). For firsocostat it could be counteracted with fibrate or fish oil (*357*), and future investigations will test the efficacy of this inhibitors in combination with other treatments to circumvent this side-effect and for the treatment of NASH (*360*).

ANTECEDENTS AND OBJECTIVES

The following sections of the thesis are divided in two parts corresponding with the two projects conducted, whose objectives are stated below.

1. Caveolin in the endoplasmic reticulum

During the last years, the lipid trafficking and disease group directed by Albert Pol has focused on the role of caveolin proteins in the homeostasis of cholesterol, while they are transported to the plasma membrane (PM).

As introduced, caveolins are key components of caveolae, which are a striking feature of the PM of many cell types and tissues (adipocytes, endothelial and muscle cells), and whose participation in mechanopro-tection, endocytosis, and signalling pathways has been the focus of research (*3, 5*). Alternatively, important functions of caveolins have been appreciated for some time, although the relevance and mechanisms remain poorly understood (*93, 94*). Indeed, organisms including Caenorhabditis elegans (C. elegans) and specific mammalian cells, such as hepatocytes, neurons, lymphocytes, and some tumour cells, seem to express caveolins without forming distinguishable caveolae, suggesting caveola-independent functions of the protein.

These non-caveolar functions of caveolins could be taking place in intracellular compartments before caveolae assembly. There, they are synthesised in the endoplasmic reticulum (ER) in a signal recognition particle-dependent process (*9*), and progressively oligomerise and binds cholesterol during its transport through the ER and Golgi complex (GC) to finally promote caveolae formation at the PM (*75*). Moreover, CAV1 has been related in previous studies of the group with the transport of lipids between different ER subdomains such as cholesterol between mitochondria-associated membranes (MAMs) (*101*) and mitochondria (*100*), or with the formation of lipid droplets (LDs) (*98*). Although still poorly understood, these functions likely mediate key physiological responses such as the regeneration of the liver after a partial hepatectomy (*98*).

Intriguingly, the pool of caveolin in the ER remains very low since it exits the compartment very fast (*75*). Thus, we hypothesized that non-caveolar caveolin at those early timepoints is highly controlled, and we decided to characterise the function and regulation of these intracellular caveolin pools. Additionally, it could provide an insight in the mechanism of pathogenesis induced by several caveolin mutants, which present a disrupted transport to the PM and an accumulation in intracellular compartments.

The specific objectives proposed for the first part of this thesis are the following:

1. **Find the mechanism by which the cell controls caveolin protein segregation either in the plasma membrane to form caveolae, or in the intracellular compartments to perform non-caveolar functions.**

2. **Provide an insight in the non-caveolar functions of caveolin in lipid droplets and the endoplasmic reticulum.**

This work is included inside the project “Novel roles of ACSL3, CAV1, and cholesterol in the Endoplasmic Reticulum: homeostatic sensors that determine cell’s survival or death” (BFU2015-66401-R) and granted with a fellowship for the realization of this thesis (BES-2016-077490). Both has been funded by el Ministerio de Economia y Competitividad del Gobierno de España.

2. Targeting lipid droplets for the treatment of type 2 diabetes mellitus and metabolic syndrome

Our group is also focused on studying the cell biology and physiology of the LD cellular organelle. While attached with the ER, it controls the distribution of stored lipids for many cellular processes (*165-168*).

It is known that the accumulation of LDs originates many lipid-related diseases such as obesity. The connection with other comorbidities such as type 2 diabetes mellitus (T2DM) is not yet fully elucidated, but it is expected to be crucial.

Nowadays, the treatment of T2DM is seen from a glucose-centred point of view and focused on lowering hyperglycaemia, which is the major consequence of the progression of this disease. The main treatment is metformin which prevents liver glucose production by gluconeogenesis inhibition (*310*). Other second-line treatments such as sulfonylureas or thiazolidinediones are also used for decreasing the high circulating glucose levels to complement metformin treatment (*361*).

Nonetheless, T2DM is strongly associated with obesity, which ultimately promotes and excessive lipid accumulation in the LDs of peripheral tissues such as muscle and liver (lipid ectopic deposition) (*260*). A high accumulation of lipids in the cells of these tissues leads to the overloading of LDs and the accumulation of freed toxic lipid species (lipotoxicity) (*169, 174, 224*), which can make those tissues resistant to insulin action, and in turn, decrease glucose uptake and promote hyperglycaemia (*362*). Thus, T2DM is a multifaceted disease which requires a multifaceted therapy.

Using the knowledge previously described by the group in LD formation (*165, 166, 180*) and consumption (*165, 345*), a new treatment to reduce lipid accumulation and the consequent LD overloading was aimed to be discovered. Decreased lipid accumulation would be translated in reduced lipotoxicity, increased insulin sensitivity and prevention of T2DM onset. Moreover, it could be useful for the concomitant treatment of associated diseases such as obesity during the progression of metabolic syndrome.

The specific objectives proposed for the second part of this thesis are the following:

3. **Find a treatment effective in targeting LDs to reduce cellular lipid accumulation and lipotoxicity.**

4. **Determine if the reduction of ectopic lipid accumulation in the lipid droplets of peripheral tissues is a successful therapeutic approach for the treatment of type 2 diabetes mellitus and other diseases associated with the metabolic syndrome.**

This work is included inside the project “Lipid droplet overloading promotes pathogenesis and progression of type 2 Diabetes: Identifying new therapeutic targets and applying upgraded therapies” funded by la Marató de TV3 foundation (201625.10).

RESULTS

CHAPTER I:

1. Differential proteostasis of caveolins during early biosynthesis

1.1. Proof of concept: Early regulation of caveolins

Following the proposed objectives, we hypothesized that protein degradation could be a mechanism for controlling the fate of non-caveolar caveolin (CAV). Caveolin degradation is now known to take place after disassembly of caveolae via endosome-lysosome compartments (*122*). For this process, caveolin is ubiquitylated and oriented to the lumen of multivesicular bodies (MVB) before its fusion with lysosomes (*123, 124*). Using MG132, a proteasome inhibitor, caveolin was shown to accumulate in endosomes because an impaired orientation of the protein (*123*). We hypothesized that another feasible option of caveolin ubiquitination could be the targeting of the protein to the proteasomal degradation since this is the fate for polyubiquitinated proteins. Treating the cells with MG132 and chasing protein accumulation in intracellular compartments (apart from endosomes) could give us a clue of how non-caveolar caveolin is controlled by degradation.

With that purpose, we used COS1 cells as a model as they are easily transfected and visualized with fluorescence microscope. Since endogenous CAV1 (endCAV1) is expressed in COS1 cells but not CAV3, we used GFP-tagged CAV3 to track only exogenous protein. By this, potential interferences between endogenous and exogenous caveolin were avoided, and assured that the effects appreciated were caused only by exogenous CAV. Cells were transfected for 24 h with GFP-CAV3 and treated for the last 16 h with 1.5 µM MG132.

Strikingly, MG132 treatment induced an aberrant accumulation of CAV3 in a structure peripheral to the nucleus (**Fig. 1A, right panel**) instead of its normal distribution to the plasma membrane (PM), Golgi complex (GC), and LD, as observed in the untreated cells (**left pane**l). Detailed observation by electron microscopy using CAV3 antibodies and APEX system revealed that this aberrant morphology consisted in a cell vesiculation, where GC was not present, and ER had a condensed morphology (**Fig. 1B**). Quantification of the percentage of cells with this morphology showed that, compared to the transmembrane ER-resident protein VAP-A (VAMP-Associated Protein A), MG132 treatment significantly induced cell vesiculation in CAV3 transfected cells (**Fig. 1C**). The structure enclosing the nucleus seemed like ER because of the reticular morphology on the cell periphery and nuclear envelope staining, and it was furtherly confirmed by immunofluorescence colocalization using endogenous VAP-A as an ER marker (**Fig. 1D**). Comparing CAV3-transfected cells (white arrowhead) with non-transfected cells (grey arrowhead), CAV3 cells presented an altered ER morphology with the mentioned stacked and condensed structure in the central cisternae, and a less structured tubular network at the periphery (**Fig. 1D**). Using TGN46 as a GC marker, MG132 treated cells did not show TGN46 staining compared to non-transfected, suggesting a disorganization of the exocytic pathway (**Fig. 1D**).

Aberrant distribution of CAV3 correlated with higher levels of protein accumulation compared to VAP-A, as shown by GFP immunoblot of total cell lysates (**Fig. 1E**). The accumulation of CAV3 in ER triggered both XBP1S (Xbox-binding protein 1 spliced) and CHOP (C/EBP-homologous protein) ER stress markers expression determined by RT-PCR (**Fig. 1F**), which confirmed the activation of a cellular response to prevent caveolin accumulation and related toxic effects.

These results demonstrated that early caveolin degradation by ER-associated degradation (ERAD) is indispensable to avoid protein accumulation and permit its transport through the exocytic pathway. From here, some technical refinements needed to be addressed to undoubtedly confirm these results and have a better detail on caveolin regulation.

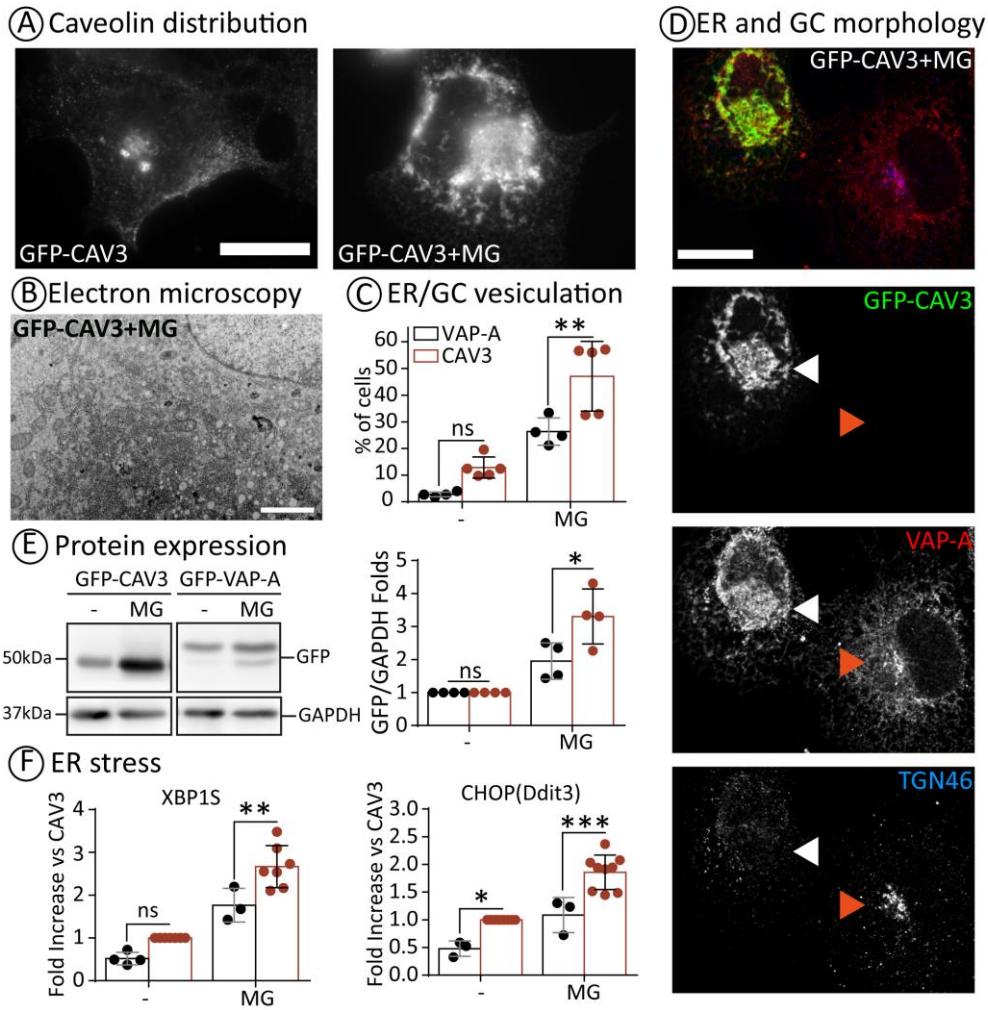

Figure 1. CAV3 is aberrantly accumulated in the ER when inhibiting the proteasomal degradation of proteins.

COS1 cells were transfected 24h and treated with 1.5µM MG132 for the last 16h. (**A**) GFP-CAV3 distribution was observed using fluorescence microscope and (**B**) electron microscopy with GFP antibodies and APEX system (scale bar= 2 µm). (**C**) Golgi complex (GC) and endoplasmic reticulum (ER) vesiculation quantified and compared to GFP-VAP-A ($n \geq 4$). (**D**) ER and GC morphology and colocalization were checked using VAP-A (in red) and TGN46 (in blue) respectively . Non-transfected (white) and transfected (grey) cells are marked with arrowheads. (**E**) Protein accumulation blotted with GFP and corrected with GAPDH as a loading control was measured by WB in total cell lysates ($n \geq 4$). (**F**) ER stress response was measured using RT-PCR gene expression of XBP1S and CHOP markers ($n \geq 3$). Scale bar is fixed at 20 µm and images were taken at the same magnification in (A) and (D) respectively. All graphs show means ±SD; where ns, not significant; *p<0.05, **p<0.01, ***p<0.001 in a two-way ANOVA test using Sidak's multiple comparisons post-test compared to VAP-A.

1.2. Short-timed expression

It was previously demonstrated that high caveolin accumulation in the cell due to long time protein transfection, could cause the formation of cytosolic aggregates of caveolin (aggresomes) (*363*) or saturate lysosomal degradation system inducing the formation of artefactual caveolin carriers called "*caveosomes"* (*122, 364*). For that reason, a synchronic short-timed expression method was optimized (see Materials and Methods and **Fig. 2A**) using cycloheximide (CHX).

Protein levels and distribution of transfected CAV3 were analysed. Although a decrease in the percentage of transfected cells was evident, less variability in protein distribution was appreciated showing a synchronized expression (**Fig. 2B**). The absence of collapses after 3h of CAV3 expression (compared to 24h, **Fig. 2B** white arrowheads) allowed to track protein distribution without dramatically affecting the overall homeostasis of the cell nor the exocytic pathway. To assure proper functioning of the timing, each step was individually controlled checking protein levels (**Fig. 2C**): transfected CAV3 was detected (2nd vs 1st lane), inhibition of protein synthesis was achieved when adding CHX (3rd lane), and 3h synchronized protein expression after CHX removal was also detected (4th lane). Moreover, transfected protein levels represented only ~10% of the endogenous (**Fig. 2D**) as shown by comparing both (GFP-tagged and endCAV1, at ~50kd and ~20kd respectively) detected using CAV1 antibodies.

Short-timed and synchronized overexpression demonstrated to bypass most of artefactual interferences previously described (*122, 364*), making it a useful tool to study non-caveolar caveolin.

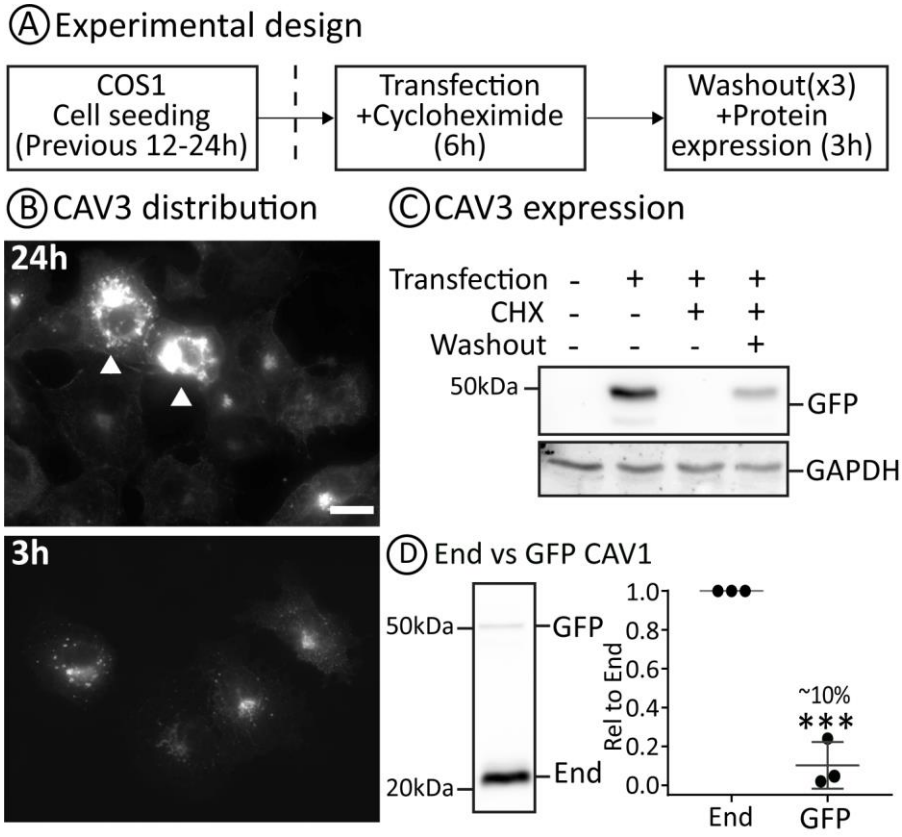

Figure 2. Optimization of short-timed transfection.
(**A**) Experimental design: Previously seeded cells were transfected in the presence of 50 µg/mL cycloheximide (CHX) for 6 h. After washing out CHX with fresh complete media, protein expression was allowed for 3 h. (**B**) Representative image of CAV3 distribution at 24 h and 3h-synchronized expression (Scale bar=: 20µm for equally magnification acquired images). (**C**) CAV3 expression levels following transfection, CHX treatment, and washout controls. (**D**) Percentage of overexpressed CAV1 relative to endogenous (end) levels, detected with CAV1 antibodies (it shows means ±SD of n = 3 and *** equals to $p<0.001$ in a paired two-tailed t-test).

1.3. Differential transport of caveolins in early biosynthetic steps

Surprisingly, CAV3 when expressed for 3 h showed a dramatic decrease of its transport to the PM, which was only appreciated in highly transfected cells (**Fig. 2B, 3 h**). It was described that CAV1 transport to the PM was reached after 45 minutes (*75*), but CAV3 was barely transported to PM after 3 h in our model. It suggested that caveolin family members could differ on their transport from ER to the PM. Until now, the mechanistic reasons for having different caveolin members remained enigmatic, as only few differences had been appreciated between them apart from its tissue-dependent expression (CAV1 and CAV2 ubiquitously, and CAV3 on muscle cells) (*16, 18*). Thus, early synthesis and transport through the exocytic pathway were studied for all caveolin members.

Transfected GFP-CAV1, CAV2, and CAV3 were expressed for 3 h in COS1 cells and their localization was compared using PM (phalloidin, cortical actin), GC (GM130), ER (Calnexin) and LD (Perilipin 3, PLIN3) antibodies (**Fig. 3A**). The percentage of cells expressing every caveolin isoform in each compartment was quantified (**Fig. 3B**). As described, CAV1 was predominantly present on PM and GC showing a fast transport through the exocytic pathway (**Fig. 3B**). On the other hand, CAV2 was mainly retained in GC showing a decreased capacity of trafficking. Strikingly, CAV3 slowly transited to PM being mainly retained in ER and LDs (**Fig. 3B**).

Figure 3. CAV1, CAV2, and CAV3 showed different early transport through the exocytic pathway.
(**A**) COS1 cells expressing GFP-tagged caveolin for 3 h were labelled with phalloidin, GM130, Calnexin, and PLIN3 antibodies as markers for PM, GC, ER, and LD localization. (**B**) The percentage of cells presenting the mentioned stainings were quantified (n = 3 including more than 80 cells per condition). All images have been taken with the same magnification (Scale bar = 20 µm). The graph shows means ±SD; **p< 0.01 and ****p< 0.0001 in a two-way ANOVA test using Sidak's multiple comparisons post-test to CAV1.

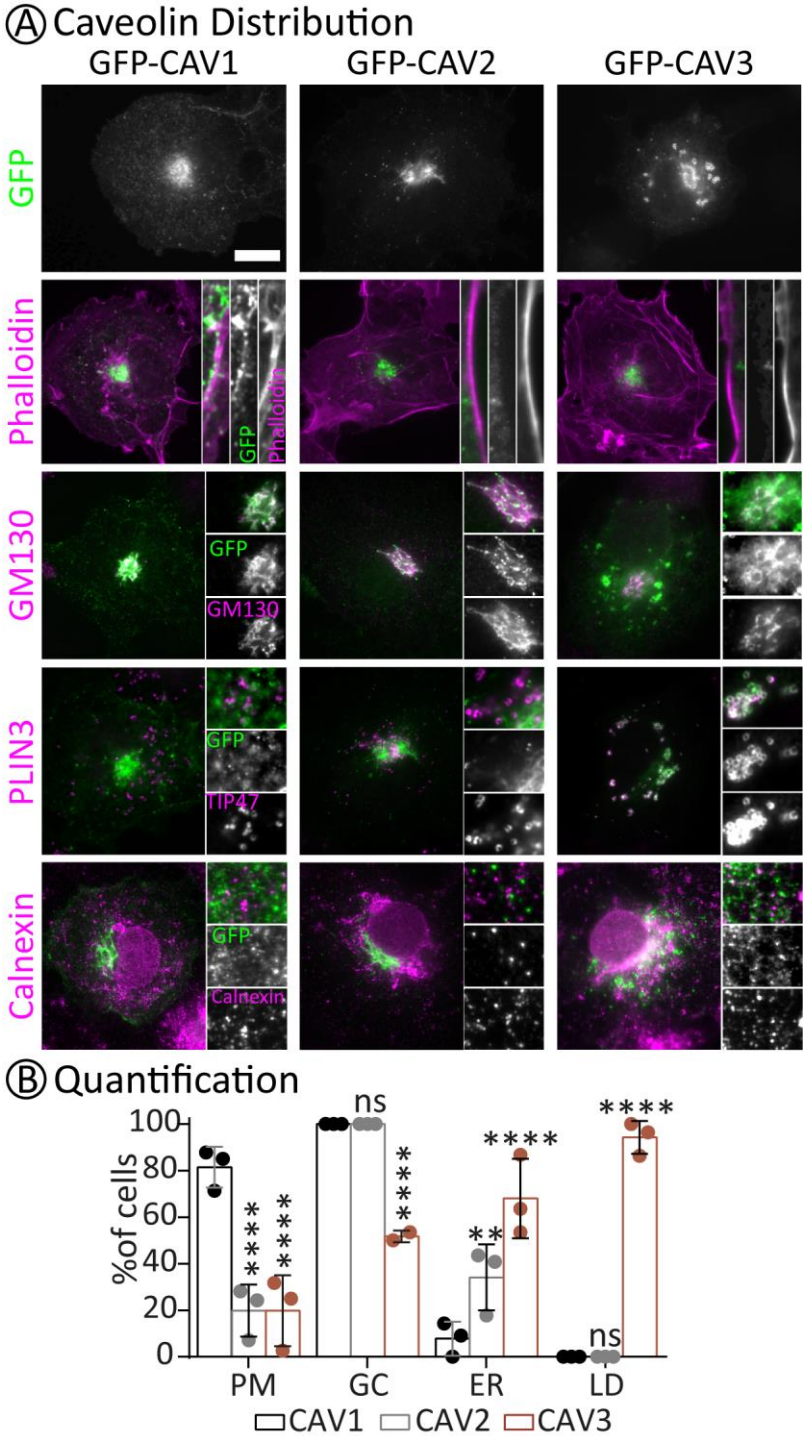
Ⓐ Caveolin Distribution
GFP-CAV1
GFP-CAV2
GFP-CAV3
GFP
Phalloidin
GM130
PLIN3
Calnexin
TIP47
Ⓑ Quantification
%of cells
100
80
60
40
20
0
ns
****
**
PM
GC
ER
LD
CAV1
CAV2
CAV3

These differences were also biochemically confirmed. Caveolin oligomerization during its transport to the PM is associated with Triton X-100 (TX) detergent insolubility gaining (*72*). Knowing that, soluble fraction of caveolin (not oligomerized) was separated from insoluble (oligomerized in PM fraction) using 1% chilled TX buffer. The results showed that only CAV1 was oligomerized and thus, transported to the PM (**Fig. 4A**). To go into more detail, cells were solubilized using 0.5% TX and loaded in sucrose velocity gradients. With this method caveolin could be separated in soluble (just synthesized), 8S (trafficking from ER to GC) and 60S (completely oligomerized and forming caveolae) fractions (*75*). CAV1 was able to form 8S (#4 fraction) and 60S (#6 fraction) complexes (see Materials and methods for more details) compared to CAV2 and CAV3, which were mainly soluble (#2 fraction) (**Fig. 4B**), suggesting a proper transport of CAV1 through the exocytic pathway. Taking advantage of LD low density, softly disrupted cells using cavitation were loaded in a floatation sucrose gradient. Once ultracentrifuged, LDs float to the top fraction due to its low density and only CAV3 was present in this fraction in a similar pattern as endogenous ACSL3, a LD-resident protein (**Fig. 4C**). Finally, we checked if different protein distribution affected the total caveolin protein levels. CAV2 and CAV3 presented lower levels of protein than CAV1, being CAV3 the lowest (**Fig. 4D**).

Figure 4. CAV1, CAV2, and CAV3 differential early transport promotes differences in oligomerization, LD trafficking, and expression.
After synchronized expression of the three caveolin proteins in COS1 cells, (**A**) solubilization was performed with 1% Triton X-100 (TX) containing buffer at 4ºC to obtain soluble fraction of caveolin and scrapped afterwards with 2% SDS lysis buffer to obtain the insoluble fraction (n ≥ 3). (**B**) Cell lysates solubilized in mild 0.5% TX lysis buffer were loaded at the top of sucrose velocity gradient and then ultracentrifuged and fractionated (n ≥ 3). (**C**) Cell lysates obtained after scrapping and cavitation were loaded in the bottom part of a floatation sucrose density gradient and ultracentrifuged (n = 3). (**D**) Caveolin expression was measured obtaining total cell lysates of transfected cells (n ≥ 5). All cell fractions or lysates were run in an SDS-page and blotted using GFP antibodies for caveolin proteins, CAV1 antibody to compare with endogenous (end), ACSL3 antibody as an ER and LD marker for floatation gradients, and GAPDH as a loading control for lysate quantification. Graphs show means ±SD; *p<0.05, **p<0.01, ***p<0.001 and ****p<0.0001 in one-way analysis test using Dunnett's multiple comparisons test compared to CAV1 for (A), (C) and (D); and two-way ANOVA test using Dunnett's multiple comparisons test compared to CAV1 for (B).

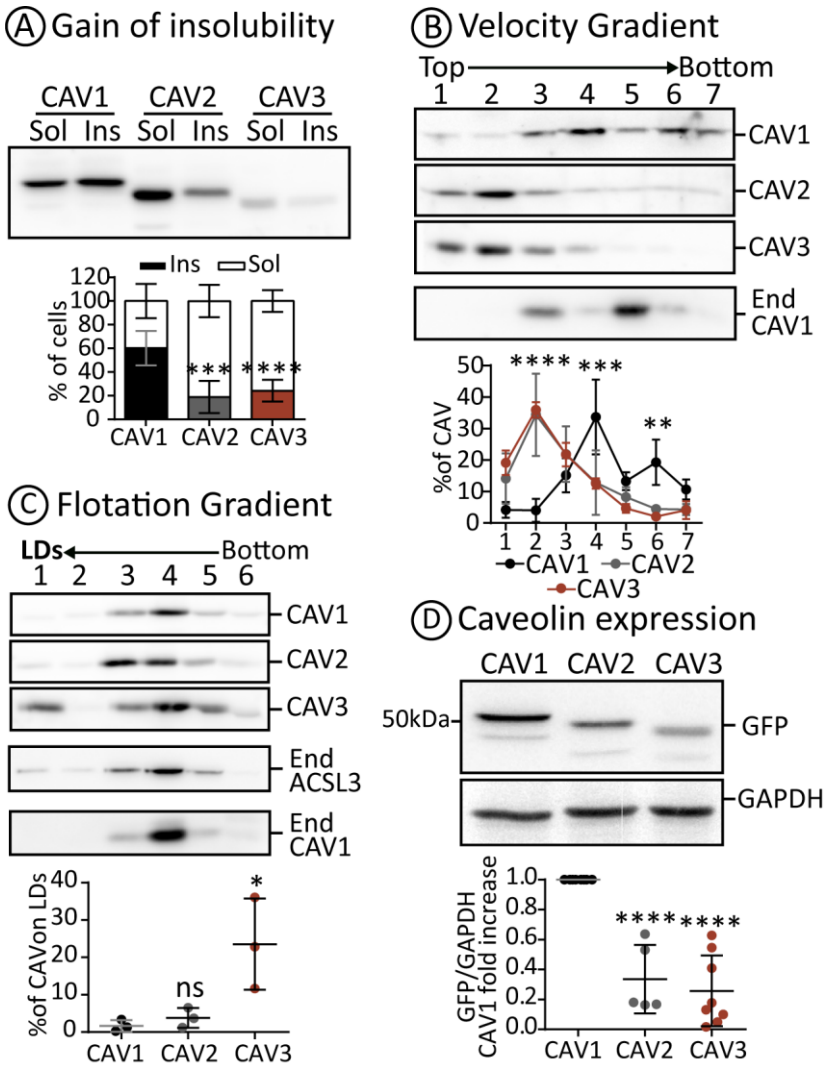
Ⓐ Gain of insolubility
CAV1 CAV2 CAV3
Sol Ins Sol Ins Sol Ins
Ins Sol
% of cells
120 100 80 60 40 20 0
*** ****
CAV1 CAV2 CAV3
Ⓑ Velocity Gradient
Top Bottom
1 2 3 4 5 6 7
CAV1
CAV2
CAV3
End CAV1
%of CAV
50 40 30 20 10 0
**** *** **
1 2 3 4 5 6 7
CAV1 CAV2 CAV3
Ⓒ Flotation Gradient
LDs Bottom
1 2 3 4 5 6
CAV1
CAV2
CAV3
End ACSL3
End CAV1
%of CAVon LDs
40 30 20 10 0
* ns
CAV1 CAV2 CAV3
Ⓓ Caveolin expression
CAV1 CAV2 CAV3
50kDa
GFP
GAPDH
GFP/GAPDH CAV1 fold increase
1.0 0.8 0.6 0.4 0.2 0.0
**** ****
CAV1 CAV2 CAV3

Having shown trafficking differences between caveolin family members, we focused on finding a plausible explanation. Our hypothesis was that protein structural differences could be affecting caveolin transport. Alternatively, different CAV-interactive partners or the fused GFP tag could also interfere. Therefore, first we checked if these differences could be explained by a technical issue.

Proteins such as cavins (*22*), EHDs (*119*), or Pacsin2 (*365*) interact post-GC with caveolins to form caveolae at the PM, but they could affect also their transport in the previous steps. These proteins present a tissue-dependent expression pattern, for example, cavin1 is expressed in most of cells of the body, whereas cavin4 is restricted to muscular tissues (*22*). Thus, caveolin-interactive proteins could not be present when expressed in a non-original tissue, such as CAV3 in non-muscular cells, misleading their correct targeting. To analyse this hypothesis, caveolin proteins were expressed in C2C12 muscular myoblasts. The results in **Fig.5 upper panels** showed that caveolin distribution and gain of insolubility remained unaffected, confirming that the interaction with other proteins is not responsible for caveolin differences in trafficking.

To control possible tag interference with caveolin transport (*366*), different tag (Myc-tag which is also smaller) and different GFP orientation (from N- to C-terminus) were analysed in COS1 cells. No differences were appreciated in both caveolin distribution and gain of insolubility (**Fig.5 middle panels**). Additionally, CAV1 and 3 cotransfection was tested to see if there is a direct interference between both caveolin expression. Even when cotransfected, CAV1 localized mainly to PM and GC, while CAV3 was retained in the GC, ER and LDs (**Fig.5 lower panels**).

With these experiments, further utility of short-timed synchronized expression was appreciated since it has been demonstrated to be robust when changing cellular context and tagging strategies. Furthermore, alternative hypothesis which could suggest the interference with other proteins or protein tagging artifacts were discarded.

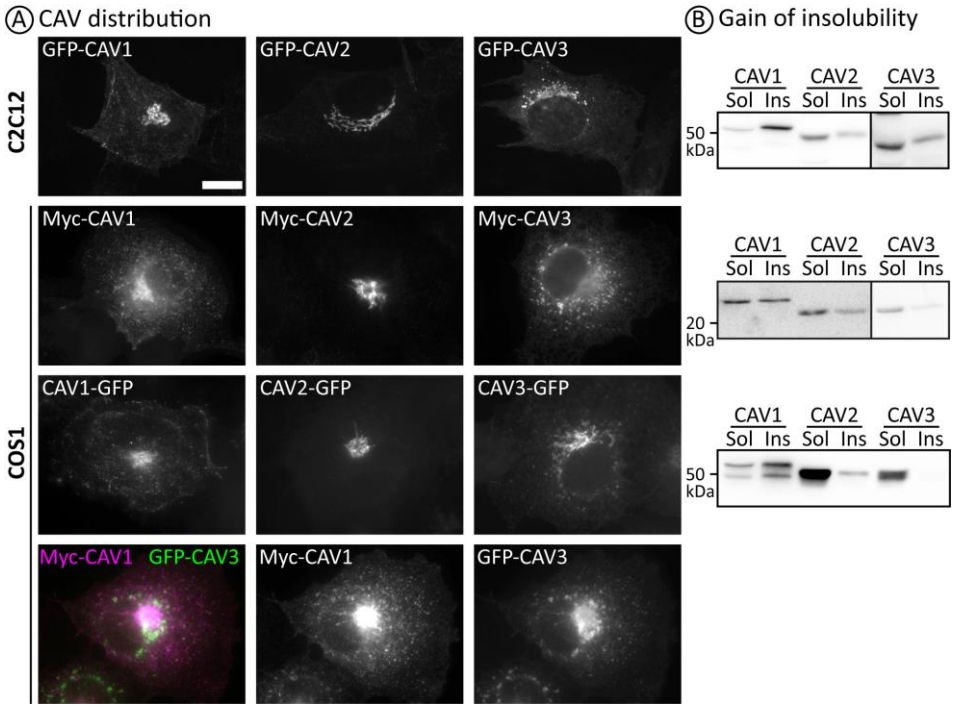

Figure 5. Cellular context, protein fusion tag, or cotransfection do not affect CAV1, CAV2, and CAV3 differential early transport.
C2C12 were short-term transfected with N-terminally tagged caveolin proteins; and COS1 cells with either N-terminally Myc, C-terminally GFP tagged caveolin proteins, or combination of both. (**A**) Representative images of caveolin distribution, which were taken at the same magnification (scale bar= 20µm), and (**B**) gain of insolubility to TX 1% are shown.

1.4. Domains of CAV3 involved in ER retention

Confirmed the differential transport of caveolin members, we focused on the protein sequence variations, which could explain this differential transport. For this study, CAV2 was not considered because it showed a high divergency from CAV1 and CAV3 sequences. In addition, no novelty was appreciated using this method as CAV2 was previously described to be accumulated in GC (*367*). Human CAV1 and CAV3 showed 65% identity using NCBI blast analysis, where both the first 15 residues and the last 20 residues of the protein present the most divergency.

1.4.1. C-terminal region

Trafficking of caveolin between ER and GC seems to be the key differential step (**Fig. 6A**). Thus, decreased ER export (from ER to GC) or increased retrograde transport (from GC to ER) could cause CAV3 retention, trafficking to LDs, and reduced access to the PM.

It was previously described that a frame-shift mutation (P158) on CAV1 C-terminal region introduced a retrieval signal consisting in 3 positive lysine residues (KKXK), which promoted caveolin accumulation in ER and LDs (*90*). Moreover, addition of a dilysine motif (KKSL) at the C-terminal region also promoted this accumulation (*89*). This is possible because retrograde GC to ER transport is mediated by retrieval signals that contain a positive charge at the C-terminus of ER resident proteins (-KDEL, -KKXX, -RRXX or -KKXK) which bind to COPI (coat complex protein I) proteins (*368*). Looking to CAV1 and CAV3 last 4 residues, CAV3 presents an arginine (R^{-4}) forming a RKXX retrieval domain, whereas CAV1 presents a glutamine (Q^{-4}) disrupting it (**Fig. 6B**). This change in CAV1 is conserved in mammals and fish but not in birds and reptiles, suggesting an evolutionary favoured substitution.

To analyse the possibility that CAV3 but not CAV1 presents a retrieval domain, the CAV1 Q175R mutant with the retrieval domain (CAV1-RKXX) and CAV3 R148Q without this retrieval domain (CAV3-QRXX) were constructed and expressed for 3 h. When the distribution of the mutants was observed by fluorescence microscopy, apparent accumulation of CAV1-RKXX at GC was observed due to decreased transport to the PM and increased ER retention (**Fig. 6C**). On the other hand, CAV3-QRXX exhibited a similar pattern of expression to wild-type (WT), but increased presence in the GC (**Fig. 6C**). Mutant distribution changes were also translated to a reduced gain of insolubility of CAV1-RKXX and increased gain of insolubility of CAV3-QRXX respect to WT protein (**Fig. 6D**). Major exposure to ER mechanisms of degradation was translated in less stability, showing less protein levels of CAV1-RKXX and more of CAV3-QRKK (**Fig. 6E**).

The addition (CAV1-RKXX) or disruption (CAV3-QKXX) of retrieval signal demonstrated that CAV1 presents less retrograde transport, although these mutations did not completely reverted CAV1 and CAV3 location as expected. Additional domains of caveolin are likely involved in the differential trafficking between both proteins.

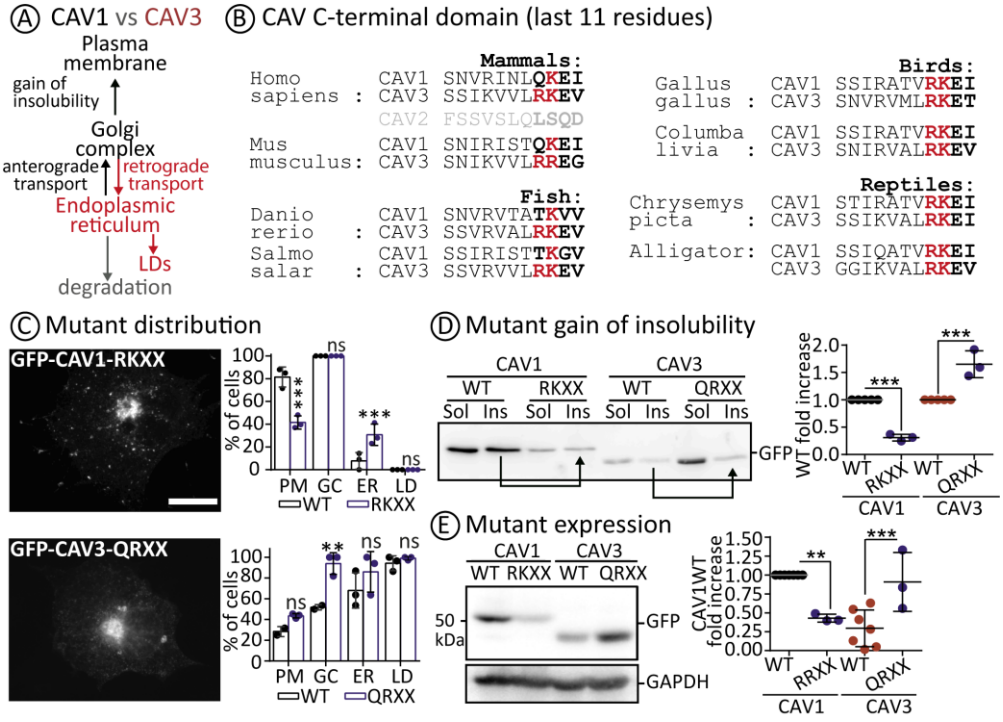

Figure 6. CAV3 C-terminus contains a retrieval transport domain promoting the retrograde transport of the protein.

(**A**) Working model of caveolin transport: CAV1 (black) is transported through the anterograde transport to the GC, where it gains insolubility, and it is finally transported to the PM. On the other hand, CAV3 (in red) is returned from the GC to the ER through the retrograde transport and redirected to LDs. Both proteins exposure to ER mechanisms of degradation decreases their stability (grey). (**B**) Last 11 residues of CAV1, CAV2, and CAV3 from different species. Last four residues forming a potential retrieval domain are bold remarked and positive residues necessary for this domain in either -3 and -4 positions are in red. CAV1-RKXX (Q175R) and CAV3-QRXX (R148Q) were expressed for 3 h and different parameters were analysed: (**C**) distribution (n = 3 including more than 100 cells per condition, Scale bar= 20 µm, and magnification is maintained for all the images), (**D**) gain of insolubility (n ≥ 3 comparing to WT insoluble fraction as indicated by arrows), and (**E**) expression (n ≥ 3). Graphs show means ±SD, where **p<0.01 and ***p<0.001 in a two-way ANOVA test using Sidak's multiple comparisons test related to WT for (C); and one-way analysis test using Bonferroni multiple comparisons test comparing each mutant to its WT for (D) and (E).

1.4.2. N-terminal region

We next analysed the dynamics of caveolin exit from the ER. ER-export of caveolin is regulated by the N-terminal region (*75*) through DXE COPII binding domains (*76*). No differences between CAV1α and β trafficking to the PM were appreciated since both proteins contain the same COPII binding domain (DEF, underlined in **Fig. 7A**) (*75*). Since CAV1β is shorter, it was compared to CAV3 to better delimit the potential retention region involved in this change. Looking closer to CAV1β and CAV3 N-terminal domain only few residue changes are evident (**Fig. 7A**, conservative in green and non-conservative in red). More hydrophobic residues are present in the CAV3 N-terminal end. The *in-silico* analysis of this sequence hydrophobic moment (μH) predicted a secondary folding forming a helix alpha (CAV1 μH=0.075 vs CAV3 μH=0.369), which in turn suggests a tight interaction with membrane bilayers and the retention of the protein to the ER.

This hypothesis was tested exchanging the initial 14 amino acids of CAV1β by the first 16 residues of CAV3 (CAV1 N-CAV3) and vice versa for CAV3 (CAV3 N-CAV1). After 3-hour expression of the mutants, CAV1-NCAV3 showed a significant ER retention, while CAV3-NCAV1 increased its transport to the PM through the GC and reduced its LD trafficking (**Fig. 7B**), when compared to the respective WT proteins. This change was translated in a decreased gain of insolubility and stability of CAV1-NCAV3 and increased of CAV3-NCAV1 (**Fig. 7C and D**).

These results showed that CAV3 contains an N-terminal ER-retention domain, and a C-terminal retrieval region that increases its retrograde transport. Consequently, these are the determinants of CAV3 retention.

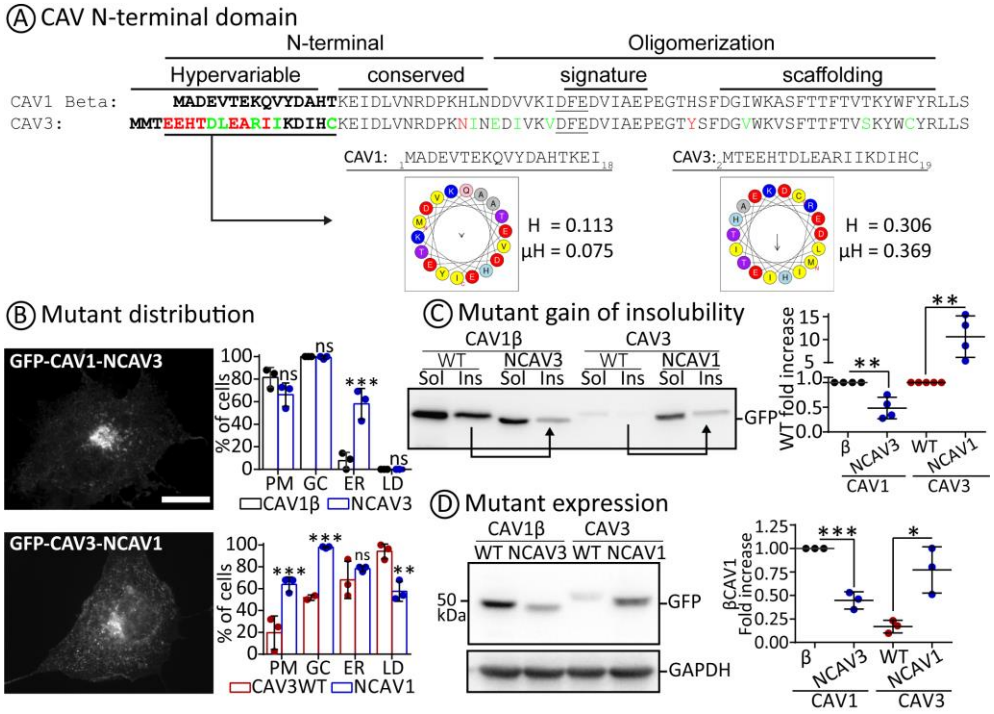

Figure 7. CAV3 N-terminus contains an ER retention domain.
(**A**) Comparison of N-terminal domains of CAV1β and CAV3 up to hydrophobic hairpin domain (starting at LLS). First 14 and 16 residues of CAV1 and CAV3 respectively forming this N-terminal hypervariable stretch are bold remarked. Conservative and non-conservative changes are respectively in green and red highlighted. COPII DFE binding motif is underlined. Hydrophobicity (H) and tendency to fold as alpha helix (hydrophobic moment or μH) of both CAV's hypervariable stretch are indicated with hydrophobic residues in yellow and charged amino acids in red (negative) or blue (positive). (**B**) Short expression of CAV1-NCAV3 (exchange of initial 14 amino acids of CAV1 by the first 16 residues of CAV3) and CAV3-NCAV1 (exchange of the 16 first amino acids of CAV3 by the first 16 residues of CAV1) revealed differences in distribution (n = 3 including 100 cells or more per condition), (**C**) solubility (n ≥ 3 comparing insoluble fractions to WT as arrow-indicated), and (**D**) stability (n = 3). Magnification of all the images was maintained (Scale bar= 20 μm). Graphs show means ±SD; where *p<0.05, **p<0.01 and ***p<0.001 in two-way ANOVA test using Sidak's multiple comparisons test related to WT for (B); and one-way analysis test using Bonferroni multiple comparisons test comparing each mutant to its WT for (C) and (D).

1.5. Early degradation of caveolins to achieve the transport to the PM

When increasing CAV1 or decreasing CAV3 ER retention, protein expression levels were respectively reduced or increased (**Fig.6 and 7**) clearly linking protein trafficking to protein degradation. Inhibition of ERAD showed to promote caveolin accumulation, affect ER and GC morphology, decrease the transport of the protein to the PM, trigger ER stress and finally promote aberrant collapse of the cell (**Fig.1**).

Thus, early targeting of caveolins after their synthesis was finely studied using the synchronized transfection method. Additionally, CAV1 and 3 mutants insensitive to ubiquitination and degradation (with all lysine residues exchanged to arginine or K*R) were utilized as previously described (*122*).

COS1 cells were transfected with WT caveolin or the non-ubiquitinable mutant K*R construct and treated with 50 µM MG132 during the 3 h expression to check for protein accumulation (**Fig. 8A**). Furthermore, controls of ER-resident transmembrane protein (VAP-A), hairpin LD- and ER- resident protein (ALDI), and transmembrane Golgi-resident (sintaxin-6, STX6) were identically expressed to ensure that the accumulation is not dependent on the organelle distribution or protein structure but specific for caveolin proteins. In all the cases caveolins were accumulated compared to VAP-A and STX6 controls, but ALDI protein was also accumulated (**Fig. 8A**). Both MG132 treatment and K*R mutant substitution strategies delayed CAV1 transport to the PM promoting the accumulation of the protein in the ER (**Fig. 8B**). For CAV3, retention in the ER and GC was also appreciated with MG132, but, unexpectedly, CAV3 K*R was partially present in the GC (**Fig. 8B**). Both strategies prevented CAV3 trafficking to the LDs (**Fig. 8B**).

Furtherly, we wanted to check if caveolin accumulation in the ER after inhibition of ERAD was followed by a decrease in caveolin oligomerization and gain of insolubility. MG132 treatment and K*R mutant prevented CAV1 oligomerization (decrease in #4 and #6, 8S and 60S fractions respectively), but induced CAV1 ordering into heavier complexes which precipitated at the bottom of the gradient (#7 fraction, **Fig. 8C**). This suggests an abnormal organization of caveolins likely due to high oligomerization in non-native aggregates. CAV3, when treated with MG132, also sedimented at the bottom of the gradient (**Fig. 8C**). CAV3 K*R mutation did not promote the same level of protein sedimentation as after MG132 treatment, nonetheless intermediate sedimentation was appreciated (increase in #4-5 fractions) (**Fig. 8C**).

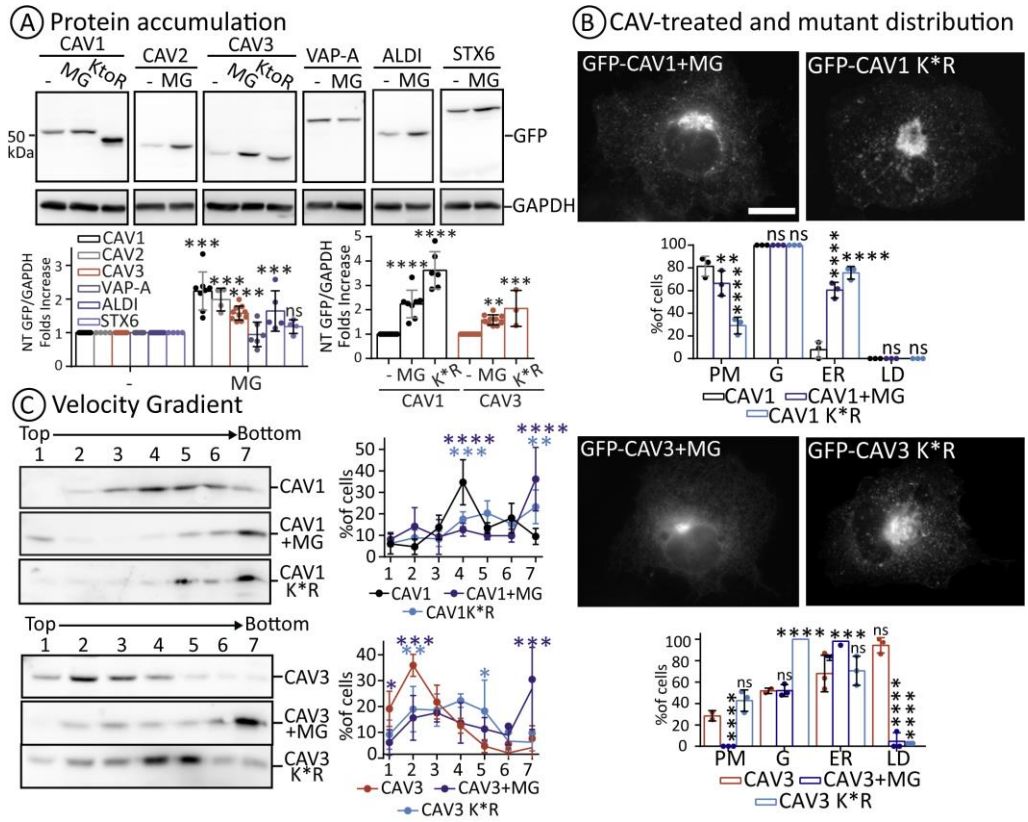

Figure 8. Caveolins are degraded by ERAD to avoid aggregation.
(**A**) 3 h of caveolin protein expression with 50 µM MG132 treatment compared to VAP-A, ALDI, and STX6 (n ≥ 3). Caveolins K*R mutants (insensitive to proteasomal degradation) were also analysed in parallel. Protein distribution was analysed with both (**B**) fluorescence microscope image quantification (n = 3 independent experiments including 100 cells or more per condition) and (**C**) Velocity gradient centrifugation and fractioning (n = 3). Graphs show means ±SD; where *p<0.05, **p<0.01, ***p<0.001 and ****p<0.0001 in two-way ANOVA test using Dunnett's multiple comparisons test related to non-treated cells for (A), and to WT protein for (B) and (C).

In conclusion, caveolin proteins are degraded by ERAD to ensure a proper oligomerization and distribution. The precise nature of these heavier forms of caveolin or whether it interacts with other proteins deserves further investigation.

CAV3 prevention of ubiquitination (K*R mutant) showed less ER retention compared to MG132 treatment. It suggests that even when not ubiquitylated, CAV3 in ER can be partially targeted to degradation independently of proteasome, which is the last step of ERAD. Autophagy could be also a mechanism by which caveolin is degraded in the ER, since, together with proteasomal degradation, they are the two major cell mechanism involved in protein degradation in eukaryotes (*162*). Autophagy in ER (ER-phagy) is acting in both selective (ubiquitin-mediated) and non-selective (bulk protein degradation) mechanisms (*163*). Moreover, non-selective macro autophagy (macro-ER-phagy) is triggered when there is an increase of misfolded protein aggregates (*163*), and could be the specific mechanism promoting caveolin degradation in the ER.

To unveil if autophagy plays a role in caveolin protein degradation after synthesis, COS1 transfected cells were expressed for 3 h with caveolins while treated with 10 mM 3-methyladenine (3MA) autophagy inhibitor. Autophagy inhibition Increased CAV1 and CAV3 retention in the ER, similarly than MG132 treatment, which also partially decreased CAV3 trafficking to LDs (**Fig. 9A**). Retention in the ER was correlated with accumulation of both proteins when measuring their expression with 3MA treatment (**Fig. 9B**). Protein levels were synergistically increased when using MG132 and 3MA (**Fig. 9B**), confirming the complementation of both pathways in this regulation. When measuring caveolin oligomerization with sucrose velocity gradients after the treatment with 3MA, only CAV1 showed an altered oligomerisation (increase in the #7 heavy fraction), but it was lower than with MG132 treatment.

Therefore, we have shown that autophagic degradation of caveolin in the ER is important to complement ERAD degradation in preventing the accumulation, misfolding, and aggregation of the protein.

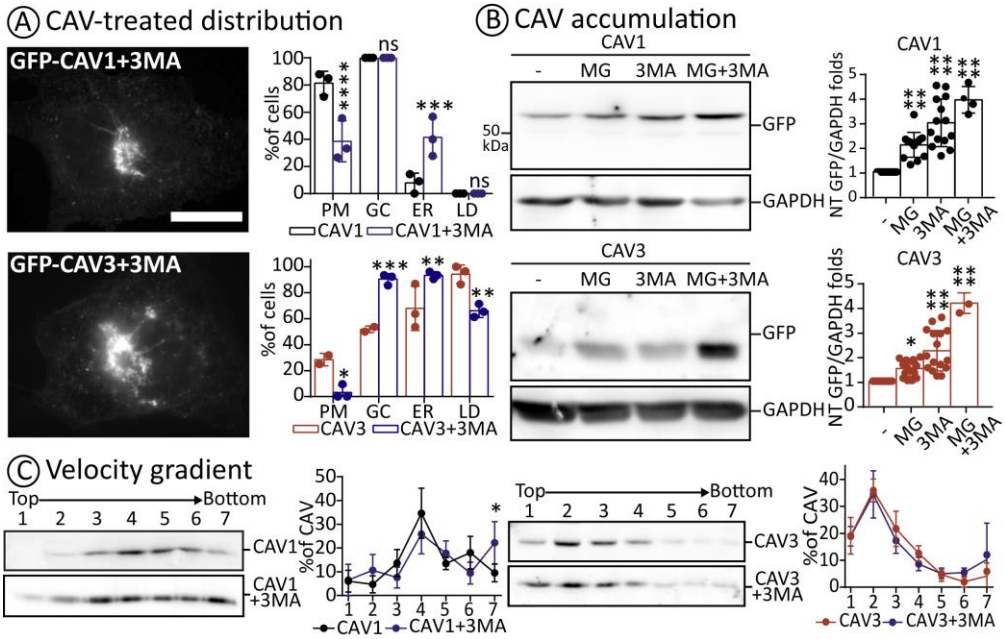

Figure 9. Caveolins are complementary degraded by ER-phagy during early transport. COS1 cells were treated with MG132, 3MA, or both treatments during the short-timed expression of CAV1 and CAV3. (**A**) Protein distribution was counted in more than 100 cells per condition (n = 3, scale bar= 20 nm). (**B**) Protein expression using the combination of both inhibitors were detected to check the sensitivity of CAV1 and CAV3 to proteasomal or autophagy degradation (n ≥ 3). (**C**) Oligomerization state of CAV1 and CAV3 was checked after 3MA treatment using sucrose velocity gradients (n ≥ 3). Images shown are taken in the same magnification. Graphs show means ±SD; *p<0.05, **p<0.01, ***p<0.001 and ****p<0.0001 in two-way ANOVA test using Sidak's multiple comparisons test related to non-treated (NT) cells for (A) and related to non-treated cells for (B); and Dunnett's multiple comparisons test for (C).

1.6. Relevance of caveolin early degradation

Next, the impact on ER stress after inhibition of caveolin degradation was analysed. ER stress induction was measured as in **Fig.1** using XBP1S and CHOP markers after expression of all the caveolin members and control proteins when inhibiting caveolin degradation. These experiments were performed under long-term expression times, because differences in ER stress induction between constructs were not appreciated after 3 h due to the low percentage of transfected cells and protein levels (results not shown).

Synchronized expression was allowed for 16 h and ER stress induction was measured. The MG132 treatment triggered a higher ER stress response of both markers for caveolins compared to VAP-A and STX6 (**Fig. 10A**). Interestingly, ALDI triggered a similar XBP1S folding response than caveolins without inducing the CHOP proapoptotic response (**Fig. 10A**) likely extending this mechanism to hairpin proteins. Both CAV1 and CAV3 non-ubiquitinable mutants triggered XBP1S, but CHOP was only induced by CAV1 K*R expression (**Fig. 10A**). As previously shown, CAV3 K*R mutation was not fully promoting CAV3 sedimentation and ER retention. That could be the explanation for the incomplete induction of ER stress (positive for XBP1S response but not for the CHOP response, **Fig. 10A**).

It must be stressed that although this experimental approach is very convenient to explore the intracellular traffic of caveolins, the conclusions about the physiological effect are limited as it is an overexpression system. Genome-edited cells could be used in the future to fully understand the physiological relevance of caveolin degradation in the ER and its effect in the ER homeostasis.

However, as a first approach we look at endCAV1. Non-transfected COS1 cells were treated with 5 µM MG132 for 16 h and endCAV1 distribution was tracked using CAV1 antibodies (**Fig. 10B**). EndCAV1 present in the GC and PM radically changed its localization to the ER after MG132 treatment, showing a clear reticular morphology at the cell periphery, central ER cisternae, and nuclear envelope staining, which was further confirmed using calnexin ER marker (**Fig. 10B**). CAV1end ER retention also promoted the aggregation of the protein (increase in the #7 fraction) (**Fig. 10C**).

ER accumulation and aggregation of caveolins has a negative impact in cells since it triggers ER stress response. This mechanism could be also extended to hairpin proteins such as ALDI. Moving to EndCAV1, cell uses proteasomal degradation to avoid caveolin retention and aggregation in the ER

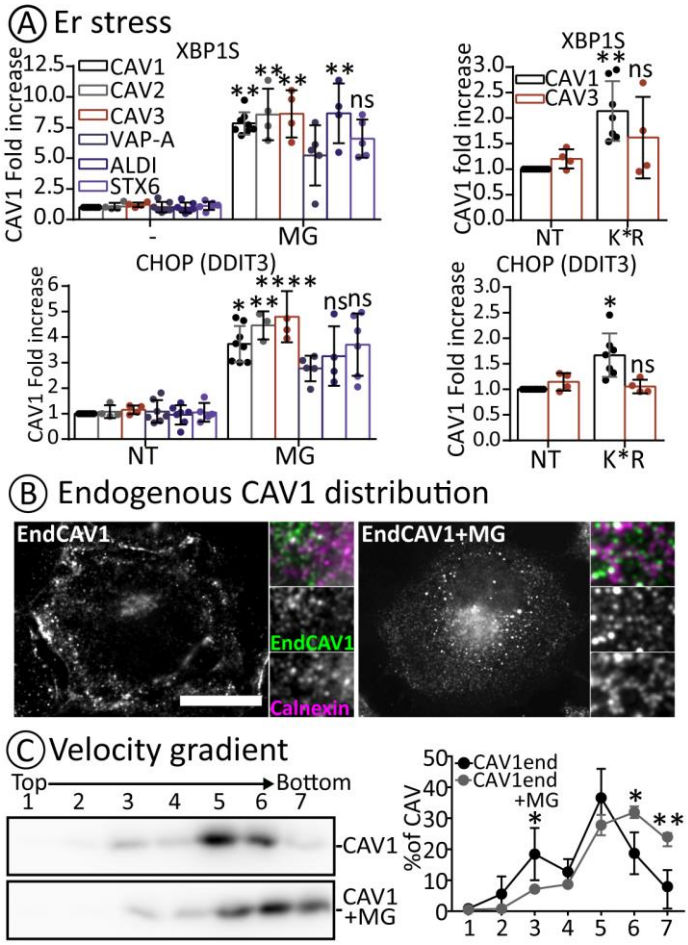

Figure 10. Targeting caveolins and hairpin proteins to ERAD prevents the cells from ER stress, protein retention, and aggregation.
(**A**) Synchronized expression was allowed for 16 h in transfected COS1 cells with CAV, K*R mutants or control proteins treated with 5 µM MG132 (MG) to measure ER stress response triggering (n ≥ 4). (**B**) Non-transfected cells were treated for 16 h with MG132 and visualized using anti-CAV1 and anti-Calnexin antibodies at the same magnification (Scale bar= 20 nm). (**C**) Oligomerization and aggregation of EndCAV1 were measured in sucrose density gradients. Graphs show means ±SD; where *p<0.05, **p<0.01 and ****p<0.0001 in two-way ANOVA test using Bonferroni multiple comparisons test related to CAV1 for (A) and Sidak's multiple comparisons test related to EndCAV1 for (C).

.

1.7. Differential degradation of caveolin isoforms and naturally occurring pathogenic mutants

Following the methodology developed for this project, we aimed to explore some unknown processes in which caveolin degradation in the ER could be relevant.

The existence of CAV1α and β isoforms have been puzzling, since, despite some differences in caveolae formation and the deepness of these invaginations have been appreciated (*14*), no functional explanation has been described. Until now, it has been assumed that both isoforms have identical trafficking, although some relevant differences may be considered. However, we observed that the N-terminal region of CAV1α (lacking in β isoform) contains numerous lysine that could be potentially ubiquitinated (*123*), and target the protein to degradation. Thus, we speculated that CAV1β should be a more stable protein than CAV1α, and we compared both isoforms using the short transfection method.

When shortly expressing both isoforms, no clear difference was appreciated in the distribution (**Fig. 11A, upper panel**), nor in the oligomerization with MG132 treatment (**Fig. 11C, upper panel**) of both proteins. The expression levels of β isoform were higher (**Fig. 11B, upper panel).**

Thus, CAV1β exhibits a lower early ERAD degradation when compared to the α, which could explain the mentioned functional differences between both isoforms.

Some mutations in CAV1 and many mutations in CAV3, promote the retention of both proteins in the GC and ER preventing caveolae formation (*73, 369*). CAV1 P132L and CAV3 P104L has been used as a model to study the altered transport of caveolin mutants since they contain a mutation in the hydrophobic domain that prevents a normal hairpin topology (*84, 86, 109*). Therefore, we wanted to confirm if early ERAD degradation could be determinant for the pathogeny of these mutants.

COS1 cells expressing CAV1 P132L mutation showed a clear retention of CAV1 to the GC, completely preventing the transport of the protein to the PM (**Fig. 11A, middle panel).** When compared to CAV1, the P132L mutant displayed a decreased protein stability (**Fig. 11B, middle panel**), which would be caused by a major exposure to the ERAD by the delayed transport of the mutant to the PM. Looking to oligomerization, CAV1 P132L mutation increased the protein soluble fraction (fractions #1-2) showing defects in oligomerization (**Fig. 11C, middle panel**). After proteasomal inhibition only a slight fraction of the protein sedimented into high molecular weight densities, while soluble fraction was predominant (**Fig. 11C, middle panel**) contrasting to CAV1. Incorrect folding of the protein clearly induced ER stress despite being less accumulated and aggregated than WT protein (**Fig. 11D, upper panel**).

The results suggests that P132L mutant is unable to oligomerise and traffic into the PM, therefore, it is intracellularly retained finally reducing the protein stability by a higher protein degradation from the ER. Strikingly, changes at CAV1 conformation by P132L mutation prevented CAV1 sedimentation in the bottom of sucrose gradients when treated with MG132, suggesting that a correct hairpin topology and likely oligomerisation are required to form these high weight and non-native molecular forms.

The same experiment was then performed with the CAV3 P104L mutant. Unexpectedly, CAV3 P104L mutation apparently increased CAV3 transport out of the ER and favoured the retention of the protein in GC, instead of promoting ER accumulation (**Fig. 11A, low panel**). As for CAV1 P132L, CAV3 P104L mutant completely failed to reach PM and the LD trafficking was prevented (**Fig. 11A, low panel**). GC accumulation of the mutant resulted in a more stable protein (**Fig. 11B, low panel**). Intriguingly, P104L mutation showed a higher sedimentation in sucrose gradients into the fractions hypothetically containing low molecular weight oligomers (increase in intermediate phases #3-5, **Fig. 11C, low panel**). When treated with MG132 inhibitor, CAV3 P104L displayed the high sedimentation in sucrose gradients previously observed for CAV3 (increase in fraction #7). In this case, delayed transport to the PM also induced ER stress (**Fig. 11D low panel**).

Contrasting with CAV1 P132L, CAV3 P104L mutant did not further increase the retention of the protein in the ER, but slightly speed their transport to the GC.

Therefore, CAV1 P132L and CAV3 P104L could differently induce pathogenicity although both mutants were accumulated in the GC and triggered the ER stress response. On the one hand, P132L lack of oligomerisation decreased PM transport, stability, and insolubility of the CAV1 mutant. On the other hand, P104L increase on oligomerization, promoted the transport of the protein to GC, which increased the stability and insolubility of the CAV3 mutant.

Figure 11. Differential proteostasis of caveolin isoforms and mutants.
CAV1 α and β isoforms (n ≥ 2); CAV1 WT and P132L (n ≥ 3); and CAV3 WT and P104L (n ≥ 3) were pairwise compared using short expression method.
(**A**) trafficking (more than 100 cells per condition), (**B**) stability, and (**C**) oligomerization during the early steps of protein synthesis and transport. (**E**) The ER stress (n ≥ 4) derived of 16 h synchronized expression of both P132L and P104L was measured. Scale bar= 20 µm with representing images taken at the same magnification. Graphs show means ±SD; *p < 0.05, **p < 0.01, ***p < 0.001 and ****p < 0.0001 in two-way ANOVA test using Sidak's multiple comparisons test related to WT for (A), and Bonferroni multiple comparisons test related to non-treated condition for (C); and in paired two-tailed t-test for (B) and (D).

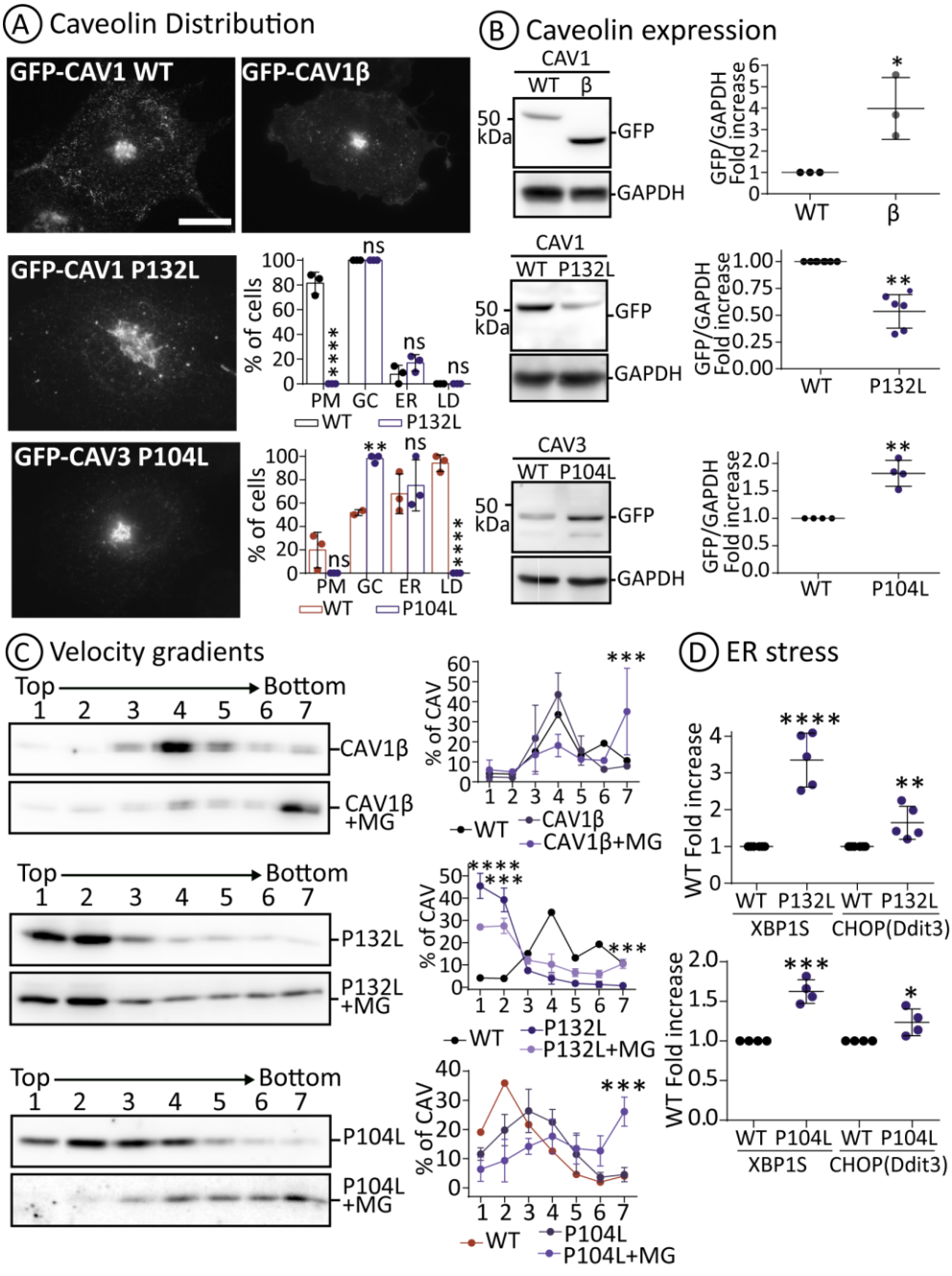
A Caveolin Distribution
GFP-CAV1 WT
GFP-CAV1β
GFP-CAV1 P132L
GFP-CAV3 P104L
% of cells
PM GC ER LD
WT
P132L
P104L
B Caveolin expression
CAV1
WT β
50 kDa
GFP
GAPDH
GFP/GAPDH Fold increase
WT
β
CAV1
WT P132L
P132L
CAV3
WT P104L
P104L
C Velocity gradients
Top
Bottom
1 2 3 4 5 6 7
CAV1β
CAV1β +MG
P132L
P132L +MG
P104L
P104L +MG
% of CAV
WT
CAV1β
CAV1β+MG
P132L
P132L+MG
P104L
P104L+MG
D ER stress
WT Fold increase
XBP1S
CHOP(Ddit3)

1.8. CAV3 trafficking to LDs and function

1.8.1. Proteostasis and trafficking of LD-resident proteins

In the previous sections, it has been shown that correct CAV3 proteostasis is required for LD trafficking. When inhibiting caveolin degradation (MG and 3MA treatment, or non-ubiquitinable mutant), the transport of CAV3 to LDs was prevented (**Fig. 8 and 9).** Furthermore, P104L mutation, which showed differences in stability and oligomerization, also prevented this transport. In this part of the project, we focused on studying the early transport of caveolin proteins to the LDs, and we used CAV3 because CAV1 was not observed in these organelles during this short period.

CAV3 was described to laterally diffuse within the ER to LDs in a process mediated by the hydrophobic domain and amphipathic helices of the protein (*181*). This transport is characteristic of class I hairpin LD-resident proteins and contrasts with class II proteins (such as PLINs), which are transported from the cytoplasm (*175*). Since ALDI (type I LD protein) showed like CAV3 to be degraded by ERAD (**Fig.8**), and promote ER stress (**Fig.10**), we checked if this early degradation system is a shared mechanism of LD proteins, which could help for example in the correct location of those proteins into LDs.

CAV3 short expression was compared to ALDI type I protein and PLIN2 and 3 type II proteins. Interestingly, the transport of CAV3 into LDs was completely abolished when the cells were treated with MG132, which was also reproduced by the expression of the non-ubiquitinable CAV3 (**Fig. 12A**). These results were biochemically confirmed using flotation gradients, where proteasomal inhibition completely blocked the accumulation of CAV3 and ALDI in LDs; and did not affected the distribution of PLIN2 and PLIN3 into the organelle (**Fig. 12B**).

Although more experiments are required to further understand this phenomenon, the correct trafficking of type I proteins (such as CAV3 and ALDI) is dependent of the dynamic degradation of the proteins to allow the lateral diffusion to LDs (*370*). On the other hand, type II proteins (PLIN2 and 3) do not require this regulation since they are targeted to LDs from the cytoplasm.

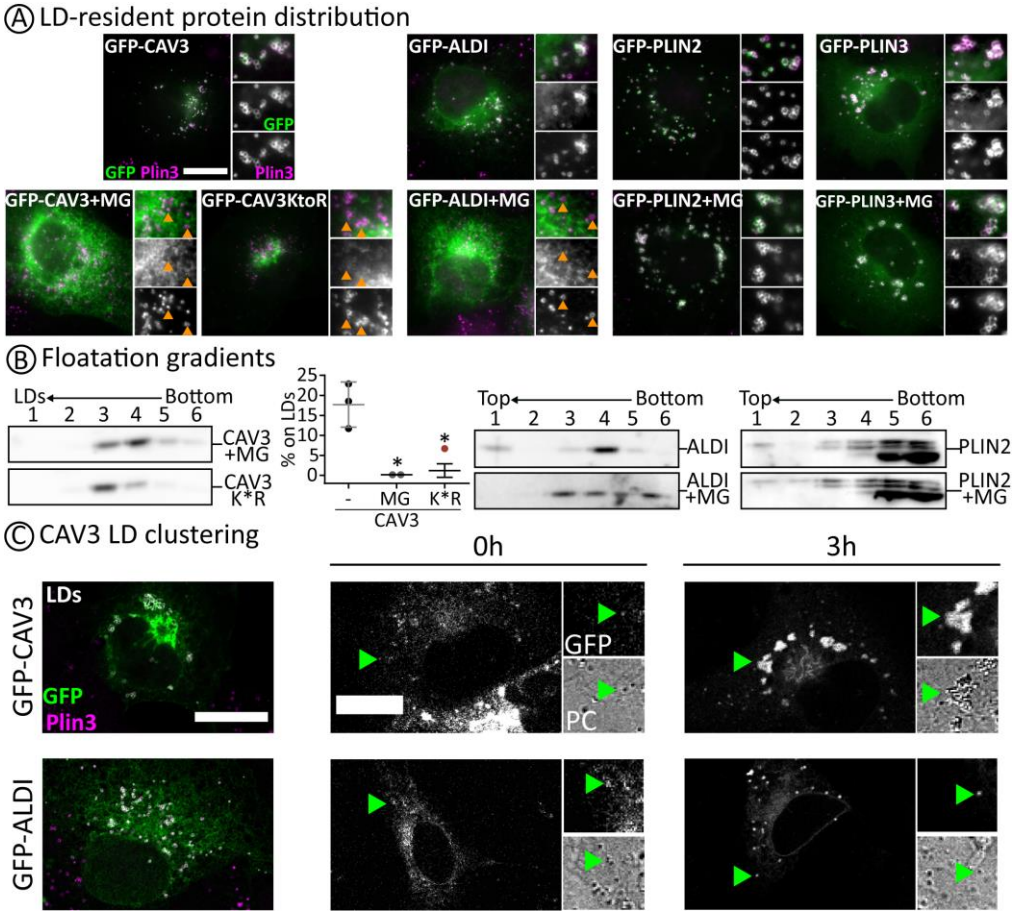

Figure 12. Hairpin proteins require early degradation for LD transport.
(**A**) LD trafficking of short-expressed type I (CAV3 and ALDI) and II LD-resident (PLIN2 and PLIN3 detected with PLIN3 antibody) proteins, either with or without MG132 treatment or K*R mutation. Orange arrowheads mark the absence of LD trafficking. (**B**) Flotation sucrose gradient fractioning of LD at phase #1 of aggregated CAV3 (n = 2, graph show means ±SD; *p<0.05 using One-way ANOVA test using Dunnett's multiple comparison test) and representative images of ALDI and PLIN2 after MG132 treatment. (**C**) After CHX removal tracking of cells expressing either CAV3 or ALDI (20 cells per condition) was done taking images of the cells every 2 minutes for a 3 h lapse of time, while maintaining them at 37ºC and 5% CO_2. Representative images of cells are shown at 0 h, were GFP expression is barely detected, and at 3 h (images are contrasted). Correlative phase contrast (PC) images are also shown to better appreciate LD morphology (green arrowheads). Time-lapse experiment images were compared to fixed cells also stained with PLIN3 antibodies to better appreciate LD change of distribution. Scale bar = 20 µm for all the images, which were taken at the same magnification in the respective experiment.

Finally, it was also appreciated that after only 3 h of expression, the LDs accumulating CAV3 demonstrated a clustered distribution, in contrast to the LDs containing ALDI (**Fig. 12C**). LD clustering is associated with a decrease in fatty acid oxidation (FAO) compared to dispersed LDs (*345*). Accordingly, we wanted to see if CAV3 trafficking to LDs could be affecting cell lipid metabolism through the regulation of LD distribution, and we used time lapse fluorescence microscopy to compare from 0 to 3 h the distribution of LDs in cells expressing CAV3 and ALDI (**Fig. 12C**). Whereas at time 0 h LDs (green arrows) on both CAV3 and ALDI demonstrated the same dispersed distribution, CAV3 induced a full clustering of LDs around the perinuclear region at 3 h, which was not appreciated in ALDI expressing cells (**Fig. 12C**).

It was presented an initial evidence that non-caveolar CAV3 has an active role in LD metabolism by changing the distribution of these organelles, and possibly determining the FAO of LDs in a timing as fast as 3 h.

1.8.2. LDs as CAV3 depots

Alternatively, CAV3 LD trafficking could be protecting the cells from defects in the ER protein quality control. Supporting this, CAV3 was shown to be relocated to LDs when directly blocking exocytic pathway with Brefeldin A (*89*) likely to avoid the damage in the ER. LDs, on the other hand, act as protein depots (*170*) and insults in the ER homeostasis promote the formation of them (*133, 136, 137*). Gathered evidence led us to hypothesize that caveolin accumulation in ER triggers ER stress, which in turn promotes LD formation and the transport of CAV3 into LDs.

To link this mechanism, long-term transfection like in **Fig.1** was used to detect ER stress. CAV3 and VAP-A were expressed for 24 h in COS1 cells, treated with 1.5 µM MG132 for 16 h and supplemented with 300 µg/mL oleic acid (OA) for the last 3 h to induce LD formation. OA did not affect protein accumulation after MG132 treatment (**Fig. 13A**), but CAV3 trafficking to LDs was improved decreasing the disorganization of the mentioned ER aberrant morphology (**Fig. 13B**). Noteworthy, OA treatment rescued CAV3 PM trafficking in most of the cells (**Fig. 13B**). Avoiding the saturation of the ER machinery alleviated CAV3 proapoptotic ER stress response (CHOP) without altering the folding response (XBP1S) (**Fig. 13C**). In all the cases, VAP-A remained unaltered demonstrating that all the cell effects were specific for the transport of CAV3 (**Fig. 13A-C**).

The beneficial effects of LD trafficking were further investigated. Previously described CAV3 mutants were long-term expressed and treated (**Fig. 13D**): CAV3 DGV mutant (deletion of N-terminal, 1-55 residues), LLS mutant (deletion of N-terminal and SCD domains, 1-75 residues), and LLSΔEnd (LLS mutant with last 8 residues removal) (*181, 371*). Deletion of the N-terminal region (CAV3 DGV and LLS) prevented CAV3 transport to the PM and the accumulation of both in the ER and LDs (**Fig. 13E**). Additional deletion of C-terminal residues (LLSΔEnd) retained almost all CAV3 in the ER (**Fig. 13E**). Decreased ER exit of CAV3 mutants promoted a lower stability of the proteins: DGV, LLS, and LLSΔEnd only presented respectively a 50%, 35% and 15% of the total CAV3 expression (**Fig. 13F**). MG132 treatment promoted a greater accumulation of DGV, LLS, and LLSΔEnd mutants than CAV3 WT, being LLSΔEnd (ER-retained) the greatest. Autophagy remained the same for all the mutants and WT protein (**Fig. 13F**). LD trafficking of the mutants did not affect the XBP1S response to ER stress (**Fig. 13G**). Accumulation of DGV and LLS after MG132 treatment triggered a higher response than WT, which was ameliorated by OA treatment (**Fig. 13G**). LLSΔEnd, although expressed in much lower levels, achieved a similar CHOP response than CAV3 WT, which was not ameliorated by OA treatment (**Fig. 13G**).

Conclusively, LD trafficking of CAV3 prevented the accumulation of this protein in the ER and the triggering of ER stress, showing that LDs can act as depots for buffering the toxic CAV3 from the ER.

Figure 13. LD trafficking is a complementary mechanism for alleviating caveolin accumulation in the ER and the consequent ER stress.
(A-E) Cells were non-synchronic transfected for 24 h with CAV3 or VAP-A as a control, treated for the last 16 h with 1.5 µM MG132 (MG) and supplemented with 150 µg/mL oleic acid (OA) for the last 3 h. (**A**) Electron microscopy using GFP-APEX system to track GFP-CAV3 localization (scale bar at 2 µm) was used. (**B**) Protein expression levels (n ≥ 3), (**C**) protein distribution, (**D**) prevention of ER and GC vesiculation (n ≥ 4, counting more than 100 cells per condition), and (**E**) ER stress buffering (n ≥ 3) was measured. (F) Mutants containing deleted domains of CAV3, previously described in (*181*) and used for figures F-J are represented compared to WT. (F-J) COS1 cells were transfected with CAV3 mutants using synchronized-expression method: (G) Distribution and (H) expression of the mutants without treatments, and after 3 h MG132 and 3-methyladenine (3MA, 10mM) treatment. (J) ER stress triggering after 16 h expression with or without MG132 and OA treatment was measured. For fluorescence images the scale bar is at 20 µm and they are in the same magnification. Graphs show means ±SD; *p<0.05, **p<0.01, ***p<0.001 and ****p<0.0001 in two-way ANOVA test using Sidak's multiple comparisons test comparing each condition to VAP-A and CAV3 with or without OA for A-C. Same test but comparing mutants to CAV3 in each condition and each construct with or without OA was used for G-H. One way ANOVA test with Sidak's multiple comparisons test was used for F.

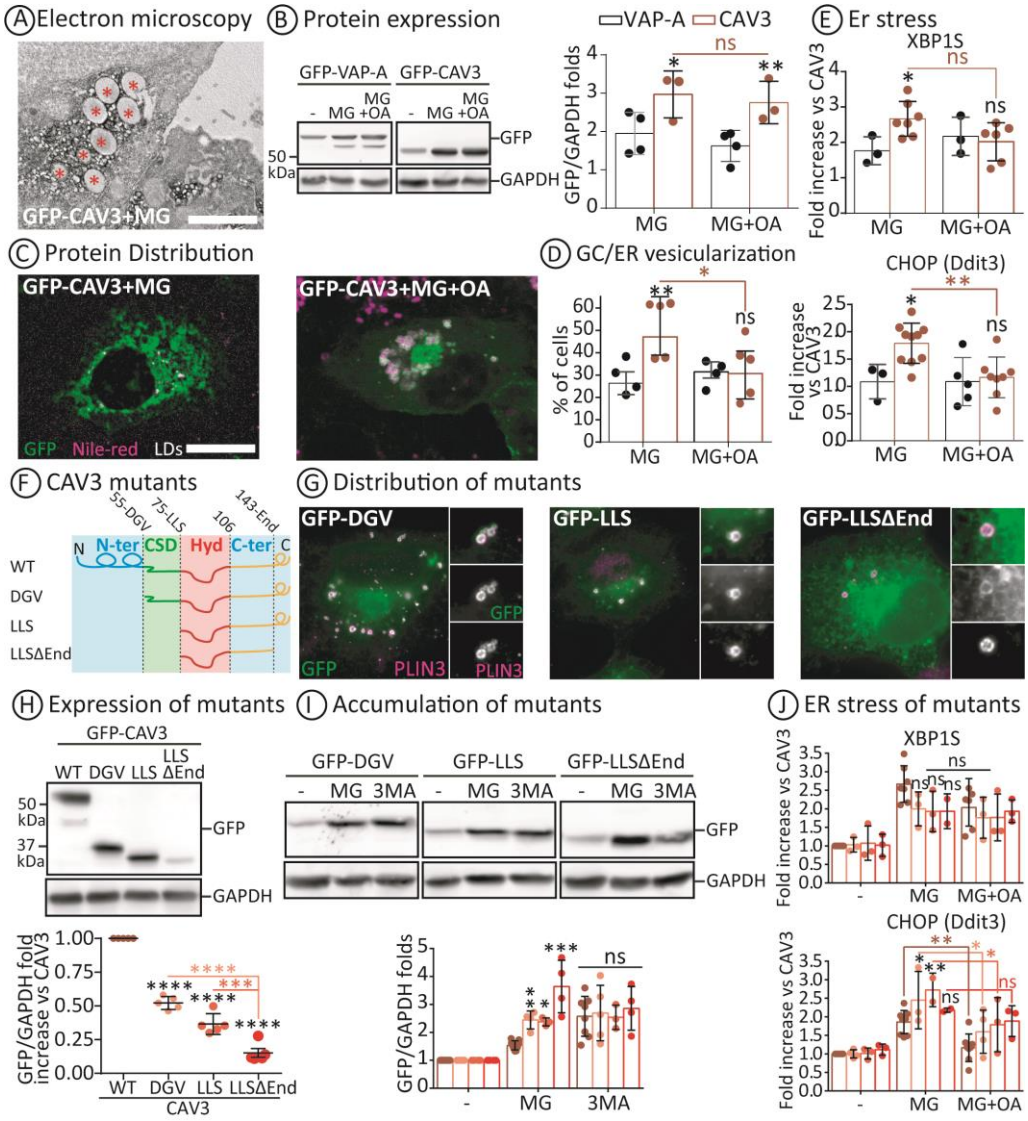
A Electron microscopy
GFP-CAV3+MG
B Protein expression
GFP-VAP-A
GFP-CAV3
MG
MG +OA
50 kDa
GFP
GAPDH
VAP-A CAV3
GFP/GAPDH folds
ns
MG
MG+OA
E Er stress
XBP1S
Fold increase vs CAV3
CHOP (Ddit3)
C Protein Distribution
GFP-CAV3+MG
GFP-CAV3+MG+OA
GFP Nile-red LDs
D GC/ER vesicularization
% of cells
F CAV3 mutants
55-DGV
75-LLS
106
143-End
N N-ter CSD Hyd C-ter C
WT
DGV
LLS
LLSΔEnd
G Distribution of mutants
GFP-DGV
GFP-LLS
GFP-LLSΔEnd
GFP
PLIN3
H Expression of mutants
GFP-CAV3
WT DGV LLS LLS ΔEnd
37 kDa
GFP/GAPDH fold increase vs CAV3
I Accumulation of mutants
3MA
J ER stress of mutants

CHAPTER II:

2. Prevention of ectopic lipid deposition for the treatment of T2DM and metabolic syndrome

2.1. *In vitro* model for the measure of LD accumulation and lipotoxicity

We first developed an *in vitro* model to check for lipid accumulation, either inside LDs or in a free form, and relate it to lipotoxicity. Since muscle cells are especially sensitive to ectopic lipid deposition (*372*), we incubated the C2C12 cells with OA and palmitic acid (PA), which are the most prevalent unsaturated and saturated FAs in the blood accounting for a 35% and 28% of the total respectively (*373*).

C2C12 myoblasts were supplemented with 100 µg/mL of OA, PA, or the combination of both (100 µg/mL OA + 100 µg/mL PA) for 24 h. LDs were visualized with fluorescence microscopy using Nile-red staining: while OA either alone or combined with PA induced LD formation, PA alone showed a diffuse lipid-staining pattern (**Fig. 14A**). This lipid accumulation was then quantified by flow cytometry using the optical properties of Nile-red (*374*). Despite all FAs were accumulated inside the cells (orange light, PE filter) (*345, 375*), OA and OA+PA were accumulated as neutral lipids inside LDs (green light, FITC filter) and PA in a more polar free form (red light, PerCP filter) (**Fig. 14B**, see materials and methods for more details). To confirm this, the LD marker PLIN2 was measured by WB (*189*): OA and OA+PA increase on LD formation was translated in a marked expression of PLIN2, which was not observed after the PA treatment (**Fig. 14A**). Regarding to the lipid species, PA is known to be accumulated as polar diacylglycerols (DAGs) (*129*), whereas OA is easily esterified as neutral triacyclglycerols (TAGs) (*376*). To analyse this in our model, lipid fractions of C2C12 cells were extracted using Bligh-Dyer method and run in TLC silica membrane to separate lipid species. The results confirmed that OA and OA+PA induced the synthesis of TAGs (in green), whereas with PA this process was less efficient promoting the accumulation of DAGs and monoacylglycerols (MAGs) (in red) (**Fig. 14B**).

Additionally, the link between FA accumulation into LDs and lipotoxicity was measured in these conditions. Compared to OA and OA+PA treatments, cells supplemented with PA radically changed to a round and detached morphology suggesting a lipotoxic-induced cell apoptosis (**Fig. 14C**). Cell death and reactive oxygen species production (ROS) were measured by cell cytometry using propidium iodide (PI) and H_2DCF-DA (DCF) staining respectively. Further, ER stress was also measured by tracking the expression of XBP1S and CHOP markers. PA triggered cell death, ROS production, and ER stress (**Fig. 14C**). On the other hand, OA alone or combined with PA did not trigger any lipotoxicity at all (**Fig. 14C**).

In conclusion, these experiments demonstrate that unsaturated FAs such as OA induce the synthesis of TAGs, which are then accumulated in LDs and are innocuous for the cell. On the contrary, saturated FAs such as PA are not properly stored as TAGs inside LDs leading to the accumulation of intermediates such as DAGs and MAGs, which promote cell death, ROS, and ER stress. Thus, incubation with PA was used in the following experiments to trigger lipotoxicity for the emulation of the lipid ectopic deposition promoted during obesity.

Figure 14. Unsaturated fatty acids (FAs) such as oleic acid (OA) trigger lipid accumulation on LDs to prevent the cell from lipotoxicity, contrasting with saturated FAs such as palmitic acid (PA). C2C12 cells were supplemented with 100 µg/mL of OA, 100 µg/mL of palmitic acid (PA), or 100 µg/mL OA plus 100 µg/mL PA (OA+PA) for 24 h. (**A**) Representative images of LD formation on cells stained with Nile-red and visualized using fluorescence microscope are shown. Further quantification of lipid accumulation and LD formation was performed using FACS analysis ($n \geq 6$) separating green, orange, or red fluorescence as described on material and methods section. PLIN2 immunoblotting ($n \geq 5$) was used to confirm LD formation and validate flow cytometry results. (**B**) Quantification of TAGs ($n \geq 5$), DAGs ($n \geq 3$), or monoacylglycerols (MAGs $n \geq 3$) compared to phospholipids (PLs, $n \geq 6$) as the lipid species isolated from lipid fractions. (**C**) Lipotoxicity measure using propidium iodide (PI, $n \geq 11$) and H_2DCF-DA (DCF, $n \geq 15$) staining for apoptosis or ROS production respectively (double staining is described on material and methods section). ER stress ($n \geq 7$) was also measured using XBP1S and CHOP markers. Images were taken with the same magnification between experiments and the scale bar is 20 µm and 200 µm for (B) and (C) respectively. Graphs show means ±SD; *p<0.05, **p<0.01, ***p<0.001 and ****p<0.0001 in one-way ANOVA test using Sidak's multiple comparisons test comparing each condition to non-treated cells (-).

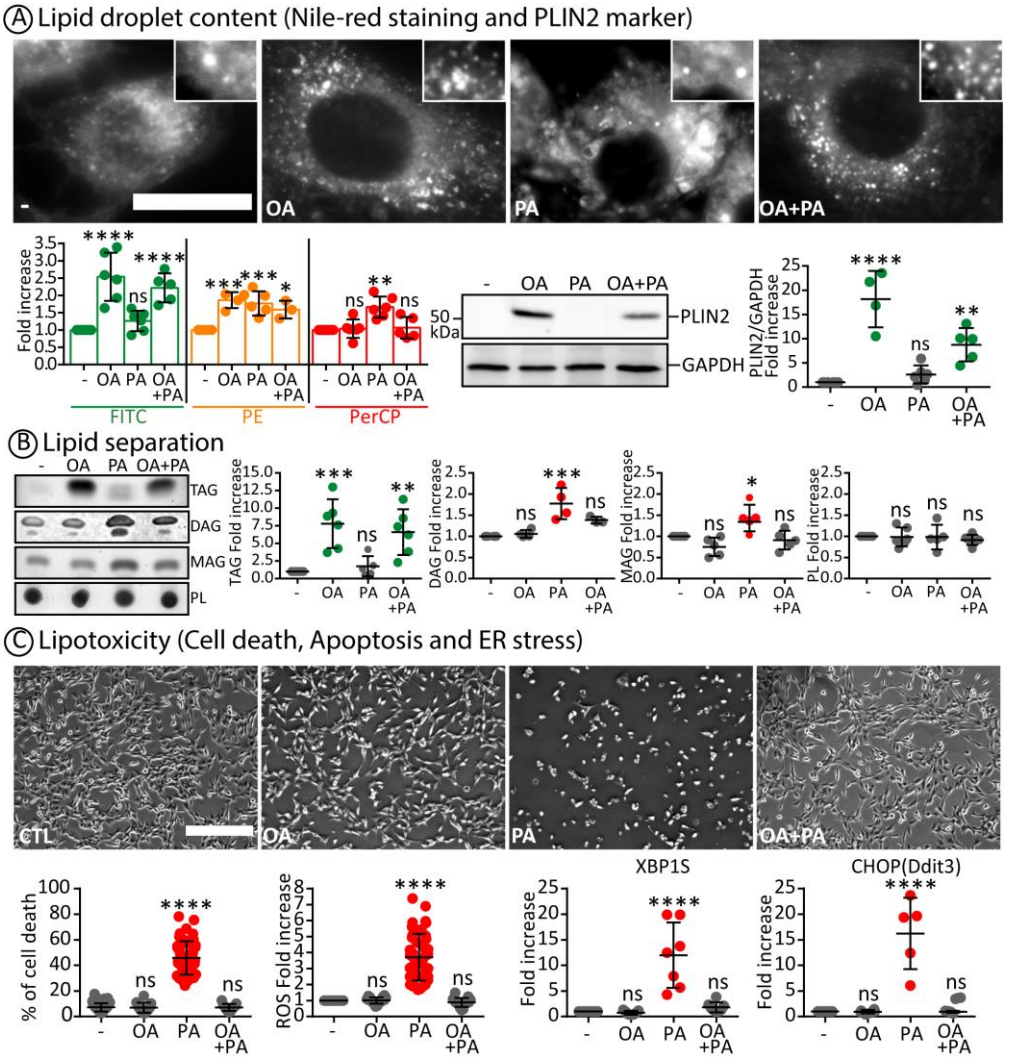
Ⓐ Lipid droplet content (Nile-red staining and PLIN2 marker)
-
OA
PA
OA+PA
Fold increase
FITC
PE
PerCP
50 kDa
PLIN2
GAPDH
PLIN2/GAPDH Fold increase
Ⓑ Lipid separation
TAG
DAG
MAG
PL
TAG Fold increase
DAG Fold increase
MAG Fold increase
PL Fold increase
Ⓒ Lipotoxicity (Cell death, Apoptosis and ER stress)
CTL
% of cell death
ROS Fold increase
XBP1S
CHOP(Ddit3)
Fold increase

2.2. Effects of metformin and ACC inhibitors on the reduction of ectopic lipid accumulation and lipotoxicity

The next aim of the project was to find an effective treatment for reducing lipid accumulation and lipotoxicity.

Since this lipid-lowering agent was expected to be used in combination with metformin, which is the first line treatment for type 2 diabetes mellitus (T2DM) (*361*), the effects of metformin on LD accumulation and lipotoxicity were first tested. Then, the acetyl-CoA carboxylase (ACC) inhibitor TOFA, which exhibited a marked LD reduction on previous studies of the group (*345*), was evaluated. It was also compared to firsocostat, a more recently developed ACC inhibitor (*355*) (also called ND630), to check for the efficacy of these drugs in preventing lipid deposition and lipotoxicity. They are expected to increase FAO by increasing the FA import into the mitochondria (*318*) (see below the mechanism of action), and the main difference between them is the site of ACC inhibition (*377*), which is a factor to be tested since it is related to the therapeutic efficacy of ACC inhibitors (*277*).

C2C12 cells supplemented with OA, PA, and OA+PA for 24 h were treated with 50 mM metformin, 100 µM TOFA, or 50 µM firsocostat for the last 16 h. LD and non-esterified lipid accumulation were measured using Nile-red detection at green and red spectra respectively. Metformin promoted the accumulation of both esterified and non-esterified lipids in all the conditions (**Fig. 15, A and B**). ACC inhibitors exhibited a reduction on those parameters: TOFA significantly decreased lipid accumulation in all the conditions and firsocostat only in cells treated with OA (**Fig. 15, A and B**).

Then, lipotoxicity was measured by means of cell death and ROS production. Regarding ACC inhibitors, ROS overproduction due to mitochondrial hyperactivation was anticipated to overload the natural antioxidant mechanisms (*378*). Thus, glutathione (GSH) antioxidant cotreatment was also tested at 0.5 mM. Metformin did not show any difference in cell death but an increase in ROS production of the cells (**Fig. 15C and D).** Both ACC inhibitors reduced the percentage of cell death (10% and 20% for TOFA and firsocostat respectively) (**Fig. 15C**), but TOFA also triggered ROS production in the presence of PA and absence of FAs. GSH partially counteracted this ROS production promoted by TOFA contributing to the improvement of the results of cell death (from 10% to 15%) (**Fig. 15C and D**). Firsocostat did not trigger ROS production (**Fig. 15D**). The effects of TOFA on ER stress were also measured, and the reduced PA accumulation promoted by TOFA correlated with a decreased activation of the CHOP proapoptic response, but not XBP1S (**Fig. 15E**). On the other hand, TOFA increased ER stress in cells without FAs, which was partially counteracted with antioxidant supplementation (restores CHOP basal levels, but not XBP1S) (**Fig. 15E**).

Since some ACC inhibitors are among the advanced treatments for non-alcoholic fatty liver disease (NAFLD) (*280*), the effects of these inhibitors were measured also in isolated hepatocytes to provide a higher relevance *in vivo,* and to confirm that they also act in other peripheral tissues. Therefore, isolated hepatocytes were loaded with a dose response of the lipotoxic PA (ranging from 0 to 500 µg/mL), and administered with 100 µM TOFA, 50 µM firsocostat, and 0.5 mM GSH treatments. They were incubated for 4 h to measure ROS production, 8 h for LD formation, and 24 h for viability measure.

PA induced LD accumulation in hepatocytes, but it was dramatically reduced after both TOFA and firsocostat treatments (**Fig. 15F**). Although stored in LDs, PA promoted a decrease on viability and increase on ROS production (**Fig. 15G**). TOFA and firsocostat reduced both signs of lipotoxicity (ROS and viability read-outs), but TOFA complemented with 0.5 mM GSH became the treatment that better decreased the lipotoxic effects of PA (**Fig. 15G**).

Metformin induced LD accumulation in C2C12 cells in the presence of FAs, which aggravated ROS production. It was probably due to the inhibition of OXPHOS (oxidative phosphorylation) mitochondrial complex I (*379*). Among the ACC inhibitors, TOFA and firsocostat showed to be effective on reducing lipid ectopic accumulation and lipotoxicity in both C2C12 cells and isolated hepatocytes. Since the effect on LD reduction was much pronounced with TOFA in C2C12 cells, we chose this promising drug for further evaluation of its efficacy.

Figure 15. ACC inhibitors decrease ectopic lipid accumulation.
C2C12 were supplemented with 100 µg/mL of OA, PA, or OA plus PA for 24 h (like in Fig.14), and either treated for the last 16 h with metformin (50 mM), TOFA (100 µM), or firsocostat (50 µM). (**A**) Lipid accumulation into LDs (n ≥ 3, in green) or (**B**) outside LDs (n ≥ 3, in red) was measured using Nile-red difference in emission of light. (**C**) Lipotoxic cell death (n ≥ 3), and (**D**) ROS production after the mentioned treatments using flow cytometry. (**E)** ER stress induction using XBP1S, and CHOP markers was also measured after TOFA treatment. Isolated hepatocytes were treated with a dose-response of PA (from 0 µg/mL to 500 µg/mL) alone or in combination with 100 µM TOFA, 50 µM firsocostat, and 0.5 mM GSH. (**F**) LD accumulation was visualized using fluorescence microscopy of Nile-red staining after 8 h of treatment (representative image of each condition with cells taken at the same magnification, scale bar= 20 nm). (**G**) ROS production and viability of the cells were respectively measured after 4 h or 24 h of the treatment addition. Graphs show means ±SD; *p<0.05, **p<0.01, ***p<0.001 and ****p<0.0001 in two-way ANOVA test using Tukey's multiple comparisons test comparing all the conditions in each FA treatment for (A-E), or in two-way ANOVA test using Dunnett's multiple comparisons between the non-treated conditions (- and NT) for (G).

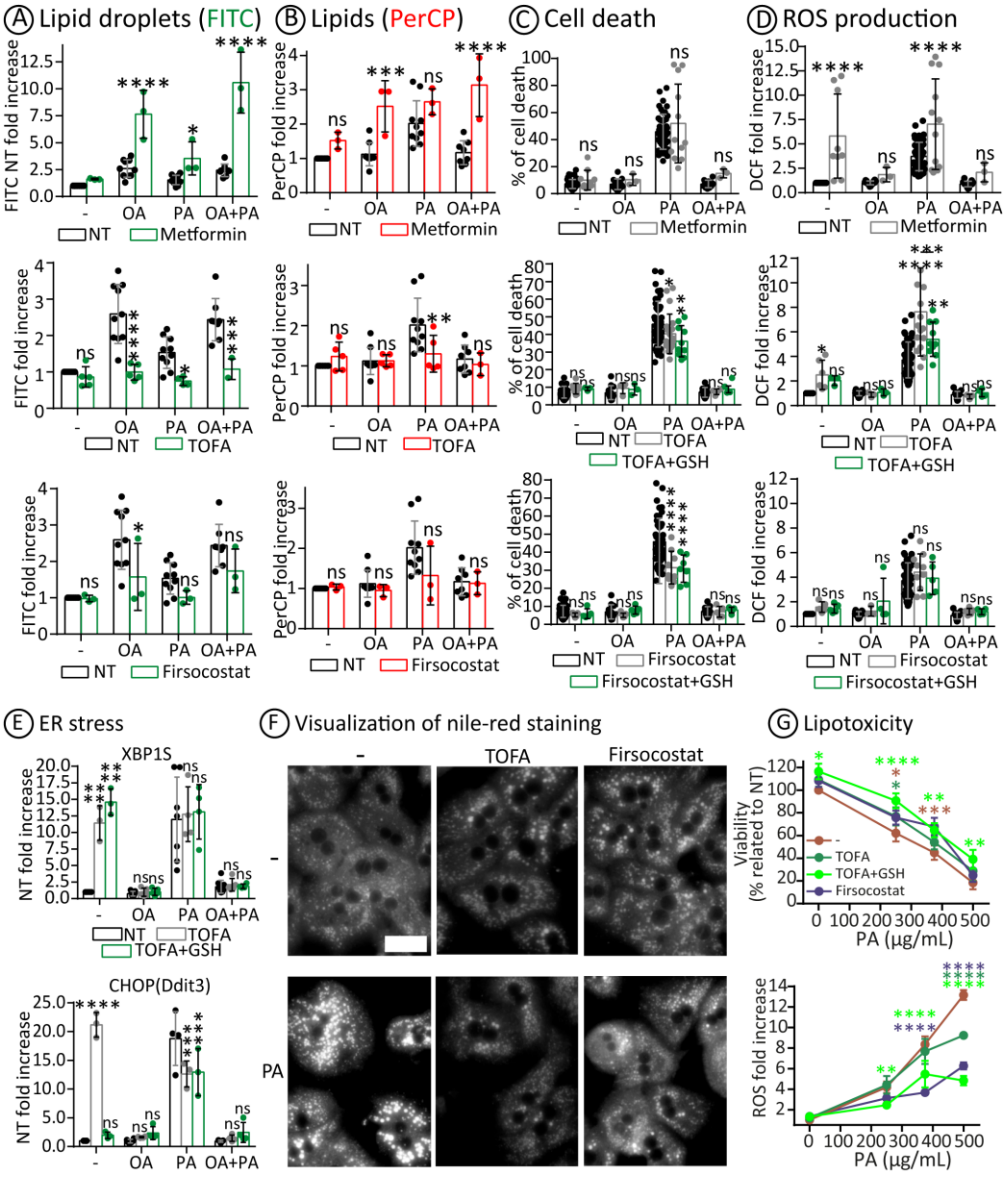
Ⓐ Lipid droplets (FITC)
Ⓑ Lipids (PerCP)
Ⓒ Cell death
Ⓓ ROS production
FITC NT fold increase
PerCP fold increase
% of cell death
DCF fold increase
FITC fold increase
NT
Metformin
TOFA
TOFA+GSH
Firsocostat
Firsocostat+GSH
- OA PA OA+PA
Ⓔ ER stress
XBP1S
CHOP(Ddit3)
NT fold increase
Ⓕ Visualization of nile-red staining
TOFA
Firsocostat
PA
Ⓖ Lipotoxicity
Viability (% related to NT)
ROS fold increase
PA (µg/mL)

2.3. Mechanism of TOFA-mediated reduction of ectopic lipid accumulation

ACC inhibitors such as TOFA could promote their effects in two steps. First, ACC activity is inhibited preventing malonyl-CoA formation, which is the substrate of FA synthase (FAS), and so stopping DNL (*de novo lipogenesis*) (**Fig. 16A** in red underlined). Second, low malonyl-CoA levels could prevent the allosteric inhibition of the mitochondrial CPT1 and increase FAO (**Fig. 16A**). Since both mechanisms would promote a decrease in LD content, we wanted to elucidate which of them is triggered by TOFA treatment. Because ACC expression is tissue-dependent (*323*), these experiments were performed in both muscle C2C12 and liver AML12 cell lines. Muscle presents a major ACC2 isoform expression since it is an oxidative tissue, whereas liver presents a balanced expression of both ACC1 and ACC2 isoforms due to both oxidative and lipogenic capacity of this tissue (*323*).

First, the effect of TOFA on ACC activity and DNL was analysed by measuring the incorporation of ^{14}C-acetate into the lipid fraction (**Fig. 16A** in green). Cells were first pretreated with 100 µM of TOFA for 2 h and incubated with 1 µCi of ^{14}C-acetate for the next 6 h (**Fig. 16B**). Radioactive counting (CPM) from isolated lipid fractions showed that TOFA inhibited acetate incorporation into LDs with and without FA supplementation and in both cell types (**Fig. 16B**).

These results confirmed that TOFA inhibited the activity of ACC1 and ACC2 by decreasing the levels of malonyl-CoA and the subsequent DNL, even in the presence of FAs.

Second, we focused on determining if the TOFA reduction on malonyl-CoA levels prevents the allosteric inhibition of CPT1 (**Fig. 16A** in red), and thus increases lipid import from LDs to the mitochondria for their oxidation. In this case, LD consumption would require both the release of FAs from the TAGs inside LDs through lipolysis, and the entry of FAs into the mitochondria through CPT1 (**Fig. 16A**) (*345*). Accordingly, we considered to measure TOFA-activated LD consumption by the cotreatment with 1) DEUP inhibitor of lipolysis and 2) etomoxir (ETO) inhibitor of FA mitochondrial uptake (**Fig. 16A**). If TOFA effect is on increasing this LD-mitochondria lipid transfer, the cotreatment with the mentioned inhibitors would prevent such consumption. To do that, FA loaded C2C12 and AML12 cells (OA+PA) were treated with TOFA and one cotreatment, DEUP or etomoxir. LD content was analysed by flow cytometry afterwards. In liver cells, TOFA decrease in LD content was prevented when cotreating with ETO and DEUP (**Fig. 16C**). However, the reduction in LD content showed in muscle cells was only partially affected by the same cotreatments (**Fig. 16C**).

These results suggest that TOFA showed a different mechanism of action in liver (AML12) and muscle (C2C12) cells regarding to LD formation and consumption. While in liver, TOFA promotes LD consumption by activation of lipolysis and mitochondrial FA uptake, in muscle the reduction on LD content is the result of a combined action between DNL inhibition and activation of FAO.

Third, we wanted to check whether LD-mediated transfer of lipids into the mitochondria culminates with an activation of FAO, so it was directly tested in oxidative isolated hepatocytes. They were treated with TOFA plus 1 µCi of radioactively labelled ^{14}C-OA and ^{14}C-PA in the presence or absence of FAs. Complete FAO occurs when FAs undergo β-oxidation and carboxylic acid cycle (CAC), which promotes the release of CO_2 and the accumulation of acid-soluble products (ASP) as intermediates (*380*) (**Fig. 16A** in blue). Strikingly, TOFA promoted an approximately 10% decrease in the production of CO_2 and a 10% increase on ASP (**Fig. 16D**), indicating an increase of incomplete FAO.

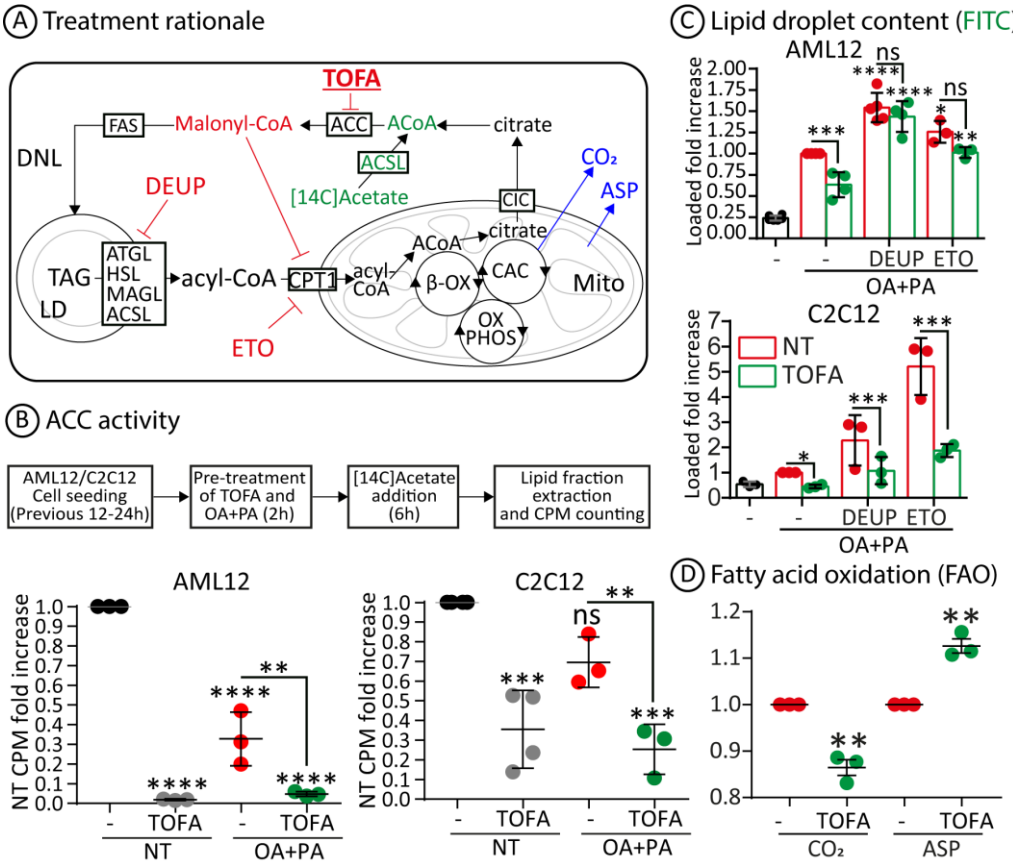

Figure 16. TOFA mechanism of action.
(**A**) Transference of lipids between LD and mitochondria: during starvation, TAGs from LDs are hydrolysed by the action of lipases and transported to the mitochondria for its consumption through CPT1. In nutrient rich conditions, the excess of mitochondrial activity is sensed by an increase of citrate, which is then transformed to lipids through DNL. In this last step, the intermediate malonyl-CoA is accumulated after ACC reaction and allosterically inhibits CPT1 activity. Acetate incorporation into acetyl-CoA is highlighted in green. Malonyl-CoA, TOFA, DEUP, and Etomoxir (ETO) inhibitory effects are in red. Release of CO_2 or accumulation of acid-soluble products (ASP) as a read-out of FA oxidation (FAO) assays is in blue. (**B**) ^{14}C- Acetate incorporation into lipids timings and assay to check for ACC activity (n ≥ 3). (**C**) LD accumulation detected by green fluorescence FITC filter (n ≥ 3) after an OA+PA (100 µg/mL +100 µg/mL) incubation for 24h and the TOFA (100 µM), DEUP (0.5 mM) and ETO (1 mM) treatments for the last 16h. (**D**) Isolated hepatocytes were treated with OA+PA (100 µg/mL + 100 µg/mL) alone or in combination with 100 µM TOFA to measure FA oxidation (FAO) rate after 24 h (n = 3). Graphs show means ±SD; where *p<0.05, **p<0.01, ***p<0.001 and ****p<0.0001 in one-way ANOVA test using Bonferroni's multiple comparisons test compared to non-treated (-) for (B), and two-way ANOVA test using Sidak's multiple comparisons test comparing to the non-treated for (C).

2.4. Benefits of TOFA in diet-induced mouse models of obesity and T2DM

Once demonstrated that TOFA reduces lipid accumulation in both muscle and liver cell lines by increasing LD consumption (**Fig. 15 and 16**), these effects were tested in a diet-induced mice model of obesity and T2DM to determine the *in vivo* relevance of TOFA for the treatment of both diseases.

2.4.1. Effects on physiological parameters

For this purpose, 6 weeks old C57BL/6J male mice were fed *ad libitum* for 6 weeks with either CTL (70% carbohydrate, 20% protein and 10% lipids) or high fat diet (HFD; 20% carbohydrate, 20% protein and 60% lipids) (**Fig. 17A**). At this point, mice became preobese and prediabetic (*381*). TOFA effectivity was measured by intraperitoneally injecting the mice with 100 mg/kg of TOFA five days per week for the next 8 weeks (**Fig. 17A**). The onset of both diseases after TOFA injection was then evaluated. TOFA reduced approximately 10% of whole-body weight gain on HFD fed mice without altering CTL diet fed mice (**Fig. 17B and D**). The reduction in visceral and subcutaneous white adipose tissue (WAT), but not brown adipose tissue (BAT), accounts for this decreased body weight (**Table 1**). Food intake remained the same for both diets and treatments (**Fig. 17C**) discarding the hypothesis that TOFA could affect mice appetite.

Table 1. Adipose tissue, liver, and muscle weight. Tissues were weighed in g at the end of the experiment to measure lipid accumulation and progression of obesity.

Tissue (g)	Control diet		High fat diet (HFD)	
	Saline	TOFA, 100 $mg \cdot kg^{-1} \cdot d^{-1}$	Saline	TOFA, 100 $mg \cdot kg^{-1} \cdot d^{-1}$
ingWAT	0.089 ± 0.008	0.051 ± 0.005	0.194 ± 0.026	0.113 ± 0.014**
gWAT	0.272 ± 0.013	0.242 ± 0.029	0.964 ± 0.060	0.725 ± 0.090*
iBAT	0.120 ± 0.008	0.112 ± 0.007	0.140 ± 0.011	0.137 ± 0.007
Liver	1.191 ± 0.033	1.263 ± 0.052	1.429 ± 0.052	1.266 ± 0.033*
muscle	0.159 ± 0.004	0.146 ± 0.005	0.169 ± 0.004	0.168 ± 0.004

Graphs show means ±SEM ($n \geq 6$); where *$p<0.05$ and **$p<0.01$ in one-way ANOVA test using Bonferroni's multiple comparisons test comparing TOFA-treated to non-treated mice. **Abbreviations:** ingWAT, subcutaneous inguinal white adipose tissue; gWAT, visceral gonadal WAT; iBAT, intraescapular brown adipose tissue; and muscle, gastrocnemius skeletal muscle.

In the last week of the experiment, glucose homeostasis was studied to evaluate T2DM pathogenicity. Mice were injected intraperitoneally with either 2 g/kg glucose or 0.3 U/kg insulin, for glucose tolerance test (GTT) or insulin tolerance test (ITT) respectively. Glucose levels were then measured for the next 90 min. After glucose injection, HFD mice treated with TOFA exhibited a better blood glucose clearance than the HFD group (**Fig. 17C**). In CTL group these differences were not appreciated (**Fig. 17C**). When injecting insulin, HFD fed mice with TOFA treatment restored glucose clearance to similar levels than CTL mice (**Fig. 17C**). It clearly contrasted with the insulin resistance showed in HFD fed mice without TOFA (**Fig. 17C**). CTL mice injected with TOFA treatment also showed an increase in insulin sensitivity (**Fig. 17C**). HFD fed mice presented a higher water intake at the last two weeks of the experiment, which is called polydipsia and is a symptom of T2DM (**Fig. 17D**). It was completely prevented in mice treated with TOFA (**Fig. 17D**).

The decrease in mice fat depots suggested that TOFA could counteract fat accumulation from HFD ingestion by activating lipid consumption. Using indirect calorimetry, both lipid and glucose oxidation were measured in mice. Most of the differences were presented during daytime when mice are less active (**Fig. 17E**). Glucose oxidation was significantly decreased but compensated with an increase in lipid oxidation (**Fig. 17E**). This was confirmed by a shift in respiratory energy ratio (RER) from 0.85 to 0.8 approximately (where 1 is associated with only glucose oxidation and 0.7 to only lipid oxidation) (**Fig. 17E**). This shift from glucose to lipid metabolism was further appreciated when representing RER and body weight covariance graph in mice with a similar body weight. In the HFD group, mice with high body weight were associated with lipid oxidation and mice with low body weight with glucose oxidation (**Fig. 17E**). Mice treated with TOFA, completely reverted this tendency (**Fig. 17E**).

Figure 17. TOFA decreases obesity and type 2 diabetes mellitus (T2DM) progression by shifting mice body metabolism from glucose to lipid oxidation.
(**A**) Mice feeding and treatment timing: after a 2-week acclimation, 6-week-old mice were first *ad-libitum* fed with either CTL or HFD for 6 weeks to induce preobese and prediabetic state, and then injected with 100mg/kg TOFA five days per week for the following 8 weeks. Glucose homeostatic or indirect calorimetry tests were performed the last week of the treatment before mice sacrifice and tissue collection. (**B**) weight gain measure starting at first week of TOFA treatment (n ≥ 13). (**C**) Glucose tolerance test (n ≥ 9) and Insulin tolerance test (n ≥ 7) were performed during the 90 min after the injection of 2 g/kg glucose or 0.3 U/kg insulin injection. (**D**) Food (n ≥ 6) and water (n ≥ 6) intake during all the days of the experiment. (**E**) Glucose oxidation, lipid oxidation and RER measurements using indirect calorimetry (n ≥ 4). Graphs show means ±SEM; where *p<0.05, **p<0.01, ***p<0.001 and ****p<0.0001 in two-way ANOVA test using Tukey's multiple comparisons test compared to HFD fed mice for (B), (C) and (D); paired two-tailed t-test for (E); and linear regression slope comparation for RER vs Body weight graph in (E).

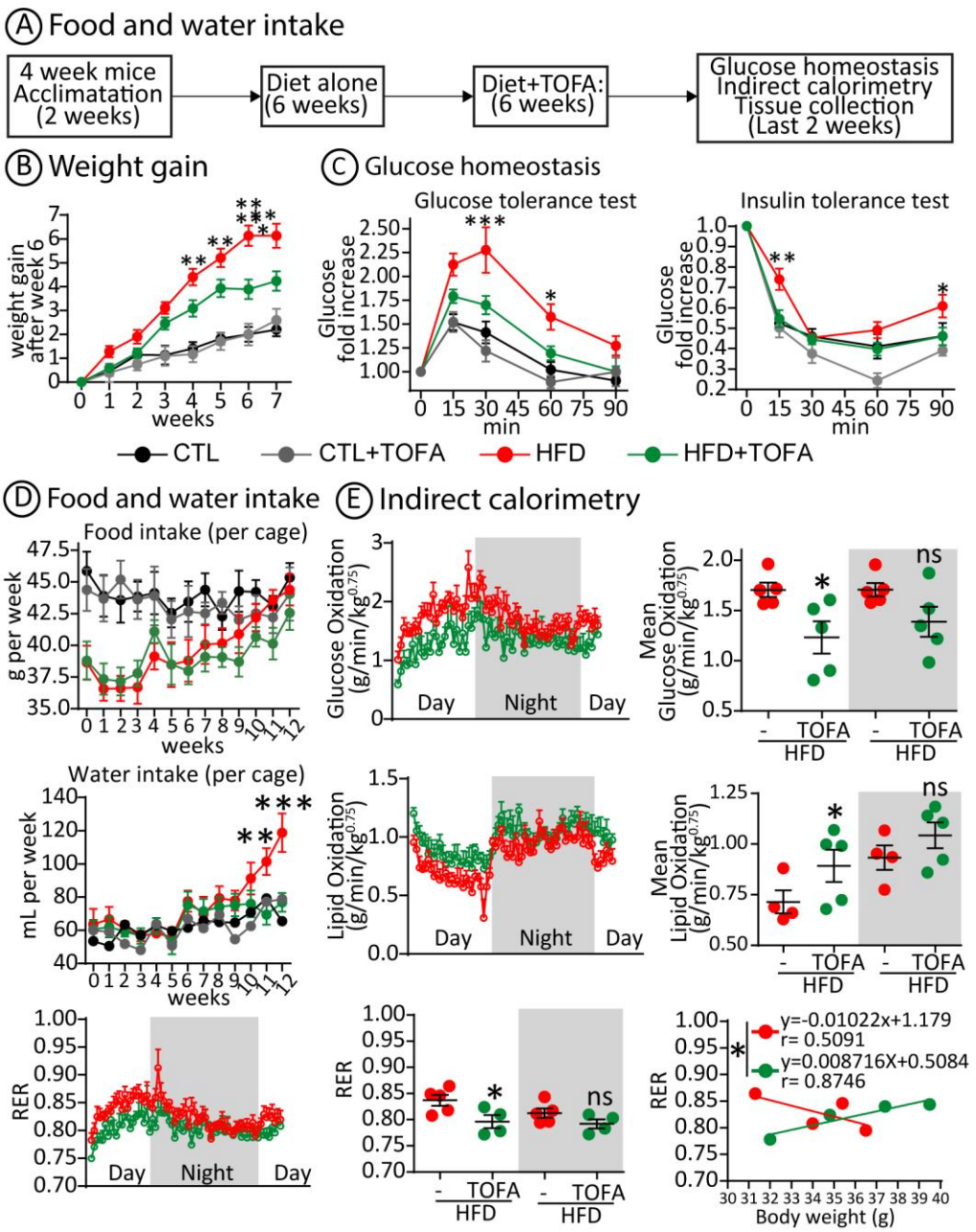

In summary, these results show that chronic injection of TOFA promoted mild but continuous shift from glucose to lipid oxidation. In the long term, this shift prevented fat accumulation in WAT depots and resulted in better insulin sensitivity and T2DM prevention. TOFA treatment restored glucose and insulin homeostasis of HFD mice in a similar way than CTL mice.

2.4.2. Effects on peripheral tissues

The improvement of mice metabolic parameters by TOFA injection suggested an improvement of lipid ectopic deposition on peripheral tissues, which was afterwards evaluated. First, liver injury was analysed by means of AST (aspartate aminotransferase) and ALT (alanine aminotransferase) levels (**Table 2**). Hepatic damage induced by HFD was significantly reduced by TOFA treatment, which matches with the observed reduction in liver weight (**Table 1**). Nevertheless, cholesterol metabolism and triglyceridemia were unaffected (**Table 2**).

Table 2. Mice serum parameters. Blood collected at the end of the experiment was analysed to follow the progression of metabolic syndrome.

Parameter	Control diet		High fat diet (HFD)	
	Saline	TOFA, 100mg·kg^{-1}·d^{-1}	Saline	TOFA, 100mg·kg^{-1}·d^{-1}
AST, U/L	78.5 ± 9.3	40.8 ± 7.7	116.6 ± 16.8	68.7 ± 7.8**
ALT, U/L	15.7 ± 1.06	19.7 ± 3.7	22.0 ± 1.8	18.4 ± 1.2*
Total cholesterol, mg/dL	103.7 ± 6.7	104.8 ± 5.3	137.8 ± 4.4	139.6 ± 5.3
HDL, mg/dL	53.4 ± 2.5	54.8 ± 6.6	70.8 ± 2.5	68.2 ± 3.1
LDL, mg/dL	25.1 ± 3.3	28.4 ± 2.9	47.7 ± 6.0	43.9 ± 4.9
TAG, mg/dL	102.2 ± 13.1	110 ± 11.6	165.7 ± 28.9	157.3 ± 20.6

Graphs show means ±SEM (n≥5); where *p<0.05 and **p<0.01 in one-way ANOVA test using Bonferroni's multiple comparisons test comparing TOFA treated to saline-injected mice. **Abbreviations:** AST, aspartate aminotransferase; ALT, alanine aminotransferase; HDL, high density lipoprotein; LDL, low density lipoprotein and TAG, tryacilglicerides.

Next ectopic lipid accumulation was further evaluated. HFD fed mice exhibited large LDs (red asterisks), which were observed by electron microscopy of liver sections and suggested steatosis (**Fig. 18A**). Moreover, few mitochondria (green asterisks) were appreciated in the vicinity or in contact with LDs (**Fig. 18A**). In livers of mice treated with TOFA, LDs were smaller and with a high number of mitochondria closely located (**Fig. 18A**). Immunoblotting of liver extracts showed that mice with TOFA treatment presented a decrease on PLIN2 expression, meaning reduced LD content (*189*), and an increase in PLIN5 expression compared to CTL mice (**Fig. 18B**). Since PLIN5 tether LD and mitochondria (*221*), the increase of the protein would imply activation of FAO and thus, major LD consumption. CPT1 protein levels were measured to check for a potential increase promoted by TOFA (*382*), but it remained unaltered in all the groups (**Fig. 18B**).

Muscle function was revised although no differences in weight between HFD fed mice groups were observed (**Table 1**). Looking by electron microscopy to the gastrocnemius muscle transverse sections, HFD group presented an absence of LD (**Fig. 18A, right panels**). On the contrary, mitochondria showed an aberrant morphology (green asterisk) and appears to contain lipids in their interior (**Fig. 18A, right panels**). When treated with TOFA, the metabolic synapse between LD and mitochondria was restored in the skeletal muscle of mice (**Fig. 18A, right panels**). In this case, to check for better muscle performance a functional treadmill assay was performed. There was no difference in the length run by mice in all the groups (**Fig. 18C**).

In conclusion, TOFA promoted a decrease in lipid ectopic accumulation which improved LD and mitochondria morphology in muscle and liver. In liver, TOFA promoted a change in PLIN2 and PLIN5 LD markers which is associated with increased LD consumption (*383*). In muscle, improvement of LD and mitochondria morphology was not related to an increased muscular performance.

Figure 18. TOFA decreases lipid ectopic accumulation in liver and muscle.
Mice after a 6-week CTL or HFD feeding and 8 weeks feeding with a daily saline or 100 mg/kg TOFA injection were sacrificed and liver and muscle samples collected for their analysis. (**A**) Electron microscopy analysis of liver and *gastrocnemius* muscle samples. LD and mitochondria are labelled with a red and green asterisk respectively. (**B**) Mitochondrial CPT1 and LD PLIN2 and 5 markers were immunodetected in liver extracts ($n \geq 5$). (**C**) Mice muscle functionality evaluated by an endurance treadmill assay ($n = 6$). Graphs show means ±SD; where *$p<0.05$ and ***$p<0.001$ in one-way ANOVA test using Bonferroni's multiple comparisons test to non-treated (-) condition for (B and C) and two-tailed t test for (E).

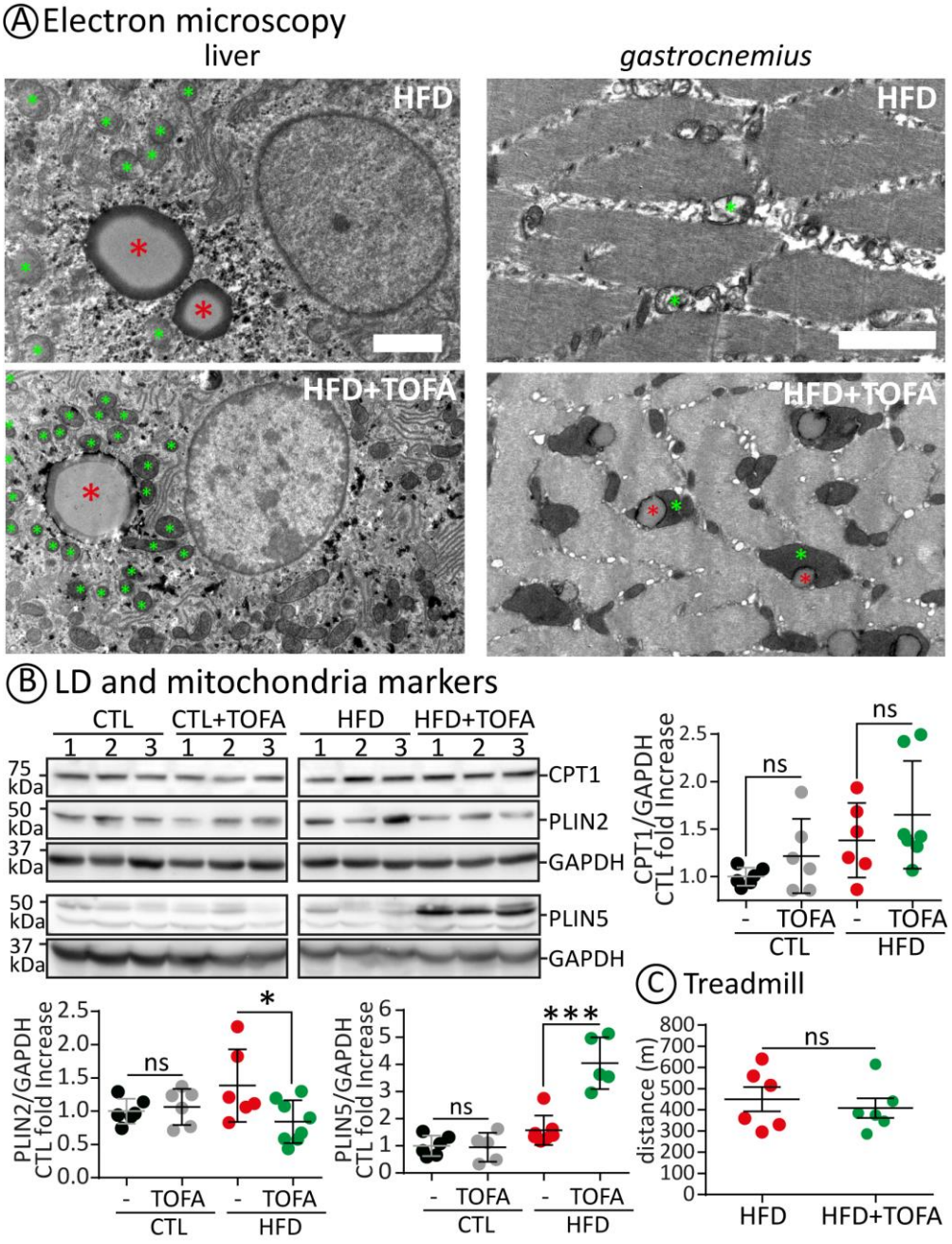
Ⓐ Electron microscopy
liver
gastrocnemius
HFD
HFD
HFD+TOFA
HFD+TOFA
Ⓑ LD and mitochondria markers
CTL
CTL+TOFA
HFD
HFD+TOFA
1 2 3 1 2 3 1 2 3 1 2 3
75 kDa
50 kDa
37 kDa
50 kDa
37 kDa
CPT1
PLIN2
GAPDH
PLIN5
GAPDH
CPT1/GAPDH CTL fold Increase
ns
ns
ns
- TOFA - TOFA
CTL
HFD
PLIN2/GAPDH CTL fold Increase
ns
*
- TOFA - TOFA
CTL
HFD
PLIN5/GAPDH CTL fold Increase
ns
***
- TOFA - TOFA
CTL
HFD
Ⓒ Treadmill
distance (m)
ns
HFD
HFD+TOFA

DISCUSSION

1. Model of caveolin early trafficking, degradation, and function

The physiological reasons for the existence of different caveolins, with an almost identical capacity to drive caveolae formation, has been puzzling (*3*). Using a cell system of synchronised expression and exclusively analysing early timepoints, we have observed for the first-time differences in the early biosynthetic trafficking of caveolin family members and isoforms. The model presented here reconciles both the transport of the protein to the plasma membrane (PM) for operating in the canonical caveolae functions (*5*), and the recently recognised intracellular functions in organelles connected to the endoplasmic reticulum (ER) (*93*). The ability of caveolins to perform these functions could be determined by the availability of intracellular lipids, which in turn would determine caveolin stability and intracellular trafficking (section 1.4).

1.1. Caveolin trafficking

Using a synchronized short expression protocol, which showed to bypass most of previously described technical shortcomings (*122, 363, 364, 366*), we show that after a 3h expression CAV1 is in the Golgi complex (GC) and PM, CAV2 at the GC, and surprisingly CAV3 in the ER and LDs (**Fig. 1A and B).** After synthesis, as previously described (*9, 75*), CAV1 demonstrated a faster transport to GC and PM, oligomerization, and acquisition of triton insolubility. CAV2 was predominantly retained in the GC as known (*18*). CAV3, which could enter the anterograde system as CAV1 and CAV2 through the coat complex protein II (COPII)-binding motif (DXE) (*75*), was however retained in the ER and only occasionally observed at the PM compared to CAV1 (**Fig. 1C**).The clear difference between CAV1 fast and CAV3 slow transport was explored at a molecular level. Exchange of the initial N-terminal stretch between CAV3 and CAV1, demonstrated that CAV3 is retained in the ER through a sequence of hydrophobic amino acids likely forming an alpha helix (**Fig. 1A**). Moreover, COPI binding motif present on the last 4 residues of CAV3 (-RKXX) but not in CAV1 (-QRXX) contributed to ER retrieval and retention (**Fig. 1B**). It also demonstrated the C-terminus participation in the retrieval transport of caveolins, which was previously suggested by the synthetic addition of a retrieval motif(-KKSL) to CAV1 (*89*) and, the CAV1 P158 frame-shift mutation introducing many acidic residues on the CAV1 C-terminus (*90*).

Although at steady-state all caveolin members can traffic to LDs (*89, 181, 371, 384*), only CAV3 was present in this compartment likely by lateral diffusion from the ER in a process mediated by the hydrophobic and amphipathic domains (at both ends of the protein) (**Fig. 1D**) (*181*). CAV1 exchange of both N- and C-terminus with CAV3 was not sufficient to target CAV1 to LDs (results not shown), so additional molecular determinants explaining these differences remain to be elucidated (**Fig. 1D**, question marks). Thus, CAV1 and CAV2 are likely arriving to LDs through alternative pathways, which could involve the direct transport from PM or from endosomes after caveolae disassembling (**Fig. 1D**, question mark). Perhaps, CAV1 and CAV2 could also follow an slow pathway from ER recently described in proteins such as ATGL (*370*). CAV1 trafficking to LDs was appreciated in adipocytes, where LDs could be connected to caveola because other caveolar components (EHD2 and cavin1) were also detected on LDs (*385*). The regulation of this system is largely unknown, but gathered evidence suggest that caveola senses lipids, whose accumulation above a critical threshold triggers caveola trafficking to LDs (*37*). Thus, CAV1 and CAV2 could use this pathway to be transported to LDs.

LD trafficking of caveolin was discovered 20 years ago (*89, 371, 384*), but the direct functions in LDs remain unknown (*41*). Only few clues indicate that caveolin can regulate lipid metabolism through LD stabilisation. Initial studies on adipocytes suggest that CAV1 on LDs interacts with perilipin 1 (PLIN1) (*386*), which limits the presence of PLIN2 (*386-388*), and therefore stabilises LDs by preventing lipolysis. Our results also show that CAV3 promotes LD clustering, suggesting that CAV3 could participate in additional functions in this organelle after early synthesis. The mitochondrial FA importer carnitine palmitoyltransferase 1 (CPT1) and CAV3 genes are regulated through the RORα (retinoic acid receptor (RAR)-related orphan receptor alpha) and coactivated by PGC-1α (peroxisome proliferator-activated receptor gamma coactivator 1-alpha), which are key regulators of mitochondrial biogenesis (*389*). Interestingly, RORα also controls expression of several genes involved in circadian rhythms. Thus, newly synthesized CAV3 could be part of an energetic program to rapidly face fluctuations in FA availability occurring, for example, during circadian cycles, starvation, or exercise.

1.2. Caveolin degradation

When CAV1 anterograde transport is decreased (NCAV3), retrograde transport increased (RKXX) or transport to PM prevented by delaying the transit through the exocytic pathway (P132L), CAV1 is longer retained in ER with a concomitant reduction of the protein levels, suggesting the existence of caveolin degradation mechanisms in the ER. These processes were further confirmed by inhibiting ER degradation systems resulting in caveolin accumulation, aggregation, and retention in the ER. These homeostatic mechanisms were unknown until now.

Caveolin oligomerisation to form caveolae is a biological intricate process involving synchrony between approximately 150 caveolin proteins and thousands of molecules of several lipids such as cholesterol (*73, 93*). Such a complexity is possibly reflected by the fact that most caveolin naturally occurring mutations that cause disease somehow affect this process (*73*). To prevent a likely detrimental accumulation of caveolins in intracellular compartments, cells could have evolved to sense degrons in misfolded caveolin oligomers, but also in the presence of an excess of the protein in a monomeric form, which would efficiently target them to a rapid degradation. This could represent a more general mechanisms since other hairpin proteins such as ALDI showed a similar accumulation on LDs and similar degradation rates by ERAD (ER-associated degradation). This observation suggest that the hairpin topology is simultaneously functioning as a LD targeting motif (*181*) and as a degron (*192*). Our results (see below) suggest that caveolin degradation could be determined by the availability of lipids, a difference previously unknown.

Then, hairpin proteins could follow a three-way degradation from ER. We first showed, that caveolin is directly targeted to ERAD in a process that could be mediated by the chaperon sensing of hydrophobic domains (*149, 150*) or through an ubiquitin-mediated process by the known CAV1 N-terminal ubiquitination (*123*) (**Fig. 1G**). The last is more plausible, because CAV1 lacking the ubiquitinable N-terminal region demonstrated an increased stability in this study. To include CAV2 and CAV3 on this degradation mechanism, ubiquitination needs to be confirmed. Caveolin could be ubiquitinated by Doa10 ubiquitin-ligase, which detects exposed hydrophobic domains in ER, resulting in the net accumulation of hairpin proteins in LDs (*192*). Retrotranslocation of proteins from the ER to the cytosol could be performed as in endolysosomal compartments by UBXD1 detection of ubiquitinated caveolin and VCP/p97 (valosin containing protein) recruitment (*123, 124, 126*), since both also participate in ERAD (*157, 390*). Finally, cytoplasmatic caveolin would be degraded by the proteasome.

We have also initially explored other degradation mechanisms of caveolin such as autophagy. It was first shown for caveolin at the PM (*391*), and we have confirmed that it is also functioning in the ER by the short use of 3-methyladenine (3MA) autophagy inhibitor (*392*). Autophagy of the ER (ER-phagy), has been described by different mechanisms, although macro-ER-phagy could be specific for caveolins because it degrades aggregated or tightly folded proteins (*163*) (**Fig. 1G**). We also confirmed that ERAD and autophagy act synergistically for caveolin degradation. As it occurs for collagens, it is likely that caveolins that scape ERAD are constitutively degraded by ER-phagy (*393*).

In LDs, we have also described that the accumulation of CAV3 promotes a rapid clustering of this organelle in central regions of the cell. Using CAV3 mutants with decreased affinity for LDs (*181, 371*), we have confirmed that LD trafficking reduces protein accumulation in the ER and in turn ER stress, suggesting that LDs act as caveolin scavengers (**Fig. 1H**). This role of LDs was initially spot because blocking the exocytic pathway with Brefeldin-A increased caveolin trafficking to LDs (*89*). Mechanistically, when the exocytic pathway is overloaded or ERAD system collapsed (*89, 195*), the ER stress induced by caveolin could trigger LD formation through unfolded protein response (UPR) (*170*) and allow protein trafficking to LDs reducing the stress. Proteins on LDs can be then accumulated (*170*) or finally degraded through retrotranslocation into the cytoplasm or autophagy machinery, which is also functioning on LDs (*175, 193, 197*).

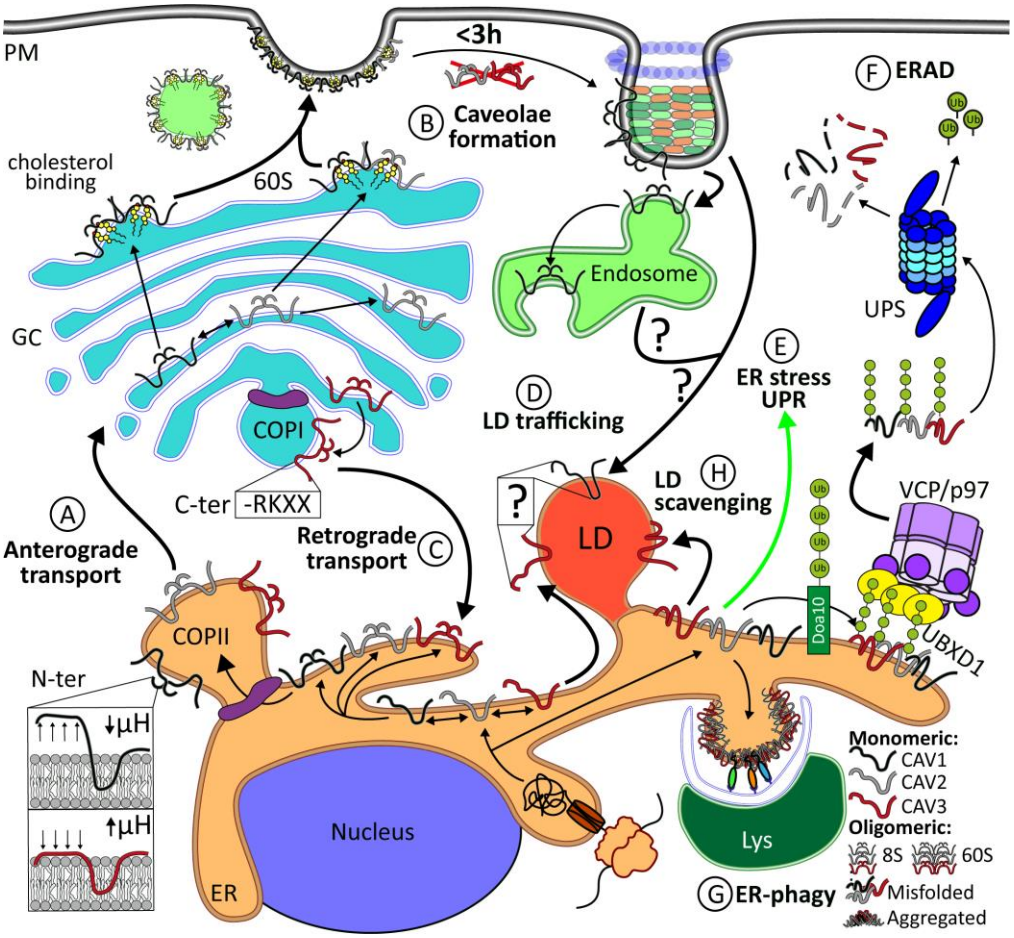

Figure 1. Model of early caveolin trafficking and degradation.
CAV1 (black), CAV2 (grey), and CAV3 (red) early trafficking after its synthesis in the ER through the (**A**) anterograde transport to GC and PM, where they (**B**) form caveolae. CAV3 is transported (**C**) from GC to ER by the retrograde transport, from where it can also (**D**) traffic to LDs. If caveolin is not properly folded it promotes (**E**) ER stress which activates UPR (in green). It can also be degraded by (**F**) ERAD, complementary (**G**) ER-phagy or, (**H**) LD scavenging. The caveolin domains involved in their transport are squared and the missing questions about the model are remarked with a question mark on the pathway involved. Thin lines indicate the transport inside the same cell organelles and thick lines between organelles. Different states of caveolin folding, and oligomerization are indicated in the figure legend.

1.3. Physiological relevance of caveolin proteostasis

Contrasting with the 10 to 36 h half-life of caveolae (*122, 394*), caveolin in the ER presented a shorter life expectancy, where almost 50% of it is degraded just after the synthesis of the protein (3 h). It is a similar rate of degradation than the CFTR (cystic fibrosis transmembrane receptor), whose 75% is eliminated just after being synthesized to avoid protein aggregation (*160*). Caveolin could also be degraded for the same reason, since caveolin aggregation was previously demonstrated to induce cell alterations such as formation of aggresomes (*363*) or caveosomes (*122, 364*). Moreover, long-term expression of caveolin mutants such as P132L also showed aggregation (*109*).

Physiologically, it is likely relevant to tightly regulate the levels of hairpin proteins such as caveolins in the ER, because their membrane-shaping capacity and curvature induction (*191*). Potential curvature-inducing accumulation and aggregation of caveolin should be deleterious for the cell since it promotes ER stress measured by the activation of folding through XBP1S (X box-binding protein 1 spliced) and the proapoptotic response through CHOP (C/EBP-homologous protein of the UPR) (*142*) (**Fig. 1E**). It was also appreciated for endogenous CAV1, increasing its relevancy *in vivo*.

The degradation of caveolin from the ER could be also important for understanding the pathogeny of CAV1 and CAV3 natural mutations, which were studied using the P132L and P104L mutants (*73, 86*). Delayed CAV1 P132L transport to the PM exposed the protein to early degradation, which fits with the known dominant negative actions of the mutant (*395*). However, CAV3 P104L transport through the exocytic pathway was strikingly increased promoting caveolin accumulation in the GC, and contrasting with the previously described loss of expression (*86*). Hypothetically, CAV3 mutations would introduce a conformational change of the protein, inducing an escape from degradation in the ER such as the non-degradable CAV3 K*R construct, which is also accumulated in the GC. The pathogenic presence of CAV3 in the GC could explain the existence of more human diseases related to CAV3 than to CAV1 (*73*). Increasing CAV3 P104L degradation, through the activation of some of the mechanisms described in the previous section, could be a therapeutic strategy to prevent CAV3 hereditary diseases.

1.4. Missing link: lipid-related functions of caveolins

Some question remained unanswered about LD trafficking and lipid-related functions of caveolin (**Fig.1**, question marks): Why CAV1 and CAV3 are differently transported to LDs? Which domain or residues allows CAV3 but not CAV1 trafficking to LDs from ER? Is specifically CAV3 playing a role in LDs which CAV1 is not? Is cholesterol binding involved in this process? The answer to these questions could be found by guiding future investigations to relate the stability and sorting of the protein to the cholesterol- and FA-related functions of caveolin which will confirm their relevance.

In this regard, ERAD not only focus the degradation to misfolded proteins, but it also modulates the function of some proteins related to cholesterol synthesis such as HMG-R (HMG-CoA reductase), whose degradation is promoted when cholesterol levels are low (*161*). The same increased degradation is appreciated for apolipoprotein B (ApoB) when translocated through ER in cholesterol- or lipid-poor conditions, and low- or very low-density lipoproteins (LDL or VLDL) synthesis is not required (*396*). With all this information, a switch mechanism for cholesterol transport of non-caveolar caveolin (*93, 94*) is proposed (**Fig. 2A**): caveolin activity in the presence of lipids is transcriptionally activated through the sterol regulatory element like sequences of the protein (*12*), and further improved by increasing the transport to PM (*11*) through the binding of cholesterol (*10*) or FAs (*397*). By these mechanisms, cholesterol imbalances in cell organelles such as mitochondria are prevented (*96, 100*). On the contrary, caveolin could be degraded by the mechanisms described in this thesis, as occurs with HMG-R or ApoB when the levels of intracellular lipids are low, because the presence of the protein is not required and toxic.

Therefore, caveolin binding of lipids would regulate early transport of the protein and the consequent protein stability. CAV1 could bind cholesterol through a cholesterol recognition sequence (CRAC motif) (*71, 398*) (**Fig. 2B** remarked in bold). In this putative cholesterol-binding region, the first valine and central tyrosine residues control cholesterol binding affinity (*81, 398*) and residues in between can be anyone but compatible with the hydrophobic membrane environment (*399*). Although with an almost identical sequence than CAV1 (**Fig. 2B**), it is not known if CAV3 binds cholesterol. A non-conservative change at the hydrophobic CAV1 phenylalanine 99 (in blue) for a cysteine in CAV3 (in red) is appreciated. Interestingly, this residue is mutated in the dystrophy associated CAV3 C71W mutant for a hydrophobic residue (tryptophane in green)(*400*). We analysed the intracellular distribution of C71W, and the mutant demonstrated a striking transport to the PM very similar to CAV1 (**Fig. 2C**). This exciting initial evidence, while lacking cholesterol binding assays, suggests that CAV1 has higher affinity for cholesterol due to the presence of a more hydrophobic CRAC motif. After cholesterol binding, this domain could mediate the transport of CAV1 to PM, whereas the low affinity of CAV3 for cholesterol due to a less hydrophobic sequence could promote CAV3 retention in the ER. Consequently, CAV3 would be better degraded or exit to the LDs, whose function could be more FA-related as described in section 1.1.

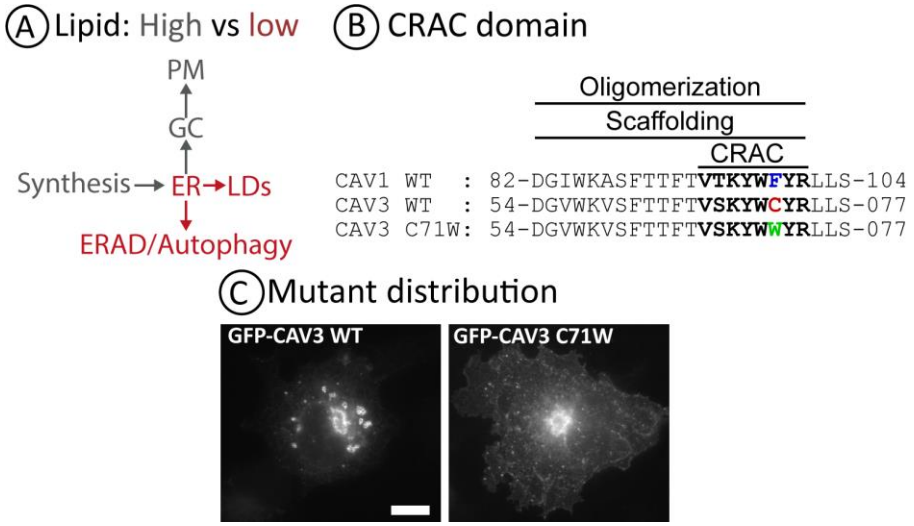

Figure 2. Cholesterol binding through CRAC as a potential trafficking and stability modifier of caveolins.
(**A**) Proposed model of caveolin fate depending on lipid availability. High and low lipid concentration are in grey or red respectively. (**B**) WT and caveolin constructs sequence in N-terminal region up to hydrophobic domain are represented. CRAC domain with bold letters and central tryptophane (in green), cysteine (in red), or phenylalanine (in blue) residues required for cholesterol binding are remarked. (**C**) Representative image of CAV3 constructs distribution visualized by fluorescence microscopy at the same scale (20 µm).

1.5. Regulation of non-caveolar caveolin: a new perspective

Altogether, combining microscopy studies, targeted mutagenesis, and a variety of biochemical techniques, we describe for the first time the existence of a complex regulatory mechanism functioning specifically on newly synthesized caveolins, which differently operate for caveolin family members: while CAV1 is rapidly transported to the PM, CAV2 is accumulated in the GC and CAV3 is retained in the ER and LDs. We also showed that the distribution of caveolin proteins is determined by two new evolutionary conserved caveolin motifs that regulate the ER retrieval and ER exit of the protein. ER retention of caveolins also have implications for the stability of these proteins, since we described the previously unnoticed regulation of them through ERAD system, which is also complemented by ER-phagy degradation and LD trafficking of the protein.

This regulation of caveolins is physiologically relevant because it prevents the cells from the accumulation of the protein in the ER, which triggers ER stress, and the unfolding protein response (UPR). Moreover, caveolin mutants that cause human diseases skip this early regulation of the protein in ER and trigger ER stress and the UPR. Since caveolins present lipid-binding proteins, these mechanisms of regulation could be sensitive to the lipid availability of the cell and act as a sensor to trigger caveolae formation at the PM or lipid storing inside LDs. Further studies directed to connect caveolin distribution, stability, and oligomerization to the lipid concentration of the cell could provide the final clue of caveolin action as a lipid sensor of the cell.

2. Decrease of lipid droplet overloading ameliorates metabolic syndrome

The intracellular accumulation of lipid droplets (LDs) in peripheral tissues such as muscle and liver, known as “ectopic lipid accumulation”, is the cellular hallmark of obesity. The overloading of LDs in those tissues occurring during obesity trigger a multifaceted cellular response which finally leads to insulin resistance and type 2 diabetes (T2DM). At the cellular level, LD overloading causes lipotoxicity and generates sustained signalling from the surplus of bioactive lipids (DAGs, ceramides or prostaglandins), ER stress, and mitochondrial malfunctioning (oxidative stress) that eventually leads to cell damage and death (*174, 231, 234*). However, T2DM is currently seen as a glucose-mediated pathology and the therapeutical approach is basically addressed to reduce glycaemia using metformin as a first-line drug (*310*). In previous studies of the group, the inhibition of acetyl-CoA carboxylase (ACC) with TOFA resulted in a marked LD reduction (*345*). Thus, we hypothesized that targeting LDs using this drug could be a useful treatment for reducing LD overloading and lipotoxicity in peripheral tissues, which in turn would prevent insulin resistance and progression of the metabolic syndrome.

Acetyl-CoA carboxylase (ACC), through malonyl-CoA formation, controls both *de novo* lipogenesis (DNL) and fatty acid oxidation (FAO) (*319-321*). These cellular processes are preferentially performed by the cytosolic ACC1 isoform in lipogenic tissues (adipose, mammary gland, and liver), and the mitochondrial ACC2 in oxidative tissues (muscle, heart, and liver) respectively (*324-326*). The inactivation of the ACC isoforms by antisense oligonucleotides or chemical inhibitors showed to reduce hepatic triacylglycerols (TAGs) in diet-induced rodent models mimicking liver steatosis (hepatic lipid accumulation) (*280, 338*). Thus, we have analysed in this project the potential therapeutic effects of TOFA, which could synergistically complement the glucose-related therapeutic effects of metformin for the treatment of T2DM and concomitantly used to treat the metabolic syndrome.

2.1. Lipotoxicity amelioration by ACC inhibitors

A cell model was developed using C2C12 myoblasts to differentiate lipids when they are free or stored inside LDs and relate it to cell lipotoxicity, which is determined as the production of reactive oxygen species production (ROS), ER stress, and cell death. Oleic acid (OA), which induce the formation of TAGs and LDs, was properly stored contrasting with palmitic acid (PA), which is known to be incorporated into LDs to a lesser extent and whose accumulation outside LDs promoted a clear deleterious effect to the cells. Cotreatment of PA with OA increased PA incorporation into TAGs and LD formation, which was followed by a reduction of lipotoxicity. These results clearly confirms the protective role of LDs by buffering lipids and that free FAs, or the derived lipid species such as monoacylglycerols (MAGs) or DAGs, are the cause of lipotoxicity (*169*).

Since we aimed to synergistically complement the glucose-related therapeutical effects of metformin, we assessed its potential crosstalk with lipid metabolism. Intriguingly, although only at the supra-pharmacological dose of 50 mM (>1 mM, (*310*)), metformin promoted the accumulation of LDs and increased ROS production. Side-inhibition of mitochondrial complex I in the oxidative phosphorylation (OXPHOS) (*401*) could explain the results, but with uncertain physiological relevance. Thus, the observation that metformin even increases the number of LDs in cells could give relevance in the study of a synergistic combination of treatments to reduce glycemia and lipaemia.

The anticipated LD reduction promoted by TOFA (*345*) was evaluated in our model and compared to the lipid-lowering effects of the advanced ACC inhibitor firsocostat (*355*). Both ACC inhibitors alleviated lipotoxic cell death by decreasing LD content and free lipids, although TOFA was much more effective in decreasing lipids. However, TOFA but not firsocostat, increased ROS production which is a possible side-effect of mitochondrial overactivation (*378*). This effect was counteracted by glutathione (GSH) antioxidant supply. *Ex-vivo* experiments using isolated hepatocytes from mice confirmed the efficacy of TOFA decreasing LD content and cell death, which likely means that their beneficial effect occurs in most peripheral tissues. In this case, TOFA did not trigger additional ROS production, which might be counteracted on liver by the robust antioxidant capacity of hepatocytes (*402*).

2.2. TOFA's mechanism of action

TOFA could promote a reduction in the LD content by a decrease in the DNL, an increase on the FA consumption, or both (*318*) (**Fig. 4A**). To elucidate which pathway is involved, TOFA effect was analysed in hepatic (AML12) and muscle (C2C12) cell lines in the presence of FAs. TOFA and FAs synergistically inhibited the DNL in both cell lines, although the inhibition in hepatic cells was almost absolute (>95%), and in muscular cells it was not (>75%).

We hypothesized that with TOFA, FA import into the mitochondria should be activated due to a decreased malonyl-CoA production and CPT1 activation, and in turn it would promote a LD consumption. The LD-mitochondria interaction was measured by assessing the lipid supply from LDs through lipolysis (inhibited by DEUP, lipase inhibitor) and the mitochondrial FA uptake (inhibited by ETO, inhibitor of the FA importer CPT1) (*345*). In AML12 cells, the decrease in LD accumulation was negligible in the presence of DEUP or ETO suggesting a high consumption of LDs with the TOFA treatment. The similar prevention of lipid consumption promoted by both inhibitors suggested that most of the lipids internalised by the mitochondria are supplied by LDs. On the other hand, in C2C12 cells, the LD reduction was only partially inhibited with DEUP or ETO, which means that DNL and mitochondrial uptake contribute to the LD reduction. Since ETO was much more effective than DEUP in reducing LDs, it suggests that the mitochondria uptake of lipids is independent from LD supply. It could be mediated by the differences appreciated between CPT1 protein in both liver and skeletal muscle tissues (*403, 404*).

To further examine the metabolic fate of LD-derived FAs after TOFA treatment, we performed a quantitative analysis of mitochondrial FAO, based on the oxidation of ^{14}C-oleate to acid-soluble radioactive products (ASP, which include partially oxidized metabolites such as acyl-carnitine, CAC intermediates, acetyl-CoA or ketonic bodies(*380*)) and release of $^{14}CO_2$. The results showed that TOFA significantly stimulates the formation of ASP, but strikingly, promoted a slight decrease on CO_2 production. Apart from the results shown in hepatocytes, same effects were also found in C2C12, Vero and AML12 cell lines, different timepoints (1h, 2h, 3h and 9h of CO_2 chasing), nutrient conditions (different OA, PA, and glucose concentrations), and TOFA dose-response assays. These results are consistent with various studies (*405-408*), but clearly contrasts with other classes of recently developed ACC inhibitors (*347, 355, 409, 410*). Thus, TOFA induces a significant activation of partial FAO to ASP, but not to CO_2 release.

2.3. The effect of TOFA in an *in vivo* obesity model

The potent reduction of lipid and LD accumulation encouraged us to examine the potential benefits of TOFA *in vivo*, which was performed using rodent diet-induced models of obesity and related comorbidities. The injection of TOFA in animals fed with a high-fat diet demonstrated after just three weeks significant benefits in muscle, liver, adipose tissue, and glucose homeostasis (**Fig. 3B**).

A clear 50% reduction in body weight gain was appreciated, an effect also shown in rat studies (*411*) and with a potential for prevention of T2DM in humans (*296*). Reduction was especially evident in the white adipose tissue (WAT), but also observed in the liver. Indirect calorimetry determined a higher lipid oxidation of mice treated with TOFA. The effect of TOFA in muscle and hepatic cells, which contribute respectively to 52% and 13% of total energy expenditure mostly by FAO (*412*), could be decisive in the body weight reduction. Importantly, TOFA administration decreases insulin resistance and ameliorates T2DM symptoms. The improved glucose homeostasis caused by TOFA could be directly reflecting the reduction of adipose tissue, which is the primary site for aggravation of obesity and T2DM (*413*). On the other hand, it also diminished hepatic damage. The potential adverse effects of TOFA on decreased β-cell insulin secretion (*414, 415*) are not likely observed in our studies, because glucose tolerance test indirectly suggests a proper functioning of the cells.

Ultrastructural studies demonstrated that TOFA restored the abnormal morphology of the skeletal muscle promoted by the high-fat diet. In TOFA treated animals the interaction between mitochondria and LDs (metabolic synapse) was restored. Curiously, we were unable to correlate this phenotype with a higher physical performance in the treadmill test. Thus, TOFA would improve the metabolic synapse and increase the mitochondrial consumption of LD-stored lipids, which is perhaps explaining the increased FAO observed by indirect calorimetry.

In liver, ACC inhibitors are a promising therapeutic approach for NAFLD, and initial studies demonstrated a dramatic reduction of liver TAGs in both mouse models and clinical trials (*280, 338, 356-359*). However, these effects were undermined since in clinical trials ACC inhibitors presented hypertriglyceridemia (*356-359*). In our study, electron microscopy images of the liver of TOFA treated mice showed a reduction in LD size and number, which was confirmed by the downregulation of PLIN2 protein, a LD marker (*189*). As shown in skeletal muscle, LDs presented a closer contact with mitochondria, which was confirmed by the upregulation of PLIN5 protein implied in the physical bridging between both organelles (*211*). Thus, ACC inhibitors could reduce hepatic steatosis by activating mitochondrial oxidation of LD-derived FAs (**Fig. 3B**). Furthermore, TOFA improved liver health by a reduction of the hepatomegaly caused by the HFD and the hepatic damage reflected by the levels of circulating transaminases. More importantly, TOFA showed a significant advantage, since no increase in blood TAG content was produced, and even a decreased apolipoprotein secretion was previously appreciated (*416, 417*).

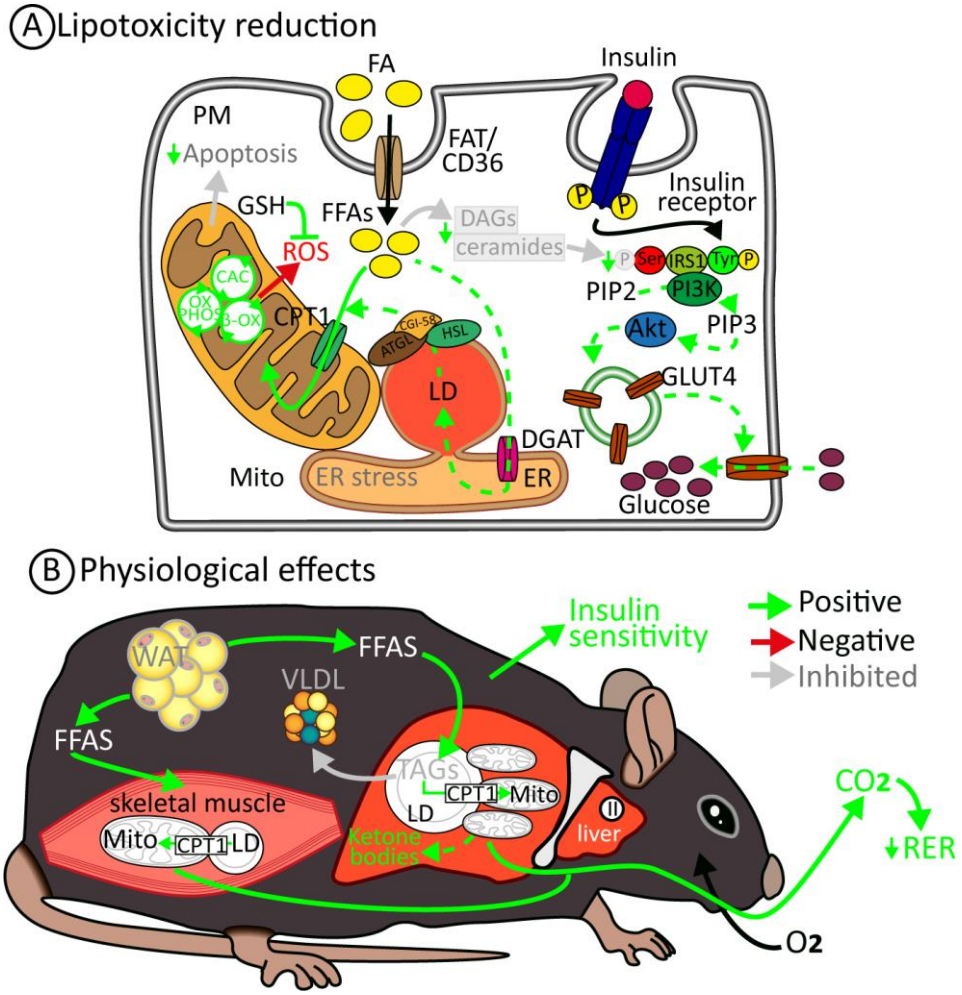

Figure 3. Effects of TOFA on cell and diet-induced mice models.
(**A**) Suggested pathways involved in the reduction of free lipids promoted by TOFA, including a proper transfer between lipid droplet and mitochondria, decrease in lipotoxicity, and increase on insulin signalling. (**B**) Physiological improvements of TOFA in mice tissues to stop the progression of metabolic syndrome. Positive effects are in green, negative in red, and inhibited pathways or substrates in grey. Inhibition or indirect effects are marked with capped and dashed lines respectively.

2.4. The singularity of TOFA and the fate of LD-derived lipids

Our work highlights that treatment with TOFA showed significant advantages over other ACC inhibitors, such as higher reduction on LD content without inducing hypertriglyceridemia as a side-effect. On the other hand, the increased ROS production observed in the *in vitro* model was not reproduced in the animal model (see below).

These differences could be caused by a different mechanism of action promoted by some particularities of TOFA molecule compared to the other ACC inhibitors. As introduced, ACC reaction is a two-step process involving the biotin carboxylation of the enzyme, and then, the transference of the carboxyl group to acetyl-CoA for malonyl-CoA production (*418*). Depending on the inhibited step, ACC inhibitors present differential effects, which in some cases can also be opposite to TOFA and promote the impairment of glucose tolerance (*419*). Similarly, the degree of isoform selectivity is important, since ACC2 inhibition improved FA metabolism in muscle (*409*) and ACC1 inhibition was rather important for cancer treatment (*348, 349*). The tissue where the drug is targeted is also relevant to determine the effects of the molecule, since some inhibitors are tissue-specific (*418*). Thus, the particularities of TOFA's action might be related to the fact that TOFA is a FA mimetic inhibitor, which inhibits the catalytic activity of ACC (class I inhibitor) and shows no isoform selectivity (*407*). Furthermore, we have demonstrated in the presented work that the action of this molecule is not tissue specific.

TOFA differences could be also explained as side effects derived from their FA mimicking structure (16:0 like PA with a non-hydrolysable furane ring), which could promote the blockage of some enzymes in the lipid metabolism (*340*). Accordingly, TOFA activates PPARα through the binding of L-FABP agonist (*382*), although the consequent upregulation of the target genes PGC1α, CPT1, PLIN2 or Cyp4a14 was not appreciated in this project (results not shown). Other FA mimetics such as ETO induce a high production of ROS as a side-effect by altering the mitochondrial complex I or adenine nucleotide transporter, leading to a deficient electron gradient formation (*420, 421*). FAs also promote the uncoupling of this gradient for their intrinsic activity or indirectly through the stabilisation of uncoupling proteins (UCP) and could also originate ROS production (*232*). Therefore, TOFA side-effects on mitochondria similarly to ETO could induce ROS production and explain the results obtained in the lipotoxicity model (**Fig. 4A**).

Despite the differences in the mechanism of action of the different ACC inhibitors, one of our major concerns was to elucidate the fate of LD-derived lipids after TOFA treatment. If the effect on LD consumption was due to mitochondrial metabolic activity, as reflected by the requirement of proper LD lipolysis and mitochondrial FA uptake, an increase in FAO and therefore CO_2 production would be expected. However, in none of the cellular models tested was found an increase in CO_2 release, but rather a significant decrease. Nonetheless, the levels of ASP were clearly upregulated in all cases. The comparison with the *in vivo* model, where TOFA's effect on FAO was validated by indirect calorimetry, point out certain divergences between the *in vitro* and the *in vivo* model.

One possible explanation could be related to the high levels of ROS found after TOFA treatment in cultured cells. ROS can interfere with the ETC (electron transfer chain) functionality for the OXPHOS (oxidative phosphorylation) and leading to the depletion of oxidized NAD^+ and FAD^{2+} (*233*) (**Fig. 4A**), as it has been described in response to metformin treatment (*312, 314*). Since these metabolites are essential for the CAC cycle and lipid β-oxidation, TOFA would ultimately disrupt these two interconnected pathways causing an accumulation of metabolic intermediates (Acetyl-CoA among others) and the decrease on CO_2.

In contrast, in the whole animal, rise of acetyl-CoA might induce ketone body production in liver, as it occurs during fasting to supply the brain with energetic substrates (*422*). Since ketogenesis is a highly oxidizing reaction, it could partially regenerate the oxidized NAD and FAD^{2+} pool, which in turn would restore the CAC activity and re-establish FAO. In fact, TOFA was previously demonstrated to induce ketogenesis (*341, 344, 408, 423, 424*). The antioxidant effect of ketone bodies could also explain the ROS counteraction found in isolated hepatocytes (*425*).

Alternatively, the observed increase in FAO *in vivo* could result from increased oxidative metabolism of other tissues different than muscle and liver, such as WAT (**Fig. 4B**). In fact, we have found a significant decrease in WAT weight after TOFA treatment, which also presented a slightly brown/beige-like phenotype. Initial evidence described that ACC inhibition of DNL prevents lipid deposition on WAT (whitening), which is translated in the browning of the tissue measured by the expression of the UCP-1 BAT marker (*426*). The compelling possibility that TOFA could promote the conversion of WAT into BAT through this mechanism and thus, towards an energy-using tissue, would require further investigation.

2.5. Efficacy of LD targeting by TOFA and future perspectives

Overall, targeting LD reduction on ectopic tissues such as skeletal muscle and liver tissues showed to be a promising strategy for the treatment of metabolic syndrome conditions. ACC inhibitors, with better efficacy of TOFA, reduced the LD content in the muscular and liver cell models ameliorating the lipotoxicity induced by lipid treatments. In mice diet-induced models of obesity, TOFA induced a metabolic switch from glucose to lipid consumption, which successfully improved most of the metabolic parameters analysed (weight gain, adipose tissue weight, glucose homeostasis, hepatic damage markers…). This fact indicates that TOFA would be beneficial for the concomitant treatment of obesity, T2DM, and NAFLD comorbidities. Moreover, TOFA did not trigger hypertriglyceridemia as a side-effect such as other ACC inhibitors. This study clearly reactivates the interest of the drug for the treatment of metabolic syndrome, which after addressing some of the discrepancies observed between the *in vitro* and *in vivo* mechanism of action, the efficacy and safety of the drug could be assessed in further preclinical studies. We apported also initial evidence that metformin does not interfere with LD metabolism, therefore, the synergistic combination with TOFA could be the next treatment to be evaluated in the future studies.

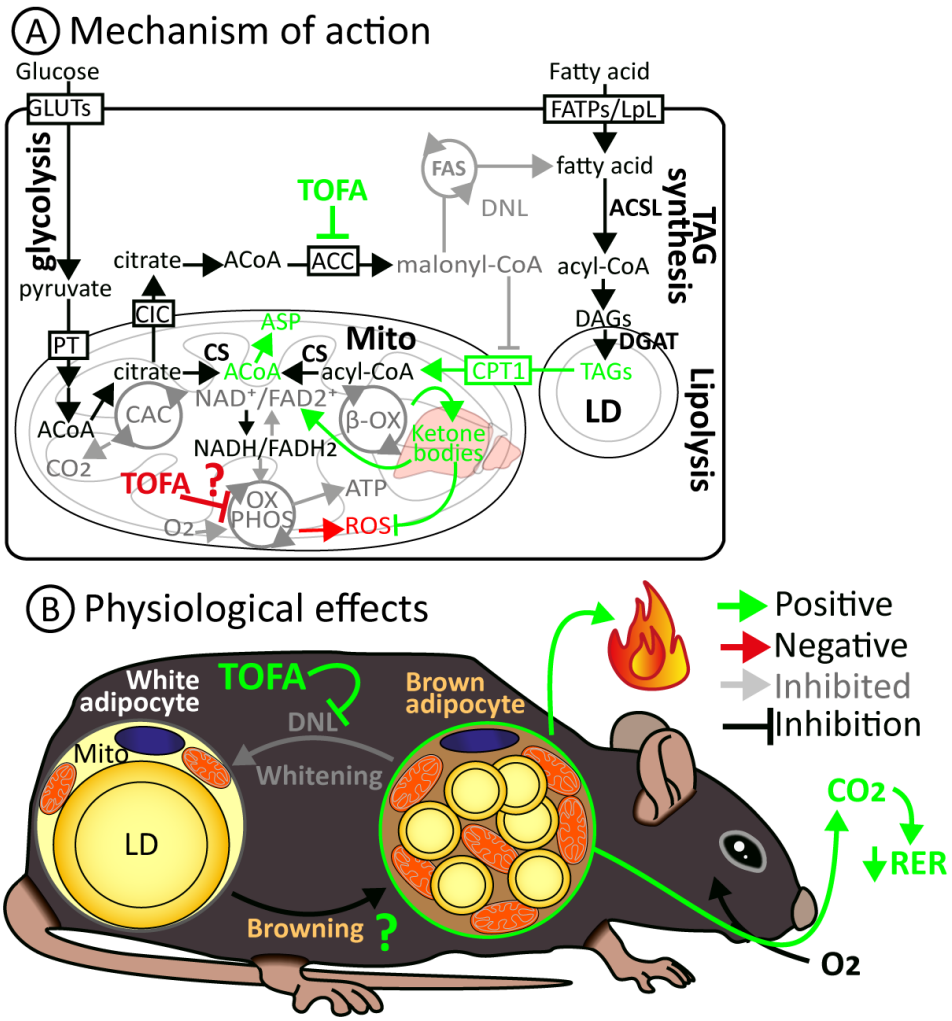

Figure 4. Potential side-effects of TOFA on cell and diet-induced mice models.
(**A**) Metabolic pathways altered by TOFA: side-inhibition of the oxidative phosphorylation pathway in the mitochondria could promote the production of ROS and the depletion of oxidized NAD^+ and FAD^{2+}, which in turn would block citric acid cycle (CAC) and lipid β-oxidation. On liver, ketogenesis could alleviate both ROS and NAD^+ and FAD^{2+} depletion, whose reduction could also be promoted on muscle by lactate production. (**B**) Potential browning of white adipocytes promoted by TOFA, which would explain the results obtained in mice models. Positive effects are in green, negative in red, inhibited pathways or substrates in grey and inhibitors of certain pathways marked with capped lines. Question marks indicate the potential step or pathway altered by TOFA.

CONCLUSIONS

CONCLUSIONS:

1. Caveolin protein members present a different speed on early trafficking through the secretory pathway, which is mediated by the presence of an N-terminal retention domain and C-terminal retrieval motif.

2. Caveolins are degraded by the endoplasmic reticulum-associated degradation during their transit from this organelle to the plasma membrane. This sorting mechanism is complemented by the degradation of the protein through autophagy in ER and the transport of the protein to lipid droplets by lateral diffusion.

3. Caveolin degradation is important to prevent the retention, accumulation, and aggregation of the protein in the endoplasmic reticulum, which triggers endoplasmic reticulum stress and further defects on the Golgi complex interrupting the secretory pathway. It is also important to prevent the pathogeny promoted by caveolin mutants.

4. Acetyl-CoA carboxylase inhibition is a successful target for the reduction of lipids both free or stored into lipid droplets, which in turn prevents muscular and hepatic cells from lipotoxic cell death.

5. Inhibition of Acetyl-CoA carboxylase by TOFA prevents the progression of metabolic syndrome by switching from glucose to lipid metabolism in diet-induced rodent mice models. Consequently, it reduces white adipose tissue weight, hepatic damage markers and insulin resistance which makes TOFA inhibitor a promising therapy for the treatment of obesity, non-alcoholic fatty liver disease, and T2DM.

MATERIALS AND METHODS

1. Plasmids and molecular cloning

All the plasmids used for this thesis are summarized in **table 1**. While cDNA stocks were conserved at -20ºC, 100 µL of each were maintained at 4ºC for their routinely use for transfection. The concentration of the aliquots was monthly checked using Nanodrop 2000c spectrophotometer (Thermo Scientific).

Table 1. Plasmids. Species: Mus musculus, m; and Homo sapiens, h. ϕ indicate the constructs subcloned for this project, and # the constructs with Wild-type (WT) protein.

cDNA	Original construct or vector (Manufacturer/Lab)	Mutations
pEGFP-C3-CAV1m	(Genscript)	#
pEGFP-C1-CAV2m	pCMV6-Myc-DDK (Origene, RC2002703) ϕ	#
pEGFP-C1-CAV3m	(Genscript)	#
pEGFP-C3-VAP-Ah	ECFP-C1 (Carles Enrich's Lab) ϕ	#
pEGFP-C1-ALDIh	Adult male kidney library from the RIKEN Genome Exploration Research. Ref (*179*)	#
pEGFP-C1-STX6m	(Carles Enrich's Lab)	#
pEGFP-C1-PLIN2m	(John McLauchlan's lab)	#
pEGFP-C3-CAV1mβ	pEGFP-C3-CAV1m ϕ	starting at CAV1β (MADEVT)
pEGFP-C1-CAV1mP132L	pUC57 (Genscript)	P132 (CCG) to L(CTG)
pEGFP-C1-CAV1mP104L	pUC57 (Genscript)	P104 (CCC) to L(CTA)
pEGFP-C3-CAV1m RKXX	pEGFP-C3-CAV1m ϕ	Q175 (CAG) to R (CGG)
pEGFP-C1-CAV3m QKXX	pEGFP-C1-CAV3m ϕ	R148 (CGA) to Q (CAA)
pEGFP-C3-CAV1m NCAV3	pEGFP-C3-CAV1m ϕ	Exchange of hypervariable regions: CAV1mβ (MADEVTEKQVYDAHT) for CAV3 (MMTEEHTDLEARIIKDIHC)
pEGFP-C1-CAV3m NCAV1mβ	pEGFP-C1-CAV3m ϕ	Exchange of hypervariable regions: CAV3 (MMTEEHTDLEARIIKDIHC) for the CAV1mβ (MADEVTEKQVYDAHT)
mEGFP CAV1h K*R	Addgene (2776)	K5, K26, K30, K39, K47, K57, K65, K86, K96, K135, K165 and K176 to R
pEGFP-C1-CAV3m K*R	pUC57 (Genscript) ϕ	K14, K19, K29, K37, K58, K68, K107 and K144 to R
pEGFP-C1-CAV3m DGV	pEGFP-C1-CAV3m	Deletion of N-terminal domain (starting at DGV). Ref (*181*)
pEGFP-C1-CAV3m LLS	pEGFP-C1-CAV3m	Lacks N-terminal and CSD domain (starts at 87-LLS). Ref (*181*)
pEGFP-C1-CAV3m LLS ΔEnd	pEGFP-C1-CAV3m	LLS mutant without the last 7 residues. Ref. (*181*)

1.1. Polymerase chain reaction (PCR)

PCR product was obtained using MyFi™ Polymerase (Bioline, BIO-21117) following the manufacturer's instructions and protocols (**Table 2**) in a Thermocycler (BIO-RAD, S1000). To assure specific amplification, PCR reaction without template was also run. Resulting samples were loaded in a 1% agarose gels stained with RedSafe (1/20,000; iNtRon, 21141). Correct length of DNA product was checked using 1kb DNA ladder GeneRuler™ (Thermo Fischer Scientific, SM0311) as a weight marker.

Table 2. PCR (MyFi™). Mix per condition and cycling parameters

Components		Volume (µL)
5x Reaction buffer		5
Template		1 (~10ng)
Primers (20µM)	**for**	0.5
	rev	0.5
DNAse free H_2O		18

Step	Temperature (ºC)	Time (s)	Cycles
Initial denaturation	95	60	1
Denaturation	95	15	25-35
Annealing	>55	15	
Extension	72	15	

1.2. Gel extraction

The gel fragment containing the amplified DNA product was cut out of the gel with a scalpel. DNA was extracted using the NucleoSpin® gel and PCR Clean-up (Machery-Nagel, 740609). Briefly, gel agarose band was weighed, dissolved in NTI buffer (100mg band:0.2mL buffer), heated at 50ºC for 5-10 min and vortexed until melted. Sample was loaded into the column and washed two times with NT3 buffer. Each step was preceded by a 30 s centrifuge at 11,000 G and discarding the flow-through afterwards. To remove the traces of buffer an extra centrifugation step was performed. DNA was eluted incubating the column with 15 µL of DNAse free H_2O for 1 min and centrifuging it at 11,000 G for 1 min.

1.3. Digestion

PCR products (15 µL) or plasmids (~2 µg DNA) were double digested to obtain the insert or vector of the new plasmid. 0.5 µL of each enzyme were mixed with 5 µL of the appropriate digestion buffer and brought to a final volume of 50 µL. Digestion was performed for 1 h at 37ºC, run in 1% agarose gel and, extracted and quantified. To assure activity of digesting enzymes, single- or no-enzyme digestions were performed.

1.4. Ligation and transformation

DNA insert and vector were joined adapting T4 DNA ligase (Promega, M1801) manufacturing instructions. Each ligation reaction consisted in 7 µL of insert and vector (5:1 molar ratio) mix, 1 µL of T4 DNA ligase (Promega, M1801), 1 µL of reaction buffer, and 1 µL of 1 M ATP. Ligation was performed for 2 to 16 h at 4ºC and 2 to 8 h at room temperature (RT) afterwards.

50 µL of Competent E coli DH5α were transformed with 5 µL of ligation reaction. To do that, bacteria and DNA mixture were incubated for 15-30 min on ice, heat-shocked at 42ºC for 1 min, and incubated for 2 min on ice. Transformed E coli were cultured for 1 h with LB at 37ºC in a shaker. Pelleted bacteria (spin at maximal speed) were resuspended in ~100 µL LB, plated in agar with Kanamycin and incubated ON at 37ºC. To check for vector religation or defects in plasmid digestion, control reaction without insert was also done.

1.5. Bacterial growth, glycerol stock, plasmid purification, and sequencing

Two or three positive colonies were grown in 8 mL LB with KAN for 16 h at 37ºC in a shaker. Glycerol stocks were prepared mixing 0.5 mL of 60% glycerol with 1.5 mL of bacterial culture and temporally stored at -20ºC.

To check for positive colonies, cDNA was purified using NucleoSpin® miniprep (MACHEREY-NAGEL, 740499) kit following the manufacturer's instructions with the remaining bacteria, which consists in alkaline lysis of bacteria, binding of cDNA, and elution with DNAse free H_2O.

Purified cDNA was sequenced in Scientific and technological centres of Universitat de Barcelona (CCiTUB) or centre for research in agricultural genomics (CRAG). The glycerol stock corresponding to the colony with correct cDNA sequence was long-term stored at -20ºC.

cDNA stocks were purified using the NucleoBond®Xtra Midi (MACHEREY-NAGEL, 740420) from 200 mL bacterial culture (LB/KAN at 37ºC for 16 h in a shaker) with the same purification principle as NucleoSpin® kit. Concentration and purity of each cDNA stock were quantified using Nanodrop.

2. Cellular model

2.1. Cell lines

All the cell lines used for this thesis are summarized in **table 3**. Cells were cultured with DMEM (Biological industries, 01-055-1A) or 1:1 DMEM:HAM (Biological Industries 01-095-1A) media supplemented with 5-10% Foetal Bovine Serum (FBS, Biological Industries, 04-001-1A), Penicilin-Estreptomicin (Biological Industries, 03-031-1B), L-Glutamine (Sigma, 49419), Pyruvate (Sigma, 5280) and non-essential amino acids (Biological industries, 01-340-1B). AML12 and Isolated hepatocytes were additionally supplemented with Dexamethasone (D4902, Sigma) and ITS (I1884, Sigma): Insulin 5 µg/mL, Transferrin 5 µg/mL and selenium 5 ng/mL. All the supplements were filtered with a 0.22 µM filter and directly added to the medium.

Table 3. Cell lines. relevant cell culture information.

Cell line/ primary culture	Cell type (species)	Culture medium (supplements)	Observations (ATCC Reference)
COS1	Kidney fibroblast (Cercopithecus aethiops)	DMEM 5% FBS	SV40 transformed. (ATCC CRL-1650)
C2C12	Myoblast (Mus musculus)	DMEM 10% FBS	(ATCC CRL-1772)
AML12	Hepatocyte (Mus musculus)	DMEM:HAM's(1:1) 10% (40 ng/mL dexamethasone, ITS)	From mouse hepatocytes transgenic for human TGF alpha (CD1 strain, line MMT42; ATCC CRL-2254)
Isolated hepatocytes	Primary hepatocyte (Mus Musculus)	DMEM:HAM's (1:1) 10% (40 ng/mL dexamethasone, ITS)	Obtained in collaboration, see section 8.4

2.2. Cell culture: maintenance, passaging, seeding, thawing, and freezing

Cells were rapidly thawed from 1 mL vials stored at -200ºC liquid nitrogen tanks, diluted in 9 mL of media at RT, and centrifuged at 800 G for 4 min. The pelleted cells were resuspended in 5 mL complete fresh media, seeded into T25 cm^2 and maintained at 37ºC, 5% CO_2, and 95% humidity.

Cell passaging (**Table 4**) was performed to prevent cells from arriving at 90% confluence with a maximum of ~40 passages. On the other hand, cell seeding (**Table 4**) was done to allow the cells reach 90-100% confluence at the time of sample collection. Once media is removed and cells are washed with PBS (Phosphate Buffered Saline; 8.5 g/L NaCl, 1.075 g/L $NaH_2PO_4 \cdot H_2O$, 0.35 g/L $NaH_2PO_4 \cdot 2H_2O$ at pH7.2), trypsin (Gibco, 15400-054) was added to the cells (2 mL for a T50 cm^2) and incubated at 37ºC until cells were detached. Trypsin was neutralized adding complete fresh media (8 mL for a T50 cm^2). Cells were diluted to be maintained 2-3 days or seeded to perform experiments after cell counting with a Neubauer chamber.

For freezing cells, approximately $3.5 \cdot 10^6$ (a 90% confluent T150 cm^2 flask for 6x1 mL aliquots) were pelleted by centrifugation at 800 G for 4 min and resuspended with 3 mL DMEM 20% FBS. Additionally, 3 mL of freezing media (DMEM 20% FBS-20% DMSO (Sigma, D4540)) were added dropwise, and aliquots of 1 mL were stored at -80ºC for a maximum of one week and then moved to a liquid nitrogen tank.

Table 4. Cell seeding. Passaging dilution and number of cells seeded depending on cell line and days to maintain the cells.

Cell line	Passaging dilution		Number of cells (million)/ 35mm plate	
	2-day	3-day	1-day	2-day
COS1	1/6	1/10	0.5	0.25
C2C12	1/6	1/10	0.5	0.2
AML12	1/3	1/6	-	0.4
VERO	1/6	1/10	0.5	0.25
Isolated hepatocytes	-	-	0.5	0.5

2.3. Cell transfection

Lipofectamine® LTX (LTX, Invitrogen, 153338100) and GenJet™ Plus (GenJet, Signagen, SL100500) reagents were used to transfect C2C12 and COS1 cells respectively to track for exogenous protein expression and transport.

In both cases, DNA and reagent tubes were prepared separately and mixed to form a lipid-DNA complex with the capacity to transfect cells. Prior to transfection, both reagents recommend complete fresh medium replacement to increase transfection efficiency. If protein synchronization was required, this step was modified as explained in section 2.3.3.

2.3.1. Lipofectamine® LTX reagent (LTX)

LTX was prepared in a 3 µg DNA: 4 µL reagent ratio. Using the manufacturer's guide, the following tubes were prepared for a 35 mm plate:

-*DNA tube:* 150 µL of OPTIMEM (Gibco, 31985-037) 0%FBS + 12 µL of PLUS™ Reagent + 3 µg of the desired DNA.

-*LTX tube:* 150 µL of OPTIMEM 0%FBS + 4 µL of LTX.

Both tubes were vortexed, spun down and incubated 5 min at RT. The content of LTX tube was then added in the DNA tube followed by another vortex and spin cycle. The mix was then allowed to form a complex for 20 min and next was dropwise added into the wells.

2.3.2. Genjet™ Plus reagent (GenJet)

GenJet was prepared in a ratio of 1 µg DNA:3 µL Reagent. Using the manufacturer's guide, the following tubes were prepared for a 35 mm plate:

-*DNA tube:* 50 µL of DMEM 0%FBS + 1 µg of the desired DNA to transfect.

-*GenJet tube:* 50 µL of DMEM 0%FBS + 3 µL of GenJet reagent.

Both tubes were vortexed and spun down. The content of GenJet tube was then added in the DNA tube (it is required to mix them in this order) followed by another vortex and spin cycle. The mix was then allowed to form a complex for 15 min and then was dropwise added into the wells.

2.3.3. Synchronized expression

To synchronize protein expression of transfected cells, cell medium was replaced by complete fresh medium containing cycloheximide (CHX, 50 µg/mL) before the addition of the DNA-reagent complex.

That way, protein transduction was stopped during 6 h, which is the recommended time for complete plasmid transfection. Next, media containing CHX was removed and replaced by complete fresh media followed by a 10 s of vigorous tapping of the well plate. This step was repeated 3 times to properly mix de fresh media with the remains of media containing residual CHX, which must be completely washout. At this point, a pulse of newly synthesized protein was produced and chased at a short (3 h) or long (16 h) period with or without cell treatments.

2.4. Cell treatments

2.4.1. Fatty acid treatments

Fatty acids (FA) were prepared conjugated with FA-free BSA (Sigma, A8806) in a BSA:FA 6:1 molar ratio to favour its entry into the cells. Two different stocks were prepared: a concentrated stock of the FA, which is conserved long-term at -20ºC light-protected, and a diluted stock in the culture medium to be used, which is stored at 4ºC light-protected. Diluted stock was used only for few weeks and if a white precipitate appeared it was discarded.

2.4.1.1. Oleic Acid (OA)

Concentrated OA stock (177 mM) was prepared dissolving 0.1 g of oleic acid (Calbiochem, 4954) in 2 mL of ethanol.

For the diluted OA stock (1.77 mM or 500 µg/mL), 0.5 g of FA-free BSA were dissolved in 25.68 mL of the corresponding cell culture media and filtrated with a 0.22 µM filter. 256.8 µL of concentrated OA were added and vortexed vigorously. To properly mix and avoid FA precipitation, diluted stock was agitated at 400-450 rpm for 1 h at RT in an orbital lab shaker.

2.4.1.2. Palmitic Acid (PA)

Concentrated PA stock (100 mM) was prepared by dissolving 0.0256 g of PA (Sigma, A8806) in 1 mL of NaOH in a 2 mL flat glass tube with a stir bar inside. The mix was heated at 70ºC and agitated at the same time. It was aliquoted or used before it cooled down.

For the diluted PA stock (1.77 mM or 500 µg/mL), 0.487 g of FA-free BSA were dissolved in 25 mL of the corresponding cell culture media and filtrated through a 0.22 µM filter. BSA mix and concentrated stock were parallelly preheated at 37ºC and 60ºC respectively. Conjugation of both was achieved by the dropwise addition of 442.58 µL preheated concentrated PA stock into the BSA mix. At the same time, the 50 mL tube with BSA mix was vortexed (spilling was avoided by adjusting the vortex intensity and properly gripping the tube by its upper part). To properly mix and avoid fatty acid precipitation, diluted stock was agitated at 400-450 rpm for 24 h at RT in an orbital lab shaker.

2.4.1.3. Lipid loading

The effects of FA and treatments in LD formation and lipotoxicity were measured in lipid loading conditions.

Lipid loading consisted in 8 h hour preincubation of seeded cells in 12-well for 8 h with OA (100 µg/mL), PA (100 µg/mL), or OA+PA (100+100 µg/mL), diluted in DMEM with high-glucose (Biological Industries, 01-057-1A), and then the addition of the treatment for 16 h unless otherwise stated.

2.4.2. Drugs

All the drugs used in this thesis have been summarized in **Table 3**. For small drug volumes, 100 µl of the culture plate media were collected in a 1.5 mL tube where the drug was mixed. After the addition of the drug, a vortex and spin cycle were performed, and the mixture was put back into the cell culture plate.

Table 5. Drugs for cell treatment. Relevant preparation and storage information.

Drug	Manufacturer (reference)	Preparation (storage)	Effect (mechanism of action)	Final concentration
Cycloheximide (CHX)	Sigma (C7698)	10 mg/mL in cell medium with 25 mM HEPES (4ºC)	Protein translation inhibitor (interferes the translocation of mRNA in the ribosome)	50 µg/mL
MG132	Merk (474790)	10 mM in DMSO (-20ºC)	Proteosome inhibitor (direct reversible inhibitor)	Transfected CAV: 50 µM for 3 h and 1.5 µM for 16 h Endogenous CAV: 5 µM for 16 h
3-Methyl-adenine (3MA)	Sigma (M9281)	200 mM in miliQ H_2O 60ºC (-20ºC)	Autophagy inhibitor (Class III PtdIns-3-kinase inhibitor)	10 mM
1,1-dimethylbiguanide hydrochloride (Metformin)	Sigma (D150959)	1 M in freshly prepared media	Glucose-lowering (hepatic glucose production inhibition)	50 mM
5-Tetradecyloxy-2-furoic acid (TOFA)	Santa Cruz (sc-200574)	30 mM in DMSO (-20ºC)	ACC1 and ACC2 inhibitor	100 µM
Firsocostat (ND-630, GS-0976, NDI-010976)	MedChem Express (HY-16901)	50 mM in DMSO (-20ºC)	ACC1 and ACC2 inhibitor	50µM
Etomoxir (ETO)	Sigma (E1905)	50 mM in miliQ H_2O (-20ºC)	Prevents FA internalization into the mitochondria (CPT1 inhibitor)	1 mM
Diethylumbe-liferyl phosphate (DEUP)	Sigma (D7692)	500 mM in DMSO (-20ºC)	Inhibits lipolysis (Cholesterol esterase inhibitor)	0.5 mM
Reduced Glutathione (GSH)	Sigma (G4251)	500 mM in cell medium and then diluted to 50 mM (freshly prepared)	Antioxidant (Substrate of Glutathione peroxidase)	0.5 mM

3. Animal model

3.1. Ethics

All animals received human care in compliance with institutional guidelines regulated by the European Community. All the animal procedures have been approved by the *Comitè ètic d'experimentació animal* of the *Universitat de Barcelona* (CEEA-UB, Project 419.18 and its posterior modification), the *Comitè Ètic d'Experimentació animal of the Parc Científic* de Barcelona *(CEEA-PCB),* and the *Direcció General de Polítiques Ambientals i Medi Natural of the Generalitat de Catalunya* (Expedient FUE-2019-00975055 and approval number 10466).

3.2. Mouse strain and gender

The studies were conducted in *Mus musculus* C57BL/6J mice. This is widely used because it is able to reproduce obesity and diabetes symptoms under a high-fat diet (HFD) in a relatively short period of time, such as 20-30% of body weight increase (16-20 weeks) or hyperglycaemia and hyperinsulinemia (4 weeks) (*381*).

Male mice have been used in this study since they are more sensible to develop these diseases symptoms. For example, female mice develop less hyperinsulinemia, hyperglycaemia, and hypertriglyceridemia (*427*). In further studies, once the treatment would become adjusted, it will be tested in female mice.

3.3. Housing, supervision conditions and endpoint criteria

Animals were provided by Charles River Laboratories (FRANCE, A 69208 1301).

All the procedures were conducted inside the Unitat d'Experimentació Animal Medicina-Casanova (UB, registry number: B-9900020) and the Estabulari Parc Científic de Barcelona (UB, B-9900044). Mice were housed in the SPF facility under 12:12h dark:light cycle and at 22-25ºC with food and water ad-libitum if starvation was not required.

Welfare of the animals was assured by checking weekly its health state using a supervision protocol modified from (*428*) were weight gain, aspect, spontaneous and manipulation behaviour were evaluated and punctuated. This punctuation ranged from 0 to 2 points for moderate and 9 points for critical symptoms. If animals received 0-3 points no intervention was produced; from 4-8 the supervision test frequency was increased at daily and analgesia was

administered (if no recuperation of the mice is appreciated in 2 days, the punctuation is increased to 9) and 9 or greater the animals were euthanized by cervical luxation and permanent decease of circulation confirmation.

3.4. Animal treatments and injections

Animals were intraperitoneally injected with a 30G needle (BD Biosciences, 304000) and a syringe with the following treatments summed up in **Table 6**. To increase the volume of the treatments into an injectable volume, they were diluted from its initial stock. For chronic intraperitoneally injection of either saline or TOFA, the site of injection was alternated daily between the four quadrans of the peritoneum to avoid potential injuries.

Table 6. Drugs for animal treatments. Relevant preparation and storage information.

Drug	Manufacturer (reference)	Concentrated stock (diluter)	Dilution (in saline)	Volume injected (µl/g)	Specifications	Dose
TOFA	Santa Cruz (sc-200574)	30 mM (DMSO)	1/500 (30 µL in 15 mL)	5	1.5 mL aliquots stored at -20ºC for months or 4ºC 1-2 days	100 mg/kg
Glucose	Sigma (G8270)	Solid powder	10% w:v (1 g in 10 mL)	10	Prepared fresh	2 g/kg
Insulin	Sigma (I9278)	247 U/mL	1/5000 (3 µL in 15 mL)	6	Conserved at 4ºC	0.3 U/kg
Ketamine (Ketamidor®)	Richter pharma (2695 ESP)	100 mg/mL	1/10 (0.5 mL with 1 mL xilacine in 8.5)	10	Conserved light-protected for few months at 4ºC	100 mg/kg
Xilacine hidroclorur (Rompum®)	Rompum (1977 ESP)	20 mg/mL	1/20 (1 mL with 0.5 mL ketamine in 8.5)	10	Conserved light-protected for few months at 4ºC	10 mg/kg

3.5. Experimental design

C57BL/6J male mice were obtained at 4 weeks old, randomly separated in cages containing two animals and acclimated at house conditions for 2 weeks.

Once adapted, mice were feed for 6 weeks with either control (CTL, Research Diets, D12450K, 70% carbohydrate, 20% protein and 10% lipids, conserved at -20ºC) or HFD (Research Diets, D12492, 20% carbohydrate, 20% protein and 60% lipids, conserved at -20ºC) to induce preobesity and prediabetes.

At week 6 treatment started: mice were intraperitoneally injected with either saline or TOFA for the next 6 weeks. At week 12 and 13, glucose and insulin homeostasis or metabolic tests were performed. At the end of week 13 or beginning of week 14, animals were sacrificed, and tissues collected. A timing scheme of animal experimental design is provided in the results section.

3.6. Weekly measurements and cage maintenance

Animal weight, and food and water intake were weekly measured to follow obesity and type 2 diabetes mellitus progression (T2DM) progression.

Cages were changed every Monday morning. Animals, diet rests and drinking water bottles (with the remaining water inside) were weighed. New full drinking water bottles and frozen diet were added to the cages after weighing them.

Food and water intake were calculated as the weighed fresh diet or water added on Monday minus the remaining water or diet weighed the following Monday. Water intake value was corrected by subtracting also the water lost during the transport of the cages.

3.7. Glucose and insulin homeostasis tests

Progression of T2DM was checked performing glucose and insulin homeostasis tests.

All the tests were performed after a 6 h starvation to detect the differences between groups. Water bottle was maintained. To measure glucose levels a blood drop obtained by cutting with scissor the tail edge of mice (as short as possible) was collected and measured with a glucometer (NovaPro, DIA019MN01) and strips (NovaPro, 53881). During all the test, mice were maintained awake and trying to minimize the external stimulus. The delay between mice injection and glucose measuring were assumed as equal.

3.7.1. Intraperitoneal glucose tolerance test (IGTT)

Mice capacity of blood glucose clearance in fed conditions (simulated with glucose injection) was checked using IGTT.

Glucose (2g/kg) was intraperitoneally administered, and glucose levels measured at 15, 30, 60, and 90 min after injection.

3.7.2. Intraperitoneal insulin tolerance test (IITT)

Mice responsiveness to insulin after feeding (induced with exogenous insulin injection) was checked using IITT.

Insulin (0.3 U/kg) was intraperitoneally administered, and glucose levels measured at 15, 30, 60, and 90 min after injection. Since insulin highly decreases blood glucose levels, a solution of glucose (2 g/kg) was also ready to be used if a potential hypoglycaemic shock occurs. If mice became lethargic and unresponsive to manual manipulation (usually due to a decrease in glucose levels below 20 mg/dL) glucose solution was injected, and red light applied to them to avoid a drastic corporal temperature decrease.

3.8. Metabolic tests

These experiments were performed in collaboration with the group of complex disease and mitochondria of Dr Zorzano at IRB (Parc Científic UB), with the help of David Sebastián and as previously described (*429*).

3.8.1. Indirect calorimetry

The source of energy used (glucose or lipids) was measured by indirect calorimetry.

Animals were housed inside a chamber (Oxymax®-CLAMS, Columbus Instruments) for 4 days. First- and second- days were left only to be acclimated, but third- and fourth-day oxygen consumption (VO_2) and CO_2 production (VCO_2) were measured every 20 min maintaining room air composition to 20.5% O_2 and 0.05% CO_2. Food and animal weight were daily checked to correct these parameters. Using VO_2 and VCO_2 parameters, glucose oxidation (in $g/min/kg^{0.75}$=[4.545xVCO_2-3.205xVO_2]/1,000), lipid oxidation (in $g/min/kg^{0.75}$=1.672x[VO_2-VCO_2]) and Respiratory exchange ratio (RER=VCO_2/VO_2) were calculated.

3.8.2. Exercise tolerance test (treadmill)

To evaluate muscle and cardiopulmonary activity of animals an exercise tolerance test was performed.

4 days before the test, animals were put inside one of the lanes of the treadmill (Panlab, Harvard apparatus). After a few minutes of acclimatation, treadmill was turn on at 14 cm/s for 10 min. Shock grid was also connected to motivate the animals to run but at minimum voltage. 2 days before the experiment, the process was repeated. The day of the experiment animals were prepared as the previous days, but with the following test regimen: 14 cm/s for the first 8 min and then increasing the speed 2cm/s every 2 min up to 46 cm/s (maximum speed). Animals run until exhaustion, which was defined as the point when the animals were unable to run avoiding the repetitive shocks of the shock grid. Run distance and time were recorded for each animal.

3.9. Tissue collection

The necropsy of the animal was performed on aluminium foil with the area previously disinfected with 70% ethanol. Animals were terminally anaesthetized with ketamine/xilacine cocktail. The following procedures were consecutively done in that order.

3.9.1. Intracardiac puncture

Once foot reflex was not observed after pinching animal extremities, intracardiac puncture was performed to obtain a large blood sample from the heart and confirm animal's death by exsanguination.

Chest was palpated to localize the hearth of the animal and then Intercostal puncture was done horizontal with a 25 G needle and the syringe slightly open. Once blood entered the syringe tip, 600-800 µL of blood were aspirated and collected to a Microtainer tube (BD Biosciences, 365986). Plasma was obtained after centrifuging blood sample at 6,000 Gs for 5 min and was stored at -20ºC.

3.9.2. Fat depots extraction

Three fat depots were extracted and weighed: intrascapular Brown adipose tissue (iBAT), inguinal subcutaneous white adipose tissue (ingWAT), and gonadal visceral white adipose tissue (gWAT) to evaluate obesity progression (**Fig. 1A, B and C**).

A transverse incision below the diaphragm with tweezers and scissors was performed after soaking the zone with ethanol 96º. Mice were laid down in a supine position and the skin was pulled up (**Fig. 1AI**). Underneath and stacked to interscapular white adipose tissue (isWAT), iBAT was localized (**Fig. 1AII** dashed line). Both tissues were extracted by detaching them from the cavity (before **Fig. 1AII** and after **Fig. 1AIII**). iBAT with butterfly morphology and orange/brown colour tone was isolated discarding isWAT (**Fig. 1AIV** red arrowhead).

ingWAT was exposed changing the animal in a prone position and pulling down skin (**Fig. 1BI**). It was first detached from its leg end in the inguinal cavity with tweezers and scissors (before **Fig. 1BII** and after **Fig. 1BIII** encircled with dashed line). It was also detached from the skin end following the natural border of the depot (**Fig. 1BIII**) to extract it as a whole piece (**Fig. 1BIV**).

Close to the inguinal region with the animal placed in prone position (**Fig. 1CI**), the testicle can be observed with the gWAT depot connected. By making a small incision in the peritoneum (**Fig.1CII** solid line), both could be pulled out from the peritoneum cavity using the tweezers (**Fig. 1CIII**). gWAT was isolated by cutting its connexion with testicles and removing other parts of the reproductive system (before **Fig. 1CIII** and after **Fig. 1CIV** dashed line).

3.9.3. Liver extraction

Liver was extracted and weighed to follow the progression of non-alcoholic fatty liver disease (NAFLD) symptoms. Mice in prone position (**Fig. 1DI**) got an incision in the peritoneum with scissors below the sternum and rib for intrabdominal cavity opening (**Fig. 1DII** solid line). Liver is connected by its upper part to the diaphragm, which was cut by pinching it with the tweezers and cutting the circumference around it (**Fig. 1DIII** arrowhead and dashed line and black arrowhead). Liver was pulled out from the intrabdominal cavity and if it was stick to parts of the intestine, kidney, or other organs they could be separated with the scissors (**Fig. 1DIII** dashed line). Once extracted, liver could be cleaned by cutting the remains of the diaphragm and separating the biliary vesicle (**Fig. 1DIII**).

3.9.4. Gastrocnemius muscle extraction

This technique was shared by Dr Postigo group of Transcriptional regulation of Gene expression (IDIBAPS-FCRB, Barcelona) and adapted. Muscle was extracted to weight it and follow ectopic lipid deposition.

Mice in a supine position (**Fig. 1EI**) were subjected three needles to a lid covered with silver foil: one next to the neck and two others in both ankles to tighten the leg muscles (**Fig. 1EII**). The muscle to be extracted was properly oriented and tightened to facilitate its extraction. Skin was then cut starting close to the ankle and up to the knee with tweezers and scissors and without pinching nor cutting the Achille's tendon. Remaining skin sticked to the muscle was separated using another needle and following the natural border of the muscle. It was also subjected to the porexpan lid with another needle. Extraction of gastrocnemius was performed subjecting with the tweezers and cutting with the scissors the Achilles tendon to pull up the medial and lateral head of the muscle (**Fig. 1EIII** black arrowhead). Tibialis muscle, which was not studied in this thesis, was eliminated by separating it from the gastrocnemius (**Fig. 1EIII** red arrowhead). Finally, gastrocnemius could be whole piece isolated by maintaining Achille's tendon subjection and cutting it from the femur (**Fig. 1EIII** black arrowhead and dashed line). Once extracted, it could be isolated by cutting the remaining Achilles tendon.

3.10. Serum analysis

ALT (Alanine aminotransferase), AST (aspartate aminotransferase), triacylglycerol (TAG); and total, LDL (low-density lipoprotein), and HDL (high-density lipoprotein) cholesterol levels were measured from plasma samples at Hospital Clínic i Provincial de Barcelona using Molecular Absorption Spectrometry (Siemens, ADVIA 2400).

Figure 1. Tissue collection.
The process for the collection of (**A**) intrascapular brown adipose tissue (iBAT), (**B**) inguinal white adipose tissue (ingWAT), (**C**) gonadal WAT (gWAT), (**D**) liver, and (**E**) gastrocnemius muscle. Dashed lines indicate the tissue to be extracted, solid the incisions to be performed, black arrowheads the required tweezer subjection, and red arrowhead the tissue to be discarded.

4. Protein analysis

Protein levels, localization, and oligomerization were measured from sample lysates or ultracentrifuged samples. All the procedure for protein extraction and fractioning were done on ice to avoid protein degradation unless it is stated. Processed samples were stored at -20ºC.

4.1. Cell lysates

Protein levels were measured from total cell lysates which were obtained from transfected cells in a 35 mm plate.

Cells were washed two times with cold PBS (meticulously aspiring the second) and gently scrapping them with 80 µL of lysis buffer (50 mM Tris HCl pH 7.5, 150 mM NaCl and 5 mM EDTA supplemented with protease and phosphatase inhibitor cocktail [10 µg/mL Aprotinin (Sigma, A1153), 10 µg/mL Leupeptin (Sigma, L2884), 1 mM PMSF (Sigma, P7626), and 1 mM Sodium Orthovanadate (Sigma, 36508)] with 0.1% Triton X-100 [TX, Sigma, T8787]) to favour cell disruption. Collected samples were completely disrupted by sonication for 20 s at 30 A.

4.2. Tissue homogenates

Liver homogenates were obtained by chopping them for 2 min with two scalpels on a fixed petri dish. Approximately 1mg of chopped liver was required to proceed. It was further homogenized with 1 mL of lysis buffer with inhibitors in Rino® microcentrifuge tubes (Next Advance, TUBE1R5-S) and using the Bullet blender® (Next Advance, B724M) at 12,000 rpm for 5 min and 4ºC. Samples were diluted 1/10 with lysis buffer and sonicated for 20 s at 30 A.

To obtain muscle homogenates, approximately 1 mg of muscle was chopped with the same procedure than liver and sonicated 20 s at 30 A. Samples were diluted 1/10 with lysis buffer and sonicated a second time.

4.3. Triton solubilization assay

Insoluble oligomerized caveolin, forming caveolae at the PM, was separated from soluble intracellular fraction of the protein, at its first steps of synthesis and transport, by using its differential detergent solubility. The method was adapted from (*72*).

Transfected cells in 35 mm well plates were washed two times with cooled PBS. Cells were solubilized by adding 300 µL of chilled lysis buffer (increasing TX to 1%) for 35 min on ice without agitation nor scrapping. The soluble fraction was then collected by decantation and pipetting. The insoluble fraction remaining in the well was collected by scrapping cells with 300 µL of SDS lysis buffer (2% SDS, 1%Tris-HCl pH6.4) at RT. Insoluble fraction was passed through a 25 G needle 10 times to avoid sample viscosity.

4.4. Sucrose velocity gradient

CAV fractions in different oligomerization steps were separated in an isopycnic sucrose velocity gradient according to its differential density, which promotes a differential velocity to sediment during ultracentrifugation. It was adapted from (*75*).

Cells grown in 60 mm well plates were gently scrapped in 500 µL of PBS after two washes with PBS at RT. Then, they were pelleted by centrifugation at 800 G for 4 min at RT. After aspiration of supernatant, pelleted cells were permeabilized in 200 µL of lysis buffer increasing TX to 0.5% for 20 min at RT. To avoid insolubilized cells, centrifugation at 1,100 G and RT for 5 min was done and supernatant was collected. It was loaded at the upper phase of a sucrose gradient (phases and volumes are summed up in **Table 7**) and mounted in a Polypropylene centrifuge tube (Beckman Coulter, 347357). All the phases %w/v were checked using a refractometer (Nippon Optical Works, No.501). Gradient tubes were then ultracentrifuged (Thermo Scientific, Sorval MX 150) with the Hitachi (S55S) rotor at 55,000 rpm for 4 h 15 min at 4ºC. Seven 310 µL cell phases were collected by pipetting from top to bottom (**Table 7**).

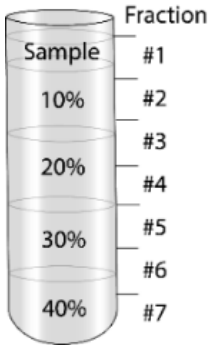

Table 7. Sucrose velocity gradient. Phase preparation, mounting and fraction collection

Sucrose phases (%w/w)	Sucrose 2.56M (mL)	Lysis buffer (mL)	Loading volume (µL)
10	0.225	2.175	500
20	0.5	1.75	500
30	1	1.64	500
40	1.25	1.125	500

Half of the fractions were collected compared to the original method (*75*) to make the process more efficient without affecting the result (**Fig. 2A and B**). Caveolin oligomerization can be divided in 4 different steps: soluble (caveolin after synthesis), 8S (first oligomerization step during the ER to GC trafficking), 60S (fully oligomerized and forming caveolae at the PM) and aggregated (forming non-native protein complexes due to malfunctioning of regulatory machinery). 8S and 60S complexes of endogenous CAV1 (endCAV1) could be clearly observed in fraction #3 (#4-6 when separated in 14 fractions) and #5 (#9-11 for 14 fractions) (**Fig. 2A and B**). Soluble (fractions #1-2) and aggregated bands (#7) were appreciated in the results section. Comparing endCAV1 with GFP-CAV1, a shift between both was appreciated (arrows in **Fig. 2A and C**) due to the higher molecular weight of CAV1 fused to the GFP tag, but the same oligomerization state and bands were observed.

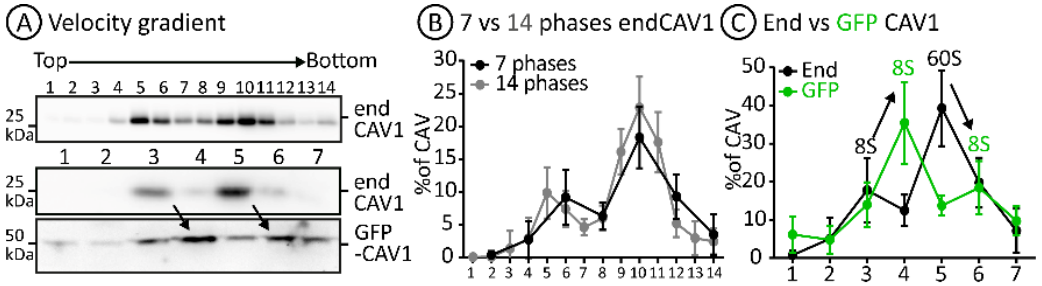

Figure 2. Optimization of sucrose velocity gradient.
(**A**) CAV1 was detected in 7 or 14 phases sucrose velocity gradient using CAV1 for both endogenous (end) and GFP-fused. (**B**) Comparisons between 7 and 14 phases gradients, and (**C**) between end and GFP-CAV1. Arrows mark the shift in 8S and 60S fractions between endogenous (End) and transfected (GFP-) CAV1.

4.5. Sucrose floatation gradient

LD fraction of caveolin was isolated after a soft disruption of cells and ultracentrifugation in an isopycnic sucrose gradient taking advantage of the LD low density.

Two 100 mm plates of transfected cells were used for each condition. After two washes with PBS, cells on the first plate were gently scrapped with 300 µL lysis buffer without TX. Cell lysate was then transferred to the other plate (previously washed with PBS) and scrapped without adding more buffer. It is crucial to meticulously aspire all the PBS washes to avoid remains and volume increase of the sample. Cells were then cavitated (Parr Instrument Company, 4639) at 55 Bar for 15 min and 4ºC and then carefully collected in a 1.5 mL tube. Samples were passed throughout a 22 G needle 25 times and centrifuged for 5 min at 1500 G and 4ºC. 500 µL of the supernatant fraction was then mixed with 500 µL of 65% sucrose in the centrifuge tube (Beckman Coulter, 347357). The phases of sucrose summed up in **Table 8** were loaded on top of the sample. Gradient tubes were then ultracentrifuged (Thermo Scientific, Sorval MX 150) at 50,000 rpm with the Hitachi (S55S) rotor for 3 h at 4ºC. Six cell phases were collected with the tube slicer (Beckman, 347960) from top to bottom (**Table 8**). The ultracentrifuged tube was cut with tube slicer to collect five fractions of ~300 µL. The remaining gradient volume in the bottom phase was directly collected by pipetting (~700 µL).

Using this technique floating LDs could be isolated in fraction #1 while the other cell organelles sedimented on fractions #3-6.

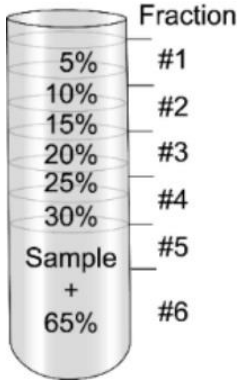

Table 8. Sucrose floatation gradient. Phase preparation, mounting, and fraction collection

Sucrose (%w/w)	Sucrose 2.56M (µL)	Lysis buffer (mL)	Loading volume (µL)
5	60	1.47	200
10	135	1.31	200
15	225	1.21	200
20	300	1.05	200
25	480	1.07	200
30	600	0.98	500

4.6. Bradford quantification

Cell sample protein levels were quantified to load in an SDS-page the same amount of protein in each condition for cell lysates or tissue homogenates. Additionally, protein levels were quantified to relativize results to the amount of protein in the sample. To do that, Bradford assay (*430*) corrected by Absorbance ratio analysis A_{600nm}/A_{450nm} (*431*) was performed in 96 well plates.

Standard curve wells were prepared by mixing increasing volumes of 1 mg/mL BSA (0, 0.5, 1, 2, 4 and 8 µL) with 2 µL of lysis buffer and brought to 40 µL final volume with miliQ H_2O. It was run in duplicates.

Sample wells were prepared by pipetting 2 µL of each sample into the well, where 38 µL of miliQ H_2O were previously added. It was run in triplicates

160 µL of 5:1 miliQ H_2O:Bradford reactive (Biorad, 500-0006) were added in all the wells and incubated for 10 min at RT without agitation.

A_{600nm}/A_{450nm} was read in a spectrophotometer and correlated with BSA concentration of the standard curve. Protein concentration was interpolated from the ratio of absorbances measured and using the standard curve.

4.7. Sample preparation

The same volume of sample per fraction obtained from triton solubilization assay, sucrose velocity, or sucrose density gradient assays were prepared with 4x running buffer (30 mM $Na_2HPO_4 \cdot 2H_2O$ pH 7.0; 30% Glycerol; 7.5% SDS; 4.5% Dithiothreitol (DTT); 0.05 % Bromophenol blue). For 15-well polyacrylamide gels, 30 µL of sample with 10 µL of running buffer were prepared. For cell lysates or tissue homogenates, the same amount of protein was prepared per sample (30-60 µg) brought to 30 µL with lysis buffer and mixed with 10 µL of 4x running buffer. The exact amount of protein to be loaded was established as the maximum µg of protein in 30 µL of the less concentrated sample. Samples were boiled at 100ºC for 5 min in a Thermoblock.

4.8. Gel Electrophoresis and wet transference

Prepared samples were separated depending on their electrophoretic mobility in a 10/15-well SDS-PAGE and transferred to a nitrocellulose membrane to be further immunoblotted.

Gels were prepared using the MiniProtean III system (Bio-Rad, 165-3301) in which a spacer and short glass plates were mounted in the casting frame and supported in the casting stand. Resolving (80% of total gel volume) and stacking (20%) gel solutions were polymerized between glasses and capped with a comb.

Resolving gel was prepared in the chosen acrylamide percentage (30%, PanReac, UN3426) (**Table 9**). Diluted acrylamide was mixed with 5 mL of solution 1 (0.75 M TrisHCl, 0.2% SDS at pH 8.8), 50 µL Ammonium persulfate (APS, Sigma, 21,558-9) and 14 µL of TEMED (BioRad, 160801). It was poured between both plates and allowed to polymerize covered with 2-propanol. Once polymerized, propanol was washed-out with miliQ H_2O. Stacking gel solution was prepared mixing 1.2 mL miliQ H_2O, 5 mL of solution 3 (0.75 M TrisHCl, 0.2% SDS at pH 8.8), 360 µL of Acrylamide, 30 µL APS, and 7.5 µL TEMED. It was poured, allowed to polymerize, and capped with a 10- or 15-well comb.

Table 9. Resolving gel. % of gel preparation with miliQ H_2O and Acrylamide volumes

%	6	7	8	10	12	15
miliQ H_2O (mL)	3	2.6	2.2	1.6	1	0
Acrylamide (mL)	2	2.4	2.8	3.4	4	5

Gels were assembled in a cassette sandwich and put inside the electrode assembly. The inner part of the system was filled with electrophoresis buffer (1 g/L SDS; 3.03 g/L Tris-HCl; and 14.41 g/L glycine), combs were pulled out and samples loaded inside the wells with a Hamilton syringe (Hamilton, 80600). Precision Plus Protein™ standard (BIO-RAD, 161-0374) was also loaded to determine the molecular weight of the target proteins. After completely filling the tank with buffer, samples were run at 100 V/constant for the first half of the gel and 150 V/constant the second part connected to power supply (Thermo, 250-90). When the blue front dye (running buffer) was to escape from the gel, electrophoresis was stopped.

Separated proteins from the gel were transferred into a nitrocellulose membrane (0.45 µM, BIO-RAD, 10484060) using the Mini Trans-blot® system (BIO-RAD, 170-3930). A wet transference sandwich was prepared assembling the components from bottom (black) to top (white): a sponge piece, a Whatman® paper piece, the gel with the samples, nitrocellulose membrane, another Whatman® paper and another piece of sponge. Sandwich was closed tightening the layers (avoid bubble formation) until it was put inside the cuvette half-full of transference buffer (25 mM Tris-HCl pH 8.3; 192 mM glycine; 0.02 % SDS; 20 % methanol). After fully filling the tank, the transference was run at 70 V for 2 h connected to power supply.

4.9. Western-Blot analysis (WB)

Detection of the protein of interest was done by immunoblotting of nitrocellulose transferred proteins.

Nitrocellulose membrane was maintained on agitation in an orbital lab shaker and membrane drying was avoided during all the steps. It was blocked with 5% dry milk for 1 h at RT to avoid potential unspecific binding of the antibody. Two 1-min TBS-T washes (Tris-HCl 1.45 g/L, NaCl 8.7 g/L and Tween20 0.5%) were performed to remove the excess of milk and then it was incubated with primary antibody ON at 4ºC or for 1 h at RT (**Table 10**). Three TBS-T wash (5 min, 10 min, and 10 min) were performed to remove unbound primary antibody.

Secondary antibody or Protein-A conjugated with horseradish peroxidase (HRP, Bio-Rad) were incubated for 45 min or 30 min respectively at RT. Three more washes were performed to remove unbound secondary antibody and membranes were maintained with TBS and visualized using the EZ-ECL peroxidase-based chemiluminescent method (Biological Industries, 2035660). Images were taken with LAS400 at 480 nM excitation filter for no more than 15 min.

4.10. Quantification

Bands were quantified using the Gel analyzer macro from Fiji/ImageJ (*432*). For cell lysates or tissue homogenates, values from the protein of interest were corrected using GAPDH as a loading control (unaltered by all the treatments). Once obtained GFP/GAPDH ratio it was relativized to control condition and expressed as a fold increase. For triton solubility assays, soluble or insoluble fractions were compared to the control condition or represented as a percentage of the total protein. For density and velocity gradients the value of each fraction versus the total (all fractions) were represented as a percentage.

Table 10. Primary antibodies used for Western Blot.

Target antigen	Manufacturer (reference)	Species	Final dilution	Molecular weight (kDa)	Observations
GFP-tag	Abcam (ab290)	Rabbit	1/5,000	27+fused protein	ON at 4ºC. Prot A-HRP as secondary antibody
GAPDH	Genscript (A00191)	Goat	1/5,000	37	1 h RT
ACSL3	ABNOVA (H00002181-B01P)	Mouse	1/1,000	75	ON at 4ºC, use of PBS and PBS-T instead of TBS and TBS-T
CAV1	BD Biosciences (610060)	Rabbit	1/3,000	20	ON at 4ºC
Myc-tag	Abcam (ab32)	Mouse	1/1,000	1.2+fused protein	ON at 4ºC
PLIN2	Abcam	Rabbit	1/5,000	50	1 h RT
CPT1	GeneTex (GTX114337)	Rabbit	1/1,000	88	ON at 4ºC
PLIN5	Progen (GP31)	Guinea pig	1/5,000	51	ON at 4ºC

5. Gene expression

Gene expression was measured in RNA extracts from cells, retrotranscribed to cDNA, and amplified using qRT-PCR technology.

5.1. RNA extraction

Purified samples, due to RNA lability, were either fast put on ice if the process was to be continued, or long-term stored at -80ºC. Concentration and purity (A260/280~1.8) of RNA was measured using Nanodrop 2000c spectrophotometer (Thermo Scientific).

35-mm plate per condition was required. RNA was extracted using the EZ-10 DNAaway RNA Mini-Prep's kit (Biobasic, BS88136) following the guide at RT. Cells were scrapped with 350 µL of Lysis-DR buffer after two washes with PBS. Genomic DNA (gDNA) was removed by passing the lysate through the gDNA Eliminator column. Flow through was mixed with 250 µL ethanol by pipetting up and down and transferred to a RZ-10 column to isolate RNA. It was washed two times with 500 µL GT buffer and one with 500 µL NT buffer. All the steps were preceded by a centrifugation at 9,000 G for 1 min. To avoid traces of buffer, a 9,000 G centrifugation for 2 min and a 3 min incubation of the tube with the lid open were done. RNA was eluted incubating the column with 30 µL of RNAse-free water and centrifuging it at 9,000 G for 2 min in a new 1.5 mL tube.

5.2. RNA reverse transcription (RT-PCR)

1 μg of RNA was retrotranscribed to cDNA with the High-Capacity cDNA reverse transcription kit (Applied Biosystems, 4368814). 1 μg of RNA diluted in 14.2 μL of RNAse-free H_2O was prepared in 0.2 mL PCR tubes. Then, 5.8 μL of the reaction mix were added and the PCR was run with (mix volumes and PCR conditions at **Table 11)**. cDNA could be stored at 4ºC for weeks or at -20ºC long-term.

Table 11. RT-PCR mix and cycling conditions.

Components	μL /reaction
Buffer x10	2
dNTPs x25	0.8
Random primers x10	2
Reverse Transcriptase	1

Cycles	Temperature (ºC)	Incubation (min)
Annealing	25	10
Reverse transcription	37	120
Inactivation	85	5
Cooling/ storage	4	Forever

5.3. Real time PCR (qRT-PCR)

A cDNA mix was prepared diluting the retrotranscribed samples 1/20 with DNAse free H_2O. In parallel, reaction mixes for each gen of interest or house-keeping gene (HK, unaltered by the treatments used) (**Table 12**) was prepared following the recipe of SYBRGreen-based technology GoTaq® qPCR master-mix (Promega, A600A) (**Table 13)**. Each condition was run in triplicates. In a 96-wellplate support, required 0.2 mL-tube 8-well strips (Thermo Scientific, AB-1770) were placed. 2 µL of cDNA mix were added (visualizing and controlling a proper well loading), followed by the addition of 10.5 µL of the reaction mix. When charged all the tubes, they were covered with strip caps and a spin centrifuge was done with the adapted rotor for 8-strips. qRT-PCR was run using LightCycler 96® (Roche) following the PCR conditions (**Table 13**).

Table 12. Primers used for qRT-PCR.

Gene	Species	primer	Sequence 5'-3'	Origin
36B4 (House-keeping)	Human	Forward	CAGCAAGTGGGAAGGTGTAATCC	(*433*)
		Reverse	CCCATTCTATCATCAACGGGTACAA	
CHOP (Ddit3)	Human	Forward	CAGCAAGTGGGAAGGTGTAATCC	Previously designed and validated in the lab
		Reverse	CCCATTCTATCATCAACGGGTACAA	
XBP1s	Human	Forward	GGTCTGCTGAGTCCGCAGCAGG	
		Reverse	AGTTCATTAATGGCTTCCAGCT	

Table 13. qRT-PCR mix and cycling conditions.

Components	µL/ reaction
Master Mix	6.25
Forward primer (10mM)	1
Reverse primer (10mM)	1
DNAse free H_2O	4.25

Cycles	Temperature (ºC)	Incubation (s)	cycles
Initial denaturation	95	600	1
Denaturation	95	30	40
Annealing	60	15	
Elongation	72	30	
Melting curves	95	10	1
	65	60	
	97	1	

5.4. Analysis

Analysis of gene expression was performed using the $\Delta\Delta C_t$ method (*434*). Briefly, the cycle at which SYBRGreen fluorescence exceeds the threshold (C_t) was exported from LightCycler 96® software. ΔC_t were obtained subtracting the Ct value of the HK to the value of the gene of interest in each condition. All the conditions were relativized to a CTL condition by subtracting the ΔC_t of the control condition to the ΔC_t value of the experimental condition, obtaining the $\Delta\Delta C_t$. $\Delta\Delta C_t$ represents the negative increment of cycles in which the gene of interest (corrected by HK) is expressed compared to the control condition. Therefore, fold increase value in gene expression of each condition was obtained as: fold increase= $2^{-\Delta\Delta Ct}$

6. Flow cytometry

Flow cytometry was used to analyse either **reactive oxygen species (ROS) and cell death** or **LD and lipid content** using a 90%-confluent well of 12 well plate per condition.

6.1. Lipotoxicity: ROS and cell death

This protocol was adapted to measure reactive oxygen species (ROS) production with H_2DCF-DA (DCF, Invitrogen, D-399) and cell death with propidium Iodide (PI, Sigma, P4864) simultaneously. Correct separation of early and late apoptotic cells from alive cells was assured by also using the APC-Annexin V staining (1:20, BD Pharmingen, 550474) (**Fig.3**). Once optimized, PI and DCF were used without Annexin V staining because it did not apported additional information.

Cultured cells were stained with 15 µM DCF (0.15 µL of DCF with 5 µL of fresh media and directly added to the well from the 100 mM stock in DMSO at -20ºC). Plates were incubated 30 min with the dye inside the incubator. All the steps were performed with the lights of the gas hood off.

Cells were then detached from the well by a trypsinization step as follows: 0.5 mL of media from the cell was collected by pipetting (most of death cells are present). Attached cells were washed with 0.25 mL PBS, incubated with 0.25 mL of trypsin, neutralized with 0.5 mL of fresh media, and collecting all the solutions of each step. For C2C12 and AML12 cell lines, an additional up and down pipetting step was performed while in trypsin to avoid cell clump formation. 1.5 mL final volume of all the cells was pelleted with a centrifugation at 800 G for 5 min at RT. Cells were washed with PBS and resuspended by pipetting up and down with 200 µL PBS with PI (1/10,000 in PBS from a 1 mg/mL). Cells were immediately analysed with the cell cytometer.

To ensure that the signal measured was specific, the following controls were used:

-Autofluorescence: cells without staining to measure basal signal detection from the cells.

-Unstimulated stained cells: Untreated cells to measure basal fluorescence emission of each dye.

-Stimulated stained cells: treated cells to ensure an increase in cell dye brightness from unstained cells (signal shift). PA (>200 µg/mL) or 100 µM Rotenone (stock at 10 mM in DMSO at -20ºC, Sigma, R8875) for cell death; and 50 µM Rotenone for ROS measurement.

Data was collected in the FACS Facility of IDIBAPS using a FACSCanto™ 2L (BD Biosciences). A 488 laser was used as a light source and emitted light was detected with FSC and SSC, FITC (230/330), PE (585/42), and PerCP (670 LP) emission filters. Data was collected using the FACSDiva™ software (BD Biosciences) at 500-1000 cell/events per second with a minimum of 10,000 events. Data was analysed and represented using FlowJo™ software (BD Biosciences).

Single cells were isolated first separating them from cell debris (**Fig. 3A)** and then from cell clumps (**Fig. 3B**). Cells inside these gates were considered as events. For cell death calculation, early and late apoptotic cells were separated from living cells and represented as a percentage. Early (AnxV and slight IP positive) and late (AnxV and IP positive) apoptotic cells could be gate-separated from alive cells since they are stained with IP and unstained with DCF (**Fig. 3C**). ROS was measured using the mean intensity detected by FITC of alive cells (**Fig. 3C**).

6.2. Lipid and LD Content

Using Nile Red, both lipids, esterified into LDs and non-esterified lipids, were analysed.

Cells were detached by trypsinization as in the previous section without collecting medium nor PBS washes (only attached cells were analysed). Pelleted cells were fixed by resuspending them with 0.2 mL of 4% Paraformaldehyde (PFA, Electron Microscope systems, 15710) for 1 h at RT and washed with PBS. At this point, cells could be stored for few days at 4ºC or directly resuspended with Nile Red (5 µg/mL from the 2.5 mg/mL stock in DMSO at -20ºC, Sigma, N3013), incubated for 30 min, and analysed with cell cytometer.

The same negative controls as for lipotoxicity assays were used, but OA (>100 µg/mL) was used to stimulate the stained cells as a positive control.

The data of individual cells was collected and gated the same way as the previous experiment (**Fig. 3A and B**), but green, orange, and red emitted lights were separately detected by FITC, PE, and PerCP FACS filters respectively and separately analysed. Thus, due to the properties of Nile-red (*374*), it emits light of different wavelength depending on how hydrophobic the environment is (solvatochromism). Therefore, while global lipid accumulation was well detected with orange fluorescence as in previous studies (*345, 375*), neutral lipids (mainly hydrophobic TAGs inside LDs) were detected with the green light and polar lipids (less hydrophobic lipids outside LDs) with the red light.

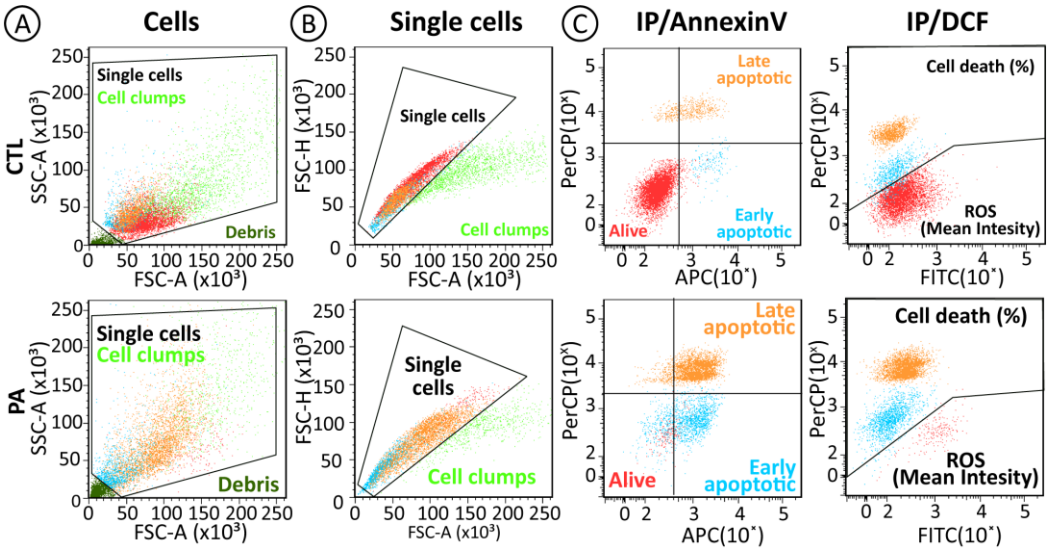

Figure 3. Gates and cell populations analysed by FACS.
(**A**) Cell separation gates, (**B**) Single cell separation gate, and (**C**) Cell death and alive cell separation gates confirmed with Annexin V (AnxV) staining. CTL and PA-treated conditions are used as an example to compare the differential staining of the cells.

7. Cell imaging

7.1. Immunocitofluorescence

Cells grown in a coverslip (usually placed inside a 35 mm plate which is used for other experiments) were fixed with 4% PFA for 1h after a PBS wash. They were afterwards permeabilized with 0.1% saponin (0.01 g in 10 mL PBS, Sigma, S4521) for 10 min and blocked with 1% BSA for 10 min. Primary antibody was incubated for 1 h (**Table 14**), and then secondary antibody (against appropriate specie and conjugated with 488-,555-,568- or 647-alexa fluor, Invitrogen) for 45 min both diluted in blocking solution (0.1% BSA and 0.02% saponin). After all the steps 3 PBS washes were performed. Coverslips were mounted with 4 µL of Mowiol mounting media (Calbiochem, 475904) after rinse with miliQ H_2O. Cell dyes (**Table 15**) were incubated with the secondary antibody solution or directly diluted in Mowiol mounting media.

Table 14. Primary Antibodies used for immunofluorescence.

Target protein	Manufacturer (reference)	Species	Final dilution
VAP-A	Abcam (ab181067)	Rabbit	1/40
TGN46	Biorad (AHP500GT)	Sheep	1/300
GM130	BD Biosciences (810822)	Mouse	1/300
Plin3	Progen (GP32)	Guinea pig	1/700
Myc-tag	Abcam (ab32)	Mouse	1/50
Calnexin	BD Biosciences (610523)	Mouse	1/50
CAV1	BD Biosciences (610060)	Rabbit	1/100

Table 15. Cell dyes used for immunofluorescence. Mow, mowiol.

Cell dye	Manufacturer (reference)	Stock (storage)	Staining (mechanism of action)	Dilution	Excitation/ Emission (nm)
Nile-Red	Sigma (N3013)	in acetone at -20ºC	LDs (neutral lipid staining)	1/5,000 in Mow	552/636
Alexa fluor® 350 phalloidin	Invitrogen (A22281)	in ethanol at -20ºC	Cell membrane (cortical actin staining)	1/10 in blocking solution	346/442

7.1.1. Epifluorescence and confocal microscopy

Images were taken with Leica AF600 microscope (Leica Microsystems, Manheim, Germany) or Zeiss Axiovert 200 Upright Microscope Stand (Zeiss, Oberkochen, Germany) with LSM 710 Meta Confocal Scanner using the x63 oil immersion objective lens. Images were analysed using ImageJ (NIH).

7.1.2. Time-lapse microscopy

Transfected cells with CHX were visualized using Zeiss Anxiovert 200 confocal microscope equipped with an incubation control system (37ºC, 5% CO2). Once settings were adjusted, CHX was washout and images from 20 fields per condition were captured every 2 min for 3 h using the x63 oil immersion objective lens. Movies were digitally treated with Zen blue software (Zeiss, version 3.3) and ImageJ.

7.2. Electron microscopy

These experiments were performed by our collaborators at the group of Dr Rob Parton in the Institute for molecular Bioscience (University of Queensland, Brisbane, Australia) and as previously described (*173, 375, 435*).

For visualizing transfected cells, GFP-CAV1 and a plasmid consisting of APEX (modified soybean ascorbate peroxidase) fused to a GFP-binding peptide (APEX-GBP) were cotransfected using lipofectamine 2000 in COS1 cells using a 1:1 ratio. At 24 h of expression, cells were fixed in 2.5% glutaraldehyde and washed with 0.1 M sodium cacodylate. GFP-CAV1 localization, where APEX-GBP was bound, was stained by the incubation of DAB in the presence of H_2O_2 for 30 min at RT inducing the formation of a brown precipitate. The samples were then washed with sodium cacodylate buffer, fixed in 1% osmium tetroxide, washed another time, and dehydrated by the serial incubation with solutions containing increasing ethanol concentrations.

Isolated liver and muscle samples were cut in approximately 0.25 cm^3 pieces on a 35 mm plate with two scalpels, fixed on 2.5% glutaraldehyde for 8 h, washed 2 times in PBS and postfixed in 2% OsO4 with 1.5% potassium ferricyanide. Samples were then stained with 1% uranyl acetate and with a lead aspirate solution (20 mM lead nitrate, 30 mM aspartic acid, pH 5.5). After an acetone serial dehydration, samples were infiltrated with durcupan resin and polymerised.

Ultrathin sections of the samples cut on a ultramicrotome were imaged using a Hitachi 7700 (Tokyo, Japan) at 80 kV.

8. Lipid and metabolic assays

8.1. ACC and de novo lipogenesis activity

To ensure TOFA inhibition of ACC activity and the subsequent DNL, the accumulation of radioactively labelled ^{14}C- acetate into the lipidic fraction of the cells was checked. ^{14}C-Acetate is transformed to labelled ^{14}C-Acetyl-CoA, which in turn is the substrate of ACC. When ACC is functional, malonyl-CoA is formed from acetyl-CoA, and it undergoes FA synthase (FAS) cycle and the synthesis of TAGs which are incorporated into LDs (*165*).

Cells seeded in 12 well plates were pre-treated with or without OA and PA (100 µg/mL+100 µg/mL) and with or without TOFA (100 µM) for 2 h. 1 µL of ^{14}C-Acetate (1µCI from 1 mCI stock dissolved in ethanol, PerkinElmer, NEC084H001mC) was then added to each well. Lipids were extracted using Bligh and Dyer method (see section 8.3) and radioactivity of lipid fraction was measured (see section 8.5). The CPM value of each fraction was relativized to control condition and expressed as a fold increase.

8.2. Lipid extraction

Lipid fraction from cells was extracted using Bligh and Dyer method (*430*).

Cells from 35 mm plates (for TLC) or 12 well plates (for acetate incorporation assays) were washed with PBS, trypsinized, collected with cell medium, and pelleted with a centrifugation at 800 G for 4 min. Cells were resuspended with 50 µL of PBS and pipetted up and down to avoid cell clumping in the following steps. Methanol:Chloroform (1:2 volume ratio) was added to dissolve lipids and mixed by pipetting up and down. 250 µL of chloroform and 250 µL of miliQH_2O were added to form aqueous phase to separate non-lipid components of the cells (e.g., proteins and RNA). After a 10 s vortex to properly mix all the components, lipid and aqueous phases were separated by a centrifugation at 1,700 G for 5 min.

After aspiring part of the upper aqueous face, the organic fraction was pipetted from the bottom of the tube without altering the aqueous phase.

8.3. Thin-layer chromatography (TLC)

Lipid fractions were run in a TLC to analyse the lipid intermediates on the FA esterification into TAGs.

Organic phase was evaporated using nitrogen gas inside the fume hood. In parallel, lysates which followed the same treatment and obtained from a 35 mm plate, were quantified using Bradford method. Once evaporated, each lipid fraction was resuspended with 30 µL of chloroform and cautiously loaded in TLC Silica gel plates (Merck, 1.05553.0001; 7 cm height, 1 cm between sample or borders and charged 1.5 cm from bottom), according to their protein content. After drying the plate, it was run with a mobile phase containing hexane, diethyl ether, and acetic acid (70:30:1 volume ratio in 50.5 mL) inside a capped glass cuvette into the fume hood. Lipid migration through the plate was stopped when it reached 75% of the plate and let dry inside the hood.

Results were obtained after developing the TLCs either with iodine vapours or by the soaking of them in phosphomolybdic acid solution (2 g phosphomolybdic acid/40 mL ethanol/2 mL H_2SO_4) 1 min with manual agitation and heating the plate at 100ºC for up to 5 min. Images were analysed using the gel analyser macro from Fiji/ImageJ and represented as a fold increase related to a control condition.

8.4. Isolated hepatocytes

The primary culture of hepatocytes was obtained as previously described (*100*) by Montserrat Marí in collaboration with cell death and proliferation department from Institute of Biomedical Research of Barcelona (IIBB-CSIC). They were plated in 12-well plates with coverslips.

8.4.1. LD content, ROS production and viability

Since hepatocytes were attached to the plate surface using a collagen coating, alternative methods to the FACS analysis, which requires the resuspension of the cells, were used to analyse lipid content and lipotoxicity.

Hepatocytes were incubated in lipid loading conditions using a dose-response of PA (from 0 µg/mL to 500 µg/mL). The respective treatments of TOFA (100 µM), firsocostat (50 µM), and GSH were added at the same time as PA.

At 4 h of incubation, cells were stained with the ROS marker DCF as described in section 6.1. Then, ROS production was recorded in a fluorometer with excitation at 380 nm and emission at 460 nm. The values were relativized to the control condition.

The coverslips were collected at 8h of incubation, stained with Nile red (section 7.1 and **Table 15**), and visualized by the fluorescence microscope (section 7.1.1).

A colorimetric MTT assay was then performed to measure cell survival after 24 h of incubation. At this timepoint, 100 µl of MTT solution (5 mg/ml diluted in PBS) were added and incubated in the dark inside a CO_2 incubator for 2 h. The medium was then removed, and the Formazan crystals formed were dissolved with 500 µl of isopropanol and transfered into 96 well plate. A multiwell scanner was used to measure the absorbance at 570–630 nm dual wavelengths. The untreated controls were assigned a value of 100%.

8.4.2. Fatty acid oxidation (FAO)

Conversion of radioactive-labelled FA into CO_2 or FA oxidation intermediates (acid-soluble products, ASP) were chased in lipid loading conditions.

First of all, concentrated stocks of radioactively labelled ^{14}C-OA and ^{14}C-PA were prepared at 10 µCi/mL and 2.5 mM FA to facilitate their addition to the experiments. 500µL of radioactive OA (50 µCi) (NEC317050UC, PerkinElmer) or PA (NEC075H050UC, PerkinElmer) were evaporated ON at 37ºC. Non-radioactive OA (70.62µL of 177mM OA stock) or PA (125 µL of 100 mM PA stock) were added. BSA conjugation was performed adding 5 mL of FA-free BSA at 2.7% solution (0.138 g of BSA in 0.9% NaCl) to obtain a 6:1 FA:BSA ratio. Aliquots were stored at -20ºC. Radioactive stock was diluted 1/10 with medium to be used at 1 µCi and 70.6 µg/mL (radioactive FA concentration is considered negligible). If additional concentration of FA was required, it was added from non-radioactive diluted stock.

FAO was measured in triplicates. Cells were only seeded in the 3 wells at both ends of a 12 well plate (**Fig. 4A**): at one end the first condition to be analysed (C1) with each triplicate (C1.1, C1.2 and C1.3) and at the other end the second condition (C2) with the same disposition. The 6 wells in the middle of the plate were left only with medium to be used as diffusion controls (d1-d6, **Fig. 4A**).

Cells were incubated 8 h with ^{14}C-OA and ^{14}C-PA as pretreatment: both ^{14}C-OA and ^{14}C-PA were diluted 1/10 (1 µCi/mL, 70.62 µg/mL) and brought to 300 µL of 100 µg/mL OA + 100 µg/mL PA with non-radioactive OA and PA. After that, CO_2 chasing was performed for 16 h with or without TOFA (100 µM). Reaction was stopped by the addition of perchloric acid and samples were collected 24 h after.

CO_2 was measured using a sealed parafilm chamber to avoid diffusion between cells. CO_2 liberated after FAO was captured in a Whatman filter paper piece placed at the top of each well (**Fig. 4B**). Parafilm chamber was mounted after treatment addition, by sealing the uncovered well plate with parafilm (**Fig. 4BI**). To properly seal it, parafilm was first mounted on the rectangular margins of the plate and then fixed on each well using the fingertips: starting from the circular side and continuing with the upper part of the well (**Fig. 4BII**). Once covered and using a scalpel, two ~0.5 cm incisions were performed at the centre of each well forming a cross (**Fig. 4BIII**) and pulling down the four resulting triangular sections to allow CO_2 exchange (**Fig. 4BIV**). One Whatman filter paper piece (0.75x0.75 cm) was placed upper fully covering the resulting 0.5 cm^2 opening and soaked with 75 µL of 0.1 M KOH (**Fig. 4BV**). CO_2 was retained in the paper in form of CO_3K_2 precipitate after reacting with KOH. It all was covered with another parafilm layer mounted with the same procedure, covered with the plate (**Fig. 4BVI**), and left for the incubation time.

Once FAO reaction time finished, 75 µL of perchloric acid were injected into the well crossing the parafilm layers using a syringe with a 30 G (**VII**). That way, all the cells were lysed, metabolic reactions were stopped, and all the produced CO_2 liberated from the media. Once injected, another layer of parafilm was added to avoid leakage of CO_2 during the next 24 h incubation (**Fig. 4BVIII**).

Finally, all the Whatman filter papers were collected disassembling the parafilm chamber. For measuring the amount of substrate (^{14}C-OA and ^{14}C-PA) partially oxidized to ASP (such as acyl-carnitine, carboxylic acid cycle intermediates, Acetyl-CoA, or ketonic bodies (*380*)), the media after 24 h perchloric acid incubation was collected. To isolate ASP from FAs and other cell products remaining in the media (which precipitate), the sample was centrifuged at 2,500 G for 5 min, and the supernatant collected. When measuring the radioactive CO_2, diffusion control counts should be negligible, unless sealing of parafilm was not properly achieved. In that case there would be a CO_2 leakage invalidating the experiment. The CPM value of each fraction was relativized to control condition and expressed as a fold increase.

8.5. Radioactivity measure

Whatman filter paper pieces (FAO assay), ASP (FAO assay) or lipid fractions (Acetate incorporation assay) were added to vials containing 5 mL scintillation liquid to measure its radioactivity. Then, 5 s vortex at maximum potency was applied to all the vials and radioactivity was measured for 5 min using the liquid scintillation counter (Wallac, 1409).

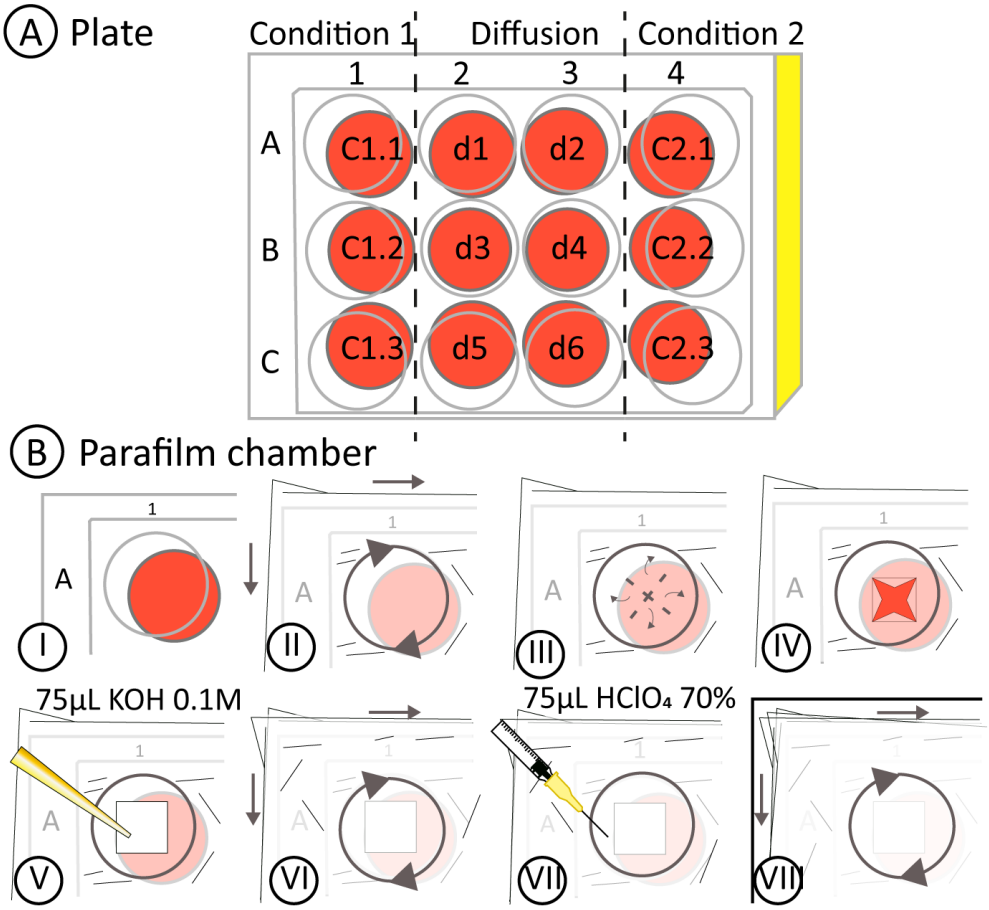

Figure 4. Fatty acid oxidation assay.
A) Experimental conditions and diffusion controls disposition in a 12 well plate. B) Stepwise assembly of CO_2 parafilm trap: first layer of parafilm addition (I-II), parafilm cutting (III-IV), KOH addition (V), second layer of parafilm addition (VI), perchloric addition to stop reaction (VII) and closing of the plate (VIII).

9. Data collection, statistical analysis and presentation

All the measured raw data was collected individually and then fused with all the replicates in Microsoft Excel files (365 version, Microsoft Office). It was statistically analysed and represented in graphs using Prism (version 7, GraphPad). How data is represented, the statistical tests performed for each graph, and the number of independent experiments realized (n) are indicated in the figure caption. Results and graphs were presented in figures using Illustrator 2021 (Adobe, v25.1.0.90) or presentations using Power Point (365 version, Microsoft Office). All the texts were written and mounted using Word (365 version, Microsoft Office.

REFERENCES

1. P. GE, Fine structure of blood capillaries. *J Appl Phys*, 24:1424 (1953).
2. E. Yamada, The fine structure of the gall bladder epithelium of the mouse. *J Biophys Biochem Cytol* **1**, 445-458 (1955).
3. R. G. Parton, Caveolae: Structure, Function, and Relationship to Disease. *Annu Rev Cell Dev Biol* **34**, 111-136 (2018).
4. H. Thorn *et al.*, Cell surface orifices of caveolae and localization of caveolin to the necks of caveolae in adipocytes. *Mol Biol Cell* **14**, 3967-3976 (2003).
5. N. Ariotti, R. G. Parton, SnapShot: caveolae, caveolins, and cavins. *Cell* **154**, 704-704 e701 (2013).
6. T. V. Kurzchalia *et al.*, VIP21, a 21-kD membrane protein is an integral component of trans-Golgi-network-derived transport vesicles. *J Cell Biol* **118**, 1003-1014 (1992).
7. K. G. Rothberg *et al.*, Caveolin, a protein component of caveolae membrane coats. *Cell* **68**, 673-682 (1992).
8. A. M. Fra, E. Williamson, K. Simons, R. G. Parton, De novo formation of caveolae in lymphocytes by expression of VIP21-caveolin. *Proc Natl Acad Sci U S A* **92**, 8655-8659 (1995).
9. S. Monier *et al.*, VIP21-caveolin, a membrane protein constituent of the caveolar coat, oligomerizes in vivo and in vitro. *Mol Biol Cell* **6**, 911-927 (1995).
10. M. Murata *et al.*, VIP21/caveolin is a cholesterol-binding protein. *Proc Natl Acad Sci U S A* **92**, 10339-10343 (1995).
11. A. Pol *et al.*, Cholesterol and fatty acids regulate dynamic caveolin trafficking through the Golgi complex and between the cell surface and lipid bodies. *Mol Biol Cell* **16**, 2091-2105 (2005).
12. A. Bist, P. E. Fielding, C. J. Fielding, Two sterol regulatory element-like sequences mediate up-regulation of caveolin gene transcription in response to low density lipoprotein free cholesterol. *Proc Natl Acad Sci U S A* **94**, 10693-10698 (1997).
13. P. E. Scherer *et al.*, Caveolin isoforms differ in their N-terminal protein sequence and subcellular distribution. Identification and epitope mapping of an isoform-specific monoclonal antibody probe. *J Biol Chem* **270**, 16395-16401 (1995).
14. T. Fujimoto, H. Kogo, R. Nomura, T. Une, Isoforms of caveolin-1 and caveolar structure. *J Cell Sci* **113 Pt 19**, 3509-3517 (2000).
15. P. E. Scherer *et al.*, Identification, sequence, and expression of caveolin-2 defines a caveolin gene family. *Proc Natl Acad Sci U S A* **93**, 131-135 (1996).
16. M. Way, R. G. Parton, M-caveolin, a muscle-specific caveolin-related protein. *FEBS Lett* **378**, 108-112 (1996).
17. J. A. Engelman, X. L. Zhang, M. P. Lisanti, Sequence and detailed organization of the human caveolin-1 and -2 genes located near the D7S522 locus (7q31.1). Methylation of a CpG island in the 5' promoter region of the caveolin-1 gene in human breast cancer cell lines. *FEBS Lett* **448**, 221-230 (1999).
18. I. Parolini *et al.*, Expression of caveolin-1 is required for the transport of caveolin-2 to the plasma membrane. Retention of caveolin-2 at the level of the golgi complex. *J Biol Chem* **274**, 25718-25725 (1999).
19. C. Minetti *et al.*, Mutations in the caveolin-3 gene cause autosomal dominant limb-girdle muscular dystrophy. *Nat Genet* **18**, 365-368 (1998).
20. C. Minetti *et al.*, Impairment of caveolae formation and T-system disorganization in human muscular dystrophy with caveolin-3 deficiency. *Am J Pathol* **160**, 265-270 (2002).
21. R. G. Parton, M. Way, N. Zorzi, E. Stang, Caveolin-3 associates with developing T-tubules during muscle differentiation. *J Cell Biol* **136**, 137-154 (1997).
22. O. Kovtun, V. A. Tillu, N. Ariotti, R. G. Parton, B. M. Collins, Cavin family proteins and the assembly of caveolae. *J Cell Sci* **128**, 1269-1278 (2015).
23. Y. Gambin *et al.*, Single-molecule analysis reveals self assembly and nanoscale segregation of two distinct cavin subcomplexes on caveolae. *Elife* **3**, e01434 (2013).
24. M. M. Hill *et al.*, PTRF-Cavin, a conserved cytoplasmic protein required for caveola formation and function. *Cell* **132**, 113-124 (2008).

25. C. G. Hansen, E. Shvets, G. Howard, K. Riento, B. J. Nichols, Deletion of cavin genes reveals tissue-specific mechanisms for morphogenesis of endothelial caveolae. *Nat Commun* **4**, 1831 (2013).
26. J. Mohan, B. Moren, E. Larsson, M. R. Holst, R. Lundmark, Cavin3 interacts with cavin1 and caveolin1 to increase surface dynamics of caveolae. *J Cell Sci* **128**, 979-991 (2015).
27. M. Bastiani *et al.*, MURC/Cavin-4 and cavin family members form tissue-specific caveolar complexes. *J Cell Biol* **185**, 1259-1273 (2009).
28. T. Yamaguchi *et al.*, ROR1 sustains caveolae and survival signalling as a scaffold of cavin-1 and caveolin-1. *Nat Commun* **7**, 10060 (2016).
29. I. Yeow *et al.*, EHD Proteins Cooperate to Generate Caveolar Clusters and to Maintain Caveolae during Repeated Mechanical Stress. *Curr Biol* **27**, 2951-2962 e2955 (2017).
30. E. Seemann *et al.*, Deciphering caveolar functions by syndapin III KO-mediated impairment of caveolar invagination. *Elife* **6**, (2017).
31. Y. Senju, Y. Itoh, K. Takano, S. Hamada, S. Suetsugu, Essential role of PACSIN2/syndapin-II in caveolae membrane sculpting. *J Cell Sci* **124**, 2032-2040 (2011).
32. U. Ortegren *et al.*, Lipids and glycosphingolipids in caveolae and surrounding plasma membrane of primary rat adipocytes. *Eur J Biochem* **271**, 2028-2036 (2004).
33. Y. Zhou *et al.*, Caveolin-1 and cavin1 act synergistically to generate a unique lipid environment in caveolae. *J Cell Biol* **220**, (2021).
34. M. R. Breen, M. Camps, F. Carvalho-Simoes, A. Zorzano, P. F. Pilch, Cholesterol depletion in adipocytes causes caveolae collapse concomitant with proteosomal degradation of cavin-2 in a switch-like fashion. *PLoS One* **7**, e34516 (2012).
35. R. G. Parton, B. M. Collins, Unraveling the architecture of caveolae. *Proc Natl Acad Sci U S A* **113**, 14170-14172 (2016).
36. R. G. Parton, K. A. McMahon, Y. Wu, Caveolae: Formation, dynamics, and function. *Curr Opin Cell Biol* **65**, 8-16 (2020).
37. C. Matthaeus, J. W. Taraska, Energy and Dynamics of Caveolae Trafficking. *Front Cell Dev Biol* **8**, 614472 (2020).
38. F. Galbiati *et al.*, Caveolin-3 null mice show a loss of caveolae, changes in the microdomain distribution of the dystrophin-glycoprotein complex, and t-tubule abnormalities. *J Biol Chem* **276**, 21425-21433 (2001).
39. L. Pelkmans, A. Helenius, Endocytosis via caveolae. *Traffic* **3**, 311-320 (2002).
40. E. M. Damm *et al.*, Clathrin- and caveolin-1-independent endocytosis: entry of simian virus 40 into cells devoid of caveolae. *J Cell Biol* **168**, 477-488 (2005).
41. R. G. Parton *et al.*, Caveolae: The FAQs. *Traffic* **21**, 181-185 (2020).
42. C. Fernandez-Hernando *et al.*, Genetic evidence supporting a critical role of endothelial caveolin-1 during the progression of atherosclerosis. *Cell Metab* **10**, 48-54 (2009).
43. P. G. Frank, S. Pavlides, M. P. Lisanti, Caveolae and transcytosis in endothelial cells: role in atherosclerosis. *Cell Tissue Res* **335**, 41-47 (2009).
44. H. Ju, R. Zou, V. J. Venema, R. C. Venema, Direct interaction of endothelial nitric-oxide synthase and caveolin-1 inhibits synthase activity. *J Biol Chem* **272**, 18522-18525 (1997).
45. R. H. Kretsinger, C. E. Nockolds, Carp muscle calcium-binding protein. II. Structure determination and general description. *J Biol Chem* **248**, 3313-3326 (1973).
46. X. Lian, C. Matthaeus, M. Kassmann, O. Daumke, M. Gollasch, Pathophysiological Role of Caveolae in Hypertension. *Front Med (Lausanne)* **6**, 153 (2019).
47. K. V. Kandror, J. M. Stephens, P. F. Pilch, Expression and compartmentalization of caveolin in adipose cells: coordinate regulation with and structural segregation from GLUT4. *J Cell Biol* **129**, 999-1006 (1995).
48. B. Razani *et al.*, Caveolin-1-deficient mice are lean, resistant to diet-induced obesity, and show hypertriglyceridemia with adipocyte abnormalities. *J Biol Chem* **277**, 8635-8647 (2002).
49. Y. K. Hayashi *et al.*, Human PTRF mutations cause secondary deficiency of caveolins resulting in muscular dystrophy with generalized lipodystrophy. *J Clin Invest* **119**, 2623-2633 (2009).

50. A. Ring, S. Le Lay, J. Pohl, P. Verkade, W. Stremmel, Caveolin-1 is required for fatty acid translocase (FAT/CD36) localization and function at the plasma membrane of mouse embryonic fibroblasts. *Biochim Biophys Acta* **1761**, 416-423 (2006).
51. D. Haddad, A. Al Madhoun, R. Nizam, F. Al-Mulla, Role of Caveolin-1 in Diabetes and Its Complications. *Oxid Med Cell Longev* **2020**, 9761539 (2020).
52. E. Gonzalez-Munoz *et al.*, Caveolin-1 loss of function accelerates glucose transporter 4 and insulin receptor degradation in 3T3-L1 adipocytes. *Endocrinology* **150**, 3493-3502 (2009).
53. A. W. Cohen *et al.*, Caveolin-1-deficient mice show insulin resistance and defective insulin receptor protein expression in adipose tissue. *Am J Physiol Cell Physiol* **285**, C222-235 (2003).
54. A. M. Zimnicka *et al.*, Src-dependent phosphorylation of caveolin-1 Tyr-14 promotes swelling and release of caveolae. *Mol Biol Cell* **27**, 2090-2106 (2016).
55. J. Gustavsson *et al.*, Localization of the insulin receptor in caveolae of adipocyte plasma membrane. *FASEB J* **13**, 1961-1971 (1999).
56. F. H. Nystrom, H. Chen, L. N. Cong, Y. Li, M. J. Quon, Caveolin-1 interacts with the insulin receptor and can differentially modulate insulin signaling in transfected Cos-7 cells and rat adipose cells. *Mol Endocrinol* **13**, 2013-2024 (1999).
57. A. K. Nevins, D. C. Thurmond, Caveolin-1 functions as a novel Cdc42 guanine nucleotide dissociation inhibitor in pancreatic beta-cells. *J Biol Chem* **281**, 18961-18972 (2006).
58. S. Li, R. Seitz, M. P. Lisanti, Phosphorylation of caveolin by src tyrosine kinases. The alpha-isoform of caveolin is selectively phosphorylated by v-Src in vivo. *J Biol Chem* **271**, 3863-3868 (1996).
59. E. M. Kepner *et al.*, Cool-1/betaPIX functions as a guanine nucleotide exchange factor in the cycling of Cdc42 to regulate insulin secretion. *Am J Physiol Endocrinol Metab* **301**, E1072-1080 (2011).
60. S. Daniel, M. Noda, R. A. Cerione, G. W. Sharp, A link between Cdc42 and syntaxin is involved in mastoparan-stimulated insulin release. *Biochemistry* **41**, 9663-9671 (2002).
61. B. Sinha *et al.*, Cells respond to mechanical stress by rapid disassembly of caveolae. *Cell* **144**, 402-413 (2011).
62. P. Jansa, S. W. Mason, U. Hoffmann-Rohrer, I. Grummt, Cloning and functional characterization of PTRF, a novel protein which induces dissociation of paused ternary transcription complexes. *EMBO J* **17**, 2855-2864 (1998).
63. K. A. McMahon *et al.*, Identification of intracellular cavin target proteins reveals cavin-PP1alpha interactions regulate apoptosis. *Nat Commun* **10**, 3279 (2019).
64. S. Torrino *et al.*, EHD2 is a mechanotransducer connecting caveolae dynamics with gene transcription. *J Cell Biol* **217**, 4092-4105 (2018).
65. J. H. R. Hetmanski *et al.*, Membrane Tension Orchestrates Rear Retraction in Matrix-Directed Cell Migration. *Dev Cell* **51**, 460-475 e410 (2019).
66. D. Volonte, F. Galbiati, R. G. Pestell, M. P. Lisanti, Cellular stress induces the tyrosine phosphorylation of caveolin-1 (Tyr(14)) via activation of p38 mitogen-activated protein kinase and c-Src kinase. Evidence for caveolae, the actin cytoskeleton, and focal adhesions as mechanical sensors of osmotic stress. *J Biol Chem* **276**, 8094-8103 (2001).
67. K. A. McMahon *et al.*, SRBC/cavin-3 is a caveolin adapter protein that regulates caveolae function. *EMBO J* **28**, 1001-1015 (2009).
68. M. Corrotte *et al.*, Caveolae internalization repairs wounded cells and muscle fibers. *Elife* **2**, e00926 (2013).
69. M. Dewulf *et al.*, Dystrophy-associated caveolin-3 mutations reveal that caveolae couple IL6/STAT3 signaling with mechanosensing in human muscle cells. *Nat Commun* **10**, 1974 (2019).
70. F. Sotgia *et al.*, Caveolin-3 directly interacts with the C-terminal tail of beta -dystroglycan. Identification of a central WW-like domain within caveolin family members. *J Biol Chem* **275**, 38048-38058 (2000).
71. H. Li, V. Papadopoulos, Peripheral-type benzodiazepine receptor function in cholesterol transport. Identification of a putative cholesterol recognition/interaction amino acid sequence and consensus pattern. *Endocrinology* **139**, 4991-4997 (1998).

72. A. Schlegel, R. B. Schwab, P. E. Scherer, M. P. Lisanti, A role for the caveolin scaffolding domain in mediating the membrane attachment of caveolin-1. The caveolin scaffolding domain is both necessary and sufficient for membrane binding in vitro. *J Biol Chem* **274**, 22660-22667 (1999).
73. M. Bastiani, R. G. Parton, Caveolae at a glance. *J Cell Sci* **123**, 3831-3836 (2010).
74. T. Machleidt, W. P. Li, P. Liu, R. G. Anderson, Multiple domains in caveolin-1 control its intracellular traffic. *J Cell Biol* **148**, 17-28 (2000).
75. A. Hayer, M. Stoeber, C. Bissig, A. Helenius, Biogenesis of caveolae: stepwise assembly of large caveolin and cavin complexes. *Traffic* **11**, 361-382 (2010).
76. N. Nishimura, W. E. Balch, A di-acidic signal required for selective export from the endoplasmic reticulum. *Science* **277**, 556-558 (1997).
77. A. Schlegel, P. Arvan, M. P. Lisanti, Caveolin-1 binding to endoplasmic reticulum membranes and entry into the regulated secretory pathway are regulated by serine phosphorylation. Protein sorting at the level of the endoplasmic reticulum. *J Biol Chem* **276**, 4398-4408 (2001).
78. J. Couet, S. Li, T. Okamoto, T. Ikezu, M. P. Lisanti, Identification of peptide and protein ligands for the caveolin-scaffolding domain. Implications for the interaction of caveolin with caveolae-associated proteins. *J Biol Chem* **272**, 6525-6533 (1997).
79. J. P. Gratton *et al.*, Selective inhibition of tumor microvascular permeability by cavtratin blocks tumor progression in mice. *Cancer Cell* **4**, 31-39 (2003).
80. C. L. Hoop, V. N. Sivanandam, R. Kodali, M. N. Srnec, P. C. van der Wel, Structural characterization of the caveolin scaffolding domain in association with cholesterol-rich membranes. *Biochemistry* **51**, 90-99 (2012).
81. G. Yang, H. Xu, Z. Li, F. Li, Interactions of caveolin-1 scaffolding and intramembrane regions containing a CRAC motif with cholesterol in lipid bilayers. *Biochim Biophys Acta* **1838**, 2588-2599 (2014).
82. A. Schlegel, M. P. Lisanti, A molecular dissection of caveolin-1 membrane attachment and oligomerization. Two separate regions of the caveolin-1 C-terminal domain mediate membrane binding and oligomer/oligomer interactions in vivo. *J Biol Chem* **275**, 21605-21617 (2000).
83. A. G. Ostermeyer, L. T. Ramcharan, Y. Zeng, D. M. Lublin, D. A. Brown, Role of the hydrophobic domain in targeting caveolin-1 to lipid droplets. *J Cell Biol* **164**, 69-78 (2004).
84. B. M. Abell *et al.*, Role of the proline knot motif in oleosin endoplasmic reticulum topology and oil body targeting. *Plant Cell* **9**, 1481-1493 (1997).
85. M. D. Rieth, J. Lee, K. J. Glover, Probing the caveolin-1 P132L mutant: critical insights into its oligomeric behavior and structure. *Biochemistry* **51**, 3911-3918 (2012).
86. D. S. Shah, R. B. Nisr, C. Stretton, G. Krasteva-Christ, H. S. Hundal, Caveolin-3 deficiency associated with the dystrophy P104L mutation impairs skeletal muscle mitochondrial form and function. *J Cachexia Sarcopenia Muscle* **11**, 838-858 (2020).
87. D. J. Dietzen, W. R. Hastings, D. M. Lublin, Caveolin is palmitoylated on multiple cysteine residues. Palmitoylation is not necessary for localization of caveolin to caveolae. *J Biol Chem* **270**, 6838-6842 (1995).
88. S. Monier, D. J. Dietzen, W. R. Hastings, D. M. Lublin, T. V. Kurzchalia, Oligomerization of VIP21-caveolin in vitro is stabilized by long chain fatty acylation or cholesterol. *FEBS Lett* **388**, 143-149 (1996).
89. A. G. Ostermeyer *et al.*, Accumulation of caveolin in the endoplasmic reticulum redirects the protein to lipid storage droplets. *J Cell Biol* **152**, 1071-1078 (2001).
90. C. A. Copeland *et al.*, A disease-associated frameshift mutation in caveolin-1 disrupts caveolae formation and function through introduction of a de novo ER retention signal. *Mol Biol Cell* **28**, 3095-3111 (2017).
91. R. G. Parton, M. Hanzal-Bayer, J. F. Hancock, Biogenesis of caveolae: a structural model for caveolin-induced domain formation. *J Cell Sci* **119**, 787-796 (2006).
92. J. H. Kim *et al.*, A pH-Mediated Topological Switch within the N-Terminal Domain of Human Caveolin-3. *Biophys J* **110**, 2475-2485 (2016).

93. A. Pol, F. Morales-Paytuvi, M. Bosch, R. G. Parton, Non-caveolar caveolins - duties outside the caves. *J Cell Sci* **133**, (2020).
94. B. P. Head, P. A. Insel, Do caveolins regulate cells by actions outside of caveolae? *Trends Cell Biol* **17**, 51-57 (2007).
95. I. M. Khater, Q. Liu, K. C. Chou, G. Hamarneh, I. R. Nabi, Super-resolution modularity analysis shows polyhedral caveolin-1 oligomers combine to form scaffolds and caveolae. *Sci Rep* **9**, 9888 (2019).
96. M. Bosch, M. Mari, S. P. Gross, J. C. Fernandez-Checa, A. Pol, Mitochondrial cholesterol: a connection between caveolin, metabolism, and disease. *Traffic* **12**, 1483-1489 (2011).
97. A. Pol, M. Calvo, C. Enrich, Isolated endosomes from quiescent rat liver contain the signal transduction machinery. Differential distribution of activated Raf-1 and Mek in the endocytic compartment. *FEBS Lett* **441**, 34-38 (1998).
98. M. A. Fernandez *et al.*, Caveolin-1 is essential for liver regeneration. *Science* **313**, 1628-1632 (2006).
99. M. A. Fernandez-Rojo *et al.*, Caveolin-1 is necessary for hepatic oxidative lipid metabolism: evidence for crosstalk between caveolin-1 and bile acid signaling. *Cell Rep* **4**, 238-247 (2013).
100. M. Bosch *et al.*, Caveolin-1 deficiency causes cholesterol-dependent mitochondrial dysfunction and apoptotic susceptibility. *Curr Biol* **21**, 681-686 (2011).
101. A. Sala-Vila *et al.*, Interplay between hepatic mitochondria-associated membranes, lipid metabolism and caveolin-1 in mice. *Sci Rep* **6**, 27351 (2016).
102. E. Trushina, J. Du Charme, J. Parisi, C. T. McMurray, Neurological abnormalities in caveolin-1 knock out mice. *Behav Brain Res* **172**, 24-32 (2006).
103. S. Manes, A. C. Martinez, Cholesterol domains regulate the actin cytoskeleton at the leading edge of moving cells. *Trends Cell Biol* **14**, 275-278 (2004).
104. S. Minguet *et al.*, Caveolin-1-dependent nanoscale organization of the BCR regulates B cell tolerance. *Nat Immunol* **18**, 1150-1159 (2017).
105. F. A. Medina, T. M. Williams, F. Sotgia, H. B. Tanowitz, M. P. Lisanti, A novel role for caveolin-1 in B lymphocyte function and the development of thymus-independent immune responses. *Cell Cycle* **5**, 1865-1871 (2006).
106. T. Tomassian *et al.*, Caveolin-1 orchestrates TCR synaptic polarity, signal specificity, and function in CD8 T cells. *J Immunol* **187**, 2993-3002 (2011).
107. F. A. Medina *et al.*, Caveolin-1-deficient mice show defects in innate immunity and inflammatory immune response during Salmonella enterica serovar Typhimurium infection. *Infect Immun* **74**, 6665-6674 (2006).
108. F. A. Medina *et al.*, Immune dysfunction in caveolin-1 null mice following infection with Trypanosoma cruzi (Tulahuen strain). *Microbes Infect* **9**, 325-333 (2007).
109. H. Lee *et al.*, Caveolin-1 mutations (P132L and null) and the pathogenesis of breast cancer: caveolin-1 (P132L) behaves in a dominant-negative manner and caveolin-1 (-/-) null mice show mammary epithelial cell hyperplasia. *Am J Pathol* **161**, 1357-1369 (2002).
110. N. Patani *et al.*, Non-existence of caveolin-1 gene mutations in human breast cancer. *Breast Cancer Res Treat* **131**, 307-310 (2012).
111. G. Ayala *et al.*, Loss of caveolin-1 in prostate cancer stroma correlates with reduced relapse-free survival and is functionally relevant to tumour progression. *J Pathol* **231**, 77-87 (2013).
112. T. M. Williams *et al.*, Caveolin-1 gene disruption promotes mammary tumorigenesis and dramatically enhances lung metastasis in vivo. Role of Cav-1 in cell invasiveness and matrix metalloproteinase (MMP-2/9) secretion. *J Biol Chem* **279**, 51630-51646 (2004).
113. G. Yang *et al.*, Elevated expression of caveolin is associated with prostate and breast cancer. *Clin Cancer Res* **4**, 1873-1880 (1998).
114. E. Sontag, Protein phosphatase 2A: the Trojan Horse of cellular signaling. *Cell Signal* **13**, 7-16 (2001).
115. F. Sotgia *et al.*, Phenotypic behavior of caveolin-3 R26Q, a mutant associated with hyperCKemia, distal myopathy, and rippling muscle disease. *Am J Physiol Cell Physiol* **285**, C1150-1160 (2003).

116. B. Han *et al.*, Structure and assembly of CAV1 8S complexes revealed by single particle electron microscopy. *Sci Adv* **6**, (2020).
117. A. Tagawa *et al.*, Assembly and trafficking of caveolar domains in the cell: caveolae as stable, cargo-triggered, vesicular transporters. *J Cell Biol* **170**, 769-779 (2005).
118. E. Boucrot, M. T. Howes, T. Kirchhausen, R. G. Parton, Redistribution of caveolae during mitosis. *J Cell Sci* **124**, 1965-1972 (2011).
119. B. Moren *et al.*, EHD2 regulates caveolar dynamics via ATP-driven targeting and oligomerization. *Mol Biol Cell* **23**, 1316-1329 (2012).
120. O. Daumke, G. J. Praefcke, Invited review: Mechanisms of GTP hydrolysis and conformational transitions in the dynamin superfamily. *Biopolymers* **105**, 580-593 (2016).
121. L. Pelkmans, T. Burli, M. Zerial, A. Helenius, Caveolin-stabilized membrane domains as multifunctional transport and sorting devices in endocytic membrane traffic. *Cell* **118**, 767-780 (2004).
122. A. Hayer *et al.*, Caveolin-1 is ubiquitinated and targeted to intralumenal vesicles in endolysosomes for degradation. *The Journal of cell biology* **191**, 615-629 (2010).
123. P. Kirchner, M. Bug, H. Meyer, Ubiquitination of the N-terminal region of caveolin-1 regulates endosomal sorting by the VCP/p97 AAA-ATPase. *J Biol Chem* **288**, 7363-7372 (2013).
124. D. Ritz *et al.*, Endolysosomal sorting of ubiquitylated caveolin-1 is regulated by VCP and UBXD1 and impaired by VCP disease mutations. *Nat Cell Biol* **13**, 1116-1123 (2011).
125. K. Haglund, I. Dikic, The role of ubiquitylation in receptor endocytosis and endosomal sorting. *J Cell Sci* **125**, 265-275 (2012).
126. D. Burana *et al.*, The Ankrd13 Family of Ubiquitin-interacting Motif-bearing Proteins Regulates Valosin-containing Protein/p97 Protein-mediated Lysosomal Trafficking of Caveolin 1. *J Biol Chem* **291**, 6218-6231 (2016).
127. W. E. Balch, R. I. Morimoto, A. Dillin, J. W. Kelly, Adapting proteostasis for disease intervention. *Science* **319**, 916-919 (2008).
128. D. S. Schwarz, M. D. Blower, The endoplasmic reticulum: structure, function and response to cellular signaling. *Cell Mol Life Sci* **73**, 79-94 (2016).
129. L. D. Ly *et al.*, Oxidative stress and calcium dysregulation by palmitate in type 2 diabetes. *Exp Mol Med* **49**, e291 (2017).
130. S. Stefanovic, R. S. Hegde, Identification of a targeting factor for posttranslational membrane protein insertion into the ER. *Cell* **128**, 1147-1159 (2007).
131. W. J. Ou, P. H. Cameron, D. Y. Thomas, J. J. Bergeron, Association of folding intermediates of glycoproteins with calnexin during protein maturation. *Nature* **364**, 771-776 (1993).
132. M. C. Sousa, M. A. Ferrero-Garcia, A. J. Parodi, Recognition of the oligosaccharide and protein moieties of glycoproteins by the UDP-Glc:glycoprotein glucosyltransferase. *Biochemistry* **31**, 97-105 (1992).
133. I. Braakman, J. Helenius, A. Helenius, Role of ATP and disulphide bonds during protein folding in the endoplasmic reticulum. *Nature* **356**, 260-262 (1992).
134. R. Daniels, B. Kurowski, A. E. Johnson, D. N. Hebert, N-linked glycans direct the cotranslational folding pathway of influenza hemagglutinin. *Mol Cell* **11**, 79-90 (2003).
135. A. Herscovics, Structure and function of Class I alpha 1,2-mannosidases involved in glycoprotein synthesis and endoplasmic reticulum quality control. *Biochimie* **83**, 757-762 (2001).
136. A. Heifetz, R. W. Keenan, A. D. Elbein, Mechanism of action of tunicamycin on the UDP-GlcNAc:dolichyl-phosphate Glc-NAc-1-phosphate transferase. *Biochemistry* **18**, 2186-2192 (1979).
137. J. Lytton, M. Westlin, M. R. Hanley, Thapsigargin inhibits the sarcoplasmic or endoplasmic reticulum Ca-ATPase family of calcium pumps. *J Biol Chem* **266**, 17067-17071 (1991).
138. A. Bertolotti, Y. Zhang, L. M. Hendershot, H. P. Harding, D. Ron, Dynamic interaction of BiP and ER stress transducers in the unfolded-protein response. *Nat Cell Biol* **2**, 326-332 (2000).
139. M. Calfon *et al.*, IRE1 couples endoplasmic reticulum load to secretory capacity by processing the XBP-1 mRNA. *Nature* **415**, 92-96 (2002).
140. K. Ameri, A. L. Harris, Activating transcription factor 4. *Int J Biochem Cell Biol* **40**, 14-21 (2008).

141. J. Shen, X. Chen, L. Hendershot, R. Prywes, ER stress regulation of ATF6 localization by dissociation of BiP/GRP78 binding and unmasking of Golgi localization signals. *Dev Cell* **3**, 99-111 (2002).
142. C. Hetz, The unfolded protein response: controlling cell fate decisions under ER stress and beyond. *Nat Rev Mol Cell Biol* **13**, 89-102 (2012).
143. H. P. Harding *et al.*, Regulated translation initiation controls stress-induced gene expression in mammalian cells. *Mol Cell* **6**, 1099-1108 (2000).
144. J. Hollien, J. S. Weissman, Decay of endoplasmic reticulum-localized mRNAs during the unfolded protein response. *Science* **313**, 104-107 (2006).
145. S. W. Tait, D. R. Green, Mitochondria and cell death: outer membrane permeabilization and beyond. *Nat Rev Mol Cell Biol* **11**, 621-632 (2010).
146. K. D. McCullough, J. L. Martindale, L. O. Klotz, T. Y. Aw, N. J. Holbrook, Gadd153 sensitizes cells to endoplasmic reticulum stress by down-regulating Bcl2 and perturbing the cellular redox state. *Mol Cell Biol* **21**, 1249-1259 (2001).
147. M. Wang, R. J. Kaufman, The impact of the endoplasmic reticulum protein-folding environment on cancer development. *Nat Rev Cancer* **14**, 581-597 (2014).
148. S. S. Vembar, J. L. Brodsky, One step at a time: endoplasmic reticulum-associated degradation. *Nat Rev Mol Cell Biol* **9**, 944-957 (2008).
149. M. Dong, J. P. Bridges, K. Apsley, Y. Xu, T. E. Weaver, ERdj4 and ERdj5 are required for endoplasmic reticulum-associated protein degradation of misfolded surfactant protein C. *Mol Biol Cell* **19**, 2620-2630 (2008).
150. A. Schmitz, M. Maintz, T. Kehle, V. Herzog, In vivo iodination of a misfolded proinsulin reveals co-localized signals for Bip binding and for degradation in the ER. *EMBO J* **14**, 1091-1098 (1995).
151. A. T. van der Goot, M. M. P. Pearce, D. E. Leto, T. A. Shaler, R. R. Kopito, Redundant and Antagonistic Roles of XTP3B and OS9 in Decoding Glycan and Non-glycan Degrons in ER-Associated Degradation. *Mol Cell* **70**, 516-530 e516 (2018).
152. B. Tsai, C. Rodighiero, W. I. Lencer, T. A. Rapoport, Protein disulfide isomerase acts as a redox-dependent chaperone to unfold cholera toxin. *Cell* **104**, 937-948 (2001).
153. A. Bhattacharya, L. Qi, ER-associated degradation in health and disease - from substrate to organism. *J Cell Sci* **132**, (2019).
154. K. Romisch, A Case for Sec61 Channel Involvement in ERAD. *Trends Biochem Sci* **42**, 171-179 (2017).
155. B. N. Lilley, H. L. Ploegh, A membrane protein required for dislocation of misfolded proteins from the ER. *Nature* **429**, 834-840 (2004).
156. M. Kikkert *et al.*, Human HRD1 is an E3 ubiquitin ligase involved in degradation of proteins from the endoplasmic reticulum. *J Biol Chem* **279**, 3525-3534 (2004).
157. J. van den Boom, H. Meyer, VCP/p97-Mediated Unfolding as a Principle in Protein Homeostasis and Signaling. *Mol Cell* **69**, 182-194 (2018).
158. H. Meyer, M. Bug, S. Bremer, Emerging functions of the VCP/p97 AAA-ATPase in the ubiquitin system. *Nat Cell Biol* **14**, 117-123 (2012).
159. H. Kroeger *et al.*, Endoplasmic reticulum-associated degradation (ERAD) and autophagy cooperate to degrade polymerogenic mutant serpins. *J Biol Chem* **284**, 22793-22802 (2009).
160. K. Varga *et al.*, Efficient intracellular processing of the endogenous cystic fibrosis transmembrane conductance regulator in epithelial cell lines. *J Biol Chem* **279**, 22578-22584 (2004).
161. B. M. Johnson, R. A. DeBose-Boyd, Underlying mechanisms for sterol-induced ubiquitination and ER-associated degradation of HMG CoA reductase. *Semin Cell Dev Biol* **81**, 121-128 (2018).
162. N. M. Kocaturk, D. Gozuacik, Crosstalk Between Mammalian Autophagy and the Ubiquitin-Proteasome System. *Front Cell Dev Biol* **6**, 128 (2018).
163. H. Chino, N. Mizushima, ER-Phagy: Quality Control and Turnover of Endoplasmic Reticulum. *Trends Cell Biol* **30**, 384-398 (2020).

164. X. Li, S. He, B. Ma, Autophagy and autophagy-related proteins in cancer. *Mol Cancer* **19**, 12 (2020).
165. M. Bosch, R. G. Parton, A. Pol, Lipid droplets, bioenergetic fluxes, and metabolic flexibility. *Semin Cell Dev Biol* **108**, 33-46 (2020).
166. A. Pol, S. P. Gross, R. G. Parton, Review: biogenesis of the multifunctional lipid droplet: lipids, proteins, and sites. *J Cell Biol* **204**, 635-646 (2014).
167. K. D. Chapman, J. M. Dyer, R. T. Mullen, Biogenesis and functions of lipid droplets in plants: Thematic Review Series: Lipid Droplet Synthesis and Metabolism: from Yeast to Man. *J Lipid Res* **53**, 215-226 (2012).
168. R. P. Kuhnlein, Thematic review series: Lipid droplet synthesis and metabolism: from yeast to man. Lipid droplet-based storage fat metabolism in Drosophila. *J Lipid Res* **53**, 1430-1436 (2012).
169. J. A. Olzmann, P. Carvalho, Dynamics and functions of lipid droplets. *Nat Rev Mol Cell Biol* **20**, 137-155 (2019).
170. S. Cermelli, Y. Guo, S. P. Gross, M. A. Welte, The lipid-droplet proteome reveals that droplets are a protein-storage depot. *Curr Biol* **16**, 1783-1795 (2006).
171. X. Zhang, K. Zhang, Endoplasmic Reticulum Stress-Associated Lipid Droplet Formation and Type II Diabetes. *Biochem Res Int* **2012**, 247275 (2012).
172. M. A. Welte, A. P. Gould, Lipid droplet functions beyond energy storage. *Biochim Biophys Acta Mol Cell Biol Lipids* **1862**, 1260-1272 (2017).
173. M. Bosch *et al.*, Mammalian lipid droplets are innate immune hubs integrating cell metabolism and host defense. *Science* **370**, eaay8085 (2020).
174. A. B. Engin, in *Obesity and Lipotoxicity,* A. B. Engin, A. Engin, Eds. (Springer International Publishing, Cham, 2017), pp. 197-220.
175. K. Bersuker, J. A. Olzmann, Establishing the lipid droplet proteome: Mechanisms of lipid droplet protein targeting and degradation. *Biochim Biophys Acta Mol Cell Biol Lipids* **1862**, 1166-1177 (2017).
176. R. S. Hegde, R. J. Keenan, Tail-anchored membrane protein insertion into the endoplasmic reticulum. *Nat Rev Mol Cell Biol* **12**, 787-798 (2011).
177. B. Schrul, R. R. Kopito, Peroxin-dependent targeting of a lipid-droplet-destined membrane protein to ER subdomains. *Nat Cell Biol* **18**, 740-751 (2016).
178. A. Stevanovic, C. Thiele, Monotopic topology is required for lipid droplet targeting of ancient ubiquitous protein 1. *J Lipid Res* **54**, 503-513 (2013).
179. S. Turro *et al.*, Identification and characterization of associated with lipid droplet protein 1: A novel membrane-associated protein that resides on hepatic lipid droplets. *Traffic* **7**, 1254-1269 (2006).
180. A. Kassan *et al.*, Acyl-CoA synthetase 3 promotes lipid droplet biogenesis in ER microdomains. *J Cell Biol* **203**, 985-1001 (2013).
181. M. Ingelmo-Torres *et al.*, Hydrophobic and basic domains target proteins to lipid droplets. *Traffic* **10**, 1785-1801 (2009).
182. J. Bigay, B. Antonny, Curvature, lipid packing, and electrostatics of membrane organelles: defining cellular territories in determining specificity. *Dev Cell* **23**, 886-895 (2012).
183. E. R. Rowe *et al.*, Conserved Amphipathic Helices Mediate Lipid Droplet Targeting of Perilipins 1-3. *J Biol Chem* **291**, 6664-6678 (2016).
184. R. B. Cornell, Membrane lipid compositional sensing by the inducible amphipathic helix of CCT. *Biochim Biophys Acta* **1861**, 847-861 (2016).
185. A. R. Kimmel, D. L. Brasaemle, M. McAndrews-Hill, C. Sztalryd, C. Londos, Adoption of PERILIPIN as a unifying nomenclature for the mammalian PAT-family of intracellular lipid storage droplet proteins. *J Lipid Res* **51**, 468-471 (2010).
186. H. Itabe, T. Yamaguchi, S. Nimura, N. Sasabe, Perilipins: a diversity of intracellular lipid droplet proteins. *Lipids Health Dis* **16**, 83 (2017).
187. K. Hsieh *et al.*, Perilipin family members preferentially sequester to either triacylglycerol-specific or cholesteryl-ester-specific intracellular lipid storage droplets. *J Cell Sci* **125**, 4067-4076 (2012).

188. J. R. Skinner *et al.*, Diacylglycerol enrichment of endoplasmic reticulum or lipid droplets recruits perilipin 3/TIP47 during lipid storage and mobilization. *J Biol Chem* **284**, 30941-30948 (2009).
189. M. Imamura *et al.*, ADRP stimulates lipid accumulation and lipid droplet formation in murine fibroblasts. *Am J Physiol Endocrinol Metab* **283**, E775-783 (2002).
190. N. E. Wolins, D. L. Brasaemle, P. E. Bickel, A proposed model of fat packaging by exchangeable lipid droplet proteins. *FEBS Lett* **580**, 5484-5491 (2006).
191. N. Zurek, L. Sparks, G. Voeltz, Reticulon short hairpin transmembrane domains are used to shape ER tubules. *Traffic* **12**, 28-41 (2011).
192. A. Ruggiano, G. Mora, L. Buxo, P. Carvalho, Spatial control of lipid droplet proteins by the ERAD ubiquitin ligase Doa10. *EMBO J* **35**, 1644-1655 (2016).
193. N. Kory, R. V. Farese, Jr., T. C. Walther, Targeting Fat: Mechanisms of Protein Localization to Lipid Droplets. *Trends Cell Biol* **26**, 535-546 (2016).
194. M. A. Welte, Proteins under new management: lipid droplets deliver. *Trends Cell Biol* **17**, 363-369 (2007).
195. H. L. Ploegh, A lipid-based model for the creation of an escape hatch from the endoplasmic reticulum. *Nature* **448**, 435-438 (2007).
196. C. Ward *et al.*, Autophagy, lipophagy and lysosomal lipid storage disorders. *Biochim Biophys Acta* **1861**, 269-284 (2016).
197. R. Singh *et al.*, Autophagy regulates lipid metabolism. *Nature* **458**, 1131-1135 (2009).
198. S. Kaushik, A. M. Cuervo, Degradation of lipid droplet-associated proteins by chaperone-mediated autophagy facilitates lipolysis. *Nat Cell Biol* **17**, 759-770 (2015).
199. N. Kory, A. R. Thiam, R. V. Farese, Jr., T. C. Walther, Protein Crowding Is a Determinant of Lipid Droplet Protein Composition. *Dev Cell* **34**, 351-363 (2015).
200. D. J. Murphy, J. Vance, Mechanisms of lipid-body formation. *Trends Biochem Sci* **24**, 109-115 (1999).
201. P. A. Watkins, Fatty acid activation. *Prog Lipid Res* **36**, 55-83 (1997).
202. P. C. Kienesberger, T. Pulinilkunnil, J. Nagendran, J. R. Dyck, Myocardial triacylglycerol metabolism. *J Mol Cell Cardiol* **55**, 101-110 (2013).
203. T. Y. Chang, B. L. Li, C. C. Chang, Y. Urano, Acyl-coenzyme A:cholesterol acyltransferases. *Am J Physiol Endocrinol Metab* **297**, E1-9 (2009).
204. D. A. Gross, C. Zhan, D. L. Silver, Direct binding of triglyceride to fat storage-inducing transmembrane proteins 1 and 2 is important for lipid droplet formation. *Proc Natl Acad Sci U S A* **108**, 19581-19586 (2011).
205. F. Wilfling *et al.*, Triacylglycerol synthesis enzymes mediate lipid droplet growth by relocalizing from the ER to lipid droplets. *Dev Cell* **24**, 384-399 (2013).
206. A. Gubern *et al.*, Group IVA phospholipase A2 is necessary for the biogenesis of lipid droplets. *J Biol Chem* **283**, 27369-27382 (2008).
207. N. Fuller, R. P. Rand, The influence of lysolipids on the spontaneous curvature and bending elasticity of phospholipid membranes. *Biophys J* **81**, 243-254 (2001).
208. H. Wang *et al.*, Seipin is required for converting nascent to mature lipid droplets. *Elife* **5**, (2016).
209. N. Kumar *et al.*, VPS13A and VPS13C are lipid transport proteins differentially localized at ER contact sites. *J Cell Biol* **217**, 3625-3639 (2018).
210. C. Sztalryd, A. R. Kimmel, Perilipins: lipid droplet coat proteins adapted for tissue-specific energy storage and utilization, and lipid cytoprotection. *Biochimie* **96**, 96-101 (2014).
211. J. L. McManaman *et al.*, Perilipin-2-null mice are protected against diet-induced obesity, adipose inflammation, and fatty liver disease. *J Lipid Res* **54**, 1346-1359 (2013).
212. J. T. Tansey *et al.*, Perilipin ablation results in a lean mouse with aberrant adipocyte lipolysis, enhanced leptin production, and resistance to diet-induced obesity. *Proc Natl Acad Sci U S A* **98**, 6494-6499 (2001).
213. J. T. Tansey *et al.*, Functional studies on native and mutated forms of perilipins. A role in protein kinase A-mediated lipolysis of triacylglycerols. *J Biol Chem* **278**, 8401-8406 (2003).

214. B. Lee, J. Zhu, N. E. Wolins, J. X. Cheng, K. K. Buhman, Differential association of adipophilin and TIP47 proteins with cytoplasmic lipid droplets in mouse enterocytes during dietary fat absorption. *Biochim Biophys Acta* **1791**, 1173-1180 (2009).
215. M. Gao, X. Huang, B. L. Song, H. Yang, The biogenesis of lipid droplets: Lipids take center stage. *Prog Lipid Res* **75**, 100989 (2019).
216. A. R. Kimmel, C. Sztalryd, The Perilipins: Major Cytosolic Lipid Droplet-Associated Proteins and Their Roles in Cellular Lipid Storage, Mobilization, and Systemic Homeostasis. *Annu Rev Nutr* **36**, 471-509 (2016).
217. T. Yamaguchi, N. Omatsu, S. Matsushita, T. Osumi, CGI-58 interacts with perilipin and is localized to lipid droplets. Possible involvement of CGI-58 mislocalization in Chanarin-Dorfman syndrome. *J Biol Chem* **279**, 30490-30497 (2004).
218. M. Ahmadian *et al.*, Desnutrin/ATGL is regulated by AMPK and is required for a brown adipose phenotype. *Cell Metab* **13**, 739-748 (2011).
219. D. L. Brasaemle, D. M. Levin, D. C. Adler-Wailes, C. Londos, The lipolytic stimulation of 3T3-L1 adipocytes promotes the translocation of hormone-sensitive lipase to the surfaces of lipid storage droplets. *Biochim Biophys Acta* **1483**, 251-262 (2000).
220. S. J. Kim *et al.*, AMPK Phosphorylates Desnutrin/ATGL and Hormone-Sensitive Lipase To Regulate Lipolysis and Fatty Acid Oxidation within Adipose Tissue. *Mol Cell Biol* **36**, 1961-1976 (2016).
221. H. Wang *et al.*, Perilipin 5, a lipid droplet-associated protein, provides physical and metabolic linkage to mitochondria. *J Lipid Res* **52**, 2159-2168 (2011).
222. M. Boutant *et al.*, Mfn2 is critical for brown adipose tissue thermogenic function. *EMBO J* **36**, 1543-1558 (2017).
223. C. P. Najt *et al.*, Lipid Droplet-Derived Monounsaturated Fatty Acids Traffic via PLIN5 to Allosterically Activate SIRT1. *Mol Cell* **77**, 810-824 e818 (2020).
224. R. Belfort *et al.*, Dose-response effect of elevated plasma free fatty acid on insulin signaling. *Diabetes* **54**, 1640-1648 (2005).
225. L. Liu *et al.*, DGAT1 expression increases heart triglyceride content but ameliorates lipotoxicity. *J Biol Chem* **284**, 36312-36323 (2009).
226. J. Sieber *et al.*, Susceptibility of podocytes to palmitic acid is regulated by stearoyl-CoA desaturases 1 and 2. *Am J Pathol* **183**, 735-744 (2013).
227. L. Salvado *et al.*, Oleate prevents saturated-fatty-acid-induced ER stress, inflammation and insulin resistance in skeletal muscle cells through an AMPK-dependent mechanism. *Diabetologia* **56**, 1372-1382 (2013).
228. T. R. Koves *et al.*, Mitochondrial overload and incomplete fatty acid oxidation contribute to skeletal muscle insulin resistance. *Cell Metab* **7**, 45-56 (2008).
229. P. Mitchell, Coupling of phosphorylation to electron and hydrogen transfer by a chemi-osmotic type of mechanism. *Nature* **191**, 144-148 (1961).
230. V. Adam-Vizi, C. Chinopoulos, Bioenergetics and the formation of mitochondrial reactive oxygen species. *Trends Pharmacol Sci* **27**, 639-645 (2006).
231. M. A. Abdul-Ghani *et al.*, Deleterious action of FA metabolites on ATP synthesis: possible link between lipotoxicity, mitochondrial dysfunction, and insulin resistance. *Am J Physiol Endocrinol Metab* **295**, E678-685 (2008).
232. E. Rial *et al.*, Lipotoxicity, fatty acid uncoupling and mitochondrial carrier function. *Biochim Biophys Acta* **1797**, 800-806 (2010).
233. G. Kroemer, L. Galluzzi, C. Brenner, Mitochondrial membrane permeabilization in cell death. *Physiol Rev* **87**, 99-163 (2007).
234. S. A. Summers, Ceramides in insulin resistance and lipotoxicity. *Prog Lipid Res* **45**, 42-72 (2006).
235. M. D. Mantzaris, E. V. Tsianos, D. Galaris, Interruption of triacylglycerol synthesis in the endoplasmic reticulum is the initiating event for saturated fatty acid-induced lipotoxicity in liver cells. *FEBS J* **278**, 519-530 (2011).
236. N. M. Borradaile *et al.*, Disruption of endoplasmic reticulum structure and integrity in lipotoxic cell death. *J Lipid Res* **47**, 2726-2737 (2006).

237. A. C. Baldwin, C. D. Green, L. K. Olson, M. A. Moxley, J. A. Corbett, A role for aberrant protein palmitoylation in FFA-induced ER stress and beta-cell death. *Am J Physiol Endocrinol Metab* **302**, E1390-1398 (2012).
238. K. M. Fang *et al.*, Free fatty acids act as endogenous ionophores, resulting in Na+ and Ca2+ influx and myocyte apoptosis. *Cardiovasc Res* **78**, 533-545 (2008).
239. Y. Ma, L. M. Hendershot, ER chaperone functions during normal and stress conditions. *J Chem Neuroanat* **28**, 51-65 (2004).
240. Z. Liu *et al.*, Induction of ER stress-mediated apoptosis by ceramide via disruption of ER Ca(2+) homeostasis in human adenoid cystic carcinoma cells. *Cell Biosci* **4**, 71 (2014).
241. D. E. Clapham, Calcium signaling. *Cell* **131**, 1047-1058 (2007).
242. L. C. Joseph *et al.*, Correction: Inhibition of NAPDH Oxidase 2 (NOX2) Prevents Oxidative Stress and Mitochondrial Abnormalities Caused by Saturated Fat in Cardiomyocytes. *PLoS One* **12**, e0174525 (2017).
243. K. D. Siegenthaler, C. S. Sevier, Working Together: Redox Signaling between the Endoplasmic Reticulum and Mitochondria. *Chem Res Toxicol* **32**, 342-344 (2019).
244. B. P. Tu, J. S. Weissman, Oxidative protein folding in eukaryotes: mechanisms and consequences. *J Cell Biol* **164**, 341-346 (2004).
245. G. Li *et al.*, Role of ERO1-alpha-mediated stimulation of inositol 1,4,5-triphosphate receptor activity in endoplasmic reticulum stress-induced apoptosis. *J Cell Biol* **186**, 783-792 (2009).
246. H. Xu *et al.*, IP3R-Grp75-VDAC1-MCU calcium regulation axis antagonists protect podocytes from apoptosis and decrease proteinuria in an Adriamycin nephropathy rat model. *BMC Nephrol* **19**, 140 (2018).
247. S. J. Marciniak *et al.*, CHOP induces death by promoting protein synthesis and oxidation in the stressed endoplasmic reticulum. *Genes Dev* **18**, 3066-3077 (2004).
248. P. De Meyts, in *Endotext,* K. R. Feingold *et al.*, Eds. (South Dartmouth (MA), 2000).
249. Y. Kido, J. Nakae, D. Accili, Clinical review 125: The insulin receptor and its cellular targets. *J Clin Endocrinol Metab* **86**, 972-979 (2001).
250. G. Wilcox, Insulin and insulin resistance. *Clin Biochem Rev* **26**, 19-39 (2005).
251. V. A. Fonseca, Defining and characterizing the progression of type 2 diabetes. *Diabetes Care* **32 Suppl 2**, S151-156 (2009).
252. A. Brunetti, E. Chiefari, D. Foti, Recent advances in the molecular genetics of type 2 diabetes mellitus. *World J Diabetes* **5**, 128-140 (2014).
253. P. J. Randle, P. B. Garland, C. N. Hales, E. A. Newsholme, The glucose fatty-acid cycle. Its role in insulin sensitivity and the metabolic disturbances of diabetes mellitus. *Lancet* **1**, 785-789 (1963).
254. M. Roden *et al.*, Mechanism of free fatty acid-induced insulin resistance in humans. *J Clin Invest* **97**, 2859-2865 (1996).
255. Y. Le Marchand-Brustel *et al.*, Fatty acid-induced insulin resistance: role of insulin receptor substrate 1 serine phosphorylation in the retroregulation of insulin signalling. *Biochem Soc Trans* **31**, 1152-1156 (2003).
256. J. Szendroedi *et al.*, Role of diacylglycerol activation of PKCtheta in lipid-induced muscle insulin resistance in humans. *Proc Natl Acad Sci U S A* **111**, 9597-9602 (2014).
257. R. Zhande, J. J. Mitchell, J. Wu, X. J. Sun, Molecular mechanism of insulin-induced degradation of insulin receptor substrate 1. *Mol Cell Biol* **22**, 1016-1026 (2002).
258. K. Paz *et al.*, A molecular basis for insulin resistance. Elevated serine/threonine phosphorylation of IRS-1 and IRS-2 inhibits their binding to the juxtamembrane region of the insulin receptor and impairs their ability to undergo insulin-induced tyrosine phosphorylation. *J Biol Chem* **272**, 29911-29918 (1997).
259. T. J. Wilkin, L. D. Voss, Metabolic syndrome: maladaptation to a modern world. *J R Soc Med* **97**, 511-520 (2004).
260. A. Guilherme, J. V. Virbasius, V. Puri, M. P. Czech, Adipocyte dysfunctions linking obesity to insulin resistance and type 2 diabetes. *Nat Rev Mol Cell Biol* **9**, 367-377 (2008).
261. M. Morelli *et al.*, Ectopic fat: the true culprit linking obesity and cardiovascular disease? *Thromb Haemost* **110**, 651-660 (2013).

262. S. Xu, X. Zhang, P. Liu, Lipid droplet proteins and metabolic diseases. *Biochim Biophys Acta Mol Basis Dis* **1864**, 1968-1983 (2018).
263. P. L. Huang, A comprehensive definition for metabolic syndrome. *Dis Model Mech* **2**, 231-237 (2009).
264. F. Q. Nuttall, Body Mass Index: Obesity, BMI, and Health: A Critical Review. *Nutr Today* **50**, 117-128 (2015).
265. A. Chiolero, Why causality, and not prediction, should guide obesity prevention policy. *Lancet Public Health* **3**, e461-e462 (2018).
266. H. Hauner, Managing type 2 diabetes mellitus in patients with obesity. *Treat Endocrinol* **3**, 223-232 (2004).
267. V. T. Samuel, G. I. Shulman, The pathogenesis of insulin resistance: integrating signaling pathways and substrate flux. *J Clin Invest* **126**, 12-22 (2016).
268. O. Sovik, H. Vestergaard, O. Trygstad, O. Pedersen, Studies of insulin resistance in congenital generalized lipodystrophy. *Acta Paediatr Suppl* **413**, 29-37 (1996).
269. Q. Luong, J. Huang, K. Y. Lee, Deciphering White Adipose Tissue Heterogeneity. *Biology (Basel)* **8**, (2019).
270. A. Bartelt, J. Heeren, Adipose tissue browning and metabolic health. *Nat Rev Endocrinol* **10**, 24-36 (2014).
271. K. N. Frayn *et al.*, Regulation of fatty acid movement in human adipose tissue in the postabsorptive-to-postprandial transition. *Am J Physiol* **266**, E308-317 (1994).
272. C. Lagathu *et al.*, Long-term treatment with interleukin-1beta induces insulin resistance in murine and human adipocytes. *Diabetologia* **49**, 2162-2173 (2006).
273. F. Amati *et al.*, Skeletal muscle triglycerides, diacylglycerols, and ceramides in insulin resistance: another paradox in endurance-trained athletes? *Diabetes* **60**, 2588-2597 (2011).
274. N. Chalasani *et al.*, The diagnosis and management of nonalcoholic fatty liver disease: Practice guidance from the American Association for the Study of Liver Diseases. *Hepatology* **67**, 328-357 (2018).
275. K. F. Petersen, D. Laurent, D. L. Rothman, G. W. Cline, G. I. Shulman, Mechanism by which glucose and insulin inhibit net hepatic glycogenolysis in humans. *J Clin Invest* **101**, 1203-1209 (1998).
276. J. Nakae, T. Kitamura, D. L. Silver, D. Accili, The forkhead transcription factor Foxo1 (Fkhr) confers insulin sensitivity onto glucose-6-phosphatase expression. *J Clin Invest* **108**, 1359-1367 (2001).
277. V. T. Samuel, G. I. Shulman, Nonalcoholic Fatty Liver Disease as a Nexus of Metabolic and Hepatic Diseases. *Cell Metab* **27**, 22-41 (2018).
278. D. F. Vatner *et al.*, Insulin-independent regulation of hepatic triglyceride synthesis by fatty acids. *Proc Natl Acad Sci U S A* **112**, 1143-1148 (2015).
279. N. Higuchi *et al.*, Liver X receptor in cooperation with SREBP-1c is a major lipid synthesis regulator in nonalcoholic fatty liver disease. *Hepatol Res* **38**, 1122-1129 (2008).
280. D. Ferguson, B. N. Finck, Emerging therapeutic approaches for the treatment of NAFLD and type 2 diabetes mellitus. *Nat Rev Endocrinol* **17**, 484-495 (2021).
281. F. M. Ashcroft, P. Rorsman, Diabetes mellitus and the beta cell: the last ten years. *Cell* **148**, 1160-1171 (2012).
282. R. Goyal, I. Jialal, in *StatPearls*. (Treasure Island (FL), 2021).
283. S. E. Kahn *et al.*, Quantification of the relationship between insulin sensitivity and beta-cell function in human subjects. Evidence for a hyperbolic function. *Diabetes* **42**, 1663-1672 (1993).
284. C. Chen, C. M. Cohrs, J. Stertmann, R. Bozsak, S. Speier, Human beta cell mass and function in diabetes: Recent advances in knowledge and technologies to understand disease pathogenesis. *Mol Metab* **6**, 943-957 (2017).
285. H. Brandhorst, D. Brandhorst, B. J. Hering, K. Federlin, R. G. Bretzel, Body mass index of pancreatic donors: a decisive factor for human islet isolation. *Exp Clin Endocrinol Diabetes* **103 Suppl 2**, 23-26 (1995).
286. S. Lenzen, Oxidative stress: the vulnerable beta-cell. *Biochem Soc Trans* **36**, 343-347 (2008).

287. M. Y. Donath, S. E. Shoelson, Type 2 diabetes as an inflammatory disease. *Nat Rev Immunol* **11**, 98-107 (2011).
288. G. B. D. O. Collaborators *et al.*, Health Effects of Overweight and Obesity in 195 Countries over 25 Years. *N Engl J Med* **377**, 13-27 (2017).
289. M. A. B. Khan *et al.*, Epidemiology of Type 2 Diabetes - Global Burden of Disease and Forecasted Trends. *J Epidemiol Glob Health* **10**, 107-111 (2020).
290. Z. M. Younossi *et al.*, Global epidemiology of nonalcoholic fatty liver disease-Meta-analytic assessment of prevalence, incidence, and outcomes. *Hepatology* **64**, 73-84 (2016).
291. S. K. Asrani, H. Devarbhavi, J. Eaton, P. S. Kamath, Burden of liver diseases in the world. *J Hepatol* **70**, 151-171 (2019).
292. S. Cernea, A. Cahn, I. Raz, Pharmacological management of nonalcoholic fatty liver disease in type 2 diabetes. *Expert Rev Clin Pharmacol* **10**, 535-547 (2017).
293. T. Tsuchida, S. L. Friedman, Mechanisms of hepatic stellate cell activation. *Nat Rev Gastroenterol Hepatol* **14**, 397-411 (2017).
294. Q. M. Anstee, G. Targher, C. P. Day, Progression of NAFLD to diabetes mellitus, cardiovascular disease or cirrhosis. *Nat Rev Gastroenterol Hepatol* **10**, 330-344 (2013).
295. S. M. Grundy *et al.*, Diagnosis and management of the metabolic syndrome: an American Heart Association/National Heart, Lung, and Blood Institute scientific statement. *Curr Opin Cardiol* **21**, 1-6 (2006).
296. K. F. Petersen *et al.*, Reversal of nonalcoholic hepatic steatosis, hepatic insulin resistance, and hyperglycemia by moderate weight reduction in patients with type 2 diabetes. *Diabetes* **54**, 603-608 (2005).
297. S. Castro-Barquero, A. M. Ruiz-Leon, M. Sierra-Perez, R. Estruch, R. Casas, Dietary Strategies for Metabolic Syndrome: A Comprehensive Review. *Nutrients* **12**, (2020).
298. J. Godos *et al.*, Adherence to the Mediterranean diet is inversely associated with metabolic syndrome occurrence: a meta-analysis of observational studies. *Int J Food Sci Nutr* **68**, 138-148 (2017).
299. J. J. Gaforio *et al.*, Virgin Olive Oil and Health: Summary of the III International Conference on Virgin Olive Oil and Health Consensus Report, JAEN (Spain) 2018. *Nutrients* **11**, (2019).
300. C. C. Curioni, P. M. Lourenco, Long-term weight loss after diet and exercise: a systematic review. *Int J Obes (Lond)* **29**, 1168-1174 (2005).
301. V. S. Hubbard, W. H. Hall, Gastrointestinal Surgery for Severe Obesity. *Obes Surg* **1**, 257-265 (1991).
302. V. Ionut, R. N. Bergman, Mechanisms responsible for excess weight loss after bariatric surgery. *J Diabetes Sci Technol* **5**, 1263-1282 (2011).
303. P. E. O'Brien *et al.*, Long-Term Outcomes After Bariatric Surgery: a Systematic Review and Meta-analysis of Weight Loss at 10 or More Years for All Bariatric Procedures and a Single-Centre Review of 20-Year Outcomes After Adjustable Gastric Banding. *Obes Surg* **29**, 3-14 (2019).
304. A. S. Schneck *et al.*, Roux-En Y Gastric Bypass Results in Long-Term Remission of Hepatocyte Apoptosis and Hepatic Histological Features of Non-alcoholic Steatohepatitis. *Front Physiol* **7**, 344 (2016).
305. H. Buchwald *et al.*, Bariatric surgery: a systematic review and meta-analysis. *JAMA* **292**, 1724-1737 (2004).
306. P. Del Corral, P. C. Chandler-Laney, K. Casazza, B. A. Gower, G. R. Hunter, Effect of dietary adherence with or without exercise on weight loss: a mechanistic approach to a global problem. *J Clin Endocrinol Metab* **94**, 1602-1607 (2009).
307. J. Ponce, N. T. Nguyen, M. Hutter, R. Sudan, J. M. Morton, American Society for Metabolic and Bariatric Surgery estimation of bariatric surgery procedures in the United States, 2011-2014. *Surg Obes Relat Dis* **11**, 1199-1200 (2015).
308. D. M. Williams, A. Nawaz, M. Evans, Drug Therapy in Obesity: A Review of Current and Emerging Treatments. *Diabetes Ther* **11**, 1199-1216 (2020).

309. A. K. Singh, R. Singh, Pharmacotherapy in obesity: a systematic review and meta-analysis of randomized controlled trials of anti-obesity drugs. *Expert Rev Clin Pharmacol* **13**, 53-64 (2020).
310. T. E. LaMoia, G. I. Shulman, Cellular and Molecular Mechanisms of Metformin Action. *Endocr Rev* **42**, 77-96 (2021).
311. S. E. Inzucchi *et al.*, Efficacy and metabolic effects of metformin and troglitazone in type II diabetes mellitus. *N Engl J Med* **338**, 867-872 (1998).
312. M. C. Petersen, D. F. Vatner, G. I. Shulman, Regulation of hepatic glucose metabolism in health and disease. *Nat Rev Endocrinol* **13**, 572-587 (2017).
313. M. Foretz *et al.*, Metformin inhibits hepatic gluconeogenesis in mice independently of the LKB1/AMPK pathway via a decrease in hepatic energy state. *J Clin Invest* **120**, 2355-2369 (2010).
314. A. K. Madiraju *et al.*, Metformin suppresses gluconeogenesis by inhibiting mitochondrial glycerophosphate dehydrogenase. *Nature* **510**, 542-546 (2014).
315. A. K. Madiraju *et al.*, Metformin inhibits gluconeogenesis via a redox-dependent mechanism in vivo. *Nat Med* **24**, 1384-1394 (2018).
316. C. J. Bailey, C. Day, Treatment of type 2 diabetes: future approaches. *Br Med Bull* **126**, 123-137 (2018).
317. L. Perreault, J. S. Skyler, J. Rosenstock, Novel therapies with precision mechanisms for type 2 diabetes mellitus. *Nat Rev Endocrinol* **17**, 364-377 (2021).
318. L. Tong, H. J. Harwood, Jr., Acetyl-coenzyme A carboxylases: versatile targets for drug discovery. *J Cell Biochem* **99**, 1476-1488 (2006).
319. A. W. Alberts, A. M. Nervi, P. R. Vagelos, Acetyl CoA carboxylase, II. Deomonstration of biotin-protein and biotin carboxylase subunits. *Proc Natl Acad Sci U S A* **63**, 1319-1326 (1969).
320. A. W. Alberts, P. R. Vagelos, Acetyl CoA carboxylase. I. Requirement for two protein fractions. *Proc Natl Acad Sci U S A* **59**, 561-568 (1968).
321. N. B. Ruderman, A. K. Saha, D. Vavvas, L. A. Witters, Malonyl-CoA, fuel sensing, and insulin resistance. *Am J Physiol* **276**, E1-E18 (1999).
322. J. D. McGarry, N. F. Brown, The mitochondrial carnitine palmitoyltransferase system. From concept to molecular analysis. *Eur J Biochem* **244**, 1-14 (1997).
323. N. Imai, D. E. Cohen, Trimming the Fat: Acetyl-CoA Carboxylase Inhibition for the Management of NAFLD. *Hepatology* **68**, 2062-2065 (2018).
324. L. Abu-Elheiga *et al.*, Mutant mice lacking acetyl-CoA carboxylase 1 are embryonically lethal. *Proc Natl Acad Sci U S A* **102**, 12011-12016 (2005).
325. L. Abu-Elheiga *et al.*, The subcellular localization of acetyl-CoA carboxylase 2. *Proc Natl Acad Sci U S A* **97**, 1444-1449 (2000).
326. J. D. Chow *et al.*, Genetic inhibition of hepatic acetyl-CoA carboxylase activity increases liver fat and alters global protein acetylation. *Mol Metab* **3**, 419-431 (2014).
327. R. W. Brownsey, A. N. Boone, J. E. Elliott, J. E. Kulpa, W. M. Lee, Regulation of acetyl-CoA carboxylase. *Biochem Soc Trans* **34**, 223-227 (2006).
328. A. K. Kleinschmidt, J. Moss, D. M. Lane, Acetyl coenzyme A carboxylase: filamentous nature of the animal enzymes. *Science* **166**, 1276-1278 (1969).
329. C. W. Kim *et al.*, Induced polymerization of mammalian acetyl-CoA carboxylase by MIG12 provides a tertiary level of regulation of fatty acid synthesis. *Proc Natl Acad Sci U S A* **107**, 9626-9631 (2010).
330. J. Ha, S. Daniel, S. S. Broyles, K. H. Kim, Critical phosphorylation sites for acetyl-CoA carboxylase activity. *J Biol Chem* **269**, 22162-22168 (1994).
331. D. G. Hardie, F. A. Ross, S. A. Hawley, AMPK: a nutrient and energy sensor that maintains energy homeostasis. *Nat Rev Mol Cell Biol* **13**, 251-262 (2012).
332. H. Yang, L. Yang, Targeting cAMP/PKA pathway for glycemic control and type 2 diabetes therapy. *J Mol Endocrinol* **57**, R93-R108 (2016).
333. K. Moreau *et al.*, BRCA1 affects lipid synthesis through its interaction with acetyl-CoA carboxylase. *J Biol Chem* **281**, 3172-3181 (2006).

334. J. Mao *et al.*, aP2-Cre-mediated inactivation of acetyl-CoA carboxylase 1 causes growth retardation and reduced lipid accumulation in adipose tissues. *Proc Natl Acad Sci U S A* **106**, 17576-17581 (2009).
335. J. Mao *et al.*, Liver-specific deletion of acetyl-CoA carboxylase 1 reduces hepatic triglyceride accumulation without affecting glucose homeostasis. *Proc Natl Acad Sci U S A* **103**, 8552-8557 (2006).
336. L. Abu-Elheiga, H. Wu, Z. Gu, R. Bressler, S. J. Wakil, Acetyl-CoA carboxylase 2-/- mutant mice are protected against fatty liver under high-fat, high-carbohydrate dietary and de novo lipogenic conditions. *J Biol Chem* **287**, 12578-12588 (2012).
337. K. L. Hoehn, N. Turner, G. J. Cooney, D. E. James, Phenotypic discrepancies in acetyl-CoA carboxylase 2-deficient mice. *J Biol Chem* **287**, 15801; author reply 15802 (2012).
338. D. B. Savage *et al.*, Reversal of diet-induced hepatic steatosis and hepatic insulin resistance by antisense oligonucleotide inhibitors of acetyl-CoA carboxylases 1 and 2. *J Clin Invest* **116**, 817-824 (2006).
339. H. J. Harwood, Jr., Treating the metabolic syndrome: acetyl-CoA carboxylase inhibition. *Expert Opin Ther Targets* **9**, 267-281 (2005).
340. R. A. Parker, T. Kariya, J. M. Grisar, V. Petrow, 5-(Tetradecyloxy)-2-furancarboxylic acid and related hypolipidemic fatty acid-like alkyloxyarylcarboxylic acids. *J Med Chem* **20**, 781-791 (1977).
341. S. A. McCune, R. A. Harris, Mechanism responsible for 5-(tetradecyloxy)-2-furoic acid inhibition of hepatic lipogenesis. *J Biol Chem* **254**, 10095-10101 (1979).
342. C. M. Arbeeny, D. S. Meyers, K. E. Bergquist, R. E. Gregg, Inhibition of fatty acid synthesis decreases very low density lipoprotein secretion in the hamster. *J Lipid Res* **33**, 843-851 (1992).
343. J. Triscari, A. C. Sullivan, Anti-obesity activity of a novel lipid synthesis inhibitor. *Int J Obes* **8 Suppl 1**, 227-239 (1984).
344. N. Fukuda, J. A. Ontko, Interactions between fatty acid synthesis, oxidation, and esterification in the production of triglyceride-rich lipoproteins by the liver. *J Lipid Res* **25**, 831-842 (1984).
345. A. Herms *et al.*, AMPK activation promotes lipid droplet dispersion on detyrosinated microtubules to increase mitochondrial fatty acid oxidation. *Nat Commun* **6**, 7176 (2015).
346. X. Wu, T. Huang, Recent development in acetyl-CoA carboxylase inhibitors and their potential as novel drugs. *Future Med Chem* **12**, 533-561 (2020).
347. H. J. Harwood, Jr. *et al.*, Isozyme-nonselective N-substituted bipiperidylcarboxamide acetyl-CoA carboxylase inhibitors reduce tissue malonyl-CoA concentrations, inhibit fatty acid synthesis, and increase fatty acid oxidation in cultured cells and in experimental animals. *J Biol Chem* **278**, 37099-37111 (2003).
348. R. U. Svensson *et al.*, Inhibition of acetyl-CoA carboxylase suppresses fatty acid synthesis and tumor growth of non-small-cell lung cancer in preclinical models. *Nat Med* **22**, 1108-1119 (2016).
349. J. S. V. Lally *et al.*, Inhibition of Acetyl-CoA Carboxylase by Phosphorylation or the Inhibitor ND-654 Suppresses Lipogenesis and Hepatocellular Carcinoma. *Cell Metab* **29**, 174-182 e175 (2019).
350. M. G. Vander Heiden, L. C. Cantley, C. B. Thompson, Understanding the Warburg effect: the metabolic requirements of cell proliferation. *Science* **324**, 1029-1033 (2009).
351. D. F. Calvisi *et al.*, Increased lipogenesis, induced by AKT-mTORC1-RPS6 signaling, promotes development of human hepatocellular carcinoma. *Gastroenterology* **140**, 1071-1083 (2011).
352. K. Gerth, N. Bedorf, H. Irschik, G. Hofle, H. Reichenbach, The soraphens: a family of novel antifungal compounds from Sorangium cellulosum (Myxobacteria). I. Soraphen A1 alpha: fermentation, isolation, biological properties. *J Antibiot (Tokyo)* **47**, 23-31 (1994).
353. Y. Shen, S. L. Volrath, S. C. Weatherly, T. D. Elich, L. Tong, A mechanism for the potent inhibition of eukaryotic acetyl-coenzyme A carboxylase by soraphen A, a macrocyclic polyketide natural product. *Mol Cell* **16**, 881-891 (2004).

354. B. M. Trost, J. D. Sieber, W. Qian, R. Dhawan, Z. T. Ball, Asymmetric total synthesis of soraphen A: a flexible alkyne strategy. *Angew Chem Int Ed Engl* **48**, 5478-5481 (2009).
355. G. Harriman *et al.*, Acetyl-CoA carboxylase inhibition by ND-630 reduces hepatic steatosis, improves insulin sensitivity, and modulates dyslipidemia in rats. *Proc Natl Acad Sci U S A* **113**, E1796-1805 (2016).
356. K. Stiede *et al.*, Acetyl-coenzyme A carboxylase inhibition reduces de novo lipogenesis in overweight male subjects: A randomized, double-blind, crossover study. *Hepatology* **66**, 324-334 (2017).
357. R. Loomba *et al.*, GS-0976 Reduces Hepatic Steatosis and Fibrosis Markers in Patients With Nonalcoholic Fatty Liver Disease. *Gastroenterology* **155**, 1463-1473 e1466 (2018).
358. C. W. Kim *et al.*, Acetyl CoA Carboxylase Inhibition Reduces Hepatic Steatosis but Elevates Plasma Triglycerides in Mice and Humans: A Bedside to Bench Investigation. *Cell Metab* **26**, 394-406 e396 (2017).
359. A. Bergman *et al.*, Safety, Tolerability, Pharmacokinetics, and Pharmacodynamics of a Liver-Targeting Acetyl-CoA Carboxylase Inhibitor (PF-05221304): A Three-Part Randomized Phase 1 Study. *Clin Pharmacol Drug Dev* **9**, 514-526 (2020).
360. N. Alkhouri, E. Lawitz, M. Noureddin, R. DeFronzo, G. I. Shulman, GS-0976 (Firsocostat): an investigational liver-directed acetyl-CoA carboxylase (ACC) inhibitor for the treatment of non-alcoholic steatohepatitis (NASH). *Expert Opin Investig Drugs* **29**, 135-141 (2020).
361. J. J. Marin-Penalver, I. Martin-Timon, C. Sevillano-Collantes, F. J. Del Canizo-Gomez, Update on the treatment of type 2 diabetes mellitus. *World J Diabetes* **7**, 354-395 (2016).
362. A. S. Al-Goblan, M. A. Al-Alfi, M. Z. Khan, Mechanism linking diabetes mellitus and obesity. *Diabetes Metab Syndr Obes* **7**, 587-591 (2014).
363. A. Tiwari *et al.*, Caveolin-1 is an aggresome-inducing protein. *Sci Rep* **6**, 38681 (2016).
364. R. G. Parton, M. T. Howes, Revisiting caveolin trafficking: the end of the caveosome. *J Cell Biol* **191**, 439-441 (2010).
365. C. G. Hansen, G. Howard, B. J. Nichols, Pacsin 2 is recruited to caveolae and functions in caveolar biogenesis. *J Cell Sci* **124**, 2777-2785 (2011).
366. B. Han, A. Tiwari, A. K. Kenworthy, Tagging strategies strongly affect the fate of overexpressed caveolin-1. *Traffic* **16**, 417-438 (2015).
367. R. Mora *et al.*, Caveolin-2 localizes to the golgi complex but redistributes to plasma membrane, caveolae, and rafts when co-expressed with caveolin-1. *J Biol Chem* **274**, 25708-25717 (1999).
368. J. E. Rothman, F. T. Wieland, Protein sorting by transport vesicles. *Science* **272**, 227-234 (1996).
369. R. G. Parton, M. A. del Pozo, Caveolae as plasma membrane sensors, protectors and organizers. *Nat Rev Mol Cell Biol* **14**, 98-112 (2013).
370. J. Song *et al.*, Identification of two pathways mediating protein targeting from ER to lipid droplets. 2021.2009.2014.460330 (2021).
371. A. Pol *et al.*, A caveolin dominant negative mutant associates with lipid bodies and induces intracellular cholesterol imbalance. *J Cell Biol* **152**, 1057-1070 (2001).
372. A. Akoumi, T. Haffar, M. Mousterji, R. S. Kiss, N. Bousette, Palmitate mediated diacylglycerol accumulation causes endoplasmic reticulum stress, Plin2 degradation, and cell death in H9C2 cardiomyoblasts. *Exp Cell Res* **354**, 85-94 (2017).
373. L. Hagenfeldt, J. Wahren, B. Pernow, L. Raf, Uptake of individual free fatty acids by skeletal muscle and liver in man. *J Clin Invest* **51**, 2324-2330 (1972).
374. W. Teo *et al.*, Nile Red fluorescence spectroscopy reports early physicochemical changes in myelin with high sensitivity. *Proc Natl Acad Sci U S A* **118**, (2021).
375. A. Herms *et al.*, Cell-to-cell heterogeneity in lipid droplets suggests a mechanism to reduce lipotoxicity. *Curr Biol* **23**, 1489-1496 (2013).
376. L. L. Listenberger *et al.*, Triglyceride accumulation protects against fatty acid-induced lipotoxicity. *Proc Natl Acad Sci U S A* **100**, 3077-3082 (2003).

377. L. Chen *et al.*, Acetyl-CoA carboxylase (ACC) as a therapeutic target for metabolic syndrome and recent developments in ACC1/2 inhibitors. *Expert Opin Investig Drugs* **28**, 917-930 (2019).
378. S. C. Broome, J. S. T. Woodhead, T. L. Merry, Mitochondria-Targeted Antioxidants and Skeletal Muscle Function. *Antioxidants (Basel)* **7**, (2018).
379. C. J. Bailey, K. J. Mynett, Insulin requirement for the antihyperglycaemic effect of metformin. *Br J Pharmacol* **111**, 793-796 (1994).
380. F. K. Huynh, M. F. Green, T. R. Koves, M. D. Hirschey, Measurement of fatty acid oxidation rates in animal tissues and cell lines. *Methods Enzymol* **542**, 391-405 (2014).
381. C. Y. Wang, J. K. Liao, A mouse model of diet-induced obesity and insulin resistance. *Methods Mol Biol* **821**, 421-433 (2012).
382. H. Huang *et al.*, Inhibitors of Fatty Acid Synthesis Induce PPAR alpha -Regulated Fatty Acid beta -Oxidative Genes: Synergistic Roles of L-FABP and Glucose. *PPAR Res* **2013**, 865604 (2013).
383. H. Wang *et al.*, Unique regulation of adipose triglyceride lipase (ATGL) by perilipin 5, a lipid droplet-associated protein. *J Biol Chem* **286**, 15707-15715 (2011).
384. T. Fujimoto, H. Kogo, K. Ishiguro, K. Tauchi, R. Nomura, Caveolin-2 is targeted to lipid droplets, a new "membrane domain" in the cell. *J Cell Biol* **152**, 1079-1085 (2001).
385. C. M. Blouin *et al.*, Lipid droplet analysis in caveolin-deficient adipocytes: alterations in surface phospholipid composition and maturation defects. *J Lipid Res* **51**, 945-956 (2010).
386. A. W. Cohen *et al.*, Role of caveolin-1 in the modulation of lipolysis and lipid droplet formation. *Diabetes* **53**, 1261-1270 (2004).
387. C. Sztalryd, D. L. Brasaemle, The perilipin family of lipid droplet proteins: Gatekeepers of intracellular lipolysis. *Biochim Biophys Acta Mol Cell Biol Lipids* **1862**, 1221-1232 (2017).
388. S. M. Storey, A. L. McIntosh, S. Senthivinayagam, K. C. Moon, B. P. Atshaves, The phospholipid monolayer associated with perilipin-enriched lipid droplets is a highly organized rigid membrane structure. *Am J Physiol Endocrinol Metab* **301**, E991-E1003 (2011).
389. P. Lau, S. J. Nixon, R. G. Parton, G. E. Muscat, RORalpha regulates the expression of genes involved in lipid homeostasis in skeletal muscle cells: caveolin-3 and CPT-1 are direct targets of ROR. *The Journal of biological chemistry* **279**, 36828-36840 (2004).
390. L. Madsen *et al.*, Ubxd1 is a novel co-factor of the human p97 ATPase. *Int J Biochem Cell Biol* **40**, 2927-2942 (2008).
391. N. Ariotti *et al.*, An inverted CAV1 (caveolin 1) topology defines novel autophagy-dependent exosome secretion from prostate cancer cells. *Autophagy*, 1-17 (2020).
392. Y. T. Wu *et al.*, Dual role of 3-methyladenine in modulation of autophagy via different temporal patterns of inhibition on class I and III phosphoinositide 3-kinase. *J Biol Chem* **285**, 10850-10861 (2010).
393. Y. Ishida *et al.*, Autophagic elimination of misfolded procollagen aggregates in the endoplasmic reticulum as a means of cell protection. *Mol Biol Cell* **20**, 2744-2754 (2009).
394. P. A. Conrad, E. J. Smart, Y. S. Ying, R. G. Anderson, G. S. Bloom, Caveolin cycles between plasma membrane caveolae and the Golgi complex by microtubule-dependent and microtubule-independent steps. *The Journal of cell biology* **131**, 1421-1433 (1995).
395. C. A. Syme, L. Zhang, A. Bisello, Caveolin-1 regulates cellular trafficking and function of the glucagon-like Peptide 1 receptor. *Mol Endocrinol* **20**, 3400-3411 (2006).
396. J. L. Brodsky, E. A. Fisher, The many intersecting pathways underlying apolipoprotein B secretion and degradation. *Trends Endocrinol Metab* **19**, 254-259 (2008).
397. B. L. Trigatti, R. G. Anderson, G. E. Gerber, Identification of caveolin-1 as a fatty acid binding protein. *Biochem Biophys Res Commun* **255**, 34-39 (1999).
398. R. M. Epand, B. G. Sayer, R. F. Epand, Caveolin scaffolding region and cholesterol-rich domains in membranes. *J Mol Biol* **345**, 339-350 (2005).
399. J. Fantini, F. J. Barrantes, How cholesterol interacts with membrane proteins: an exploration of cholesterol-binding sites including CRAC, CARC, and tilted domains. *Front Physiol* **4**, 31 (2013).

400. A. J. Carozzi *et al.*, Inhibition of lipid raft-dependent signaling by a dystrophy-associated mutant of caveolin-3. *J Biol Chem* **277**, 17944-17949 (2002).
401. M. Y. El-Mir *et al.*, Dimethylbiguanide inhibits cell respiration via an indirect effect targeted on the respiratory chain complex I. *J Biol Chem* **275**, 223-228 (2000).
402. S. Casas-Grajales, P. Muriel, Antioxidants in liver health. *World J Gastrointest Pharmacol Ther* **6**, 59-72 (2015).
403. E. D. Saggerson, C. A. Carpenter, Carnitine palmitoyltransferase in liver and five extrahepatic tissues in the rat. Inhibition by DL-2-bromopalmitoyl-CoA and effect of hypothyroidism. *Biochem J* **236**, 137-141 (1986).
404. I. Tein, F. Demaugre, J. P. Bonnefont, J. M. Saudubray, Normal muscle CPT1 and CPT2 activities in hepatic presentation patients with CPT1 deficiency in fibroblasts. Tissue specific isoforms of CPT1? *J Neurol Sci* **92**, 229-245 (1989).
405. S. A. McCune, T. Nomura, R. A. Harris, Inhibition of hepatic lipogenesis by 2-tetradecylglycidic acid. *Lipids* **14**, 880-882 (1979).
406. F. Demaugre, H. Buc, J. Girard, J. P. Leroux, Role of the mitochondrial metabolism of pyruvate on the regulation of ketogenesis in rat hepatocytes. *Metabolism* **32**, 40-48 (1983).
407. D. L. Halvorson, S. A. McCune, Inhibition of fatty acid synthesis in isolated adipocytes by 5-(tetradecyloxy)-2-furoic acid. *Lipids* **19**, 851-856 (1984).
408. A. M. Robinson, D. H. Williamson, Control of glucose metabolism in isolated acini of the lactating mammary gland of the rat. The ability of glycerol to mimic some of the effects of insulin. *Biochem J* **168**, 465-474 (1977).
409. S. Glund *et al.*, Inhibition of acetyl-CoA carboxylase 2 enhances skeletal muscle fatty acid oxidation and improves whole-body glucose homeostasis in db/db mice. *Diabetologia* **55**, 2044-2053 (2012).
410. T. T. Ross *et al.*, Acetyl-CoA Carboxylase Inhibition Improves Multiple Dimensions of NASH Pathogenesis in Model Systems. *Cell Mol Gastroenterol Hepatol* **10**, 829-851 (2020).
411. J. P. Gibson *et al.*, Toxicity and teratogenicity studies with the hypolipidemic drug RMI 14,514 in rats. *Fundam Appl Toxicol* **1**, 19-25 (1981).
412. C. M. Kummitha, S. C. Kalhan, G. M. Saidel, N. Lai, Relating tissue/organ energy expenditure to metabolic fluxes in mouse and human: experimental data integrated with mathematical modeling. *Physiol Rep* **2**, (2014).
413. M. W. Lee, M. Lee, K. J. Oh, Adipose Tissue-Derived Signatures for Obesity and Type 2 Diabetes: Adipokines, Batokines and MicroRNAs. *J Clin Med* **8**, (2019).
414. S. M. Ronnebaum *et al.*, Chronic suppression of acetyl-CoA carboxylase 1 in beta-cells impairs insulin secretion via inhibition of glucose rather than lipid metabolism. *J Biol Chem* **283**, 14248-14256 (2008).
415. J. Chen, P. B. Jeppesen, I. Nordentoft, K. Hermansen, Stevioside improves pancreatic beta-cell function during glucotoxicity via regulation of acetyl-CoA carboxylase. *Am J Physiol Endocrinol Metab* **292**, E1906-1916 (2007).
416. M. Mao-Qiang, P. M. Elias, K. R. Feingold, Fatty acids are required for epidermal permeability barrier function. *J Clin Invest* **92**, 791-798 (1993).
417. H. J. Kempen *et al.*, Secretion of apolipoproteins A-I and B by HepG2 cells: regulation by substrates and metabolic inhibitors. *J Lipid Res* **36**, 1796-1806 (1995).
418. L. Goedeke *et al.*, Acetyl-CoA Carboxylase Inhibition Reverses NAFLD and Hepatic Insulin Resistance but Promotes Hypertriglyceridemia in Rodents. *Hepatology* **68**, 2197-2211 (2018).
419. M. P. Bourbeau *et al.*, Piperazine oxadiazole inhibitors of acetyl-CoA carboxylase. *J Med Chem* **56**, 10132-10141 (2013).
420. R. S. O'Connor *et al.*, The CPT1a inhibitor, etomoxir induces severe oxidative stress at commonly used concentrations. *Sci Rep* **8**, 6289 (2018).
421. B. Raud, P. J. McGuire, R. G. Jones, T. Sparwasser, L. Berod, Fatty acid metabolism in CD8(+) T cell memory: Challenging current concepts. *Immunol Rev* **283**, 213-231 (2018).
422. L. Shi, B. P. Tu, Acetyl-CoA and the regulation of metabolism: mechanisms and consequences. *Curr Opin Cell Biol* **33**, 125-131 (2015).

423. M. Benito, E. Whitelaw, D. H. Williamson, Regulation of ketogenesis during the suckling-weanling transition in the rat. Studies with isolated hepatocytes. *Biochem J* **180**, 137-144 (1979).
424. D. R. Janero, C. Burghardt, D. Feldman, Amphiphile-induced heart muscle-cell (myocyte) injury: effects of intracellular fatty acid overload. *J Cell Physiol* **137**, 1-13 (1988).
425. P. Rojas-Morales, J. Pedraza-Chaverri, E. Tapia, Ketone bodies, stress response, and redox homeostasis. *Redox Biol* **29**, 101395 (2020).
426. C. Schlein *et al.*, Endogenous Fatty Acid Synthesis Drives Brown Adipose Tissue Involution. *Cell Rep* **34**, 108624 (2021).
427. L. L. Hwang *et al.*, Sex differences in high-fat diet-induced obesity, metabolic alterations and learning, and synaptic plasticity deficits in mice. *Obesity (Silver Spring)* **18**, 463-469 (2010).
428. D. B. Morton, P. H. Griffiths, Guidelines on the recognition of pain, distress and discomfort in experimental animals and an hypothesis for assessment. *Vet Rec* **116**, 431-436 (1985).
429. D. Sebastian *et al.*, Mfn2 deficiency links age-related sarcopenia and impaired autophagy to activation of an adaptive mitophagy pathway. *EMBO J* **35**, 1677-1693 (2016).
430. M. M. Bradford, A rapid and sensitive method for the quantitation of microgram quantities of protein utilizing the principle of protein-dye binding. *Anal Biochem* **72**, 248-254 (1976).
431. T. Zor, Z. Selinger, Linearization of the Bradford protein assay increases its sensitivity: theoretical and experimental studies. *Anal Biochem* **236**, 302-308 (1996).
432. J. Schindelin *et al.*, Fiji: an open-source platform for biological-image analysis. *Nat Methods* **9**, 676-682 (2012).
433. J. H. Reiling *et al.*, A CREB3-ARF4 signalling pathway mediates the response to Golgi stress and susceptibility to pathogens. *Nat Cell Biol* **15**, 1473-1485 (2013).
434. K. J. Livak, T. D. Schmittgen, Analysis of relative gene expression data using real-time quantitative PCR and the 2(-Delta Delta C(T)) Method. *Methods* **25**, 402-408 (2001).
435. N. Ariotti *et al.*, Modular Detection of GFP-Labeled Proteins for Rapid Screening by Electron Microscopy in Cells and Organisms. *Dev Cell* **35**, 513-525 (2015).

ACKNOWLEDGMENTS

“Hagas lo que hagas ámalo,
cómo amabas la cabina del Paradiso cuando eras niño.”
Toto, Cinema Paradiso.

Evidentment, per poder fer aquesta tesi he comptat amb el suport de moltíssima gent, que han vist clar que tot podia tirar endavant sobretot quan jo no ho creia. Us estaré eternament agraït i segur que sense tots vosaltres no hauria arribat fins aquí 5 anys després (més dos de màster). Encara costa de creure que pugui arribar a ser doctor, però la tesi ja està escrita que és més del que podia desitjar. De moment, m'agradaria recordar totes aquestes bones estones que m'heu fet passar i que m'han fet sentir part de la família del laboratori (vegeu el final del capítol).

En primer lloc, vull donar les gràcies a **l'Albert Pol** com a tutor i director de la tesi. Recordo exactament el primer dia que vaig parlar directament amb tu, i abans que pogués dir res, em vas oferir aquesta increïble oportunitat de poder investigar sobre els temes que volia fer-ho, exactament on volia i podent aprendre moltíssimes tècniques noves (la β-oxidació no calia). De veritat, espero haver après a interpretar, apreciar i comunicar la feina feta com es mereix. També et volia agrair la preocupació pel meu aprenentatge, permetent-me participar en molts dels projectes del laboratori, tot els consells rebuts per la tesi i el futur, les pròrrogues, ensenyar-me a mirar tots els detalls d'una imatge del microscopi i assistir al congrés de caveolina, on crec que vaig aprendre a fer preguntes i tot.

Marta, gràcies per dirigir-me la tesi i corregir-la paraula per paraula i moltes vegades. Segur que no ha estat gens fàcil ni divertit, per sort amb l'Albert heu aconseguit que sigui llegible i que no ocupi 1,000 pàgines. Trobaré a faltar que em cridin a viva veu des de l'altre punta del laboratori per si puc venir un moment per discutir uns resultats, o quedar-me parat en veure com fas un FACS amb dos citòmetres, analizant-los mentrestant a l'excel i tot amb 10 minuts. Sigui com sigui, la diversió i adrenalina sempre estan assegurades i acaben amb moltes rialles i aventures.

Alba, es podria dir que més de la meitat dels experiments de la tesi els he fet amb tu. Sobretot els infinits westerns, gradients i transfeccions a dos mans, o les interminables hores als estabularis. Ha donat per discutir molt, per sort hi havia algú que sempre posava seny. Gràcies també, per haver-me incorporat al grup alumni de cerveses al "Gallego" amb la **Marta Sánchez**, l'**Atilla**, l'**Alba Gómez** i en **Dídac**. A tots us desitjo molta sort en la nova etapa que esteu encetant.

L'ajuda que he rebut de tots els membres de l'equip també ha estat crucial. **Andrea**, gracies per ensenyar-me algunes tècniques traient temps d'escriure la tesi i tot el que suposa. **Albert Herms** la teva tesi ha servit com a referent, un plaer haver continuat la teva feina i espero que t'agradi llegir la meva tesi. A l'**Albert Gubern** i **Olívia** gracies per haver-me fet de tiets quan tenia algun problema amb els projectes. Y aunque breve, gracias, **Elsa** por la ayuda proporcionada durante tu máster. Thank you **Rémi** for all the good vibes send during this last year (to counteract my pessimism), and to share with us some of the festa majors, language classes, partidos de la selección, cinema a la fresca, etc. **Carles** et dono molts ànims per afrontar el màster i, si tot va bé, la tesi. Si puc ajudar amb alguna cosa ja saps, amb el treball de recerca no va anar tant malament, no? Y **Alberto**, aunque no hayamos coincidido mucho, espero que vaya bien el inicio de tu carrera investigadora.

Voldria agrair també al dr. **Antonio Zorzano**, per ser el president del tribunal d'aquesta tesi i la oportunitat brindada de poder fer els experiments amb els ratolins. A la dra. **Montserrat Marí**, també per acceptar formar part del tribunal, per proporcionar-nos l'oportunitat de treballar amb els hepatòcits aïllats i per respondre sempre molt ràpid i eficientment a tots els dubtes que hem tingut. A la dra. **Maribel Geli**, també per voler formar part del tribunal i per donar bons comentaris a tots els congressos on hem coincidit. Al dr. **Robert Parton**, per les imatges de microscòpia electrònica i per tots els comentaris referents al projecte de la caveolina. I als membres del grup del dr. **Antonio Postigo** per l'ajuda proporcionada en tècniques d'extracció de múscul i per deixar-nos sempre reactius quan han fet falta.

També gràcies, **Siscu**, per establir el primer contacte amb el laboratori, i a tots els membres del seu grup. Des de llavors crec que he tingut més concentració, un humor una mica diferent i espero la venjança de l'1-O. A l'**Albert Chavero** moltes gràcies per haver-me ajudat, escoltat i fet parlar d'absolutament tots els problemes que han anat sorgint. Era bastant bo creuar la mirada, i estar rient dels mateixos "xistes" de l'Angelines o l'Ignatius, o veure que anàvem vestits igual. La teva regularitat i constància, però, és difícil d'igualar, i a tu si que et farà aconseguir tot el que et proposis. També gràcies, **David**, i company de poiata per tots aquests moments on s'ha passat de discutir del joc de paraules més absurd fins a l'entrellaçament quàntic. Per sort aquests últims dies, ho he pogut reviure breument i semblava que el temps no hagués passat. I també **Moi** per totes les converses que ens has donat. M'alegro que hagis passat a estudiar metabolisme, et desitjo sort pel que queda de tesi i espero haver complert en convidar-te per les meves terres.

Volia agrair haver pogut fer el màster al grup d'en **Carles Enrich**, el teu interès per la meva feina i per haver format part del tribunal de la tesi. Moltes gràcies, **Carles Rentero** per haver llegit les comissions de seguiment i per haver-me ajudat en els primers passos pel laboratori. També m'agradaria agrair-te, **Ana**, la teva vocació científica que des del primer minut em vas encomanar incorporant-me als teus projectes. Si penso en aquells dies, només em vé una paraula al cap, "Enjoy!". A més a més, gràcies per tot el suport i ajuda que vaig rebre al principi de la tesi, va significar moltíssim per mi. **Elsa**, gràcies per seguir parlant tot i estar molt lluny d'aquí, a veure si us puc venir a veure un dia abans que tornis. Merci, per fer-me companyia fins tard des de l'altre meitat del laboratori, i venir després per sorpresa a compartir la pena que és no tenir res a la nevera per sopar quan tornes del lab. **Patri**, pienso que tiene mucho mérito todo lo que has conseguido en tan poco tiempo, y ha servido de referencia a la hora de presentar la tesis. Guardaré anécdotas divertidas cómo darlo todo en un concierto de Camela. I merci **Marc** també per les bones excursions (i les esperes), partides a jocs de taula i les sortides a la discoteca amb un *dress code* particular. Sempre m'ha meravellat aquesta capacitat que tens per ser autèntic i per aconseguir oportunitats de sota les pedres. Gràcies també a la **Maria Molinos**, he guardat fins a l'últim moment els llibrets amb totes les anotacions que vaig fer el primer dia de lab per fer una extracció de DNA, fet que demostra la teva paciència amb nosaltres. També a la **Bárbara**, la **Maria Rodríguez**, la **Camila** i l'**Anna Alvarez** pels bons moments del màster. Finalment, gràcies a l'**Albert Lu** per fer-me una mica de companyia els dies de festa que ha tocat passar pel lab.

També volia donar les gràcies a tots els membres del grup de la **Neus,** la **Montse**, la **Sònia Brun**, en **Daniel** i la **Baraa**, per sempre posar bona cara quan veníem a pidolar algun reactiu. **Fer** gràcies per aquestes quedades random post-biblioteca o durant incubacions, on, entre llàgrimes de predoc, m'has recomanat bons podcasts, obres de la Calòrica, descobert la Sotana i regalat una sobrassada boníssima. Sento dir-te que et passo el relleu. **Débora**, espero haver-te transmès bé els coneixements sobre les RTs, ja que veig que les tècniques estan passant a les futures generacions. I merci per organitzar les sortides a Cabotro's juntament amb la **Sònia** i l'**Edu**. Ha estat molt divertit, tot i el reguetón i certs dies que s'han escapat de les mans.

També he estat encantat de participar a totes les calçotades, sopars de nadal (tradicionals i alternatius), i paelles, juntament amb **les noies del confocal**. A vosaltres també us agreixo que hagueu tingut moltíssima paciència amb tots els petits detalls que us he demanat, ja sigui sobre els microscopis o les macros. A les labmanagers, la **Sònia** i la **Maite**, per haver estat molt resolutives i haver tingut sempre la voluntat d'ajudar en tot el que hem demanat. I a la **Crisitina** de radioactivitat per haver-se preocupat més que jo per la meva integritat física i per reduir els residus radioactius que després costen tant de processar.

Només falta agrair a l'altre meitat de persones que han fet possible aquesta tesi, si bé no científicament, donant el seu suport incondicional que és igual o més important.

Primer als amics, que ja formarien part de la família. Moltíssimes gràcies **Irene** per haver aguantat tots aquests anys a l'insuportable que ara és el teu company de pis, i els comentaris de: "no puc més", "això no s'acaba" o "no sé si m'ensortiré". Però bueno, amb els teus pastissos que tant bé fas has aconseguit que la cosa sigui molt més fàcil. Espero compensar-ho tot en breus i merci també pel dibuix. **Pau**, gràcies per ser-hi sempre durant aquests anys convulsos i espero que pugui ser així durant molt de temps. També per tots els viatges a PDA i Barcelona, els àpats de pizza i pasta, i el viatge a Itàlia amb la Irene que espero que sigui el primer de molts. Gràcies **Pablo** també per totes aquestes trobades que has muntat a casa teva en els últims anys, i tot i que no és fàcil, han aconseguit que desconnecti. Juntament amb en **Jaco**, però, crec que ja heu celebrat més la tesi els tres que jo. Ja us pagaré tots els bons moments essent sempre el vostre seguidor número ú als partits dels Senglars. I bueno, **David** (o Xifri), com portes la carrera? És broma tet, agafa-t'ho amb calma que té moltíssim mèrit el que estàs fent. Gràcies per deixar-me quedar a dormir a totes les barraques de Girona/Banyoles, per tots els concerts on hem anat (i hem d'anar) i per haver-me donat bons consells en tots els monòlegs que t'he fet. També a en **Lluís**, per proposar-me molts de plans interessants (visites guiades a Badalona, museus, birres, pàdels...), i pels dinars que hem compartit periòdicament aquests últims anys. Amb l'**Aleix**, en **Pablo**, l'**Alex** i en **Joan**, moltes gràcies pels gloriosos anys de la uni. **Maria**, gràcies per totes les xerrades d'aquests últims temps, i per haver-me ensenyat l'Illustrator (l'inDesign el deixarem per una altre ocasió). Gràcies també a tots els que en algun moment m'heu ajudat i escoltat, però que malauradament hem perdut el contacte.

També a la família, que espero que vulguin ser amics a part d'això. Moltes gràcies per aguantar els canvis d'humor dels últims temps, sé que no deu haver estat fàcil. Gràcies papes, per acollir-me tots els caps de setmana que he volgut, anar-me a buscar al tren i sempre cuinar un bon plat d'arròs a la cassola quan ha calgut. Gràcies **Mama**, per aguantar totes les explicacions de què estic fent al laboratori i sobre què va la tesi, fent l'esforç d'entendre alguna cosa. També, gràcies **Papa** per tots els dies que m'has hagut de portar aviadíssim al tren i per deixar-me anar alguns dies a l'hort només per desconnectar una mica. **Daniel**, gràcies per aguantar al pesat i tossut de ton germà, per les bones partides d'escacs i espero que algun dia em portis al rocòdrom. Els tres heu aconseguit que segueixi mitjanament bé fins a dia d'avui i crec que no us ho podré agrair mai prou. Bueno, **tia Montse** ja ho sé que queda pendent que vingui un dia a sopar i al cine, però noia he estat una mica ocupat. Gràcies per parlar-me sempre, encara que jo no ho faci el suficient i per permetre el meu humor, una mica sarcàstic a vegades. Queda pendent un sopar amb en **Kiko** i la **Paulina**

també. A vosaltres moltes gràcies per haver-me anat a buscar a Caldes molts de cops, pels sopars del divendres a la nit per començar bé el cap de setmana, per totes les classes d'anglès que sembla que han donat alguns fruits i per totes les festes chill-out que heu muntat a la vostra terrassa. També a **la família de Palafrugell i Barcelona** per tots els àpats de Nadal i festa major que hem celebrat.

Toca donar les gràcies a les **meves àvies i avis**. Sense tots els cops que heu anat a buscar-nos al cole, les hores que ens heu cuidat, jugant a cartes o anant a fer brunyols, els pans amb fuet, els macarrons i en general tot el que ens heu donat no seríem res. Encara que això de la tesi no sé si farà que trobi feina a partir d'ara, gràcies per les bones xerrades i consells fent l'aperitiu del diumenge, **àvia Mercè**, i per sempre tenir paraules d'ànims i ser un públic fàcil per les meves bromes, **àvia Maria**. Les ganes de l'**avi Francisco** d'aprendre coses sempre i de perdre's a explorar tot el que vingui per davant, una mica a la seva bola com tots els Paytuví, m'acompanyaran per sempre. Però també, totes les lliçons de l'**avi Cristòfol**, explicades aquells estius on anava a l'hort no només a treure herbes i menjar bocates de mitja barra, sinó on també vaig veure l'esperit crític que em sembla que he heretat bastant.

Com sempre, sembla que no tenia gaire res a dir al principi, però al final m'he acabat animant i deixant un discurs que no s'acaba mai (casi com la tesi). Espero no haver-me deixat a ningú, ja que tot i xafardejar totes les vostres tesis per mirar com es feien els agraïments (entre d'altres seccions), he anat una mica ràpid com sempre.

Moltes gràcies per tot i fins sempre!

Frederic

“De totes les llàgrimes que hem plorat,
De totes les batalles que hem lliurat,
De tots els versos que hem escrit,
Ara reneix la nostra força.”

La Gossa Sorda (l’última volta)

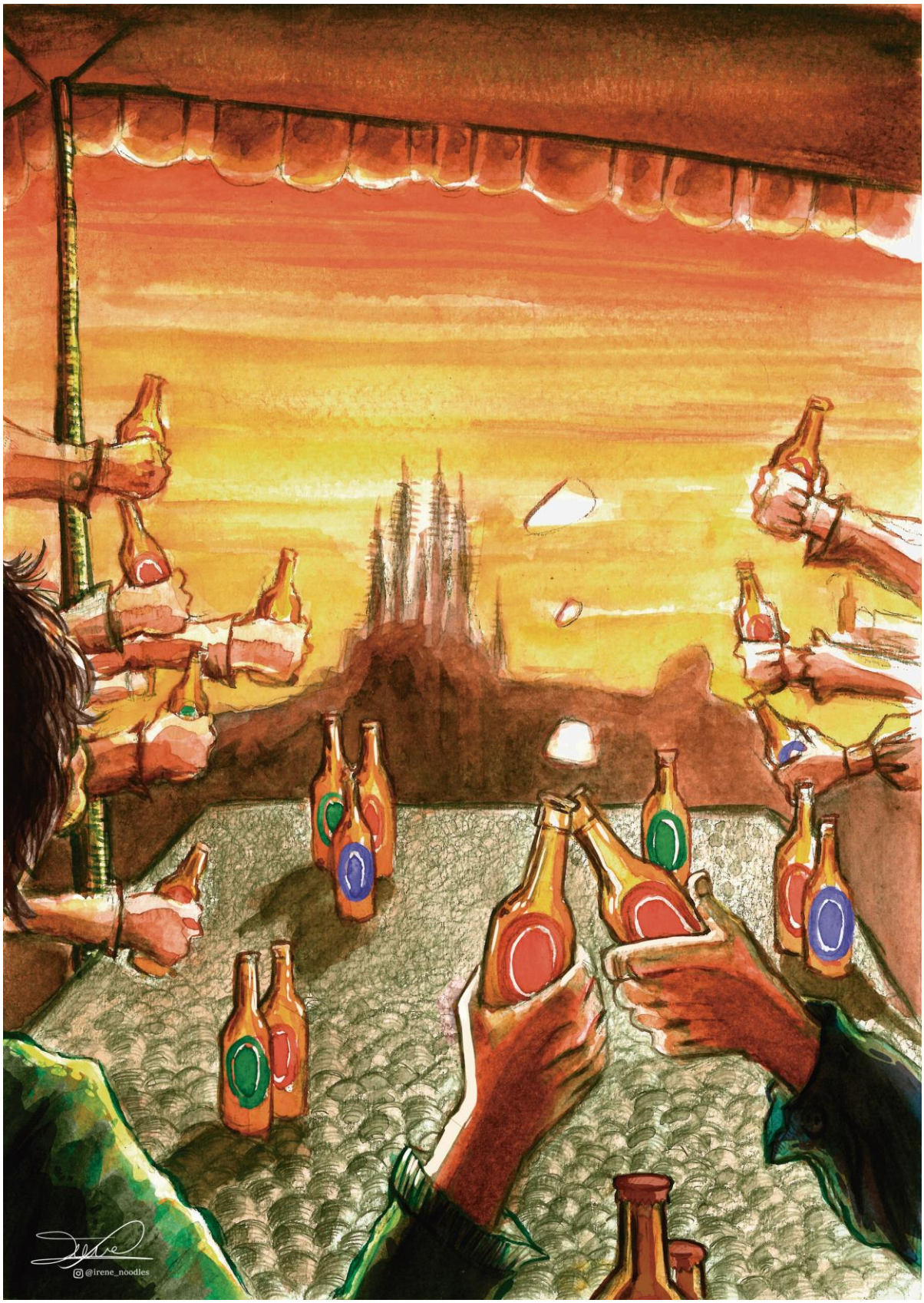
@irene_noodles

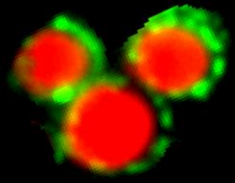

Lipids are essential molecules for many cellular processes such as the formation of cellular membrane bilayers and the production of metabolic energy. They are stored in lipid droplets (LDs), which are specialized and dynamic organelles that supply lipids on demand for these processes.

Cholesterol is necessary for the formation of caveolae, which are subdomains of the plasma membrane (PM) with a role in mechanoprotection, signalling, and endocytosis. Caveolae formation is driven by caveolins, membrane sculpting proteins synthesized in the ER and transported through the Golgi complex (GC) to the PM. During this transport, caveolins bind and distribute cholesterol and other lipids among these compartments, but the mechanisms regulating this process remain elusive. Using a synchronized and short time transfection method, in the first part of this thesis, we show that degradation of caveolins in the ER during the early steps after synthesis is necessary to maintain the correct oligomerization, transport, and stability of these proteins. Moreover, we demonstrate for the first time, that the caveolin family members present a different trafficking, which is determined by a distinct ER exit and GC to ER retrieval of the protein.

Although lipids are fundamental for life, they cause cellular damage in excess, which is generically defined as lipotoxicity. Lipid accumulation is caused by obesity, which surpass the storing capacity of LDs in adipose tissue, and in turn of peripheral tissues such as muscle and liver. Thus, free lipids induce cell death by a plethora of defects in intracellular organelles such as the ER and mitochondria. Lipid species derived from free lipids also interfere with insulin signalling, leading to high blood glucose levels and T2DM onset. However, T2DM is traditionally considered a glucose-promoted disease and, accordingly, its therapeutics have been focused on reducing hyperglycaemia. In the second part of this thesis, LD reduction was targeted as an approach for the treatment of obesity and T2DM. With this purpose, TOFA was used to inhibit acetyl-CoA carboxylase, which plays a central role in lipid metabolism. TOFA reduced the accumulation of LDs and the associated cell death in cellular *in vitro* models of lipotoxicity. Additionally, TOFA stimulated the oxidation of fatty acids, which dramatically reduced weight gain and improved insulin sensitivity in mice models of obesity. Thus, reduction of the LD content in peripheral tissues proved to be a promising target for the treatment of obesity and T2DM.

Frederic Morales Paytuví